Universitá Degli Studi di Ferrara

dottorato di ricerca in Fisica

The role of transverse momentum and spin in unpolarised Semi Inclusive Deep Inelastic Scattering

Dottoranda
Francesca Giordano

Relatore
Prof.ssa Paola Ferretti Dalpiaz

Co-Relatore
Dott. Marco Contalbrigo

A Davide

Contents

1 Introduction **1**

2 Deep Inelastic Scattering **5**
2.1 Inclusive Deep Inelastic Scattering 5
2.1.1 Kinematics 5
2.1.2 Unpolarized DIS cross-section 6
2.2 Semi Inclusive Deep Inelastic Scattering 9
2.2.1 Semi Inclusive cross-section 9
2.3 Non-collinear framework 10
2.3.1 Distribution and Fragmentation functions 12
2.4 The Boer-Mulders effect 19
2.4.1 Experimental status 25
2.4.2 Predictions for the Boer-Mulders effect at HERMES 27
2.5 The Cahn effect 29
2.5.1 Experimental status and global fit 32
2.5.2 Predictions for the Cahn effect at HERMES 36
2.6 Summary 37

3 The HERMES experiment **41**
3.1 The HERA lepton beam 41
3.2 The internal target 42
3.3 The spectrometer 44
3.3.1 The tracking detectors 46
3.3.2 The Particle IDentification detectors 47
3.4 The PID probabilistic algorithm 50
3.5 The Trigger 53
3.6 Data acquisition and structure 58

4 Data selection **61**
4.1 Monte Carlo 61
4.2 HERMES and Monte Carlo productions 64
4.3 Events selection 65
4.3.1 HERMES data 65
4.3.2 Monte Carlo data 67
4.3.3 HERMES and PYTHIA data samples 68

5 Measurement of azimuthal cosine moments **73**
5.1 Experimental extraction method . . . 73
5.1.1 One-dimensional analysis . . . 77
5.1.2 Fake moments with 1-dimensional analysis . . . 79
5.1.3 Monte Carlo test of one-dimensional analysis . . . 83
5.1.4 Multidimensional analysis . . . 85
5.1.5 Fake moments with 5-dimensional analysis . . . 88
5.1.6 Monte Carlo test of 5-dimensional analysis . . . 92
5.2 Systematic studies . . . 92
5.2.1 Top-Bottom discrepancies . . . 92
5.2.2 Target and Recoil magnet effects . . . 100
5.2.3 Vector meson contribution . . . 100
5.2.4 Detector edges . . . 105
5.2.5 Additional moments . . . 108
5.3 Raw ratio results . . . 108

6 The Born moments **117**
6.1 Events migration . . . 117
6.1.1 QED radiative effects. . . . 117
6.1.2 Detector smearing . . . 118
6.2 The unfolding formalism . . . 119
6.2.1 The procedure . . . 119
6.2.2 Monte Carlo test of the unfolding method . . . 122
6.3 Unfolded results . . . 123

7 Final results and interpretations **129**
7.1 Final results . . . 130
7.2 Theoretical predictions and interpretations . . . 132
7.2.1 Cahn contributions . . . 132
7.2.2 Boer-Mulders contributions . . . 139
7.2.3 Predictions from diquark models . . . 141

8 Summary and conclusions **147**

A Results in 5-dimensional binning **149**

B Additional figures **163**

Chapter 1

Introduction

Nam tibi de summa caeli ratione deumque
disserere incipiam et rerum primordia pandam,
..quae nos..appellare suemus et haec eadem usurpare
corpora prima, quod ex illis sunt omnia primis.

T. Lucrezio Caro, *De rerum natura*

Understanding the internal structure of matter is one of the most fascinating puzzle in the history of humankind. In the last century significant progress was made in the investigation of the fundamental constituents of matter, and, according to present understanding, all ordinary matter is composed of a small number of elementary particles, namely leptons and quarks. In particular, the quarks are bound inside the nucleons (protons and neutrons), that, together with electrons (belonging to lepton family), build up the atoms. Electrons and quarks behave as point-like objects, and their interactions are described by Quantum ElectroDynamics (QED) and Quantum ChromoDynamics (QCD) gauge theories, through the exchange of mediator particles, called gauge bosons.

In QED, the theory describing the electromagnetic interactions, the quantities of interest can be easily extracted with the use of a perturbation expansion (*perturbative theory*), as the coupling constant is sufficiently weak: $\alpha \approx 1/137$.

Besides the electromagnetic charge, quarks carry a *color* (*strong*) charge. The interactions between colored particles are described by Quantum ChromoDynamics. The main property of QCD, that makes it different from QED, is that the gauge boson of strong interactions, the gluon, has a color charge itself, contrary to the photon, the intermediator of electromagnetic interactions, which is chargeless. This results in the so-called *running* coupling constant α_s, that becomes weaker with decreasing distances of interaction.

Thus, in short-distances interactions (high momentum transfer), where the coupling constant is small, the quarks inside the nucleons behave as they are quasi-free particles, a phenomenon referred to as *asymptotic freedom*. In this condition, like in QED, a perturbative theory can be developed.

On the contrary, when large distances are involved, the interactions become no-

tably stronger and this results in *confinement* of quarks inside the nucleons. As a consequence of the strong coupling, perturbative techniques are no longer applicable, thus the internal structure of nucleons can not be directly extracted from first principles, and it is based on phenomenological parameterizations. This make experimental investigations a fundamental tool to understand quarks behaviors and interactions within a nucleon.

During the last forty years, it became increasingly evident that Deep Inelastic Scattering (DIS) processes, corresponding to scattering of leptons off nucleon constituents, is one of the most powerful tool in nucleon structure investigation. Starting from the first DIS experiments at the Stanford Linear Accelerator Center (SLAC [1]) in the late 1960s, several other experiments were developed (at CERN, SLAC, DESY, BNL), that allow further understanding of quark distributions and properties inside nucleons. In particular in the late 1980s the EMC experiment at CERN pointed out that the spin of the quarks contributes only for a small fraction (now we know to be around 30%) to the nucleon spin (the so called *spin crisis*), introducing the need of new contributions, like quark orbital momenta or contributions from other nucleon constituents as the gluons.

The *spin crisis* give rise to a number of new experiments, one of which is HERMES (HERa MEasurement of Spin), designed to measure the constituent *helicity* distributions [2, 3, 4], i.e. the distribution of quarks and gluons with their spin aligned or antialigned with the nucleon direction of motion. Besides helicity measurements, a number of other spin-dependent distribution are needed for a global comprehension of nucleon spin structure. Among these, a new family of quark distributions is considered, which are strictly related to the existence of quark intrinsic transverse motion, that has been neglected until recently. The introduction of quark intrinsic motion gives rise to unexpected new exciting aspects of nucleon structure, leading to intense theoretical investigation of this subject. On the contrary, very few measurements were performed until today, thus the experimental knowledge of quark transverse momentum distributions is so far extremely poor.

The aim of this work is to study hadron production in DIS processes, where quark intrinsic transverse motion is considered. The existence of quark transverse momentum give rise to new interesting mechanisms, resulting in azimuthal cosine modulations in hadron directions. Depending on the experimental kinematical region, several contributions can originate the cosine moments. In particular two mechanisms will be considered. The Cahn effect is a pure kinematical effect, generated directly by a non-zero intrinsic transverse motion of quarks within the nucleons [5]. The Boer-Mulders effect is generated by coupling between quark transverse momentum and spin (spin-orbit correlations) [6].

The existing measurements on these subjects are scarce, and the results available average out possible flavour dependence, since they do not separate hadron charges and types. The extraction of the $\langle \mathbf{cos}\, \boldsymbol{\phi_h} \rangle$ and $\langle \mathbf{cos}\, \mathbf{2}\boldsymbol{\phi_h} \rangle$ azimuthal moments at HERMES shown in this work distinguishes, for the first time, between positive and negative hadrons, resulting in a flavour dependent measurement. Thanks to

this flavour sensitivity of the final results, the discrimination power between the theoretical models in the HERMES kinematical regime is enhanced.

The extraction of intrinsic transverse dependent contribution to the cross-section is a very complicated task, since Monte Carlo simulations have to be used in order to disentangle the physical azimuthal dependence from the acceptance and instrumental effects.

Outline of the thesis

This thesis is organized as follows. In the second chapter a theoretical overview of Deep Inelastic Scattering (DIS) formalism will be given. The Inclusive DIS will be defined as a DIS process where only the scattered lepton is detected, then the Semi-Inclusive DIS will be introduced, where one of the produced hadrons is detected in coincidence with the lepton. Via the *factorization theorem* the concept of *parton distribution* and *fragmentation* functions will be introduced, that describe respectively the internal nucleon structure in terms of quarks, and the hadronization process that generates the final observed hadrons starting from the struck quark. Then the existence of a non-zero quark intrinsic transverse momentum will be associated with azimuthal modulations in the produced hadron directions. In particular, the contribution of the so-called *Cahn* and *Boer-Mulders effects* will be discussed, and the theoretical predictions for these mechanisms in the HERMES kinematical region will be addressed. Moreover, the experimental overview of the existing measurements is provided in this chapter.

Chapter three will introduce the HERA accelerator complex at DESY, and the HERMES experiment, describing the main features of its spectrometer, tracking and particle identification algorithms and data acquisition.

Then the basic characteristics of a Monte Carlo simulation are addressed by chapter four, together with data selection criteria both for HERMES and Monte Carlo data.

In chapter five the measurements of the hadron azimuthal distributions are presented, and the systematic uncertainties are investigated by means of a number of dedicated studies. The results obtained in this way are corrected for smearing and residual acceptance effects with an unsmearing formalism described in chapter six.

The final results are discussed in chapter seven, separately for hydrogen and deuterium targets and for positively and negatively charged hadrons, resulting in a flavour dependent measurements. In the same chapter, the results are compared with available theoretical models and predictions for the HERMES kinematical regime.

Finally, in chapter eight a summary of the analysis is provided, and the conclusion are drawn.

Chapter 2

Deep Inelastic Scattering

The comprehension of the inner nucleon structure has been one of the most important issues of particle physics in the last forty years. Already in the late sixties, experiments on high-energy inelastic lepton scatterings performed at SLAC (the Stanford Linear Accelerator Center) brought a surprising result: when probed with high energy-transfer, the proton behaves as if it is made of point-like charged objects. These experiments also pointed out that Deep Inelastic Scattering processes are an useful tool to access nucleon structure, and marked the beginning of high-energy physics as we know it today.

2.1 Inclusive Deep Inelastic Scattering

In lepton-nucleon Deep Inelastic Scattering (DIS) the structure of the nucleon is probed by the interaction of a high energy lepton and a target nucleon, via the exchange of one or more virtual bosons. During the interaction the nucleon breaks up into the final hadronic state X. In Inclusive DIS measurements only the scattered lepton is detected and the final hadronic state is completely ignored.

2.1.1 Kinematics

The DIS process

$$l(\mathbf{k}) + N(\mathbf{P}) \rightarrow l'(\mathbf{k'}) + X(\mathbf{P_X}) \tag{2.1}$$

in single photon exchange approximation is described by the diagram in Fig. 2.1, where $l(\mathbf{k})$ and $N(\mathbf{P})$ ($l'(\mathbf{k'})$ and $X(\mathbf{P_X})$) are the initial (final) lepton and hadronic states, and the quantities in parentheses are the relative four-momenta in the laboratory rest frame (*lab*):

$$\mathbf{k} \overset{lab}{=} (E, \vec{k}) \;\; \mathbf{k'} \overset{lab}{=} (E', \vec{k'}) \;\; \mathbf{P} \overset{lab}{=} (M, 0) \;\; \mathbf{P}_X \overset{lab}{=} (E_X, \vec{P}_X) \tag{2.2}$$

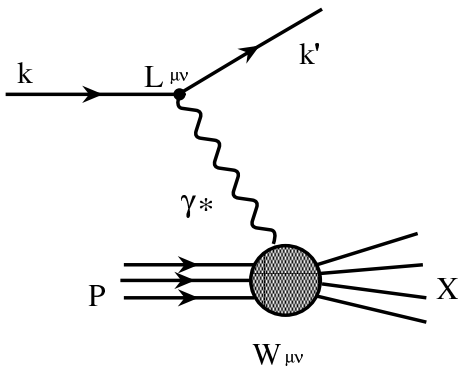

Figure 2.1: Deep Inelastic Scattering event in one photon exchange approximation.

Besides the lepton beam energy (or the center-of-mass energy s) two Lorentz-invariants are needed to describe the reaction. They can be chosen among the following:

$\mathbf{q}^2 = (\vec{k} - \vec{k}')^2$	Squared four momentum of the virtual photon
$Q^2 = -\mathbf{q}^2 \overset{lab}{\approx} -4EE' \sin^2(\theta/2)$	Negative squared four-momentum transfer
$\nu \overset{lab}{=} E - E'$	Energy of the virtual photon
$x = \frac{Q^2}{2\mathbf{Pq}} \overset{lab}{=} \frac{Q^2}{2M\nu}$	Bjørken scaling variable
$y = \frac{\mathbf{P}\cdot\mathbf{q}}{\mathbf{P}\cdot\mathbf{k}} \overset{lab}{=} \frac{E-E'}{E}$	Fractional energy of the virtual photon

where θ is the lepton scattering angle.

2.1.2 Unpolarized DIS cross-section

Assuming one photon exchange, the leptoproduction cross-section can be expressed in a general way as the contraction of the leptonic tensor $L_{\mu\nu}$, describing the emission of a virtual photon by the incident lepton, and the hadronic tensor $W^{\mu\nu}$ that provides informations about the internal structure of the target nucleon:

$$\frac{d\sigma}{dx\, dQ^2} = \frac{\alpha^2}{2sxQ^2} W^{\mu\nu} L_{\mu\nu} \tag{2.3}$$

where $\alpha = e^2/4\pi$ is the electromagnetic coupling constant.

The leptonic tensor, calculated within the Quantum ElectroDynamics (QED) framework, is given by:

$$L_{\mu\nu} = L^{(S)}_{\mu\nu} + L^{(A)}_{\mu\nu} \tag{2.4}$$

where:

$$L^{(S)}_{\mu\nu} = 2(k_\mu k'_\nu + k'_\mu k_\nu - k \cdot k' g_{\mu\nu}), \tag{2.5}$$

$$L^{(A)}_{\mu\nu} = 2i\lambda_e \epsilon_{\mu\nu\rho\sigma} k^\rho k'^\sigma. \tag{2.6}$$

Here the super-scripts (S) and (A) stand for Symmetric and Antisymmetric part of the tensor, $\epsilon_{\mu\nu\rho\sigma}$ is the completely antisymmetric four dimensional tensor, and λ_e is the lepton helicity.

The hadronic tensor in principle could be calculated in Quantum Chromodynamics (QCD), but, since QCD is infrared divergent, the perturbative techniques alone cannot be used. However, using symmetry arguments and conservation laws like Lorentz invariance, Gauge invariance and parity conservation, the hadronic tensor:

$$W_{\mu\nu} = W^{(S)}_{\mu\nu} + W^{(A)}_{\mu\nu} \tag{2.7}$$

can be expressed in a model-independent way in terms of four structure functions F_1, F_2, g_1, g_2:

$$W^{(S)}_{\mu\nu} = \Big(-g_{\mu\nu} - \frac{q_\mu q_\nu}{Q^2}\Big)\frac{F_1(x,Q^2)}{M} + \Big(P_\mu + \frac{\mathbf{P}\cdot\mathbf{q}}{Q^2}q_\mu\Big)\Big(P_\nu + \frac{\mathbf{P}\cdot\mathbf{q}}{Q^2}q_\nu\Big)\frac{F_2(x,Q^2)}{M(\mathbf{P}\cdot\mathbf{q})}, \tag{2.8}$$

$$W^{(A)}_{\mu\nu} = i\epsilon_{\mu\nu\alpha\beta}q^\alpha \frac{1}{\mathbf{P}\cdot\mathbf{q}}\Big[S^\beta g_1(x,Q^2) + \Big(S^\beta - \frac{\mathbf{S}\cdot\mathbf{q}}{\mathbf{P}\cdot\mathbf{q}}P^\beta\Big)g_2(x,Q^2)\Big] \tag{2.9}$$

where $\mathbf{S}$ is the nucleon spin four-vector.

In case of unpolarized scattering the antisymmetric parts of $L_{\mu\nu}$ and $W_{\mu\nu}$ do not contribute and the cross-section becomes:

$$\begin{aligned}\frac{d\sigma}{dx\,dQ^2} &= \frac{\alpha^2}{2sxQ^2}L^{(S)}_{\mu\nu}W^{(S)}_{\mu\nu} = \\ &\frac{2\pi\alpha^2}{Q^4}\Big\{F_1(x,Q^2)y^2 + \Big(1 - y - \frac{Mxy}{2E}\Big)\frac{F_2(x,Q^2)}{x}\Big\}\end{aligned} \tag{2.10}$$

Alternatively, if we define the quantity ϵ as the virtual photon polarization:

$$\epsilon = \frac{1 - y - \frac{1}{4}\gamma^2 y^2}{1 - y + \frac{1}{2}y^2 + \frac{1}{4}\gamma^2 y^2}, \tag{2.11}$$

the cross-section can be expressed in terms of absorption cross-sections for longitudinally (L) and transversely (T) polarized photons:

$$\frac{d\sigma}{dx\,dQ^2} = \frac{2\pi\alpha^2}{Q^4}\frac{y^2}{2x(1-\epsilon)}\{F_T(x,Q^2) + \epsilon F_L(x,Q^2)\} \tag{2.12}$$

where for the transverse component:

$$F_T(x,Q^2) = 2xF_1(x,Q^2) \tag{2.13}$$

Lepton kinematics	
$\mathbf{k} = (E, \vec{k})$, $\mathbf{k'} = (E', \vec{k'})$	Four momenta of the initial and final state leptons
$s^2 = (\mathbf{P} + \mathbf{k})^2 \overset{lab}{\approx} M^2 + 2ME$	Squared center-of-mass energy
Target kinematics	
$\mathbf{P} = (M, 0)$	Four momentum of the initial nucleon
Virtual photon kinematics	
$\mathbf{q}^2 = (\mathbf{k} - \mathbf{k'})^2$	Squared four-momentum of the virtual photon
$Q^2 = -\mathbf{q}^2 \overset{lab}{=} -4EE' sin^2(\theta/2)$	Negative squared four-momentum transfer
$\nu \overset{lab}{=} E - E'$	Energy of the virtual photon
$x = \frac{Q^2}{2\mathbf{P}\cdot\mathbf{q}} \overset{lab}{=} \frac{Q^2}{2M\nu}$	Bjørken scaling variable
$y = \frac{\mathbf{P}\cdot\mathbf{q}}{\mathbf{P}\cdot\mathbf{k}} \overset{lab}{=} \frac{E-E'}{E}$	Fractional energy of the virtual photon
Semi-inclusive variables	
$W^2 = (\mathbf{P} + \mathbf{q})^2 \overset{lab}{=} M^2 + 2M\nu - Q^2$	Squared invariant mass of final hadronic state
$\mathbf{P_h} = (E_h, \vec{P}_h)$	Four momentum of the outgoing hadron
$\vec{P}_{h\perp}$	$\mathbf{P_h}$ component transverse to the virtual-photon direction
$z = \frac{\mathbf{P}\cdot\mathbf{P_h}}{\mathbf{P}\cdot\mathbf{q}} \overset{lab}{=} \frac{E_h}{\nu}$	Fractional energy of the outgoing hadron
$x_F = \frac{P_h^{\parallel cm}}{\lvert\vec{q}\rvert} \overset{lab}{\approx} \frac{2P_h^{\parallel cm}}{W}$	Feynman variable

Table 2.1: Semi-inclusive Deep Inelastic Scattering fundamental variables.

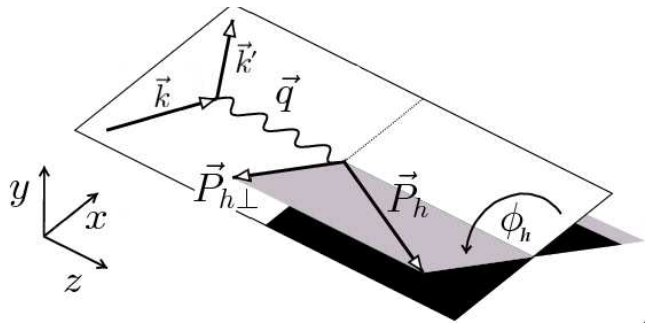

Figure 2.2: Definition of the azimuthal angle ϕ_h between the scattering plane (white) and the hadron production plane (grey).

while for the longitudinal component:

$$F_L(x, Q^2) = (1 + \gamma^2)F_2(x, Q^2) - 2xF_1(x, Q^2). \tag{2.14}$$

2.2 Semi Inclusive Deep Inelastic Scattering

Semi Inclusive Deep Inelastic Scattering is a DIS process in which at least one of the produced hadrons is detected in coincidence with the scattered beam:

$$l(\mathbf{k}) + N(\mathbf{P}) \rightarrow l'(\mathbf{k}') + h(\mathbf{P}_h) + X(\mathbf{P}_X) \tag{2.15}$$

where h is the detected hadron, X is the target remnant and the quantities in parentheses their four-momenta.

The detected hadron has fractional energy transferred from the photon $z = E_h/\nu$. To select the hadrons originated directly by the struck quark (*current fragments*) from the ones originated from the target remnants (*target fragments*), it is useful to define the Feynman variable $x_F = 2P_h^{\parallel\, cm}/W$, where W is the invariant mass of final hadronic state and $P_h^{\parallel\, cm}$ indicates the component of the hadron momentum parallel to the virtual photon direction in the photon-nucleon center-of-mass system: the requirement $x_F > 0$ selects the current region.

2.2.1 Semi Inclusive cross-section

As for inclusive processes, the differential cross-section can be calculated using the leptonic and the hadronic tensor:

$$\frac{d\sigma}{dx\, dy\, dz} = \frac{\alpha^2}{4zs^2x^2y} W^{\mu\nu} L_{\mu\nu}, \tag{2.16}$$

and, with the definition of the kinematical factors $A(y)$ and $B(y)$

$$\begin{aligned} A(y) &= \frac{y^2}{2(1-\epsilon)} \sim (1 - y + 1/2y^2) \\ B(y) &= \frac{y^2}{2(1-\epsilon)}\epsilon \sim (1-y) \end{aligned} \tag{2.17}$$

the unpolarized cross-section can be written in terms of structure functions:

$$\frac{d\sigma}{dx\,dy\,dz} = \frac{\alpha^2}{xyQ^2}\Big(1 + \frac{\gamma^2}{2x}\Big)\{A(y)\,F_{UU,T} + B(y)\,F_{UU,L}\} \tag{2.18}$$

where the subscripts UU stand for Unpolarized beam and target, while the subscript T or L indicate the Transverse or Longitudinal polarization of the virtual photon. The structure functions appearing here are connected with the inclusive structure functions $F_T(x, Q^2)$ and $F_L(x, Q^2)$ by:

$$\sum_h \int dz\, z F_{UU,T}(x, z, Q^2) \;=\; F_T(x, Q^2) \tag{2.19}$$

$$\sum_h \int dz\, z F_{UU,L}(x, z, Q^2) \;=\; F_L(x, Q^2) \tag{2.20}$$

where the sum is performed over all the hadrons in the final state.

2.3 Non-collinear framework

In the Quantum ChromoDynamics framework the virtual photon interacts elastically with point-like spin-$\frac{1}{2}$ constituents of the nucleons, called quarks. The quark momentum is

$$\vec{\kappa} = (x\vec{P}, \vec{\kappa}_T) \tag{2.21}$$

and equation 2.18 is the well known unpolarized cross-section in the approximation of quarks collinear to the direction of motion (*collinear approximation*): $\kappa_T = |\vec{\kappa}_T| = 0$. The intrinsic transverse momentum κ_T of the quarks is usually neglected, since it is small compared to its longitudinal component $x\vec{P}$. Nevertheless, if the intrinsic κ_T is taken into account, an azimuthal dependence in the outgoing hadron direction is generated and new azimuthal dependent structure functions appear in the cross-section [7]:

$$\begin{aligned} \frac{d\sigma}{dx\,dy\,dz\,dP_{h\perp}^2\,d\phi_h} = \frac{\alpha^2}{xyQ^2}(1 + \frac{\gamma^2}{2x})\{&A(y)\,F_{UU,T} + B(y)\,F_{UU,L} + \\ &C(y)\,\cos\phi_h F_{UU}^{\cos\phi_h} + B(y)\,\cos 2\phi_h F_{UU}^{\cos 2\phi_h}\} \end{aligned} \tag{2.22}$$

where $P_{h\perp} = |\vec{P}_{h\perp}|$ is the momentum of the hadron transverse to the virtual-photon direction, ϕ_h is the azimuthal angle of the hadron plane around the virtual-photon

direction (see picture 2.2):

$$\phi_h = \frac{\vec{q}\times\vec{k}\ \cdot\ \vec{P}_h}{|\vec{q}\times\vec{k}\ \cdot\ \vec{P}_h|} cos^{-1}\left(\frac{\vec{q}\times\vec{k}\ \cdot\ \vec{q}\times\vec{P}_h}{|\vec{q}\times\vec{k}||\vec{q}\times\vec{P}_h|}\right) \tag{2.23}$$

and the kinematical factor $C(y)$ is defined as follow:

$$C(y) = \frac{y^2}{2(1-\epsilon)}\sqrt{2\epsilon(1-\epsilon)} \sim (2-y)\sqrt{1-y}. \tag{2.24}$$

The aim of this work is to study the unpolarized cross-section as defined in equation 2.22, and to get access to the structure functions $F_{UU}^{\cos\phi_h}$ and $F_{UU}^{\cos 2\phi_h}$ by measuring the $\cos\phi_h$ and the $\cos 2\phi_h$ cross-section modulations. The modulations can be extracted via the so called $\langle\cos n\phi_h\rangle$-moments

$$\langle\cos n\phi_h\rangle \ = \ \frac{\int \cos n\phi_h\, d^5\sigma}{\int d^5\sigma} \tag{2.25}$$

where $\int d^5\sigma$ is the short-hand notation for the expression:

$$\int d^5\sigma = \int dx\, dy\, dz\, dP_{h\perp}^2\, d\phi_h \frac{d^5\sigma}{dx\, dy\, dz\, dP_{h\perp}^2\, d\phi_h} \tag{2.26}$$

After integrating over ϕ_h in small kinematical intervals [1], the relation between the moments and the structure functions reads:

$$\begin{aligned} \langle\boldsymbol{\cos\phi_h}\rangle \ &= \ \frac{1}{2}\frac{C(y)\, F_{UU}^{\cos\phi_h}}{A(y)\, F_{UU,T}} \\ \langle\boldsymbol{\cos 2\phi_h}\rangle \ &= \ \frac{1}{2}\frac{B(y)\, F_{UU}^{\cos\phi_h}}{A(y)\, F_{UU,T}} \end{aligned} \tag{2.27}$$

where the structure function $F_{UU,L}$ has been neglected as it is compatible with zero in first approximation [7].

Depending on the experimental kinematical region, several contributions can originate the $\langle\boldsymbol{\cos\phi_h}\rangle$ moments, and they are described in some extent in the next section.

In particular two mechanisms are considered in the following:

the Cahn effect: a pure kinematical effect, generated if a non-zero intrinsic transverse motion of quarks is taken into account, already pointed out by R. Cahn in 1978 [5] (see section 2.5);

[1] In the multidimensional analysis adopted in this thesis the event sample is binned in each of the relevant variables (*full differential analysis*).

the Boer-Mulders effect: a new interesting mechanism introduced recently (1997) by D. Boer and P. J. Mulders [6]; in this case the quark transverse momentum couples to the quark transverse spin, generating new and unexpected effects[2] (see section 2.4).

These mechanisms are expected to give important contributions to the azimuthal dependence of the unpolarized cross-section in the region of low hadron transverse momenta ($P_{h\perp}^2 << Q^2$) accessed at HERMES. Large transverse hadron momenta ($P_{h\perp}^2 \gtrsim Q^2$) cannot be generated by the small amount of intrinsic motion [9], and in this case the major azimuthal contribution is due to higher order pQCD processes, like gluon radiation [10].

2.3.1 Distribution and Fragmentation functions

The cross-section can be factorized [11] into a term that describes the photon-quark elementary process (exactly evaluated in perturbative QED), and two non-perturbative functions: Φ accounting for the quarks distribution inside the nucleon, and Δ describing the fragmentation process that generates the final observed hadron from the struck quark (see fig. 2.3):

$$W^{\mu\nu} = \frac{z}{M} \sum_q e_q^2 \int d^2\vec{p}_T d^2\vec{\kappa}_T \delta^2(\vec{p}_T + \vec{q}_T - \vec{\kappa}_T) Tr\{\Phi^q(x, \vec{\kappa}_T)\gamma^\mu \Delta^q(z, \vec{p}_T)\gamma^\nu\} \quad (2.28)$$

where q indicates the quark flavour, e_q is the electric charge of quark with flavour q, the sum is performed over all the different quark and anti-quark flavours, and $\vec{p}_T$ is the random transverse momentum the quark acquires during the fragmentation. If we assume the fragmentation process to be collinear, the transverse momentum of the struck quark will be the same before and after the reaction and the transverse momentum of the observed hadron is $P_{h\perp} = z\kappa_T$, where z is the fraction of the virtual photon energy transferred to the hadron during the interaction. Since the fragmentation process is not collinear, the azimuthal asymmetry is diluted by the random transverse momentum $p_T = |\vec{p}_T|$ added by the quark decay. The observed hadron averaged transverse momentum therefore can be written as:

$$\langle P_{h\perp}^2 \rangle = \langle p_T^2 \rangle + z^2 \langle \kappa_T^2 \rangle. \quad (2.29)$$

Leading twist

In low transverse momentum regime an expansion of the hadronic tensor in powers of M/Q can be performed [12], and the leading term of this expansion is called leading twist term. For the unpolarized cross-section the first non-zero term (leading twist) is $\propto 1/Q^2$ (as seen in eq. 2.22), the twist two. The complete cross-section expansion can be found in [13], here only leading twist ($\propto 1/Q^2$) and first sub-leading

[2] A complete review on transverse polarization and momentum phenomena is given in [8].

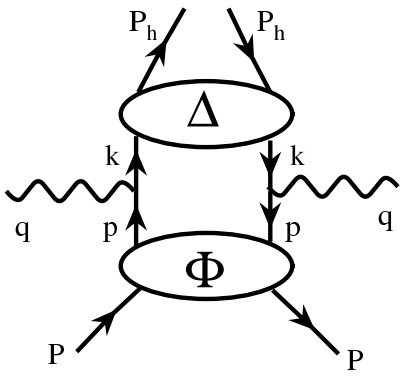

Figure 2.3: Handbag diagram for Semi Inclusive Deep Inelastic Scattering.

twist ($\propto 1/Q^3$) are considered.

If $\psi(\boldsymbol{\xi})$ is the quark field in the space-time position $\boldsymbol{\xi}$, the quark-quark correlator distribution function Φ^q, defined as

$$\Phi^q_{ij}(x,\kappa_T) = \int d^4\xi e^{i\boldsymbol{\kappa}\cdot\boldsymbol{\xi}} \langle P|\overline{\psi}_j(\mathbf{0})\,\psi_i(\boldsymbol{\xi})|P\rangle, \tag{2.30}$$

can be decomposed in a basis of Dirac matrices[3] so that at leading twist it can be written in terms of six distribution functions (DF) depending on x and κ_T^2 [7]:

$$\Phi^q(x,\kappa_T) = \frac{1}{2}\Big\{ f_1 \not{n}_+ - f_{1T}^{\perp}\frac{\epsilon_T^{\rho\sigma}\kappa_{T\rho}S_{T\sigma}}{M}\not{n}_+ + g_{1s}\gamma_5\not{n}_+ + h_{1T}\frac{[\not{S}_T,\not{n}_+]\gamma_5}{2} \\ h_{1s}^{\perp}\frac{[\not{\kappa}_T,\not{n}_+]\gamma_5}{2M} + ih_1^{\perp}\frac{[\not{\kappa}_T,\not{n}_+]}{2M}\Big\} \tag{2.31}$$

In the above equation $n_\pm$ are the light-cone components, $\epsilon_T^{\rho\sigma}$ is the transverse tensor whose only non-zero components are $\epsilon_T^{12} = -\epsilon_T^{21} = 1$ and $S_T\,(= |\vec{S}_T|)$ is the transverse nucleon spin. The subscript s in g_{1s} indicate the shorthand notation for:

$$g_{1s}(x,\vec{\kappa}_T) = S_L g_{1L}(x,\kappa_T^2) - \frac{\vec{\kappa}_T\cdot\vec{S}_T}{M} g_{1T}(x,\kappa_T^2) \tag{2.32}$$

where S_L is the longitudinal nucleon spin, and the same for $h_{1s}^{\perp}$. In general, the letters f, g and h stand respectively for unpolarized, longitudinal and transverse polarized quark distributions, the subscripts L and T indicate a non-zero Longitudinal and Transverse nuclear polarization, and the superscript $\perp$ indicate a function that vanishes when integrated over $\vec{\kappa}_T$. A summary of the leading twist distribution functions with relative polarization is given in table 2.2.

At leading twist, the DFs have a probabilistic interpretation: they are referred to as probability densities of finding a quark with momentum fraction x and intrinsic transverse momentum $\vec{\kappa}_T$ inside the nucleon. In particular, in the collinear case (if

[3] $\mathbf{1}, \gamma^\mu, \gamma^\mu\gamma_5, i\sigma^{\mu\nu}\gamma_5$, where $\sigma^{\mu\nu} = \frac{i}{2}[\gamma^\mu,\gamma^\nu]$

N/q	U	L	T
U	f_1		$h_1^\perp$
L		g_1	$h_{1L}^\perp$
T	$f_{1T}^\perp$	$g_{1T}^\perp$	h_1, $h_{1T}^\perp$

Table 2.2: Schematic of leading twist distribution functions. Horizontal labels identify the quark polarization, the vertical one give the nucleon polarization: U, L and T stand respectively for unpolarized, longitudinal polarized and transversely polarized status.

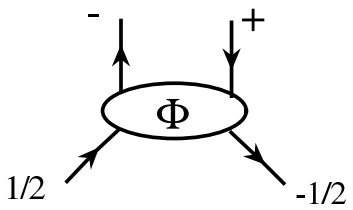

Figure 2.4: Schematic of a chiral-odd distribution function in the helicity basis: the labels refer to the spin state of of the target $(1/2, -1/2)$ and of the struck parton $(+, -)$. As shown in the picture, the peculiarity of a chiral-odd function is the simultaneous flip of the quark and the target spin, forbidden in inclusive DIS due to helicity invariance.

the Φ^q correlator is integrated over $\vec{\kappa}_T$), three distribution functions completely describe the internal nucleon structure at leading twist: $f_1(x)\,(= \int d^2\vec{\kappa}_T\, f_1(x, \kappa_T^2))$ [14], the well known unpolarized distribution function that describes the momentum quark distribution within an unpolarized nucleon, the quark helicity distribution function $g_1(x)\,(= \int d^2\vec{\kappa}_T\, g_{1L}(x, \kappa_T^2))$ [2, 3, 4], which describes quark longitudinal polarization in longitudinally polarized nucleon, and the transversity distribution function $h_1(x)$ $(= \int d^2\vec{\kappa}_T\, (h_{1T}(x, \kappa_T^2) - \frac{\kappa_T^2}{2M^2} h_{1T}^\perp(x, \kappa_T^2)))$ [15, 16], describing transverse polarized quarks in transverse polarized nucleons.

Among the other five distribution functions, $f_{1T}^\perp$ is the so-called Sivers function [17], interpreted as unpolarized quark distribution in a transversely polarized nucleon, and $h_1^\perp$ [6] is the Boer-Mulders distribution functions, which can be interpreted as the quark transverse spin distribution in an unpolarized hadron. Both these functions are T-odd under naïve time reversal transformation [4].

Initially T-odd functions were supposed to vanish due to time reversal invariance, but a number of experimental results [18, 19] provide evidence for non-zero T-odd distribution functions (like the Sivers function $f_{1T}^\perp(x)$). Meanwhile a possible mechanism was introduced that could produce T-odd effects without violating invariance principle, as described in section 2.4.

The Boer-Mulders function is also a chiral-odd object like the transversity DF; the reason is that the Boer-Mulders and the transversity DFs involve a simultaneous spin flip of the struck quark and the target, as shown in figure 2.4. Assuming

[4] The naïve time reversal transformation is defined as standard time reversal, but without the interchange of initial and final states.

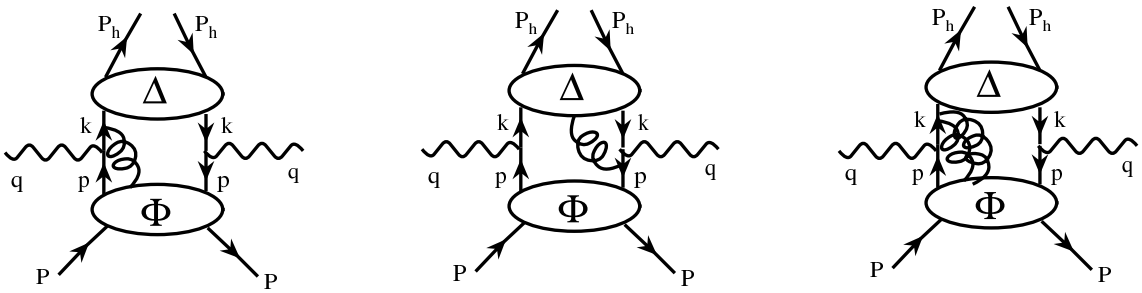

Figure 2.5: Examples of handbag diagrams for SIDIS processes with one or more additional hard gluons.

negligible current quark masses, chirality and helicity coincide [20], thus chiral-odd processes are forbidden by helicity conservation at the photon quark vertex. Therefore chiral-odd functions can be measured only in conjunction with another chiral-odd object, restoring the global chiral symmetry of the reaction. For instance the transversity DF has been already probed in polarized SIDIS [18, 19] coupled to the chiral-odd Collins fragmentation function, described below.

Similarly to the correlator function, the fragmentation correlator can be parameterized with the use of fragmentation functions (FF) [7]:

$$\begin{aligned}\Delta^q(z,\vec{p}_T) &= \frac{1}{2z}\sum_X \int d^4\boldsymbol{\xi}\, e^{i\mathbf{p}\cdot\boldsymbol{\xi}}\langle 0|\psi_j(\boldsymbol{\xi})\,\overline{\psi}(\mathbf{0})|0\rangle \\ &= \frac{1}{2}\Big\{D_1 \not{n}_- + iH_1^\perp \frac{[p_T,\not{n}_-]}{2M}\Big\}.\end{aligned} \tag{2.33}$$

Like the DFs, the FFs have a probabilistic interpretation: they represent the probability for the struck quark of flavour q to fragments into a final hadron h. The two leading twist fragmentation functions are the well known unpolarized FF $D_1(z,p_T^2)$ [3, 4] which describes the probability for a quark to fragment into a hadron with a certain fraction z of the virtual photon energy and with transverse momentum p_T, and the Collins FF $H_1^\perp(z,p_T^2)$ [21], which gives the probability for a transversely polarized quark to fragment in an unpolarized hadron. As previously anticipated, the Collins function is chiral-odd, therefore it can be measured only in conjunction with another chiral-odd functions, as the transversity or the Boer-Mulders function. It is also T-odd, but, unlike the DFs, a T-odd FF in principle is not forbidden because of the unknown hadronic final state X (see sec. 2.4).

The Collins FF coupled to the Boer-Mulders DF originates the already mentioned Boer-Mulders effect, described in detail in section 2.4.

First sub-leading twist

If we consider the expansion at first sub-leading twist (twist three), the structure of the hadronic tensor becomes more complicated since we need to take into account photon-quark interactions with an additional gluon leg as in figure 2.5.

At twist-three the quark-quark correlator can be written in terms of eighteen distribution functions:

$$\begin{aligned}\Phi^q(x,\vec{\kappa}_T) = \frac{1}{2}\Big\{ & f_1 \not{n}_+ - f_{1T}^{\perp}\frac{\epsilon_T^{\rho\sigma}\kappa_{T\rho}S_{T\sigma}}{M}\not{n}_+ + g_{1s}\gamma_5\not{n}_+ + h_{1T}\frac{[\not{S}_T,\not{n}_+]\gamma_5}{2} + \\ & h_{1s}^{\perp}\frac{[\not{\kappa}_T,\not{n}_+]\gamma_5}{2M} + ih_1^{\perp}\frac{[\not{\kappa}_T,\not{n}_+]}{2M}\Big\} \\ + \frac{M}{2P^+}\Big\{ & e - ie_s\gamma_5 - e_T^{\perp}\frac{\epsilon_T^{\rho\sigma}\kappa_{T\rho}S_{T\sigma}}{M} + f^{\perp}\frac{\not{\kappa}_T}{M} - f_T'\epsilon_T^{\rho\sigma}\gamma_\rho S_{T\sigma} \\ & - f_s^{\perp}\frac{\epsilon_T^{\rho\sigma}\gamma_{T\rho}\kappa_{T\sigma}}{M} + g_T'\gamma_5\not{S}_T + g_s^{\perp}\gamma_5\frac{\not{\kappa}_T}{M} - g^{\perp}\gamma_5\frac{\epsilon_T^{\rho\sigma}\gamma_{T\rho}\kappa_{T\sigma}}{M} \\ & + h_s\frac{[\not{n}_+,\not{n}_-]\gamma_5}{2} + h_T^{\perp}\frac{[\not{S}_T,\not{\kappa}_T]\gamma_5}{2M} + ih\frac{[\not{n}_+,\not{n}_-]}{2}\Big\}\end{aligned} \tag{2.34}$$

where the first curly parentheses include the leading twist DFs described in the last section, while in the second parentheses the twist-three DFs are listed.

With the proper gauge, the twist three DFs incorporate leading and higher twist effects: they can be decomposed in a sum of twist-two DFs and quark-gluon-quark interaction-dependent terms, indicating in the following by a tilde. The T-even twist-three terms become [7]:

$$\begin{aligned} xe &= x\tilde{e} + \frac{m}{M}f_1 \\ xf^{\perp} &= x\tilde{f}^{\perp} + f_1 \\ xg_T' &= x\tilde{g}_T' + \frac{m}{M}h_{1T} \\ xg_L^{\perp} &= x\tilde{g}_L^{\perp} + \frac{m}{M}h_{1L}^{\perp} \\ xh_L &= x\tilde{h}_L + \frac{\kappa_T^2}{M^2}h_{1L}^{\perp} + \frac{m}{M}g_{1L} \\ xh_T &= x\tilde{h}_T - h_1 + \frac{\kappa_T^2}{2M^2}h_{1T}^{\perp} + \frac{m}{M}g_{1T} \\ xh_T^{\perp} &= x\tilde{h}_T^{\perp} + h_1 + \frac{\kappa_T^2}{2M^2}h_{1T}^{\perp} \end{aligned} \tag{2.35}$$

and the T-odd functions are instead given by:

$$\begin{aligned}
xe_L &= x\tilde{e}_L \\
xe_T &= x\tilde{e}_T \\
xe_T^{\perp} &= x\tilde{e}_T^{\perp} + \frac{m}{M} f_{1T}^{\perp} \\
xf_T' &= x\tilde{f}_T' + \frac{\kappa_T^2}{M^2} f_{1T}^{\perp} \\
xf_T^{\perp} &= x\tilde{f}_T^{\perp} + f_{1T}^{\perp} \\
xf_L^{\perp} &= x\tilde{f}_L^{\perp} \\
xg^{\perp} &= x\tilde{g}^{\perp} + \frac{m}{M} h_1^{\perp} \\
xh &= x\tilde{h} + \frac{\kappa_T^2}{M^2} h_1^{\perp}
\end{aligned} \tag{2.36}$$

The notation for the subscripts L and T and the superscript $\perp$ as well as the letters f, g and h have the same meaning as for the leading functions, while the letter e, which has no counterpart at leading twist, is related to quark mass terms. Contrary to the the leading DFs, the twist-three DFs have no simple partonic interpretation, because of their dependence on the quark-gluon-quark interaction terms.

In the following the Wandzura-Wilczek [7] (WW) approximation will be assumed, meaning that the quark-gluon-quark interaction terms are neglected, and the higher twist DFs can be expressed in terms of the DF already introduced in the previous paragraph.

This approximation is tested experimentally only for one term of the DFs ($\tilde{g}_T'$) [22, 23, 24, 25] underlined by a tilde, and lattice calculation [26, 27] and the instanton model of the QCD vacuum [28] support the WW approximation for few more terms, but the general smallness of twist-three interaction terms remains to be tested in the experiments.

At first sub-leading twist, the fragmentation correlator for unpolarized hadrons can be parameterized with the use of fragmentation functions as follow:

$$\begin{aligned}
\Delta^q(z, \vec{p}_T) = &\frac{1}{2}\Big\{ D_1 \not{n}_- + i H_1^{\perp} \frac{[p_T, \not{n}_-]}{2M} \Big\} \\
&+ \frac{M_h}{2P_h^-}\Big\{ E + D^{\perp} \frac{\not{p}_T}{M_h} + iH \frac{[\not{n}_-, \not{n}_+]}{2} + G^{\perp}\gamma_5 \frac{\epsilon_T^{\rho\sigma}\gamma_\rho p_{T\rho}}{M_h} \Big\}
\end{aligned} \tag{2.37}$$

where the first and the second parentheses include respectively the leading twist and the twist-three FFs. As the DFs, also the FFs notation follows specific rules: the letter D, G, H and E are related to unpolarized, longitudinal and transverse polarized quarks and quark mass terms, respectively. The twist-three FFs have no probabilistic interpretation like the twist-three DFs. In fact, as for the DFs, there exist relations between the the twist-three FF of equation 2.37 and the quark-gluon-

quark interaction-dependent FFs labeled by a tilde:

$$\begin{aligned}
\frac{E}{z} &= \frac{\tilde{E}}{z} + \frac{m}{M_h} D_1 \\
\frac{D^\perp}{z} &= \frac{\tilde{D}^\perp}{z} + D_1 \\
\frac{G^\perp}{z} &= \frac{\tilde{G}^\perp}{z} + \frac{m}{M_h} H_1^\perp \\
\frac{H}{z} &= \frac{\tilde{H}}{z} + \frac{p_T^2}{M_h^2} H_1^\perp
\end{aligned} \tag{2.38}$$

Leptoproduction cross-section

The above parameterizations can be now used to calculate the leptoproduction cross-section at first sub-leading twist. To simplify the notation we can define the convolution integral as:

$$C[wfD] = x \sum_q e_q^2 \int d^2\vec{p}_T d^2\vec{\kappa}_T \delta^2(\vec{\kappa}_T - \vec{p}_T - \vec{P}_{h\perp}/z)\, w(\vec{\kappa}_T, \vec{p}_T) f^q(x, \kappa_T^2) D^q(z, p_T^2) \tag{2.39}$$

The unpolarized cross-section (eq. 2.22) is obtained by means of the quark distribution (eq. 2.34) and fragmentation (eq. 2.37) correlators, with the use of the relations 2.35, 2.36 and 2.38, once the terms related to polarized target and beam (the ones with subscripts L or T and s) are neglected [7]:

$$\begin{aligned}
\frac{d\sigma}{dx\, dy\, dz\, dP_{h\perp}^2\, d\phi_h} &= \frac{\alpha^2}{xyQ^2} \frac{y^2}{2(1-\epsilon)} \Big(1 + \frac{\gamma^2}{2x}\Big) \\
&\Big\{ C[f_1 D_1] + \epsilon \cos 2\phi_h C\Big[- \frac{2(\hat{h}\cdot\vec{p}_T)(\hat{h}\cdot\vec{\kappa}_T) - \vec{p}_T\cdot\vec{\kappa}_T}{M M_h} h_1^\perp H_1^\perp \Big] \Big\} \\
&+ \Big\{ \sqrt{2\epsilon(1+\epsilon)} \cos\phi_h \Big[\Big(\frac{2M}{Q} C\Big[- \frac{\hat{h}\cdot\vec{p}_T}{M_h} \Big(x h H_1^\perp + \frac{M_h}{M} f_1 \frac{\tilde{D}^\perp}{z} \Big) - \\
&\qquad \frac{\hat{h}\cdot\vec{\kappa}_T}{M} \Big(x f^\perp D_1 + \frac{M_h}{M} h_1^\perp \frac{\tilde{H}}{z} \Big) \Big] \Big) \Big] \Big\}
\end{aligned} \tag{2.40}$$

In the above cross-section expression, the first curly brackets include the leading twist terms, containing a $\cos 2\phi_h$ modulation term, whereas in the second brackets the twist-three terms appear, together with a $\cos\phi_h$ modulation.

Leading terms. At leading twist in the SIDIS unpolarized cross-section only two terms enter the game; the first is proportional to the convoluted product of the unpolarized DF f_1 and the unpolarized FF D_1, the second term is the convoluted product of the T-odd and chiral-odd Boer-Mulders ($h_1^\perp$, also called the *transversity* of the quarks) and Collins ($H_1^\perp$) functions. The partonic interpretation of the above DF and FF has been previously discussed: in any case it is interesting to notice that

thanks to the presence of T-odd effects an azimuthal $\cos 2\phi_h$ modulation appears at leading twist in the unpolarized cross-section 2.40 (see sec. 2.4) which can be described by the structure function

$$F_{UU,BM}^{\cos 2\phi_h} \approx -C\Big[\frac{2(\hat{h}\cdot\vec{p}_T)(\hat{h}\cdot\vec{\kappa}_T) \;-\; \vec{p}_T\cdot\vec{\kappa}_T}{M M_h}\, h_1^\perp H_1^\perp\Big] \tag{2.41}$$

First sub-leading twist. At twist three there exist different possible sources of the $\cos\phi_h$ modulation; in particular this work concentrates on two contributions neglecting the quark-gluon-quark interactions (WW): one is again the Boer-Mulders effect (see sec. 2.4):

$$F_{UU,BM}^{\cos\phi_h} \approx \frac{2M}{Q} C\Big[-\frac{\hat{h}\cdot\vec{p}_T}{M_h} h_1^\perp H_1^\perp\Big] \tag{2.42}$$

and the other is due to the Cahn effect (see sec. 2.5):

$$F_{UU,Cahn}^{\cos\phi_h} \approx \frac{2M}{Q} C\Big[-\frac{\hat{h}\cdot\vec{\kappa}_T}{M} f_1 D_1\Big] \tag{2.43}$$

The three azimuthal modulation contributions of equations 2.41, 2.42 and 2.43 have been object of intense theoretical works in the last few years, even if only scarce experimental data have been published on this subject. In the next sections the theoretical frameworks and predictions are described in some detail, as well as the actual status of the experimental measurements.

2.4 The Boer-Mulders effect

The existence of a non-zero intrinsic transverse motion of quarks, besides resulting in an azimuthal dependence of the produced hadron (eq. 2.40), leads to new leading non-trivial mechanisms which are T-odd. One of these mechanisms is the Boer-Mulders effect, which involves the convolution of the T-odd DF $h_1^\perp$ [6] and the T-odd Collins FF $H_1^\perp$ [21].

The Boer-Mulders distribution function

The Boer-Mulders distribution function $h_1^\perp$ was introduced in 1997 by D. Boer and P. J. Mulders [6] in relation with leading order T-odd effects due to the existence of non-zero quark intrinsic transverse motion. Sivers already in 1990 proposed the existence of a T-odd distribution function (the Sivers DF $f_{1T}^\perp$) to explain the single spin asymmetries measured in Drell-Yan processes ($pp \to \pi X$) [17], but initially the T-odd functions were supposed to vanish due to time-reversal invariance [21]. Only recently [29] a possible mechanism was introduced that could produce T-odd

effects without violating invariance principle, in which the struck quark, after the interaction with the virtual boson, re-interact with the target remnant. These Final State Interactions (FSI) can be incorporated into κ_T-dependent parton distribution functions by introducing a gauge link L between the quarks fields during the interaction [30, 31, 32], so that the quark-quark correlator (eq. 2.30) becomes:

$$\Phi^q_{ij}(x, \vec{\kappa}_T) = \int d^4\boldsymbol{\xi} e^{i\boldsymbol{\kappa}\cdot\boldsymbol{\xi}} \langle P|\overline{\psi}_j(\mathbf{0})\, L(\mathbf{0}, \boldsymbol{\xi})\, \psi_i(\boldsymbol{\xi})|P\rangle \tag{2.44}$$

where

$$L(\mathbf{0}, \boldsymbol{\xi}) \equiv P\, exp\big(-i\sqrt{4\pi\alpha_s} \int_{\mathbf{0}}^{\boldsymbol{\xi}} d\boldsymbol{\xi} A_\mu(\mathbf{0}, \boldsymbol{\xi})\big). \tag{2.45}$$

This gauge link, called Wilson line, is reversed under time-reversal, allowing theoretically the existence of non-zero T-odd DFs, but only when they appear unintegrated in intrinsic $\vec{\kappa}_T$. After integration over $\vec{\kappa}_T$, the Boer-Mulders and the Sivers T-odd DFs vanish:

$$\begin{aligned} \int d^2\vec{\kappa}_T\, h_1^\perp(x, \kappa_T^2) \;&=\; 0 \\ \int d^2\vec{\kappa}_T\, f_{1T}^\perp(x, \kappa_T^2) \;&=\; 0 \end{aligned} \tag{2.46}$$

The Sivers and the Boer-Mulders effects describe the asymmetries of the quark momentum component perpendicular respectively to the transverse nucleon spin $\vec{S}_T$ (Sivers) or to the transverse quark spin $\vec{s}_T$ in an unpolarized target (Boer-Mulders).

As explained in the following, in a semi-classical picture these asymmetries arise from the combination of a spatial distortion of the DFs in the transverse position space together with one gluon exchange FSI, that bends the struck quark in a fixed direction. In the transverse position space representation, the DFs are expressed in terms of the impact parameter $b_\perp$, which is the transverse distance of the quark to the transverse center of momentum [5].

Assuming a non-zero quarks orbital angular momentum (OAM), if the quarks are unpolarized and the nucleon is unpolarized or longitudinally polarized, all the orientations of the OAM are equally likely so that the quark distribution is axially symmetric. On the contrary, when a transverse quark (Boer-Mulders) or nucleon (Sivers) polarization is involved, spin-orbit correlations give origin to a spatial distortion of the quark densities, which appears enhanced on one side or another depending on the OAM orientation, as in figure 2.6, where the displacement is obtained by a lattice simulation [33].

In this representation, when the quark is knocked out from the target, it is still subject to the attractive field of the remaining quarks from the nucleon (spectators), therefore it would experience FSI that deflects the struck quark toward the center of momentum before it fragments. In this way the FSI can translate the initial

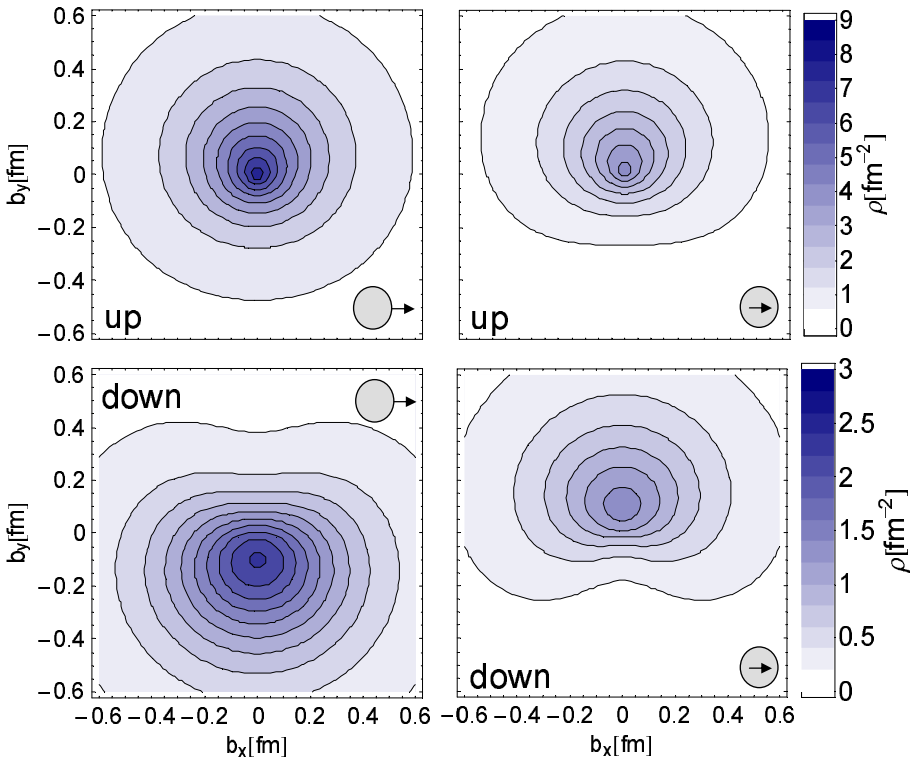

Figure 2.6: Densities of unpolarized quarks in transversely polarized nucleon (left) and transversely polarized quarks in unpolarized nucleon (right) for up (upper plots) and down (lower plots) quarks. The inner and outer arrows indicate respectively the quarks and nucleon transverse polarization.

quark transverse position asymmetry into the outgoing quark transverse momentum asymmetry.

The sign of the distortions of figures 2.6 for the up and the down quarks are determined by the signs of the anomalous proton and neutron magnetic moments due to quark orbital motion (standard magnetic moment κ) and transverse polarization (transverse magnetic moment κ_T). If κ^q is the q-flavoured quark contribution to the anomalous magnetic moment, and κ_T^q is the transverse dipole moment, the description of quark DFs in the impact parameter space [30] predicts for the Sivers and Boer-Mulders functions:

$$\begin{aligned} f_{1T}^{\perp,q} &\sim -\kappa^q \\ h_1^{\perp,q} &\sim -\kappa_T^q \end{aligned} \tag{2.47}$$

The predicted signs for the Sivers DF have been confirmed by the experimental measurement of HERMES [18].

Since they are originated by similar mechanisms, the Boer-Mulders and the Sivers functions are expected to be of the same order of magnitude, except for the factor

[5] Analog to the non-relativistic center of mass.

κ_T^q / κ^q (~ 1):

$$h_1^{\perp,q} \approx (\kappa_T^q / \kappa^q) f_{1T}^{\perp,q} \tag{2.48}$$

With the use of the impact parameter parton DFs, a first quantitative prediction was provided for the size of the $h_1^\perp$ distribution from lattice calculation [33]. Their values for the transverse dipole moments are: $\kappa^u_{T,lat} \approx 3.0$ and $\kappa^d_{T,lat} \approx 1.9$, while the values for the standard anomalous magnetic moments are known experimentally: $\kappa^u_{exp} \approx 1.67$, and $\kappa^d_{exp} \approx -2.03$ [33].

In conclusion spin-orbit correlations together with attractive final state interaction in a semi-classical framework give rise to non-zero Sivers function with opposite sign for the up and the down quarks, and predicts a Boer-Mulders function of similar size but negative both for up and down quark.

Besides the semi-classical picture, several theoretical predictions for the DF $h_1^\perp$ and its related asymmetries were performed, yielding very different flavour dependence for $h_1^\perp$ and even different relative sign between $h_1^{\perp,u}$ and $h_1^{\perp,d}$.

MIT bag model. A calculation based on the MIT bag model provide negative Boer-Mulders functions both for up and down quarks and $h_1^{\perp,d} \sim \frac{1}{2} h_1^{\perp,u}$ [34], as depicted in figure 2.7;

Large-N_c QCD. Large-N_c considerations give slightly non-zero Boer-Mulders functions both for up and down quarks with the same relative sign: $h_1^{\perp,d} \approx h_1^{\perp,u} \approx 0$ [35]. No prediction are given for the absolute sign of the DFs.

Diquark models. In a diquark model the nucleon is described as a bound state of a quark and a spectator 'diquark' [36], which does not take part in the interaction except during the FSI. A lot of sophisticated model exists, depending on the diquark wave function configuration. The predictions for the Boer-Mulders function calculated in a scalar diquark and a scalar plus an axial-vector diquark spectator model are listed here:

- The scalar diquark spectator model involve a scalar-spin 0 diquark state. Within this framework several calculation were made [37, 38, 39, 40] which predict $h_1^{\perp,d} \approx f_{1T}^{\perp,d} \sim 0$, while $h_1^{\perp,u} \approx f_{1T}^{\perp,u}$ sizable and negative [39]. In particular, in [40] predictions were made for the HERMES experiment; these results are discussed in section 2.4.2.
- In the scalar plus axial-vector diquark spectator model the axial vector-spin 1 diquark enters the game. Two calculations, using slightly different quark-diquark interactions, predicted
  - $h_1^{\perp,d}$ with a opposite sign and a rather larger size compared with $h_1^{\perp,u}$ as shown in figure 2.8 [39];
  - negative sign and comparable size for the up and down quark $h_1^\perp$ DF, shown in figure 2.9). The latter results [42], extracted in the HERMES kinematical regime are described with more details in section 2.4.2.

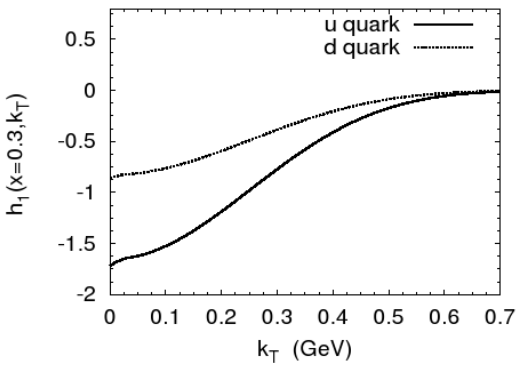

Figure 2.7: Boer-Mulders DF for up and down quarks as predicted by MIT bag model [34].

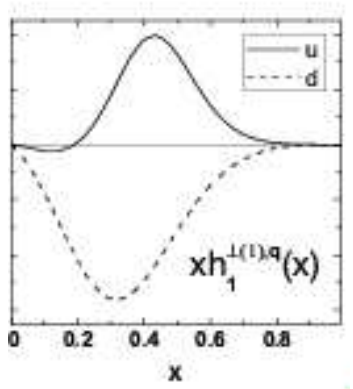

Figure 2.8: Boer-Mulders DF for up and down quarks in the spectator model with scalar and axial-vector diquark as calculated in [39]. The figure is from [41].

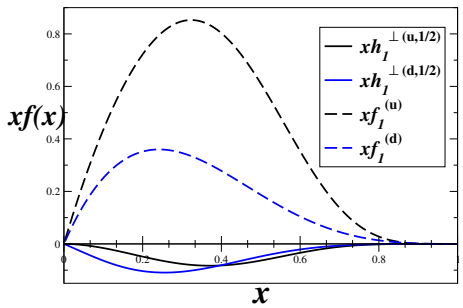

Figure 2.9: Boer-Mulders DF for up and down quarks compared to unpolarized DF (f_1) as predicted by Gamberg et al. in [42].

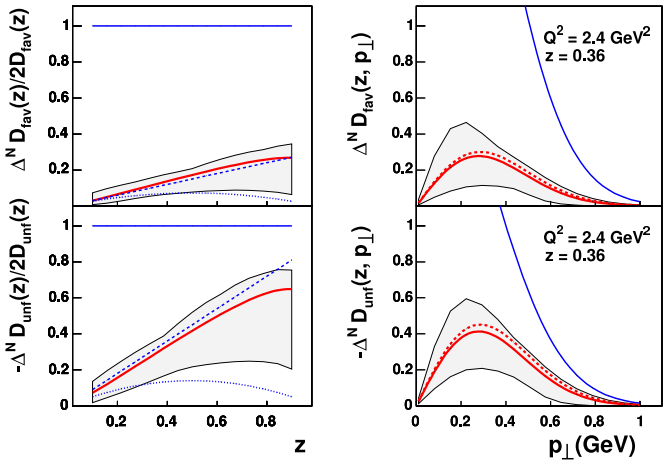

Figure 2.10: *Favoured* (upper plots) and *Unfavoured* (lower plots) Collins fragmentation functions normalize to twice the corresponding unpolarized FFs, versus the produced hadron momentum fraction z (left) and transverse momentum (right) as determined by Anselmino et al. global fit [43]. The solid red and the dashed blue lines correspond to fit based on different choices of the free parameters, and determines the uncertainties represented by the shaded areas. The upper blue solid lines correspond to the upper limits fixed by the positivity bound.

The Collins fragmentation function

The Collins FF $H_1^\perp$ describes how the transversely polarized struck quark fragments in the final observed hadron. Beyond being T-odd, $H_1^\perp$ is a chiral-odd function, therefore can be measured only in conjunction with another chiral-odd object, since QCD and hard scattering preserve chirality. One of the experimental way to access the Collins FF is the measurement of *Collins asymmetry* in SIDIS, in which $H_1^\perp$ is probed in conjunction with the chiral-odd transversity DF, describing transversely polarized quark distribution in a transversely polarized nucleon. Experimental results on the *Collins asymmetry* was published by HERMES in 2004 [18], giving the first experimental evidence for a non-zero Collins FF using a hydrogen target. Similar asymmetries but with a deuterium target was published by the COMPASS experiment [19]. Since both the transversity and the Collins functions are unknown, neither can be extracted from the *Collins asymmetry*, in which they appear in a convolution integral.
In an independent way, a more direct measurement of the Collins function was performed in the $e^+e^- \to h_1 h_2 X$ reactions by the Belle Collaboration at KEK [44], that published the convolution of two Collins fragmentation functions. Combining this result with the mentioned results from HERMES [18] and COMPASS [19], Anselmino et al. extracted simultaneously the transversity and the Collins functions [43] using a global fit. To show their results it is convenient to define a *favoured* fragmentation function if the fragmenting quark is a valence quark for the final hadron:

$$H_{1,\mathrm{fav}}^\perp \equiv H_{1,u\to\pi^+}^\perp = H_{1,\bar{d}\to\pi^+}^\perp = H_{1,d\to\pi^-}^\perp = H_{1,\bar{u}\to\pi^-}^\perp \tag{2.49}$$

and the *unfavoured* fragmentation function, in the opposite case:

$$H_{1,\mathrm{unf}}^{\perp} \equiv H_{1,d\to\pi^+}^{\perp} = H_{1,\bar{u}\to\pi^+}^{\perp} = H_{1,u\to\pi^-}^{\perp} = H_{1,\bar{d}\to\pi^-}^{\perp} = H_{1,s\to\pi^\pm}^{\perp} = H_{1,\bar{s}\to\pi^\pm}^{\perp} \tag{2.50}$$

The extracted *favoured* and *unfavoured* Collins functions are plotted in fig. 2.10: they turn out to be of same order of magnitude but opposite in sign:

$$H_{1,\mathrm{fav}}^{\perp} \approx -H_{1,\mathrm{unf}}^{\perp} > 0 \tag{2.51}$$

for pion production for instance:

$$H_{1,u\to\pi^+}^{\perp} \approx -H_{1,d\to\pi^+}^{\perp} \quad \text{and} \quad H_{1,u\to\pi^-}^{\perp} \approx -H_{1,d\to\pi^-}^{\perp} \tag{2.52}$$

In case of scattering over hydrogen target, due to the u-dominance the latter relations together with 2.51 yields:

$$H_{1,\pi^+}^{\perp} \approx -H_{1,\pi^-}^{\perp} > 0 \tag{2.53}$$

2.4.1 Experimental status

Very few measurements of the $\cos 2\phi_h$ unpolarized cross-section modulation were performed in SIDIS (figures 2.11 and 2.12) [45, 46] and in Drell-Yan processes [47], but only in Drell-Yan a sizable signal was found, see figure 2.13.

SIDIS measurements. Figures 2.11 and 2.12 show the $\langle \boldsymbol{\cos 2\phi_h} \rangle$ moments measured by the experiments EMC and ZEUS.

The EMC data [45] were collected in the scattering of 280 GeV muons off an hydrogen target. The kinematical region is fixed by the cuts:

$$x_F > 0.1 \qquad P_{h\perp} > 0.2\,\mathrm{GeV/c} \qquad y < 0.8 \qquad Q^2 > 4\,(\mathrm{GeV/c})^2$$

The extraction of the $\cos 2\phi_h$ modulation leads to results compatible with zero (figure 2.11).

Slightly positive moments are extracted by the ZEUS experiment [46] (positron-proton collision at 300 GeV), whose kinematical region is:

$$180 < Q^2 < 7220\,(\mathrm{GeV/c})^2 \qquad 0.01 < x < 0.1$$

$$0.2 < y < 0.8 \qquad 0.2 < z < 1.0$$

Drell-Yan measurements. In the Drell-Yan (DY) process a charged lepton pair is produced in a high energy hadron-hadron interaction [47]: $p\overline{p} \to l^+ l^- X$. Here the cross-section can be written as:

$$\frac{d\sigma}{d\Omega} \propto 1 + \lambda \cos^2\theta + \mu \sin 2\theta \cos\phi + \frac{\nu}{2} \sin^2\theta \cos 2\phi \tag{2.54}$$

where θ and ϕ are respectively the polar and the azimuthal angle of the positively charged lepton (l^+) in the dilepton rest frame. As suggested by Boer [48], the $\cos 2\phi_h$

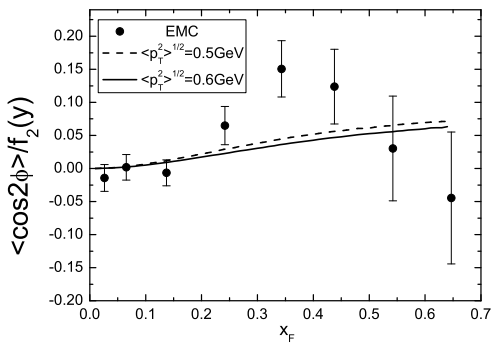

Figure 2.11: Experimental $\langle \cos 2\phi_h \rangle$ moments as measured at EMC [45], divided by the kinematical factor $f_2(y) = (1-y)/[1+(1-y)^2]$. The lines are predictions from [40] at two different κ_T values.

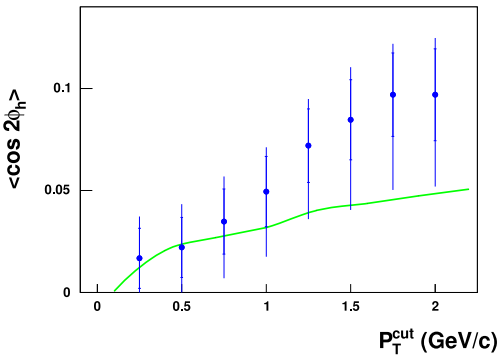

Figure 2.12: Experimental $\langle \cos 2\phi_h \rangle$ moments measured at ZEUS [46]. The line is part of the global fit described in section 2.5.

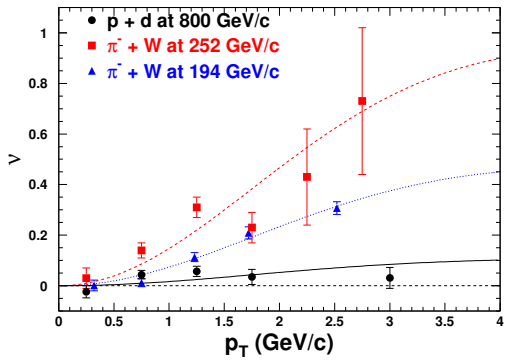

Figure 2.13: The p_T dependence of the ν quantity in the Drell-Yan experiments: sizable signal was measured for pion-induced Drell-Yan reactions (blue and red points), while compatible with zero results are measured in proton-induced Drell-Yan reactions (black points).

	$p+d$ 800 GeV/c (E866)	$\pi^- + W$ 194 GeV/c (NA10)	$\pi^- + W$ 252 GeV/c (E615)
$\langle \boldsymbol{cos}2\phi \rangle$	0.027 ± 0.010	0.091 ± 0.009	0.169 ± 0.019

Figure 2.14: Mean values of the ν parameters for three different Drell-Yan experiments. The p_T dependence of these quantities is shown in Fig. 2.13.

angular distribution in Drell-Yan could be related to the Boer-Mulders distribution function. In this case, the quantity ν should represent the DY $\cos 2\phi_h$ moment related to $h_1^\perp$. Three DY measurements of ν exist from three different experiments, and are shown in figure 2.13.

The first result, published by the NA10 Collaboration in 1986 [49], studied the reaction: $\pi^- + W$ at center-of-mass energy of 140, 194 and 286 GeV/c. The data show a positive sizable value for ν, confirmed by the later results of the E615 collaboration [50], obtained in the same reaction $\pi^- + W$ but at an energy of 252 GeV/c. A qualitatively different behavior of the ν distribution was found in $p+d$ DY reactions at 800 GeV/c by E866 more recently [47]: unlike the pion-induced Drell-Yan, the proton-induced Drell-Yan shows results for ν that are only slightly different from zero.

In SIDIS reaction the $\langle \boldsymbol{\cos 2\phi_h} \rangle$ moments are related to the product of the Boer-Mulders DF and the Collins Fragmentation function. On the contrary in Drell-Yan the equivalent quantity ν involves the product of two Boer-Mulders DFs, one from the beam and one from the target. Therefore a possible explanation of the differences between pion- and proton-induced DY is that, while pion-induced DY involves the annihilation of two valence partons (a valence antiquark from the pion and a valence quark from the nucleon), the proton-induced DY instead involves the annihilation of a valence quark with a sea antiquark. From theoretical calculation the Boer-Mulders distribution function is expected to be small for the sea quarks, and the ν result by E866 seems to confirm that $h_1^\perp$ for the nucleon sea quarks is significantly smaller than the one for the valence quarks.

2.4.2 Predictions for the Boer-Mulders effect at HERMES

Among the theoretical calculations of $h_1^\perp$, two predictions about the azimuthal asymmetry produced by the Boer-Mulders effect were dedicated to the HERMES experiment kinematical region.

The first one in chronological order is described in [40]. The prediction is based on the leading (Boer-Mulders) and the twist-four [6] (Cahn) contributions to the $\cos 2\phi_h$ modulation of the unpolarized cross-section, and was made selecting the HERMES kinematical region.

For the Boer-Mulders function the distribution adopted is the same provided

[6] The twist-four term contributing to the $\cos 2\phi_h$ modulation is due to the Cahn mechanism, as discussed in section 2.5.

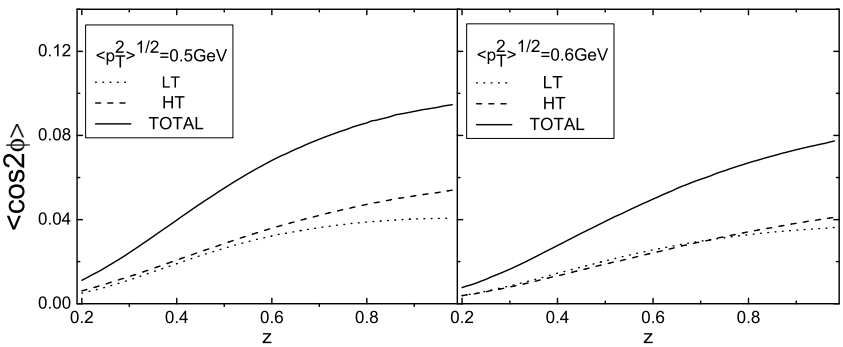

Figure 2.15: $\langle \cos 2\phi_h \rangle$ azimuthal moments predicted by [40] for positive pion production at the HERMES experiments. The dotted and the dashed curves indicate respectively the leading and Next-To-Leading twist calculation. The solid line is the sum of the above two contributions.

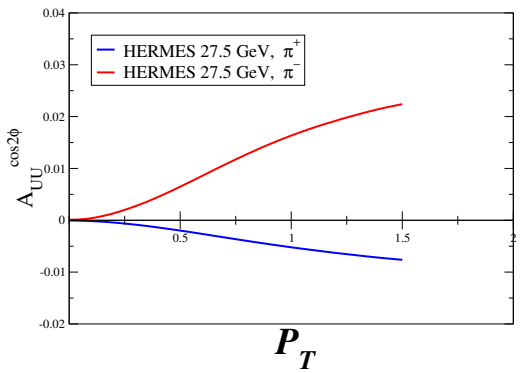

Figure 2.16: $\langle \cos 2\phi_h \rangle$ moments for positive and negative pions as predicted in [42] within the HERMES kinematical region.

by [37] calculated using a scalar diquark spectator framework, while as regards the fragmentation function, the authors used the parameterization suggested by Collins in [21]. The combination of these two functions leads to the positive $\langle \mathbf{cos\,2\phi_h} \rangle$ azimuthal moments for positive pions plotted in figure 2.15

$$\langle \mathbf{cos\,2\phi_h} \rangle_{\pi^+} \propto C[h_1^{\perp} H_1^{\perp,\pi^+}] > 0. \tag{2.55}$$

No prediction are explicitly calculated for the negative pions, anyway the sign of $\langle \mathbf{cos\,2\phi_h} \rangle_{\pi^-}$ can be estimated. In the u-dominance regime the Collins FF is positive for positive pions and negative for negative pions (equation 2.51), and $h_1^{\perp} = h_1^{\perp,u} > 0$ (see eq. 2.55), therefore

$$\langle \mathbf{cos\,2\phi_h} \rangle_{\pi^-} \propto C[h_1^{\perp} H_1^{\perp,\pi^-}] < 0 \tag{2.56}$$

so the azimuthal moments we expect from this model are negative for negative pions.

More recently, a refined diquark spectator model including both scalar and axial-vector diquarks [42] yields *negative* Boer-Mulders functions for both up and down quarks, as already shown in fig. 2.9. This predictions together with the Collins functions calculated in [51] with a spectator model, allows the extraction of the $\langle \mathbf{cos\,2\phi_h} \rangle$ moments for positive and negative pions shown in fig. 2.16 within the HERMES kinematical region.

In summary the theoretical calculations for the HERMES experiment just discussed predict a Boer-Mulders asymmetry of a few percent with opposite signs between π^+ and π^-, but, while for the first model the $\langle \mathbf{cos\,2\phi_h} \rangle$ moments are expected to be positive for positive pions (fig. 2.15) and negative for negative pions, for the second model the signs of the $\langle \mathbf{cos\,2\phi_h} \rangle$ moments are reversed (fig. 2.16).

2.5 The Cahn effect

In 1978 Robert Cahn demonstrated [5] that the naïve Quark Parton Model (PQM) does give azimuthal dependence for the semi-inclusive cross-section. As a consequence of being confined in fact, the quarks have a non-zero transverse momentum, and this condition, alone, provides an azimuthal dependence in the Semi-Inclusive unpolarized cross-section.

The quark momentum $\vec{\kappa}$ can be written as a function of the longitudinal nucleon momentum $\vec{P}$ as:

$$\vec{\kappa} = x\vec{P} + \vec{\kappa}_T = (xP, \kappa_T \cos\phi_h, \kappa_T \sin\phi_h) \tag{2.57}$$

If the incident (outgoing) lepton and struck quark four-momenta are respectively $\boldsymbol{k}$ ($\boldsymbol{k'}$) and $\boldsymbol{\kappa}$, the cross-section can be written with the Mandelstam variables $\hat{s}$ and $\hat{u}$:

$$\sigma \propto \hat{s}^2 + \hat{u}^2 \tag{2.58}$$

where

$$\begin{aligned} \hat{s} &= (\mathbf{k} + \boldsymbol{\kappa})^2 \\ \hat{u} &= (\mathbf{k}' - \boldsymbol{\kappa})^2 \end{aligned} \tag{2.59}$$

that in deep inelastic limit are:

$$\begin{aligned} \hat{s} = 2\vec{k} \cdot \vec{\kappa} \;&=\; 2\vec{k} \cdot (x\vec{P} + \vec{\kappa}_T) \approx 2MEx\Big[1 - \frac{2\kappa_T}{Q}\sqrt{(1-y)}\cos\phi_h\Big] \\ \hat{u} = -2\vec{k} \cdot \vec{\kappa} \;&=\; 2\vec{k}' \cdot (x\vec{P} + \vec{\kappa}_T) \approx 2ME'x\Big[1 - \frac{2\kappa_T}{Q\sqrt{(1-y)}}\cos\phi_h\Big] \end{aligned} \tag{2.60}$$

If the κ_T-dependent terms are neglected, the cross-section has the standard behavior $\sigma \propto \hat{s}^2 + \hat{u}^2 \propto 1 + (1-y)^2$, while, taking into account the κ_T-terms:

$$\sigma \propto \hat{s}^2 + \hat{u}^2 \propto \Big[1 - \frac{2\kappa_T}{Q}\sqrt{(1-y)}\cos\phi_h\Big]^2 + \Big[1 - \frac{2\kappa_T}{Q\sqrt{(1-y)}}\cos\phi_h\Big]^2 \tag{2.61}$$

Two azimuthal asymmetries appear in the cross-section, one proportional to $\cos\phi_h$, suppressed by a κ_T/Q factor (twist-three), and one proportional to $\cos 2\phi_h$, with a suppression of κ_T^2/Q^2 (twist-four):

$$\begin{aligned} \langle \mathbf{\cos \boldsymbol{\phi_h}} \rangle^0_{Cahn} \;&=\; -\Big(\frac{2\kappa_T}{Q}\Big)\Big(\frac{2 - y\sqrt{(1-y)}}{1 + (1-y)^2}\Big) \\ \langle \mathbf{\cos 2\boldsymbol{\phi_h}} \rangle^0_{Cahn} \;&=\; \Big(\frac{2\kappa_T^2}{Q^2}\Big)\Big(\frac{(1-y)}{1 + (1-y)^2}\Big) \end{aligned} \tag{2.62}$$

where the superscript 0 indicates the moments obtained using the original calculation performed by Cahn.

In the cross-section of eq. 2.40 the $\langle \mathbf{\cos \boldsymbol{\phi_h}} \rangle_{Cahn}$ contribution can be identified with the twist-three term proportional to $[f_1 D_1]$ (see equation 2.43):

$$F^{\langle \mathbf{\cos \boldsymbol{\phi_h}} \rangle}_{UU,Cahn} \approx \frac{2M}{Q} C\Big[- \frac{\hat{h} \cdot \vec{\kappa}_T}{M} f_1(x, \kappa_T^2) D_1(z, p_T^2)\Big] \tag{2.63}$$

The $\langle \mathbf{\cos 2\boldsymbol{\phi_h}} \rangle$ Cahn-modulation is missing in equation 2.40 because it appears at twist-four, however it would have the following expression [54]:

$$F^{\langle \mathbf{\cos 2\boldsymbol{\phi_h}} \rangle}_{UU,Cahn} \approx \frac{4M^2}{Q^2} C\Big[\frac{\kappa_T^2}{M^2} f_1(x, \kappa_T^2) D_1(z, p_T^2)\Big] \tag{2.64}$$

The azimuthal moments of the cross-section are strictly related to the parton intrinsic motion, and vanish when $\kappa_T = 0$, as evident in equations 2.62 and 2.63.

To compare the $\langle \mathbf{\cos \boldsymbol{\phi_h}} \rangle$ moments calculated in the naïve QPM by Cahn or using the SIDIS cross-section at twist-three of equation 2.40, the definition of the *Gaussian ansatz* is needed.

Gaussian ansatz

In equation 2.40 the products of distribution and fragmentation functions appear in a convolution integral over transverse momenta of quark (κ_T and p_T). As the exact κ_T-(p_T-)dependence of distribution (fragmentation) functions is unknown, it is not possible to extract the products from the integral without an assumption on transverse momentum DF and FF dependence.

One widely used ansatz is to consider a Gaussian κ_T-(p_T-)dependence[7]:

$$\begin{aligned} f_q(x,\kappa_T^2) &= f_q(x)\frac{1}{\pi\langle\kappa_T^2\rangle}e^{-\kappa_T^2/\langle\kappa_T^2\rangle} \\ D_q(z,p_T^2) &= D_q(z)\frac{1}{\pi\langle p_T^2\rangle}e^{-p_T^2/\langle p_T^2\rangle} \end{aligned} \tag{2.65}$$

where the functions $f_q(x)$ and $D_q(z)$ are the distribution and the fragmentation functions integrated over the transverse momenta (κ_T and p_T).
The Gaussian ansatz is only an approximation, but it well describes data in kinematical region where $\langle P_{h\perp}\rangle < \langle Q\rangle$, which is the case of HERMES [52, 53, 9].

Kinematical dependence of the Cahn moments

In equation 2.62, the non-collinearity of the fragmentation process is missing. Indeed the additional random transverse momentum introduced by fragmentation dilutes the effect of the quark transverse momentum. To calculate this dilution, a gaussian dependence on κ_T and p_T was assumed by Cahn for the transverse momentum parton distribution (f_{Cahn}) and the fragmentation process (D_{Cahn}):

$$\begin{aligned} f_{Cahn}(x,\kappa_T) &\propto e^{-a\kappa_T^2} \\ D_{Cahn}(z,p_T) &\propto e^{-bp_T^2}. \end{aligned} \tag{2.66}$$

Within these assumptions and considering $\kappa_T = P_{h\perp}/z$ [8], the $\langle\cos\boldsymbol{\phi_h}\rangle^0_{Cahn}$ moment becomes:

$$\langle\cos\boldsymbol{\phi_h}\rangle^0_{Cahn} \propto -\Big(\frac{2P_{h\perp}}{Q}\Big)\Big(\frac{bz}{a+bz^2}\Big)\Big(\frac{(2-y)\sqrt{(1-y)}}{1+(1-y)^2}\Big) \tag{2.67}$$

Within the Gaussian ansatz the integration in equation 2.63 can be performed analytically [9], and, since the comparison between 2.66 and 2.65 yields $\langle\kappa_T^2\rangle = 1/a$ and $\langle p_T^2\rangle = 1/b$, the result is:

$$\langle\cos\boldsymbol{\phi_h}\rangle_{Cahn} \approx -\Big(\frac{4P_{h\perp}}{Q}\Big)\Big(\frac{bz}{a+bz^2+a^{\frac{3}{2}}b^{\frac{1}{2}}z}\Big)\Big(\frac{(2-y)\sqrt{1-y}}{1+(1-y)^2}\Big) \tag{2.68}$$

[7] Here the general notation of f_q and D_q is used for a Distribution and a Fragmentation function respectively.

[8] The complete κ_T expression should take into account equation 2.29, but in his original calculation Cahn neglected the p_T contribution (see [5]).

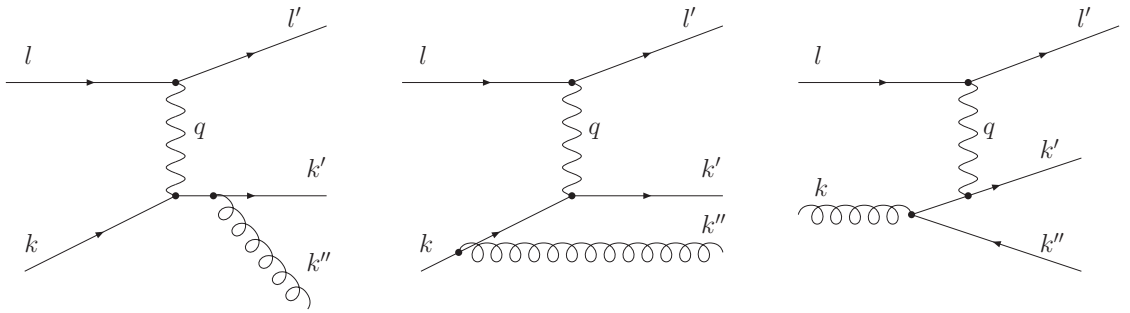

Figure 2.17: Feynman diagrams for pQCD with an additional gluon: their contributions to the cosine cross-section modulation are expected to be important in kinematical region where $P_{h\perp} > 1$ GeV/c.

By comparing Eqs. 2.67 and 2.68 it is clear that the $\langle \mathbf{cos}\, \boldsymbol{\phi_h} \rangle_{Cahn}$ moments obtained by the use of the cross-section 2.40 have almost the same kinematical behavior compared to the ones originally provided by Cahn in 1978 ($\langle \mathbf{cos}\, \boldsymbol{\phi_h} \rangle^0_{Cahn}$). The predicted sign for the Cahn effect in both case is negative, and does not depend on the quark flavour.

The above expressions for the cosine moments are valid up to leading order in α_s. In this approximation the outgoing hadron transverse momentum $P_{h\perp}$ is generated mostly by the intrinsic transverse motion of quarks, so we would expect a magnitude for $P_{h\perp}$ of the order of $\langle \kappa_T \rangle$ and $\langle p_T \rangle$. In the region where $P_{h\perp} \approx \kappa_T$ (well below 1 GeV/c), the leading order processes are dominating, and the transverse hadron momentum is strictly related to the Cahn effect. On the contrary, large hadron transverse momentum processes (typically above 1 GeV/c) cannot be generated by the small amount of intrinsic motion; for these reactions pQCD contributions need to be taken into account, in which an additional gluon participate to the processes, as in the Feynman diagrams of fig. 2.17. At HERMES typically $P_{h\perp} < 1$ GeV/c, and pQCD corrections could not be taken into account.

2.5.1 Experimental status and global fit

If the Gaussian ansatz of equations 2.65 is assumed, in the full differential cross-section 2.40 everything is known except the average transverse momenta $\langle \kappa_T^2 \rangle$ and $\langle p_T^2 \rangle$, which can be fixed by a global fit of the existing data [45, 55, 46]. Such a fit was performed by Anselmino et al. [9]. This fit comprehends the data sets collected from three different experiments [45, 55, 46], in different energy, x, Q^2 and z ranges, and the results are used to predict the azimuthal hadrons distribution in the HERMES kinematical region.
For all the calculation the authors consider the value of $P_{h\perp} = 1$ GeV/c as the transition point between leading- and NLO- dominated regions, and account for NLO effects in the $P_{h\perp} > 1$ GeV/c region.

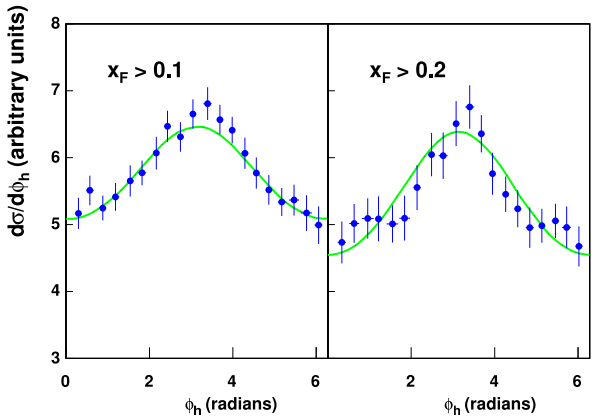

Figure 2.18: ϕ_h distribution measured at EMC in two x_F regions [45]. The solid line indicates the fit performed in [9].

EMC data. In the first fit, shown in fig. 2.18, the data are from the EMC collaboration [45] and refer to the scattering of 280 GeV muons off an hydrogen target. The kinematical region is fixed by the cuts:

$$x_F > 0.1 \qquad P_{h\perp} > 0.2\,\mathrm{GeV/c} \qquad y < 0.8 \qquad Q^2 > 4\,(\mathrm{GeV/c})^2$$

The negative $\cos\phi_h$ behavior observed in eq. 2.68 is clearly present in the data, and the fit of the ϕ_h-distribution shown in figure 2.18 yields the moments plotted in 2.19.

E665 data. The results of the E665 experiment [55] are shown in fig. 2.20. The scattering of 490 GeV muons off hydrogen and deuterium targets give access to the kinematical region:

$$Q^2 > 3\,(\mathrm{GeV/c})^2 \qquad 60 < \nu < 500\,\mathrm{GeV} \qquad E_h > 8\,GeV$$
$$0.1 < y < 0.85 \qquad Q^2 > 4\,(\mathrm{GeV/c})^2$$

The theoretical results are in qualitative agreement with the data, and in fig. 2.20 is evident that around $P_{h\perp}^{cut} \approx 1$ GeV/c the behavior of the moments change due to the increasing contribution of pQCD effects.

ZEUS data. A similar change in the behavior of unpolarized cross-section can be observed in the ZEUS data around $P_{h\perp} \sim 1$ GeV/c in fig. 2.21. For this experiment (positron-proton collision at 300 GeV), whose kinematical region is:

$$180 < Q^2 < 7220\,(\mathrm{GeV/c})^2 \qquad 0.01 < x < 0.1$$
$$0.2 < y < 0.8 \qquad 0.2 < z < 1.0$$

the prediction are in good agreement with experimental data only in the description of the cross-section (fig. 2.21), while the prediction of the moments fails, especially at low transverse momenta, as shown in fig.2.22.

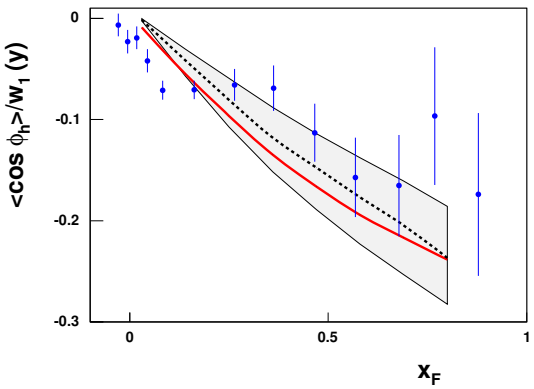

Figure 2.19: $\langle \cos \phi_h \rangle$ moments extracted by the EMC [45] data of fig. 2.18. The dashed line is obtained with the exact kinematics, while the solid line includes only leading twist terms. The shadowed region corresponds to varying the parameters $\langle \kappa_T^2 \rangle$ and $\langle p_T^2 \rangle$ by 20%.

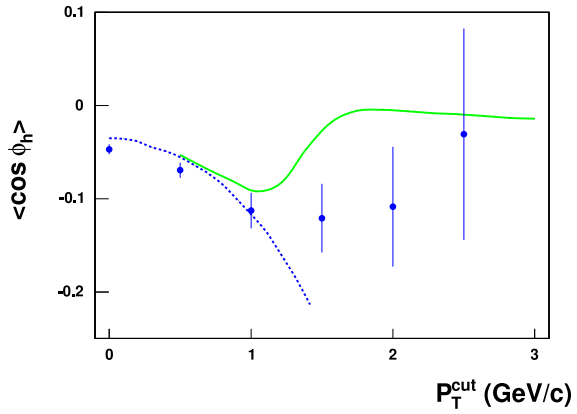

Figure 2.20: $\langle \cos \phi_h \rangle$ moments extracted from data of the E665 Collaboration [55]. The dashed line is obtained at leading order in α_S and taking into account all twist contributions; the solid line includes NLO corrections. It is possible to notice a change in the moments distribution around $P_{h\perp} \approx 1$ GeV/c due to increasing contributions of NLO terms.

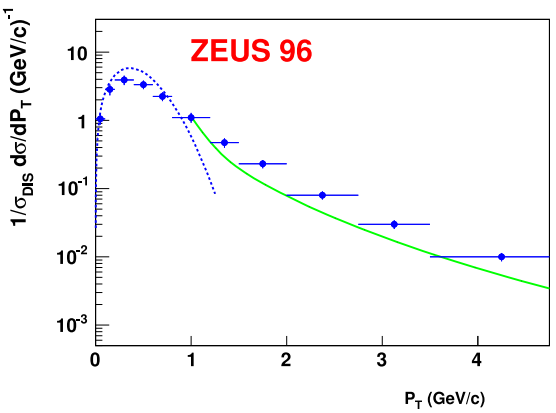

Figure 2.21: ZEUS [46] normalized cross-section for unpolarized SIDIS data; the dashed line reproduces the leading order in α_S and takes into account all twist contributions, while the solid line includes NLO corrections. A significative change in the cross-section behavior is observed around $P_{h\perp} \approx 1$ GeV/c, it can be explained by increasing contributions of NLO terms.

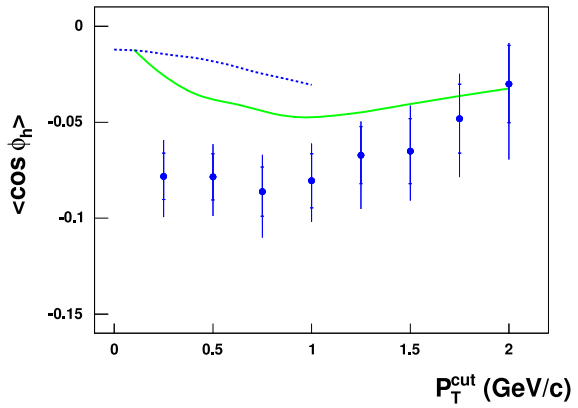

Figure 2.22: The $\langle \cos \phi_h \rangle$ moments from the ZEUS [46] data; the dashed line reproduces the leading order in α_S and takes into account all twist contributions, while the solid line includes NLO corrections.

The combined analysis of the above data leads to the best value of the parameter

$$\langle \kappa_T^2 \rangle \; = \; 0.25\,(\mathrm{GeV/c})^2 \tag{2.69}$$

and, with the use of the relation 2.29:

$$\langle p_T^2 \rangle \; = \; 0.20\,(\mathrm{GeV/c})^2. \tag{2.70}$$

Since the data samples in fig.2.19, 2.20 and 2.22 give the azimuthal dependence of SIDIS cross-section in different kinematical ranges, and for combined production of all charged hadrons, the results of equation 2.69 is valid under the assumption of a value of $\langle \kappa_T^2 \rangle$ which is constant in the whole kinematical region covered and flavour-independent.

2.5.2 Predictions for the Cahn effect at HERMES

The average values of k_T for quarks inside the proton, extracted by fitting the existing data in unpolarized SIDIS, were used to compute the predictions for the $\langle \boldsymbol{\cos \phi_h} \rangle$ in the HERMES kinematical region. The HERMES experiment (see chapter 3) investigates deep inelastic scattering between a 27.6 GeV/c lepton (electron or positron) beam and different fixed targets (i.e. hydrogen and deuterium). The authors of [9] calculated the predicted cosine moments for positive pions production in the HERMES kinematical region using the case of positron beam and hydrogen target, and with the kinematical requirements:

$$Q^2 > 1\,(\mathrm{GeV/c})^2 \qquad W^2 > 10\,\mathrm{GeV}^2 \qquad 0.023 < x < 0.4 \qquad 0.1 < y < 0.85$$

$$P_{h\perp} > 0.05\,\mathrm{GeV/c} \qquad 2 < E_h < 15\,\mathrm{GeV} \qquad 0.2 < z < 0.7$$

Being in a region of small $P_{h\perp}$ and a relatively large enough Q^2, the cross-section for HERMES is expected to be dominated by the leading terms, and pQCD corrections can be neglected. In these conditions, and using $\langle \kappa_T^2 \rangle = 0.25\,(\mathrm{GeV/c})^2$ and $\langle p_T^2 \rangle = 0.20\,(\mathrm{GeV/c})^2$ (see last section), the prediction of $\langle \boldsymbol{\cos \phi_h} \rangle$ moments for the HERMES experiment are presented in figure 2.23.

In [9] also the predictions for the twist-four $\langle \boldsymbol{\cos 2\phi_h} \rangle$ related to the Cahn effect (eq. 2.62) is calculated, and the predictions for HERMES are shown in figure 2.24. Although it is an higher twist effect with respect to the ones considered here, from this prediction the Cahn effect might have non-negligible contribution to $\cos 2\phi_h$ modulation.

The Boer-Mulders effects contributes both to $\cos \phi_h$ and $\cos 2\phi_h$ modulations of the cross-section. Therefore the prediction of the cosine moments, based only on Cahn effect, is reliable if the Boer-Mulders contribution gives negligible contribution. If this is not the case, to predict the global cosine moments both the effects should be taken into account [9]. In the hypothesis that the intrinsic κ_T is not strongly

[9] Here we are neglecting the quark-gluon-quark contribution to the $\cos \phi_h$ modulation.

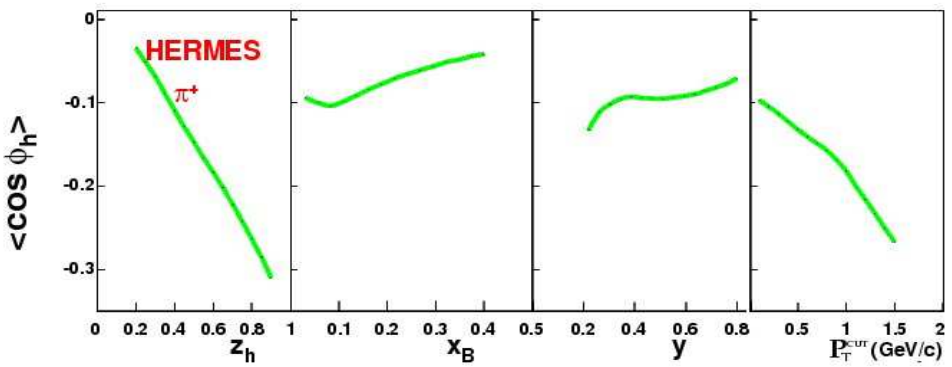

Figure 2.23: Predictions for the $\langle \cos \phi_h \rangle$ moments related to Cahn effect corresponding to production of positive pions in the HERMES experiment. Due to the low range in $P_{h\perp}$ no higher order QCD correction are included in this calculation.

dependent on the flavour, the Cahn contribution for the negative pions signal is expected to be similar to the positive pions signal of figure 2.24.

As regards the Boer-Mulders contribution, it was already discussed that the two models considered in section 2.4.2 predict different results. For both models the Boer-Mulders contribution is expected to be of few percent and with opposite sign for positive and negative pions, but the scalar diquark spectator model [40] predicts azimuthal results positive for π^+ and negative for π^-, while the signs are reversed in [42]. These predictions combined with the large negative size of the Cahn effect in $\pi^\pm$ production found by the authors of [9] lead to two different scenarios:

- according to the calculation in [40] the $\langle \cos \phi_h \rangle$ moments arise from the combination of quantities with same sign in case of π^+ and with different sign in π^- production, therefore more negative moments are expected for the negative pions than for the positive pions
- the situation is completely reversed in [42] since the sign of Boer-Mulders functions is negative, thus more negative moments are expected for the positive pions than for the negative pions.

2.6 Summary

The aim of the analysis described in this thesis is to study the azimuthal modulation of unpolarized SIDIS cross-section as defined in equation 2.22, and extract the structure functions $F_{UU}^{\cos\phi_h}$ and $F_{UU}^{\cos 2\phi_h}$ via the $\langle \cos n\phi \rangle$-moments defined in 2.25.

In this chapter the theoretical framework describing the different mechanisms contributing to the azimuthal distribution of produced hadrons have been discussed, with particular interest to the Cahn and the Boer-Mulders effects.

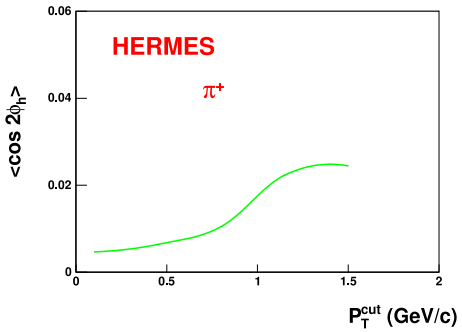

Figure 2.24: Predictions for the $\langle \cos 2\phi_h \rangle$ moments related to Cahn effect corresponding to production of positive pions in the HERMES experiment. Due to the low range in $P_{h\perp}$ no higher order QCD correction are included in this calculation.

The leading twist $\cos 2\phi_h$ modulation is generated by quark spin-orbit interactions together with final state interaction between the struck quark and the target remnant. This effect is called the Boer-Mulders mechanism. A number of theoretical models have been discussed predicting very different flavour dependence of the Boer-Mulders function and even different sign predictions for the up and the down quarks.

Within the HERMES kinematics regime two models have been presented that predict $\langle \cos 2\phi_h \rangle$ moments due to Boer-Mulders. Both predictions lead to a size signal of few percent, but different relative sign between positive and negative pions.

Up to the first sub-leading twist several terms contribute to the $\cos \phi_h$ modulation of the unpolarized cross-section, (see equation 2.40). Theoretical calculations exist for the Boer-Mulders and the Cahn contributions to this azimuthal asymmetry. The Cahn effect at HERMES is predicted to be sizable and negative both for positive and negative pions. The differences found in the predicted Boer-Mulders sign of the $\langle \cos 2\phi_h \rangle$ moments for π^+ and π^- [42, 40] can originate differences also in the $\langle \cos \phi_h \rangle$ moments for differently charged pions.

In particular the model in [42] combined with Cahn extraction of [9] predict more negative $\cos \phi_h$ asymmetry for positive than for negative pions, while, according to [40] combined with [9], the negative pions should exhibit more negative results.

Contrary to the highly investigated theoretical aspects, the Cahn and the Boer-Mulders effects are very poorly known experimentally. Very few measurements have been performed, yielding to negative sizable $\langle \cos \phi_h \rangle$ moments. The $\langle \cos 2\phi_h \rangle$ moments are compatible with zero within the statistical errors in SIDIS experiments and Drell-Yan processes with proton beam, but sizable negative results are found in Drell-Yan reactions with pions.

The existing results in SIDIS experiments [45, 55, 46] do not consider a possible flavour dependence of the measuring quantities, since they refer to hadrons without charge distinction, and involve hydrogen target only (EMC, ZEUS) or hydrogen and

deuterium target averaged together (E665).

The extraction of the $\langle \boldsymbol{\cos \phi_h} \rangle$ and $\langle \boldsymbol{\cos 2\phi_h} \rangle$ azimuthal moments at HERMES shown in this work distinguishes between positive and negative hadrons, and hydrogen and deuterium targets, resulting in a flavour dependent measurement. Thanks to this flavour sensitivity of the final results, the discrimination power between the theoretical models in the HERMES kinematical dependence is enhanced. Moreover, these results could give access to the extraction of intrinsic κ_T separately for the up and the down quark, while until now only a constant and averaged over the different flavours value has been extracted from existing results for this quantity.

Chapter 3

The HERMES experiment

HERMES (HERa MEasurement of Spin) [56] is a fixed target experiment located in the HERA[1] storage ring facility at DESY[2], designed to study the spin structure of the nucleon by Deep Inelastic Scattering. The experimental apparatus was assembled in the HERA east hall during the 1994 and dismantled in 2007.

The idea of a polarized experiment at HERA to measure the nucleon spin-dependent structure functions and isolate the contribution to the nucleon spin of the individual quark flavours as well as the contribution of gluons was introduced during the so-called *spin crisis*, after the EMC experiment observed that only a small fraction (30%) of nucleon's spin is carried by the valence quarks. Although the primary goal of HERMES was the nucleon spin structure investigation, during the time new physics topics and measurements extended the physics aims beyond the original intentions, and finally HERMES data was and still are used to investigate many aspects of hadron structure, hadron production and hadronic interactions [57].

3.1 The HERA lepton beam

The HERA complex is a high-energy particle accelerator of 6.3 Km circumference consisting in two storage rings, one for protons, usually running at 920 GeV, and the other for leptons (electrons or positrons), running in the opposite direction with an energy of 27.6 GeV. The beams collide with an invariant mass of $\sqrt{s} = 319$ GeV in two interaction points where the ZEUS and H1 experiments are located. Two more interaction points are used by HERA-B and HERMES, two fixed target experiments, where HERA-B uses only the proton beam, while HERMES utilizes only the lepton beam. The schematic view of the HERA collider is given in picture 3.1. The lepton beam is filled and ramped to operational energy, achieving initial currents of up to 50 mA. Nevertheless the beam interactions with experiments or with residual gas in

[1] Hadron Elektron Ring Anlage
[2] Deutsches Elektronen SYnchrotron

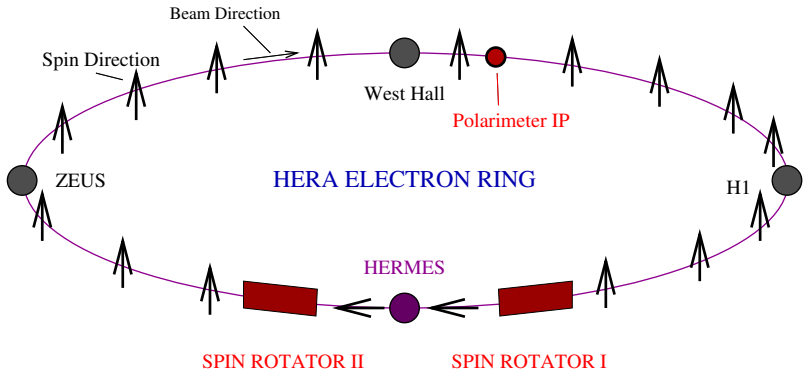

Figure 3.1: Schematic view of the HERA storage lepton-ring and its four experimental areas. The transverse beam polarization, represented by the small arrows, is rotated to longitudinal direction by the spin rotators in correspondence of the HERMES site.

the beam-pipe make the beam current decay nearly exponentially and the beam life time is around $12-14$ hours. When the current has achieved $\backsim$ 10 mA the beam is dumped to avoid running at low luminosity. When injected the lepton beam is unpolarized, but, during the circulation in the storage ring, it self-polarized because of the Sokolov-Ternov mechanism [58]: the lepton spins align themselves along the vertical magnetic field of the bending magnets in the curved regions of the ring, result in a natural transverse polarization. Spin rotators are located before and after the HERMES interaction point, to achieve a longitudinally polarized beam. The mean beam polarization is of about 40% to 60% and is continuously measured by a transverse [59] and a longitudinal [60] Compton polarimeter.

During the years the lepton beam flavour changed from electron to positron:

1995-2004 positron beam;

2005-2006 (1$^{\text{st}}$ period) electron beam;

2006 (2$^{\text{nd}}$ period)-2007 positron beam.

3.2 The internal target

Until 2005, the HERMES target system consisted in two different gas sources, a polarized source called ABS (Atomic Beam Source [61]) and an unpolarized source called UGFS (Unpolarized Gas Feed System).

The target gas is fed into a storage cell internal to the beam line to increase the target effective density by a factor $\sim$ 100 [64]. A sample gas from the target is continuously monitored by an apparatus consisting in a TGA (Target Gas Analyzer), measuring the atomic fraction, and a BRP (Breit-Rabi Polarimeter) measuring the atomic polarization [62, 63]; from the 2006 on, only the unpolarized gas source was used, and the ABS and the TGA/BRP were dismantled.

The target-gas is injected by the ABS or the UGFS system into the middle of the 40 cm-long open-ended cell [64] internal to the beam-pipe. At each end of the

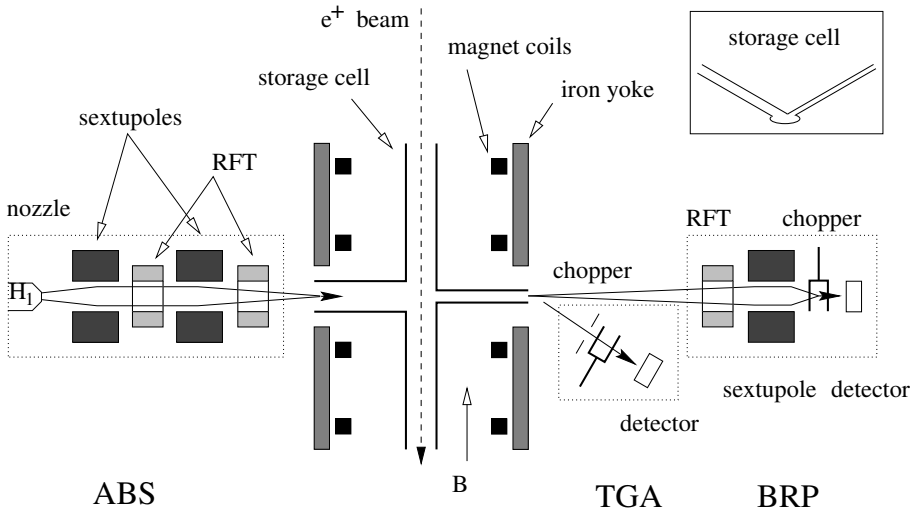

Figure 3.2: Scheme of the HERMES polarized target: in the left-hand-side the ABS inject the target atomic polarized gas into the target cell in a direction transverse to the HERA beam direction. Part of the target gas is extracted directly from the cell (right-hand-side) to be analyzed by the TGA and the BRP, providing the atomic/molecular fraction and the mean polarization.

storage cell the gas is exhausted by a pumping system resulting in a characteristic triangular profile of the target gas density inside the cell.

Polarized gas source. The *Stern-Gerlach* Atomic Beam Source [61], schematically represented in figure 3.2, generates first an atomic gas beam by a radio-frequency dissociator and a nozzle plus skimmer collimator system, then a set of sextuple magnets bended away the atoms with unwanted electron polarization and high frequency transition units transfer the polarization to the nuclei. The polarized gas is fed into the target cell immersed in an homogeneous magnetic field parallel or transverse to the beam direction for longitudinally or transversely polarized target respectively. The target monitor apparatus is continuously measuring a small sample of the gas extracted from the target. The Target Gas Analyzer [62] measured the atomic and molecular contents of the gas providing the atomic fraction, typically smaller than 1 since atoms have a non-zero probability to recombine into molecules inside the cell; at the same time the Breit-Rabi Polarimeter [63] measures the atomic polarization.

Unpolarized gas source. The unpolarized gas is injected by the UGFS system into the cell, through a different tube with respect to the one used by the ABS.

A gaseous target provides a number of advantages with respect to liquid-solid targets. The polarization is high ($> 80\%$)[3] with no dilution from not polarized materials and can be easily reversed in few milliseconds, reducing the systematic errors.

[3]For instance solid deuterium target has a polarization $\backsim 50\%$

Furthermore a gaseous target allows low-density measurements (of the order $\sim 10^{14}$ nucleons/cm^2) in agreement with HERA requirement to not have a big impact on the beam lifetime. Only at the end of a fill, when the beam current approaches low intensity, HERMES is allowed to increase target density to $\backsim 10^{16}$ nucleons/cm^2, reducing the beam lifetime to few hours. Until 2005 in the low-density target period the gas was polarized and at the end of the fill high-density unpolarized gases were used; after 2005 the fill was still divided into a low and a high density target periods, but only unpolarized gases are used.

With a gaseous target it is easy to change the type of gas injected. In 1995-2000 data taking period HERMES was running with a longitudinal polarized target, with ^{3}He (1995), hydrogen (1996-97) and deuterium (1998-2000). In 2001, during a long-time shutdown, the longitudinal target magnet was replaced by a transverse target magnet, and the 2002-2005 period was characterize by a transverse polarized hydrogen target. During another shutdown at the end of 2005 the polarized target was removed to install a large angle recoil detector and the 40 cm-long storage cell was replaced by a 15 cm-long one. During 2006-2007 data taking one hydrogen unpolarized target was employed.

The unpolarized data were collected for several nuclear species: H2, D2, ^{4}He, Ne, Kr, Xe.

After a selection of the statistically significant samples, the analysis described in this thesis is limited to hydrogen and deuterium targets collected during the 2000-2006 data taking periods:

2000 longitudinally polarized deuterium and unpolarized hydrogen and deuterium (e^+ beam);

2004-2005 unpolarized deuterium (e^+-e^- beams);

2006 (1$^{\mathbf{st}}$ period) unpolarized hydrogen (e^- beam).

All the transversely polarized target data (2004 and 2005 hydrogen runs) are rejected, as the transverse target magnet can influence the events kinematics by bending the trajectories of the scattered lepton and of the outgoing charged hadrons. The data from **2$^{\mathbf{nd}}$** period of 2006 and 2007 are rejected since they are still in the initial calibration stage, and from the first analysis checks of these data it is clear they need further corrections and re-calibrations.

Since this analysis does not require the use of polarized target or beam, the data are always averaged over the beam and the target[4] polarizations to achieve a global unpolarized sample.

3.3 The spectrometer

The HERMES spectrometer (figure 3.3) [56] is a forward angle instrument consisting in two symmetric top-bottom halves above and below the horizontal plane defined

[4] In case of polarized target.

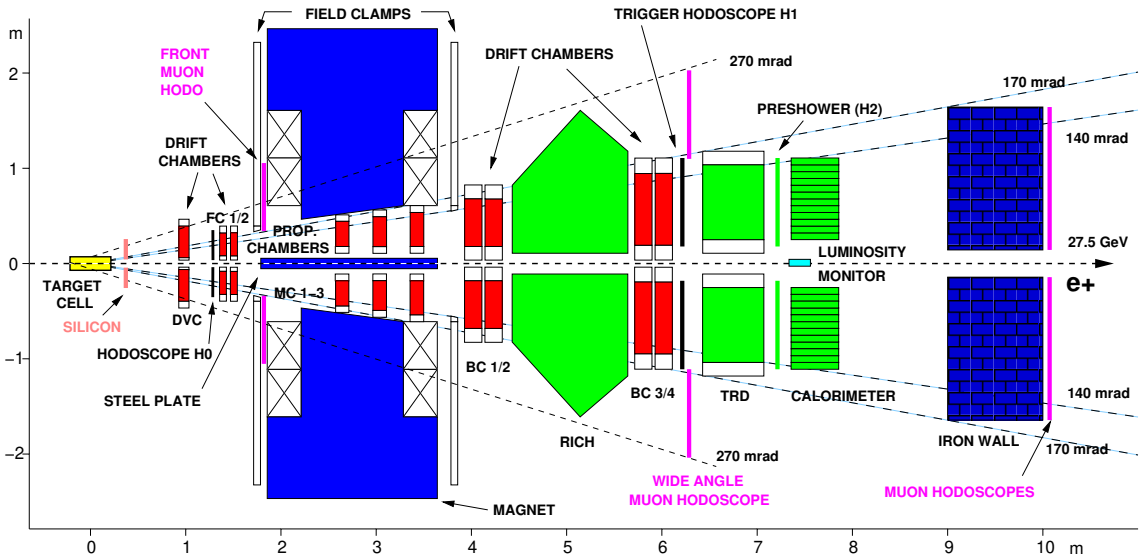

Figure 3.3: Side view of the HERMES spectrometer. The Spectrometer consists in two identical halves above and below the beam-pipe, defining the TOP and the BOTTOM part of the detectors. The spectrometer is also divided in a *front* and a *back* part, depending on detector locations with respect to the dipole magnet. Several wire chambers (in red) and Particle IDentification(PID) detectors (in green) provide the tracking and the type definition of the revealed particles.

by the lepton beam pipe. The coordinate system has the z-axis pointing in the direction of the beam, the y-axis pointing upwards and the x-axis pointing radially outside of the ring. The spectrometer magnet, that divided the detector in a *front* and a *back* part, provided an integrating deflection power of 1.3 Tm to determine the momentum of the charged tracks. Within the magnet region the beam is shielded with a steel plate, and, to compensate the remaining field components, there is a correction coil within the shielding plate. The plate limits the acceptance for small polar angles θ, while the aperture of the magnet defines the upper limits on θ, so that only particles with scattering angle within ± 170 mrad in the horizontal direction and between $+(-)40$ and $+(-)140$ mrad could be accepted, as depicted in figure 3.4.

The luminosity of the experiment is determined with the use of a Luminosity monitor [65] located close to the beam pipe at the electromagnetic calorimeter position, as shown in figure 3.3. It consists in two calorimeters above and below the beam pipe, each made of 12 $NaBi(WO_4)_2$ crystals and read out by a photomultiplier. Since its position is so close to the beam pipe, during the beam injection it is shifted away from the beam pipe to avoid radiation damage.

The luminosity monitor measures the scattering rate of the lepton beam off the shell electrons of the atomic target for three processes, Bhabha scattering

$$e^+ e^- \rightarrow e^+ e^-$$

and pair annihilation

$$e^+ e^- \rightarrow \gamma\gamma$$

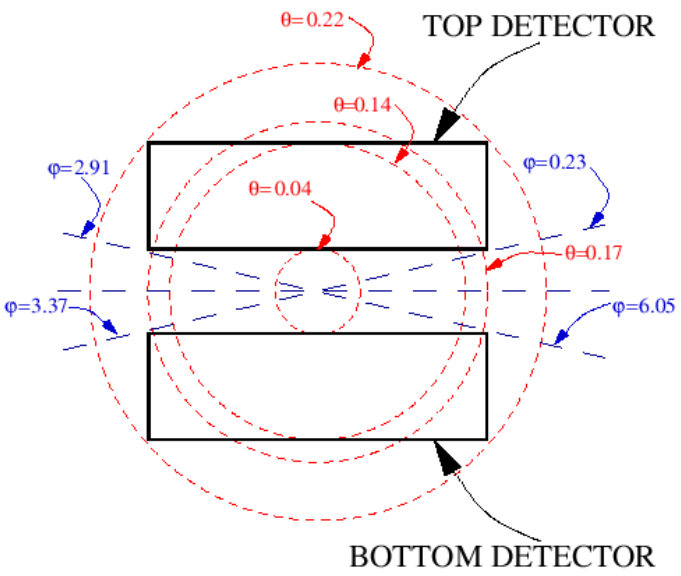

Figure 3.4: Front-scheme of HERMES spectrometer: HERMES angular acceptance is delimited in the azimuthal angle ϕ by the red dotted circles, and in the polar angle θ by the blue dotted lines.

when the positron beam is used, and the Møller scattering

$$e^- e^- \rightarrow e^- e^-$$

for the electron-beam data taking periods. The cross-section of these processes is well known, thus the luminosity is obtained from the measured rate of events normalized to the known cross-section, and finally corrected for the luminosity monitor acceptance and efficiency.

The spectrometer should serve two fundamental tasks, the reconstruction of the particle tracks, and the identification of the particle types: its components can therefore be grouped in two different categories: the tracking detectors and the Particle IDentification (PID) detectors, both described in the following sections.

3.3.1 The tracking detectors

The tracking system consists in several wire chambers that provide the *front* and the *back* tracking, depending on their position with respect to the magnet. All the tracking chambers have several wire planes with wires oriented either vertically (X plane), tilted by $\pm 30^0$ (U and V planes), or shifted by half the width of the cell perpendicular to the corresponding plane (X', U' and V' planes).

The front tracking system consists in the Drift Vertex Chambers (DVC)[56] and two Front drift Chamber (FC1/2) [66]: both have six wire planes with configuration XX'UU'VV'.

The Front Chambers have a cell width of 7 mm for a spatial resolution of 225 μm.

Radiator	P^{π}_{thresh}	P^{K}_{thresh}	P^{P}_{thresh}
Aerogel	0.6 GeV	2.0 GeV	3.8 GeV
C_4F_{10}	2.7 GeV	9.4 GeV	17.9 GeV

Table 3.1: The momentum threshold for pions, kaons and protons in the RICH Aerogel and C_4F_{10} radiators.

The Back drift Chambers (BC1-4) [68] have 6 wire planes with the XX'UU'VV' configurations. The drift cell width is of 15 mm with a measured resolution per plane of ≈ 300 μm.

In addition three multiwire proportional chambers are located inside the gap of the magnet, and are called Magnet Chambers (MC1-3) [67]. They consist of three planes with configuration UXV, and have a resolution in each plane of 700 μm. These chambers are mostly used to determine the momentum of relatively low energy particles, called *magnet* (or *short*) *tracks*, that are bended out of the acceptance of the back part of the spectrometer by the magnet field.

The front and the back partial tracks are then merged in a full track by a pattern-matching algorithm separately in each X, U and V orientation. This allows the determination of the particle momenta and charge, based on the spectrometer magnet bending. Furthermore, the Back Chambers help to associate the particle track to its signals in the PID detectors.

The complete tracking reconstruction algorithm and procedure, described in detail in [69], provides a final resolution for the track momenta of $\delta p/p < 2.2\%$, and an angular resolution of $\delta\theta < 1.4$ mrad.

3.3.2 The Particle IDentification detectors

The HERMES particle identification system consists in four detectors: a dual-radiator Ring Imaging CHerenkov (RICH) [70], which, in 1998, substituted a threshold Cherenkov counter, a Transition Radiation detector (TRD) [56], a lead-scintillator hodoscope (H2) [56] used as a preshower detector, and a lead-glass electromagnetic calorimeter [72]. For each particle the responses of the four PID detectors are combined using a Bayesian algorithm (see section 3.4), in order to define the probability for the track to be a lepton or a hadron. In the inclusive analysis this procedure provide a lepton identification efficiency $> 98\%$, with a hadron contamination less than 0.5%.

The Ring Imaging CHerenkov detector. The first PID detector a particle meet in passing through the HERMES spectrometer is a Cherenkov counter detector [56, 70]. The Cherenkov response is used to improve the separation of lepton and hadron in some kinematical region (low momenta), but its fundamental task is the identification between the different hadron type, in particular pions, kaons and protons. As its name suggests, the counter uses the Cherenkov effect: when a

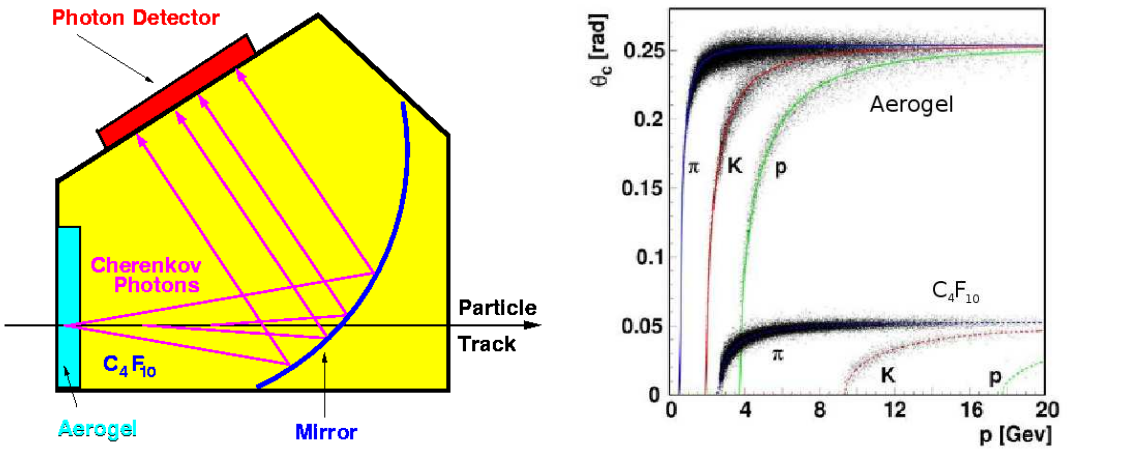

Figure 3.5: **Left:** side view of one RICH half: a particle track passing through the Aerogel radiator (the cyano zone in the left-hand-side) and the gas radiator (the larger yellow zone) emits Cherenkov photons (in pink), deflected by a spherical mirror array into the photomultiplier matrix. **Right:** the Cherenkov angle θ_c as a function of hadron momentum for pions, kaons and protons as provided by a Monte Carlo simulation. The upper curves represent the responses from the Aerogel radiator and the lower curves the ones from the gas radiator C_4F_{10}. The combination of the two detector responses allow a high efficiency hadron type identification for particles with momenta between 2 and 15 GeV.

particle pass through a dielectric medium (the radiator) with a velocity larger than the speed of light in that material, it emits a radiation (the Cherenkov radiation) with a characteristic angle θ_c depending only on the radiator refracting index n and the particle velocity v:

$$cos\theta_c = \frac{c}{nv} \tag{3.1}$$

where c is the velocity of light in vacuum. Particle with $v < c/n$ does not emit any Cherenkov radiation, or in other terms, there exist a threshold in particle momentum below which no Cherenkov radiation is emitted:

$$P < P_{thresh} = mc/\sqrt{n^2 - 1} \tag{3.2}$$

with m the particle mass. Thus, the threshold momentum P_{thresh} and the emission angle θ_c depend on the particle type. The Cherenkov threshold counter, working at HERMES from 1995 to 1997 could distinguish pions from heavier hadrons in the momentum range between 3.8 and 13.6 GeV. In 1998 this counter was replaced by a dual radiator Ring Imaging CHerenkov (RICH)[70], where the particles pass through two radiators with different refracting index. The RICH, unlike to the Cherenkov counter, measures the opening angle of the light cone emitted by radiating particles, and this information, together with the particle momentum provided by other detectors, allows to fix the particle mass, i. e. the particle type. The two radiators are colloidal silica aerogel and the heavy gas C_4F_{10} with refracting index of 1.030 and 1.001, respectively. The emitted Cherenkov light is focused by a spherical

mirror array into a photo-multiplier grid, as schematically represented in the left plot of figure 3.5.

The momentum threshold for different hadron type in the two RICH radiators are listed in table 3.1, and the Cherenkov angles θ_c versus particle momenta for different hadron type are shown in the right picture of figure 3.5. The combination of the responses of the two different radiators allow an high efficiency identification of pions, kaons, protons and the respective anti-particles, in the wide momentum range $2 - 15$ GeV.

The Transition Radiation Detector. The Transition Radiation Detector (TRD) [56] is mainly used to distinguish the electrons from the hadrons. The transition radiation is emitted when a relativistic particle is propagating through the boundary between materials with different dielectric constant ϵ. The transition photons are emitted in the forward direction at an angle $\theta \propto 1/\gamma$ with respect to the particle direction, where γ is the Lorentz boost $\gamma = \sqrt{1-\beta^2}$ [5] [71]. For ultra-relativistic particles the radiation is in the range of X-rays. Due to low emission probability in a single boundary, the HERMES TRD was build with six identical layers in a sandwich-like structure (see figure 3.6), each module consisting in a polypropylene fibers radiator and a proportional wire chamber filled by Xe/CH_4. In the wire chambers both leptons and hadrons produce a signal due to ionization losses, but only leptons emit the transition radiation, therefore two distinct peaks can be observed in the TRD response, as in the right plot of picture 3.7, when the response of the six modules is combined.

A high energy lepton or photon, when passing through a thick absorber initiates an electromagnetic shower by means of Bremsstrahlung and pair production, generating more leptons and photons of lower energy. The secondary leptons and photons continue to produce cascade of particles until their energy fall below the critical energy (~ 100 MeV), when they start to dissipate their energy primarily by ionization and excitation rather than by the generation of new shower particles. The characteristic scale of an electromagnetic cascade is the so called radiation length X_0, defined as the mean distance over which a high energy lepton looses all except $1/e$ of its energy by Bremsstrahlung.
On the contrary the hadrons, due to their higher mass, loose energy mostly through inelastic collisions, and this results in a much slower energy dissipation of hadrons with respect to the leptons. This difference was exploited both by the preshower detector and the Calorimeter to identify the lepton and the hadrons among the detected particles.

The preshower hodoscope. In the back spectrometer region there are two identical plastic scintillator hodoscopes, $H1$ and $H2$ [56], that, together with the front-region hodoscope $H0$, are used for the physics triggers and for time of flight measurements. Both the hodoscopes consist in 42 vertical scintillator panels with a thickness of 9.3 cm, that overlap by 1.5 mm to avoid acceptance gap. The hodoscope

[5] $\beta = E/m$.

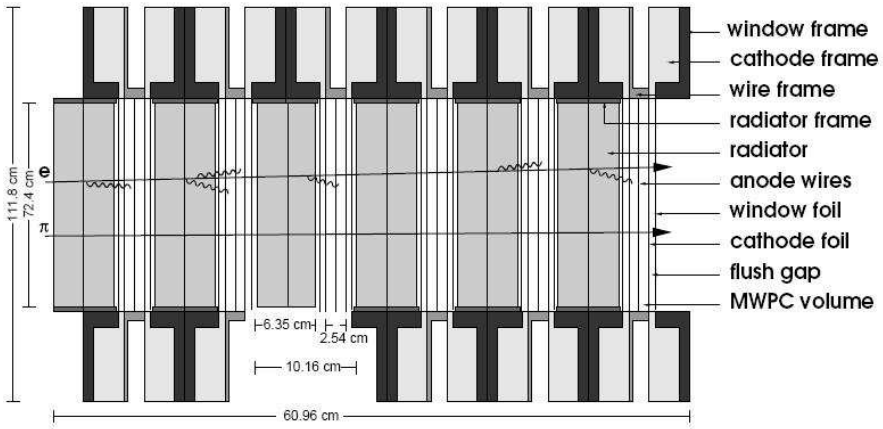

Figure 3.6: Side view of the TOP half of the TRD: when an electron track and a pion track pass through the six modules of the TRD, only the electron is emitting transition radiation photons.

$H2$ is preceded by a 1.1 cm of lead, corresponding to two radiation lengths.

While hadrons deposit a minimum ionizing particle, showering electrons or positrons give rise to a much higher signal, initiated electromagnetic showers that will develop in the adjacent calorimeter, and for this reason it was called preshower detector. The energy deposition in the preshower from leptons and hadrons are shown in the middle plot of picture 3.7: the hadrons are responsible for the peak below 5 MeV, while the deposit of leptons is higher in average (about $20 - 60$ MeV) and broader.

The electromagnetic calorimeter. As the preshower detector the calorimeter exploits the difference in energy loss of leptons and hadrons to identify the particles detected. Each half of the HERMES calorimeter [72] consists of 420 lead-glass blocks with an area of 9x9 cm^2 for each detector half, as in figure 3.8, coupled to a photomultiplier (see figure 3.8). Lead glass thickness of 50 cm, corresponding to 18 radiation lengths, combined with the lead plate of $H2$, guarantee the electromagnetic showers to be almost fully contained within the preshower and the calorimeter. The energy deposited in the preshower and the calorimeter divided by the particle momentum is very close to 1 for elector-magnetic particles, while is much less than 1 for hadrons, as shown in the right plot of figure 3.7.

To avoid radiation damage during the beam injection each calorimeter half is moved 50 cm away from the beam-pipe vertically.

3.4 The PID probabilistic algorithm

From each response of the four PID detectors described above it is possible to define the probability for a particle to be an electron (positron) or a hadron. For each PID detector D it is possible to define the probability $P_D(T, p \mid X)$ that a particle of type

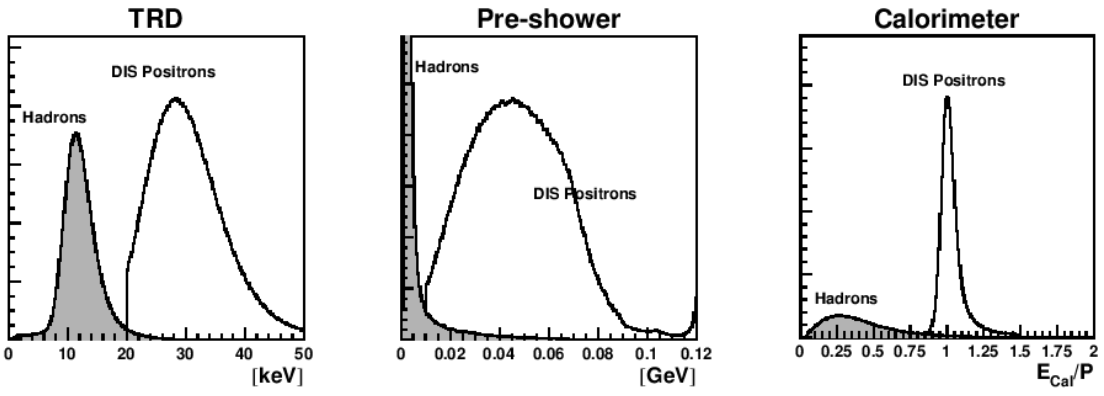

Figure 3.7: Responses of three PID detectors: Monte Carlo results for DIS positrons and hadrons energy deposition in the TRD, preshower and Calorimeter.

T with momentum p causes the detector response X. The particle type T can be *lepton* (l) or *hadron* (h), and the response X corresponds to the Cherenkov angle θ_c in case of the RICH, or to the particle energy deposition for the other detectors. The $P_D(T, p \,|\, X)$, called the *parent distribution*, can be determined by measuring the detectors response to a clean sample of lepton or hadron, that are selected by imposing hard cuts on the PID detectors other than the one under consideration. If $P(p \,|\, T)$ is the probability that a particle with momentum p is of type T then the Bayes theorem provides the probability for the measured detector response X originated by a particle with momentum p, to be caused by a particle type T:

$$P_D(X, p \,|\, T) = \frac{P(p \,|\, T) \cdot P_D(T, p \,|\, X)}{\sum_T P(p \,|\, T) \cdot P_D(T, p \,|\, X)}$$

Hence the probability that the measured response X in the detector D is due to a lepton l (hadron h) with momentum p become:

$$P_D(X, p \,|\, l(h)) = \frac{P(p \,|\, l(h)) \cdot P_D(l(h), p \,|\, X)}{P(p \,|\, l) \cdot P_D(l, p \,|\, X) + P_D(p \,|\, h) \cdot P_D(h, p \,|\, X)} \tag{3.3}$$

where $P(p \,|\, l(h))$ corresponds to the incident lepton and hadron fluxes $\phi_{l(h)}$.

The probabilities described in equation 3.3 for the lepton and the hadron can be combined into a logarithmic ratio:

$$PID'_D = log_{10} \frac{P_D(X, p \,|\, l)}{P_D(X, p \,|\, h)} \tag{3.4}$$

that in terms of *parent distributions* and lepton-hadron fluxes becomes:

$$PID'_D = log_{10} \frac{P_D(l, p \,|\, X) \cdot P(p \,|\, l)}{P_D(h, p \,|\, X) \cdot P(p \,|\, h)} = PID_D - log_{10}\Phi \tag{3.5}$$

where

$$PID_D \equiv log_{10} \frac{P_D(l, p \,|\, X)}{P_D(h, p \,|\, X)}$$

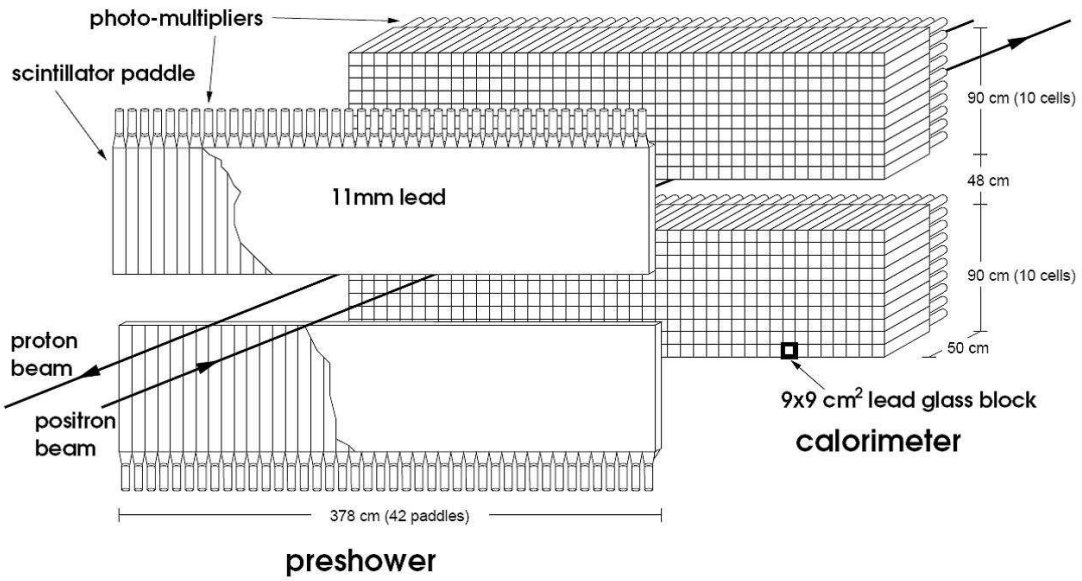

Figure 3.8: HERMES preshower $H2$ and calorimeter setup: the particles pass through the 1.1 cm thick of lead of H_2, where leptons start the production of electromagnetic showers that finish to develop in the calorimeter.

and Φ, called the flux factor, is:

$$\Phi \equiv \frac{P(p\,|\,l)}{P(p\,|\,h)} = \frac{\phi_l}{\phi_h}$$

The quantity PID'_D equals 0 when a particle has the same probability to be a lepton or a hadron, whereas $PID'_D > 0$ if the particle is more likely a lepton and $PID'_D < 0$ if it is more likely a hadron. The flux factor can be neglected in HERMES analysis, since its correction is usually small, as shown in figure 3.9.

The responses of the four PID detectors can be combined to maximize the sensitivity to the particle type. The combination commonly used at HERMES are:

$$\begin{aligned} PID2 &\equiv PID_{calo} + PID_{pre} \\ PID3 &\equiv PID_{calo} + PID_{pre} + PID_{RICH} \\ PID5 &\equiv PID_{TRD} = \sum_{i=1,6} PID_{TRD_i} \end{aligned} \tag{3.6}$$

where for the TRD the sum runs over the six modules in each detector half. Taking into account the flux factor and all the detector responses the standard criteria used at HERMES for the lepton-hadron separation are:

$$\begin{aligned} PID_3 + PID_5 &> 1 \text{ leptons} \\ PID_3 + PID_5 &< -1 \text{ hadrons} \end{aligned} \tag{3.7}$$

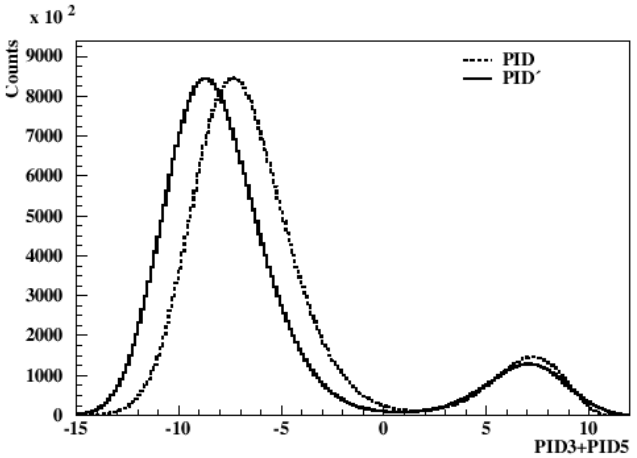

Figure 3.9: The $PID3 + PID5$ distribution with (dotted line) or without (solid line) considering the flux factor.

where the interval between -1 and 1, corresponding to a poor identification, is eliminated from the data sample. With the use of the above criteria the efficiency in lepton-hadron separation is larger than 98% and the cross-contaminations smaller than 1%. A 3-dimensional view of the positron-hadron separation is shown in figure 3.10.

A detailed description of particle identification and PID probabilistic algorithm at HERMES can be found in [73, 74, 75].

3.5 The Trigger

Several triggers are set up at HERMES for a first level selection of signal events [56]; after their very fast decision, made within 400 ns, they initiate the readout of all the detectors in case of positive response. Two triggers are mainly used as a first selection of the events produced by DIS or photoproduction processes. The detectors involved in the trigger system are shown in figure 3.11.

The selection of potential DIS events was done by the trigger 21, used in the present analysis. The trigger 21 select an event when an electron in coincidence with the HERA bunch hits the three hodoscopes $H0$, $H1$ and $H2$, and deposits enough energy in two adjacent calorimeter column in the same spectrometer half. Since the photons can generate high signal in the preshower and in the calorimeter, a signal in the hodoscopes suppresses neutral particle background. In order to discriminate hadronic and electromagnetic showers the total energy deposition in calorimeter should be above 1.4 GeV in case of low density runs, and 3.5 GeV for the high density runs, corresponding respectively to the cut $y < 0.87$ and $y < 0.91$.

Of all the events recorded as DIS by the trigger 21, approximately only $4 - 6\%$ are identified as DIS in the off-line analysis.

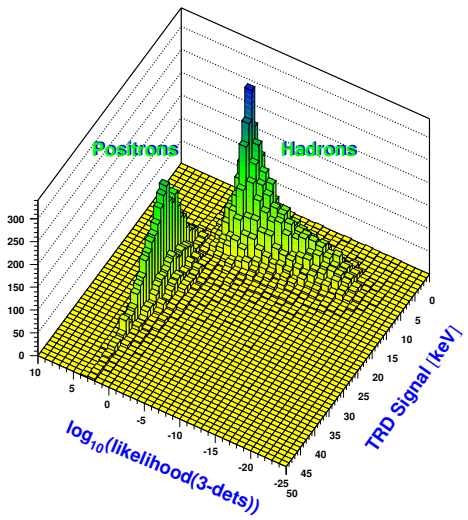

Figure 3.10: A 3-dimensional view of the positron-hadron separation due to all the four PID detectors.

The triggers efficiency (TE) is highly sensitive to the single detector components inefficiencies. The trigger 21 for instance achieved efficiencies lower than 90% in some periods, mostly due to $H0$ inefficiencies. Therefore, each analysis using the trigger 21 should take into account the inefficiencies of $H0$, $H1$, $H2$ and the calorimeter (CALO). The way to calculate these inefficiencies was pointed out in [76], and it is briefly described in the following.

The definition of trigger 21 ($Tr21$) is:

$$Tr21 = (H0 * H1 * H2 * (CALO > 1.4\,\text{GeV}))_{TOP} + ()_{BOTTOM} \tag{3.8}$$

where the + means the two detector halves are in OR, and its efficiency ($\epsilon(Tr21)$) is defined as the product of the single detector efficiency:

$$\epsilon(Tr21) = \epsilon(H0) * \epsilon(H1) * \epsilon(H2) * \epsilon(CALO) \tag{3.9}$$

Each efficiency can be calculated using a control trigger involving the same detectors in $Tr21$ except the one under study. Control triggers exist for $H0$, $H1$ and $H2$, but not for the $CALO$, whose efficiency is measured by $Tr28$, which is the close to $Tr21$ but without requirements on the $CALO$:

$$\begin{aligned}
Tr18 &= (H1 * H2 * (CALO > 1.4\,\text{GeV}))_{TOP} + ()_{BOTTOM} \quad \text{used for } H0 \\
Tr19 &= (H0 * H2 * (CALO > 1.4\,\text{GeV}))_{TOP} + ()_{BOTTOM} \quad \text{used for } H1 \\
Tr20 &= (H0 * H1 * (CALO > 1.4\,\text{GeV}))_{TOP} + ()_{BOTTOM} \quad \text{used for } H2 \\
Tr28 &= (H0 * H1 * H2 * BC)_{TOP} * ()_{BOTTOM} \quad \text{used for } CALO
\end{aligned} \tag{3.10}$$

Since the BC's are known to have high efficiency, the main difference between $Tr21$ and $Tr28$ is that the latter requires an AND between the two detector halves, i.e.

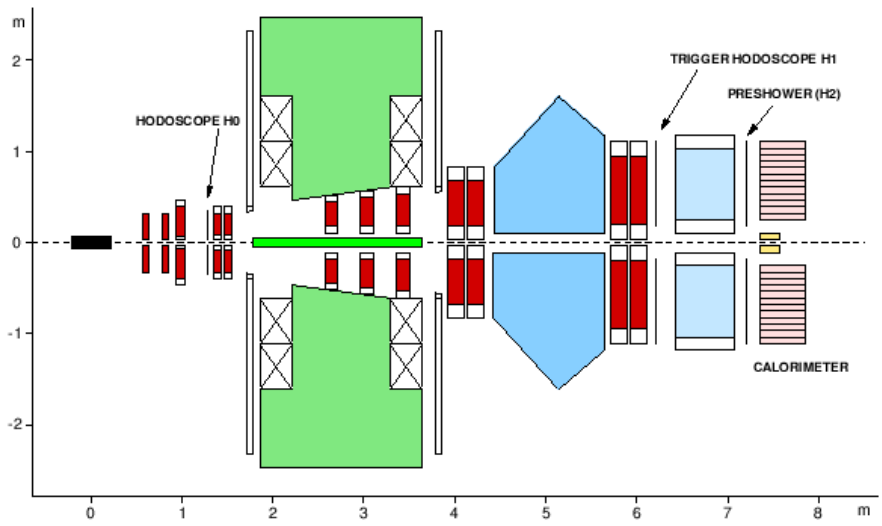

Figure 3.11: HERMES spectrometer: the positions of the detectors involved in the trigger system relevant for this analysis are highlighted.

at least two tracks for events, one in the TOP and one in the $BOTTOM$ half of the detectors, are needed. This difference cause an increase of the statistical uncertainties in the $CALO$ efficiency.

The event sample used for the efficiency study was selected subject to geometrical cuts ensuring that the tracks fall inside HERMES acceptance. The track of highest momentum is chosen to be the DIS scattered lepton, if has the same beam charge, and is identified as lepton by the TRD and the RICH, which are not involved in the trigger definitions.

If N_i is the total number of events firing trigger i, and $N_{i\&21}$ the total number of events firing trigger i and 21 together, the single detector efficiency can be written as:

$$\begin{aligned} \epsilon(H0) &= \frac{N_{18\&21}}{N_{18}} \\ \epsilon(H1) &= \frac{N_{19\&21}}{N_{19}} \\ \epsilon(H2) &= \frac{N_{20\&21}}{N_{20}} \\ \epsilon(CALO) &= \frac{N_{28\&21}}{N_{28}} \end{aligned} \tag{3.11}$$

and for each efficiency the error is

$$\delta\epsilon = \sqrt{\frac{(N_{i\&21}+1)(N_i - N_{i\&21}+1)}{(N_i+2)^2(N_i+3)}}. \tag{3.12}$$

For a detailed extraction of this formula see [77].

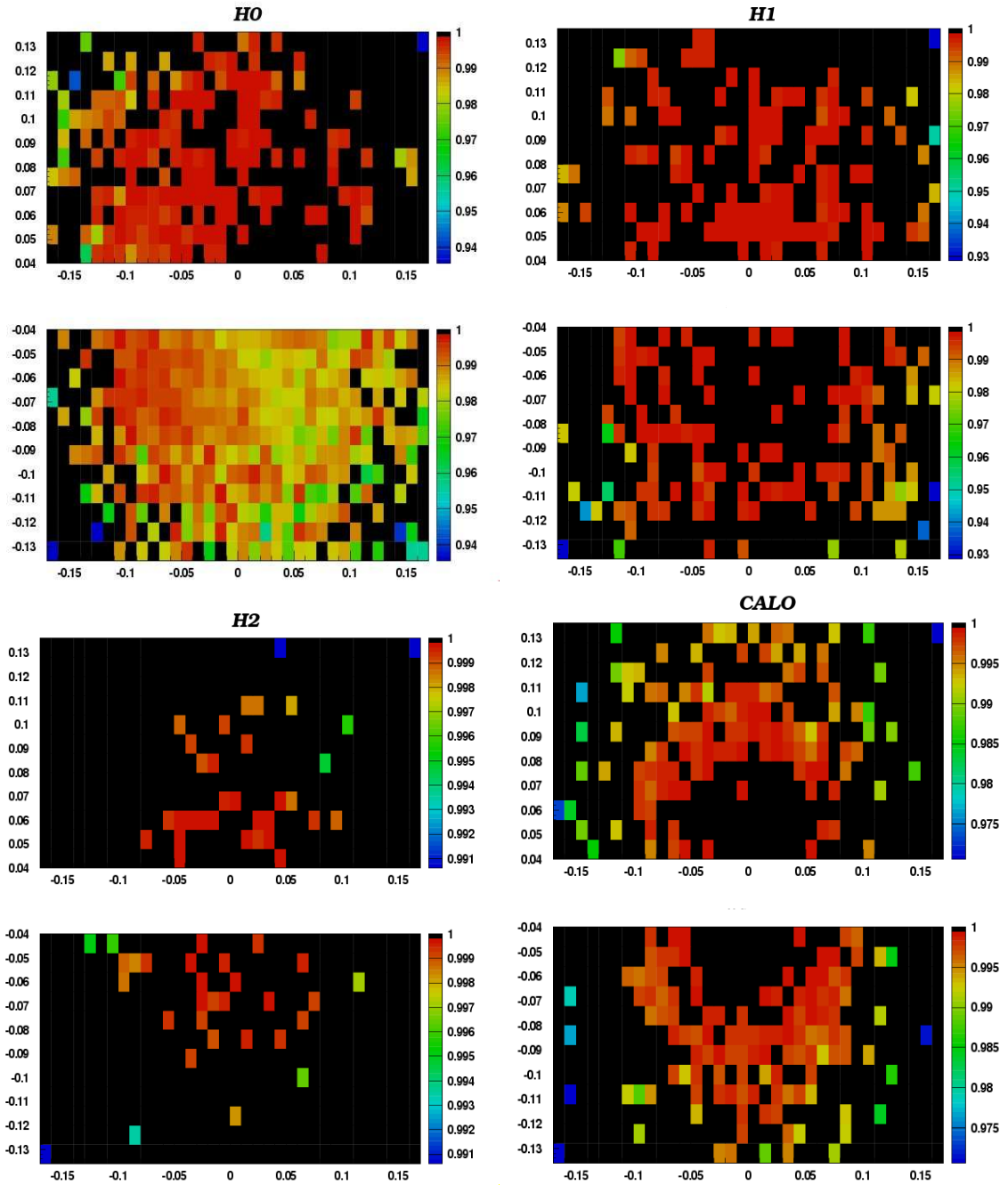

Figure 3.12: Color coded plots of Trigger 18 (top-left), 19 (top-right), 20 (bottom left) and 28 (bottom right) efficiencies. In each plot the upper and the lower pictures show the efficiencies in the TOP and in the BOTTOM detector half, respectively.

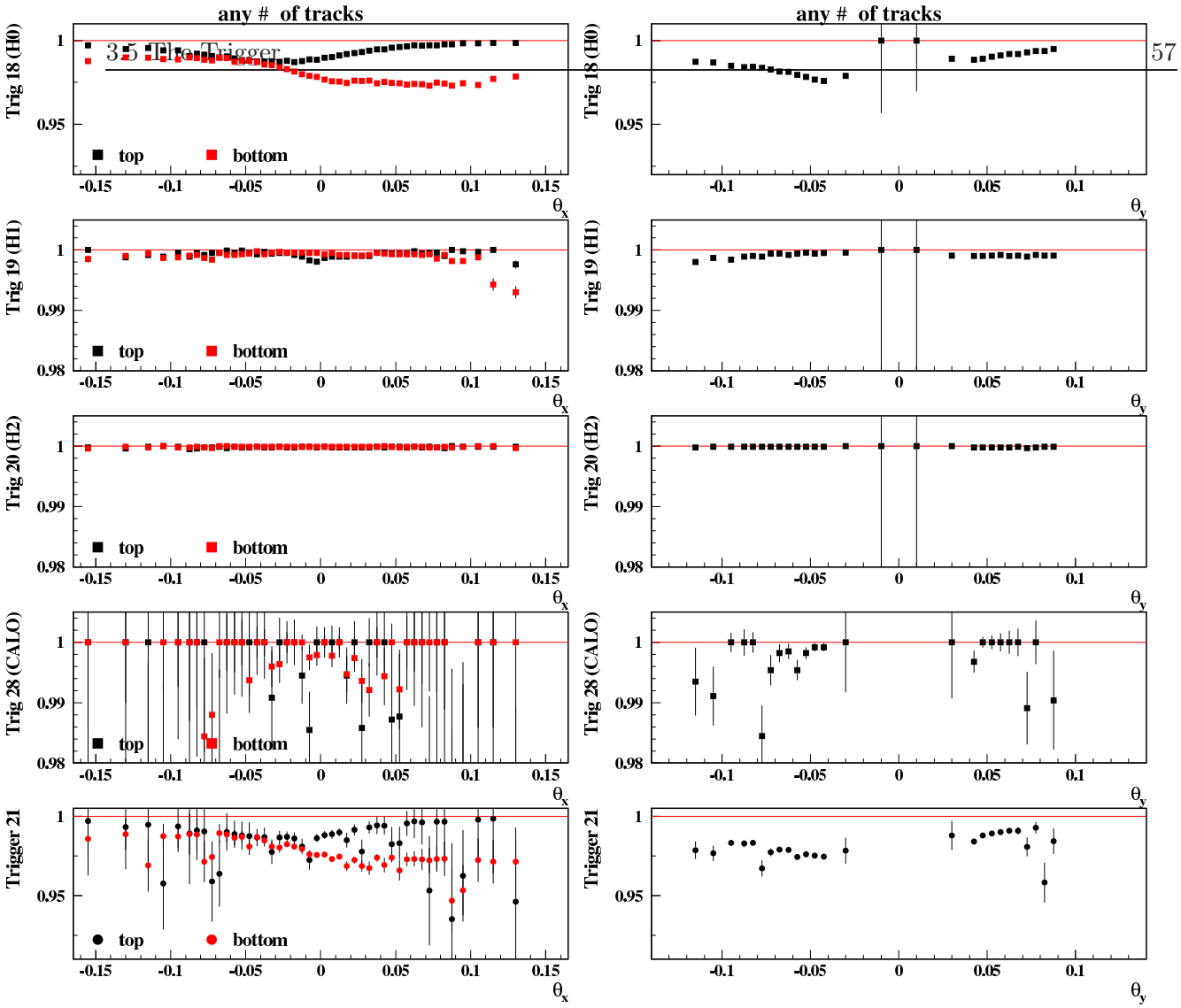

Figure 3.13: Efficiencies for the Trigger 18, 19, 20, 28 and 21 versus the angle θ_x (left plots) and θ_y (right plots), separately for the TOP and the BOTTOM detector halves.

The detectors efficiencies for 2000 run with at least two tracks in each event are plotted in two dimensional color-coded pictures in figure 3.12 as function of the angles:

$$\begin{aligned} \theta_x &= \text{arctg}(\text{tg}\theta \cos\phi) \\ \theta_y &= \text{arctg}(\text{tg}\theta \sin\phi) \end{aligned} \tag{3.13}$$

where the TOP detector half is defined by $\theta_y > 0$ and the BOTTOM half is fixed by $\theta_y < 0$. The same efficiency separately for the TOP and BOTTOM halves are shown in figure 3.13 versus θ_x and θ_y. The efficiencies of the trigger detectors is typically above 99%, but the $H0$ efficiency is generally lower, especially for the BOTTOM detector half, where reach a value around $96 - 97\%$. For 2004-2006 run the trigger 21 efficiency shows similar behavior.

The analysis described here involves the calculation of an absolute cross-section

(σ), therefore the calculated Trigger 21 efficiency should be used to weight the data:

$$\sigma = \frac{N}{\epsilon(Tr21)\ L} \tag{3.14}$$

where N is the total number of events measured and L is the luminosity. Since the angle distributions of detected particles are of fundamental interest in this analysis, data samples are corrected for the $Tr21$ efficiency in each of 40x40 equidistant bins of a two-dimensional binning in θ_x and θ_y.

3.6 Data acquisition and structure

The HERMES data production chain consists of two different parts, the Data AcQuisition (DAQ) system, responsible for the fast readout of the detector output when a trigger signal is generated, and the slow-control system, which every 10 seconds collected the slowly varying quantities like gas pressures, temperatures, high voltages, etc., providing informations about the performances of detectors components.

When a trigger fires, all the detectors informations are collected and stored on disk and tape simultaneously in the EPIO format (Experimental Physics Input Output Package). During this readout no new data can be accepted, resulting in a difference between the numbers of trigger i generated (T^i_{gen}) and accepted (T^i_{acc}). This results in a *dead time* fraction $\delta_i = 1 - (T^i_{acc}/T^i_{gen})$ (for instance for Trigger 21 δ_{21} is typically of 0.9), but only data with $\delta_i < 0.5$ are used for the analyses.

The raw data collected, consisting of single detector hits and channel numbers, are translated by the HERMES DeCoder (HDC) into the HERMES coordinate system, taking into account the all the detector geometries and calibrations. The HDC output is then stored in the so called DAD (Distributed ADamo) tables. The reconstruction of the particle tracks is performed by a tree search algorithm, called HRC (HERMES ReConstruction software), by combining the front and the back partial tracks; it also provides the particle charges, momenta, and informations about the PID.

These event-level data are synchronized to the slow control data, with the use of a timing signal registered both in the event level data and in the slow control data. The synchronized data are finally storaged in the μDST (micro-Data Summary Tape) tables, containing the fundamental informations to perform a physical analysis.

In the μDST tables the data have a specific logical units structure. For each data taking period, in which HERMES was running with a fix configuration, the longest interval is the *fill*, corresponding to the data recorded during a HERA electron-positron fill, which has a typical time interval of 12-14 hours. Within a *fill*, the data are organized into *runs*, each defined by a size of $\sim$ 450 MB of the EPIO data. Typically a run contains data collected in an interval of 10 minutes, even if this amount of time can considerably change depending on beam current, target density

and luminosity. The time scale of 10 seconds, fixed by the slow control data, defines the units called *bursts*. The shortest time interval is called *event*, and it contains all the data storaged in relation to one trigger signal.

Chapter 4

Data selection

The aim of this work is the extraction of the unpolarized structure functions $F_{UU}^{\cos\phi_h}$ and $F_{UU}^{\cos 2\phi_h}$ related to cosine modulations in the cross-section for semi-inclusive hadron productions:

$$\frac{d\sigma}{dx\,dy\,dz\,dP_{h\perp}^2\,d\phi_h} = \frac{\alpha^2}{xyQ^2}\frac{y^2}{2(1-\epsilon)}(1+\frac{\gamma^2}{2x})\{F_{UU,T}+\epsilon F_{UU,L}+ \sqrt{2\epsilon(1+\epsilon)}\cos\phi_h F_{UU}^{\cos\phi_h}+\epsilon\cos 2\phi_h F_{UU}^{\cos 2\phi_h}\} \tag{4.1}$$

Unfortunately the extraction of the above $\cos\phi_h$ and $\cos 2\phi_h$ modulations from data is not straightforward because they couple to a number of *experimental sources* of azimuthal cosine modulations, like HERMES geometrical acceptance and higher order QED effects, described in the next chapter.

To disentangle the interesting contributions from the experimental ones, the measured azimuthal distributions are compared with the azimuthal distributions simulated by a Monte Carlo and generated only by geometrical or radiative effects.

For this reason this analysis strongly depend on Monte Carlo (MC) simulations, therefore the basic steps for a MC production are discussed in the next section.

In the second part of the chapter data and MC productions employed in this analysis are listed and then the criteria to select Semi-Inclusive DIS events in real data and Monte Carlo productions are presented.

4.1 Monte Carlo

During the last thirty years Monte Carlo (MC) technique became a powerful tool in particle physics, whenever some of the fundamental laws can be written down, but they cannot be analytically solved for problems of interest. A Monte Carlo program is based on the simulation of all the possible aspects of the underlying physics known, supplying the unknown or poorly known effects with parameterizations or phenomenological models. The goal of a MC is to generate events as detailed as could be observed by a real detector, with the same average behavior and detection biases as real data. The procedure to obtain a similar event sample can be described

Monte Carlo events				
Event type	**MC chain**	**Geometry**	**Features** (determined by)	**Kinematical level available**
Born (4π)	GMC/JETSET	4π	True level physics	True
Fully tracked	GMC/JETSET RADGEN HRC	HERMES acceptance	True level physics Radiative effects Detector smearing	True Radiated Fully tracked
Smeared	GMC/JETSET RADGEN HSG	HERMES acceptance	True level physics Radiative effects Detector smearing	True Radiated Smeared

Table 4.1: Definitions of the type of events simulated with different Monte Carlo chains.

in two different stages: the **events generation** and the **detector simulation**, both consisting of different steps described below.

Events generation

A Generator Monte Carlo (GMC) provides the simulation of the initial interaction selecting the physical process involved in each event according to the cross-section, while the program RADGEN [78] modifies the event kinematics by random generation of higher order QED processes (*radiative effects*). Due to the QCD confinement mechanism, the outgoing quarks and gluons generated by GMC have to fragment into colourless hadrons via the fragmentation process (or hadronization). This process involves long distances reactions, where QCD becomes strongly interacting and perturbation theory breaks down. For this reason the fragmentation should be based on a model, and, at HERMES, the program used for this process is JETSET [79], based on the Lund String model. The JETSET parameters, originally chosen to describe the fragmentation in e^+e^- annihilation at LEP, were tuned to adjust the model to HERMES energies using the measured HERMES hadron multiplicities [80]. The latest parameter set is called 2004*c* and is the one used for this analysis.

When the Monte Carlo chain involves only GMC and JETSET, the events generated are called *Born events* (see table 4.1). Their features are due only to the physics processes selected by the generator, and they are not affected by radiative effects or detector acceptance and inefficiencies.

Among the different generators available, in this work two generators will be used, tuned to describe HERMES data [81]: PYTHIA [82] and LEPTO [83]. Both are excellent tools to study DIS process, but there are differences between them. PYTHIA generates the events kinematics according to the cross-section, while LEPTO generates the events kinematics uniformly in ν and Q^2, so that an event weight depending on the cross-section is needed. Furthermore the LEPTO MC does not include the exclusive vector mesons production which could influence the results in some kine-

matical region, while PYTHIA does not account for elastic processes which are in any case irrelevant for Semi-inclusive reactions.

Detector simulation

Once the events are generated by GMC/JETSET+RADGEN, their interaction with the detectors has to be simulated. Two different approaches can be followed at this point. The first one make use of a GEANT [84] Monte Carlo which simulates the complete path of the particles inside the detectors, such as their interaction with detector materials, bending in magnetic fields or showering in calorimeter. Since this approach is very time-consuming, sometimes it is possible to skip the full chain of detector simulation and replace it by a simplified procedure, called *Smearing Generator*, that modifies the kinematical variables taking into account only geometrical acceptance and detector randomly smearing. The events that are simulated with the first method are called *fully tracked*, the other are called *smeared events* (see table 4.1).

The fully tracked events. This stage consists of two steps. First the HERMES spectrometer is completely simulated with the HERMES Monte Carlo (HMC) based on GEANT: each particle provided by the GMC passes through the detectors and all its interactions with the detector material are simulated using the proper interaction cross-section. The HMC [85] output is similar to the real detectors digitization, since it provide the response from each single wire or detector component. The only difference with real data is that in this case we know the 'correct answer', i.e. the original generated events features, also called the *True* kinematics of the event (see table 4.1). In the second step the standard HERMES tracking algorithm (HRC) is applied to the simulated event, so that any possible bias it contains is equally introduced in real and simulated data.

The smeared events. Alternatively to HMC+HRC chain the HERMES Smearing Generator (HSG) [80] can be used for an approximated detector simulation. The comparison between generated and fully reconstructed kinematics was done in a control sample of simulated events to study the detector effects on the track sample such as the smearing of kinematical variables due to detector limited resolution. The same was done for geometrical acceptance and tracking algorithm inefficiencies and finally all these informations were collected in a set of look-up tables. With the use of these look-up tables HSG apply to the generated events the instrumental effects and the tracking inefficiencies with a significant time savings.

Figure 4.1 shows the comparison of some kinematical distributions between fully-tracked and smeared events for a PYTHIA production with the geometry of the 2000 run. Even if the agreement between the two Monte Carlo chains is not perfect, the comparison demonstrates that HSG reproduces very well the detector and the tracking influence on lepton and hadron kinematics, therefore it can be used in HERMES analysis for fast feedbacks.

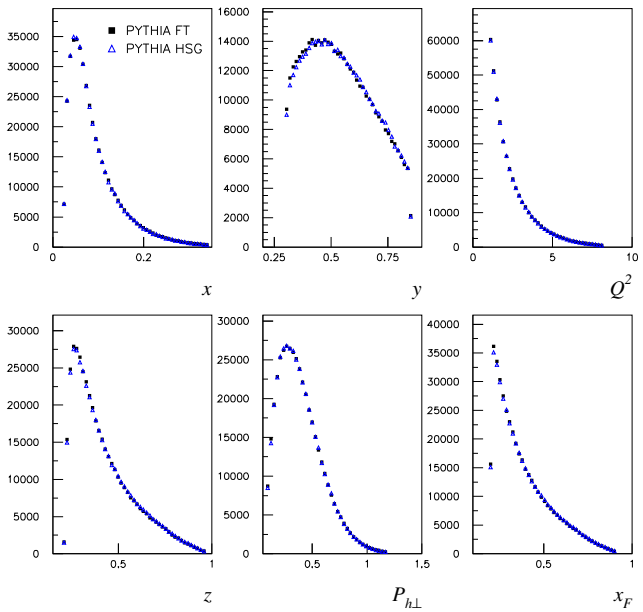

Figure 4.1: Comparison of charged hadron kinematics distributions: Fully-Tracked (FT) PYTHIA (solid squares) and Smeared (HSG) PYTHIA simulation (open triangles), both produced using the 2000 geometry.

4.2 HERMES and Monte Carlo productions

The data analyzed in this thesis involve different beam charges and both hydrogen and deuterium targets and are relative to different data taking periods: 2000, 2004, 2005 and 2006-1st period. The relative productions are labeled with 00c1, 04b2, 05b2 and 06b2, where the first two digits indicate the year when data were collected, while the last two digits identify the version of the μDST production. When data are collected at HERMES, they are stored in the a0-production, where the detector responses are interpreted using the calibration of the previous data taking period. When new calibrations are ready the data are corrected for them. New data corrections or calibrations result in productions with new letter (a,b, ...) or increased number, depending on how fundamental are the changes. Starting from the number 1 the production can be used for physical analysis.

The data productions analyzed here are characterized by:

Production	Year	Beam	Target	Target status	Target cell	Luminosity (pb^{-1})
00c1	2000	e^+	Deuterium	Polarized	40 cm long	138.7
			Deuterium	Unpolarized	40 cm long	39.3
			Hydrogen	Unpolarized	40 cm long	132.5
04b2	2004	e^+	Deuterium	Unpolarized	40 cm long	76.3
05b2	2005	e^-	Deuterium	Unpolarized	40 cm long	70.4
06b2	2006	e^-	Hydrogen	Unpolarized	15 cm long	251.1

Besides the differences in beam charge and target gas type among various years, the main change of the target setup in 2006, influenced significantly the geometry of the produced data. For this reason the data sets can be consider divided in two main periods due to target geometry: 2000-2005 and 2006.

For each data production the corresponding fully tracked Monte Carlo simulation was generated, taking into account the differences listed above and also small changes in the detector configuration occurred during the shutdowns between run periods.

4.3 Events selection

In this section the event selection criteria are presented. In the first part the constraints on the real data samples are listed, then the corresponding requirements on Monte Carlo data are reviewed.

4.3.1 HERMES data

The data sample is selected with the use of several constraints listed below.

Data quality

Several checks to ensure the high quality of data are applied at burst level. At HERMES the fundamental informations of the data sample needed to perform a physical analysis are storaged in the μDST tables as described in section 3.6. During the data taking, every 10 seconds the slow control system measured and recorded at *burst* level all the informations about the performance of the detector components. The HERMES data quality group then combined all the above informations in a bit-pattern for each burst. Each bit corresponds to a particular experimental component, and it indicates, if set to 1, that this component is properly working.

In order to define the event sample for this analysis, a good performance of PID, tracking detectors, Luminosity monitor and of the DAQ system is required. Bursts are discarded if there were not-working blocks in the Calorimeter or in the Hodoscope H2, if the luminosity was too low, if there were high voltage trips in the wire chambers, or if the DAQ dead time was larger than 50%.

Geometrical requirements

Beyond the data quality constraints, the events should satisfy several requirements to be accepted in the analysis event sample. First of all the event should contain at least two tracks, since this analysis concerns one-hadron Semi Inclusive Deep Inelastic Scattering (SIDIS). Both the tracks should not be *magnet tracks* (or *short tracks*), which means that each track of the sample should pass through all the tracking and PID detectors of the spectrometer, in order that the complete information about them was measured. Furthermore each track should satisfy the geometrical cuts described in table 4.2, which are designed to select events generated inside the target cell (Interaction point cut), and to avoid systematic effects at the edge of the spectrometer (Fiducial volume cuts).

Geometrical cuts	
No magnet tracks	
Interaction point Z-position	$-18 < V_Z < 18\,\text{cm}$
Fiducial volume:	
Front Chambers x-position	$x_{FC} < 31\,\text{cm}$
Front Chambers y-position	$7 < y_{FC} < 54\,\text{cm}$
Back Chambers x-position	$x_{BC} < 100\,\text{cm}$
Back Chambers y-position	$y_{BC} < 54\,\text{cm}$
Calorimeter x-position	$x_{calo} < 175\,\text{cm}$
Calorimeter y-position	$30 < y_{calo} < 108\,\text{cm}$
DIS cuts	
Four-momentum transfer	$W^2 > 10\,\text{GeV}^2$
Squared mass of final state	$Q^2 > 1\,\text{GeV}^2$
Fractional energy transfer	$0.3 < y < 0.85$
Bjorken scaling variable	$0.023 < x < 1$
SIDIS cuts	
Hadron energy fraction	$0.2 < z < 1$
Transverse hadron momentum	$0.05 < P_{h\perp} < 1.41\,\text{GeV}$
Angle between virtual-photon and hadron	$\theta_{\gamma^* h} > 0.02\,\text{rad}$
Feynman scaling variable	$x_F > 0.2$

Table 4.2: Geometrical and Kinematical cuts that the DIS event tracks should satisfy.

Event selection

Finally a number of requirements are designed to the selection of the specific process of interest, the Semi-Inclusive Deep Inelastic Scattering 4.2. To select a SIDIS event it is required that the track with the highest momentum is identified as a lepton by the PID algorithm (sec. 3.4): $PID_3 + PID_5 > 1$.

Then the Q^2 is asked to be larger than 1 GeV^2 to select the energy scale of Deep Inelastic Scattering, and the events with $W^2 < 10$ GeV^2 are discarded to reject the resonance region. The fractional energy transfer is limited in the region $y < 0.85$ to limit the influence of higher order QED effects. The requirement $y > 0.3$, as well as the cut $0.023 < x < 1$, basically define the kinematical acceptance of HERMES spectrometer.

In coincidence with the lepton, a second track, identified as an hadron ($PID_3 + PID_5 < -1$), should satisfy requirements on the SIDIS kinematics. The cut $0.2 < z < 1$ on the hadron energy fraction, together with the cut on W^2 and the requirement $x_F > 0.2$ improves the separation between hadrons originated directly by the struck quark (*current fragments*) from the ones originated from the target remnants (*target fragments*). Then, the requirement $\theta_{\gamma^* h} > 0.02\,\text{rad}$ reflects the resolution in the reconstruction of the angle $\theta_{\gamma^* h}$ between the virtual photon and the produced hadron, that results in limiting the hadron transverse momenta in the

interval $0.05 < P_{h\perp} < 1.41$ GeV.

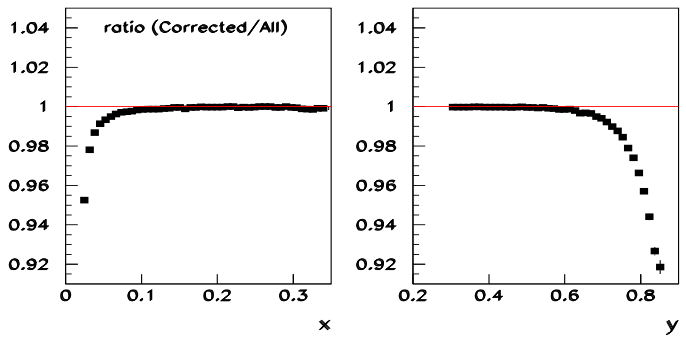

Figure 4.2: Influence of the charge symmetric background correction on the 2000 hydrogen data: the pictures show the ratio of charged hadron with and without the charge symmetric correction, as a function of x (left) and y (right).

Charge symmetric background

It is possible that a background lepton with the same charge of the lepton beam coming from pair productions in detector materials ($\gamma \rightarrow e^+e^-$) passes all the DIS cuts and is misidentified as the scattered beam lepton. When such an event contains an hadron satisfying the SIDIS cuts, enters the final event sample.

To correct the data for this background two data samples are determined: the first one, the SIDIS sample, collects SIDIS events with the correct lepton charge, while the second collects events which satisfy all the analysis cuts but the lepton charge is opposite to the beam one. As background processes like pair production or meson Dalitz decay are symmetric in the number and kinematics of positively and negatively charged leptons produced, the number of events labeled as SIDIS but with the wrong charge represents a control sample of the charge symmetric (i. e. with the same beam charge) background.

Therefore a number of events corresponding to the number of wrong-charge events is subtracted from the SIDIS sample in each kinematical bin.

The overall background fraction due to pair production source is found to be zero except in the very low range of x and high range of y, where the correction becomes bigger, as shown in figure 4.2.

4.3.2 Monte Carlo data

The Monte Carlo event sample for each production is determined by the same selection procedure used for real data and described in the last section, except that the PID detectors are not used, and the 'true' particle type (determined by GMC) is taken as identification. Furthermore no charge symmetric background is needed in MC data, because it is possible to identify the true scattered lepton from the

Born-level informations.

HYDROGEN STATISTICS (Million events)

		Positive hadrons		Negative hadrons	
Year	Beam	DATA	PYTHIA	DATA	PYTHIA
2000	e^+	0.739	4.648	0.430	3.130
2006	e^-	0.867	3.849	0.489	2.552

Table 4.3: Number of SIDIS events collected with hydrogen targets.

DEUTERIUM STATISTICS (Million events)

		Positive hadrons		Negative hadrons	
Year	Beam	DATA	PYTHIA	DATA	PYTHIA
2000	e^+	0.918	4.401	0.604	3.286
2004	e^+	0.388	4.365	0.253	3.258
2005	e^-	0.700	4.383	0.457	3.267

Table 4.4: Number of SIDIS events collected with deuterium targets.

4.3.3 HERMES and PYTHIA data samples

The number of SIDIS events satisfying the described criteria in real and MC data are summarized in table 4.3 for Hydrogen targets and in table 4.4 for Deuterium targets.

The comparison of the kinematical distributions between real data and fully-tracked PYTHIA simulation is shown for positively and negatively charged hadrons collected in 2000 and 2006 years in figures from 4.3 to 4.6. In general the comparison between data and MC is good, although not perfect, as shown in the ratios between data and PYTHIA distributions shown in figure 4.7 and 4.8.

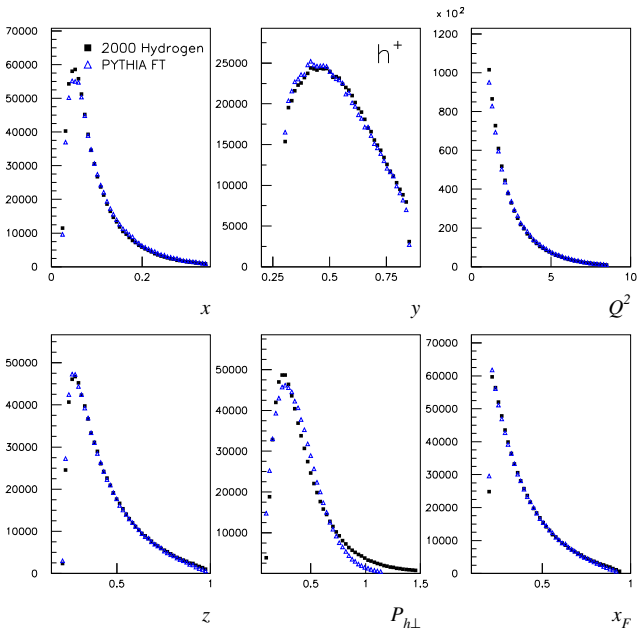

Figure 4.3: Comparison of positively charged hadron kinematics distributions between real data collected in 2000 with hydrogen target (solid squares) and Fully-Tracked PYTHIA simulation with 2000 geometry (open triangles).

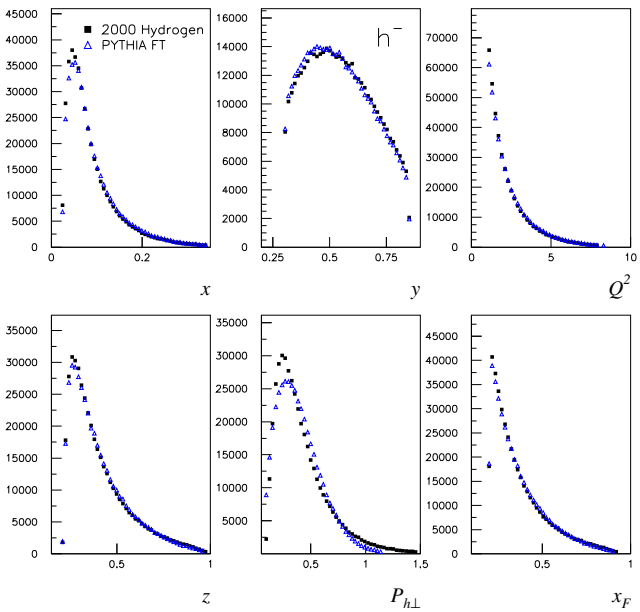

Figure 4.4: Comparison of negatively charged hadron kinematics distributions between real data collected in 2000 with hydrogen target (solid squares) and Fully-Tracked PYTHIA simulation with 2000 geometry (open triangles).

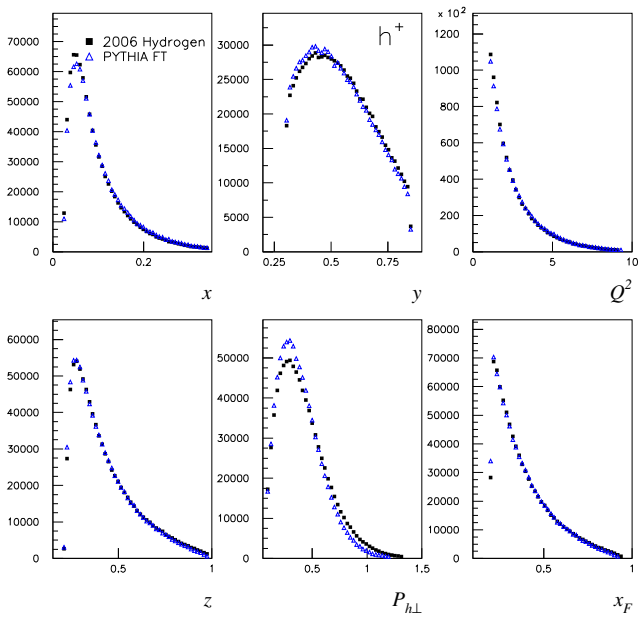

Figure 4.5: Comparison of positively charged hadron kinematics distributions between real data collected in 2006 with hydrogen target (solid squares) and Fully-Tracked PYTHIA simulation with 2006 geometry (open triangles).

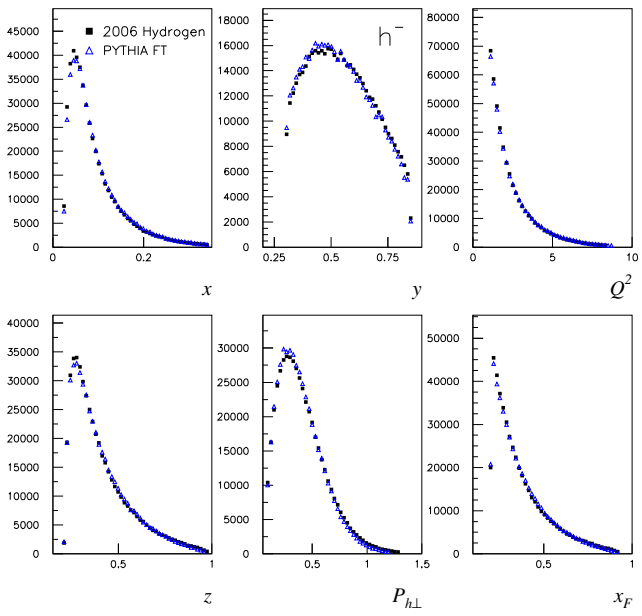

Figure 4.6: Comparison of negatively charged hadron kinematics distributions between real data collected in 2006 with hydrogen target (solid squares) and Fully-Tracked PYTHIA simulation with 2006 geometry (open triangles).

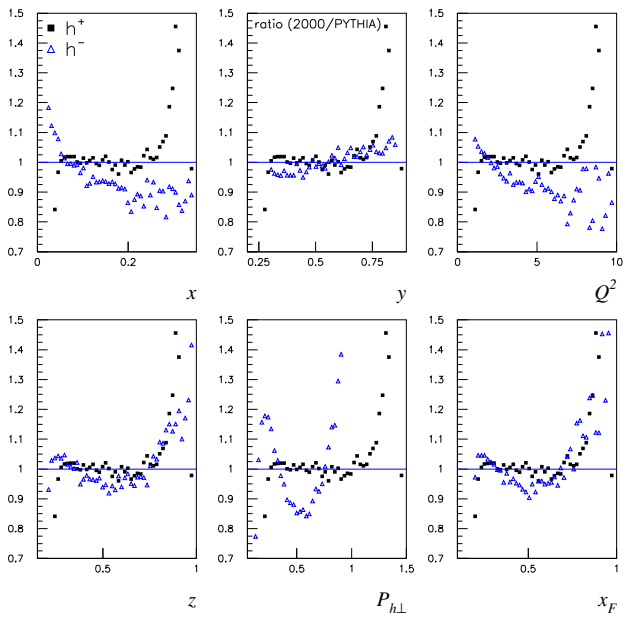

Figure 4.7: Ratio of positively (solid squares) and negatively (open triangles) charged hadron kinematics distributions of real data collected in 2000 with hydrogen target over Fully-Tracked PYTHIA simulation with 2000 geometry.

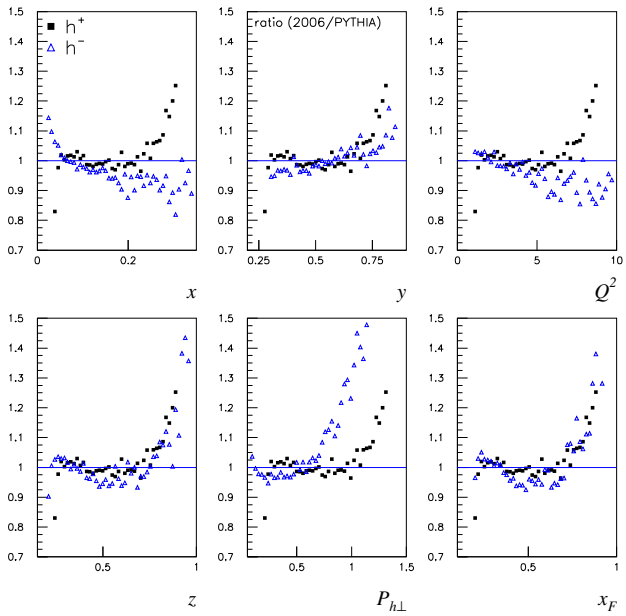

Figure 4.8: Ratio of positively (solid squares) and negatively (open triangles) charged hadron kinematics distributions (shown in fig. 4.6) of real data collected in 2006 with hydrogen target over Fully-Tracked PYTHIA simulation with 2006 geometry.

Chapter 5

Measurement of azimuthal cosine moments

The extraction of the unpolarized cosine moments of the SIDIS cross-section from HERMES data is discussed in this chapter. In the first part the experimental procedure of extraction is presented. The procedure is discussed in case of 1- and 5-dimensional analysis, with the help of a Monte Carlo that simulates the azimuthal dependence of hadron cross-section related to quark intrinsic transverse momenta. The results of the 5-dimensional analysis obtained with different beam charges and both hydrogen and deuterium targets are presented separately for positive and negative hadrons. The last step consists in the determination of possible systematics in the results, due for instance to detector or beam misalignment or non-SIDIS background events.

The results shown in this chapter are the so-called *raw moments*, to distinguish them from the *Born moments* presented in chapter 6, where they are corrected for radiative effects and detector smearing and acceptance.

5.1 Experimental extraction method

The unpolarized cross-section for semi-inclusive DIS processes is given by (see sec. 2.3):

$$\frac{d\sigma}{dx\,dy\,dz\,dP_{h\perp}^2\,d\phi_h} = \frac{\alpha^2}{xyQ^2}\frac{y^2}{2(1-\epsilon)}(1+\frac{\gamma^2}{2x})\{F_{UU,T}+\epsilon F_{UU,L}+ \sqrt{2\epsilon(1+\epsilon)}\cos\phi_h F_{UU}^{\cos\phi_h}+\epsilon\cos 2\phi_h F_{UU}^{\cos 2\phi_h}\} \tag{5.1}$$

where ϕ_h (figure 5.1) is defined in chapter 2 as the azimuthal angle of the hadron plane around the virtual-photon direction, and the structure functions $F_{UU}^{\cos 2\phi_h}$ and $F_{UU}^{\cos\phi_h}$ are directly related to existence of quark intrinsic transverse momentum and spin. These two structure functions can be related respectively to a leading and first sub-leading terms in an expansion of the cross-section in powers of M/Q, called leading and first sub-leading *twist* contributions. The leading twist term, proportional

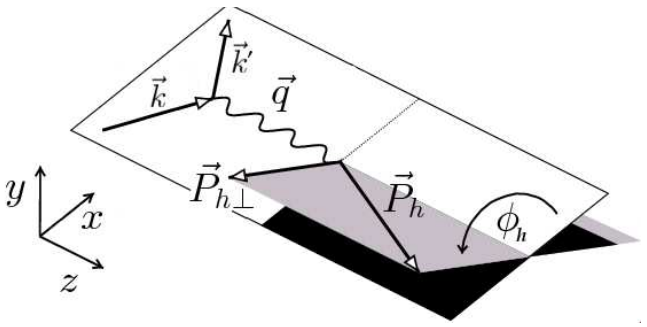

Figure 5.1: Definition of the azimuthal angle ϕ_h between the scattering plane (white) and the hadron production plane (grey).

to $\cos 2\phi_h$, is the Boer-Mulders effect (see section 2.4), and is related to the existence of quark spin-orbit correlations. On the contrary different sub-leading twist contributions lead to the $\cos\phi_h$ modulation (sec. 2.5), among these the best known theoretically are the Boer-Mulders and the Cahn effects, where the latter is a pure kinematical effect due to intrinsic motion.

The extraction of $F_{UU}^{\cos 2\phi_h}$ and $F_{UU}^{\cos\phi_h}$ can be performed by measuring the cosine moments defined as (see sec. 2.3):

$$\begin{aligned} \langle \boldsymbol{\cos \phi_h} \rangle &= \frac{\int \cos\phi_h \, d^5\sigma}{\int d^5\sigma} \\ \langle \boldsymbol{\cos 2\phi_h} \rangle &= \frac{\int \cos 2\phi_h \, d^5\sigma}{\int d^5\sigma} \end{aligned} \tag{5.2}$$

where $\int d^5\sigma$ is the short-hand notation for the expression:

$$\int d^5\sigma = \int dx\, dy\, dz\, dP_{h\perp}^2\, d\phi_h \frac{d\sigma}{dx\, dy\, dz\, dP_{h\perp}^2\, d\phi_h} \tag{5.3}$$

In case of ideal spectrometer with a 4π acceptance, the azimuthal modulation of the unpolarized cross-section (eq. 5.1) could be obtained by direct measurement of its ϕ_h distribution; however in a real experiment the angular coverage can be incomplete and, as in HERMES, the measured ϕ_h distribution can be strongly influenced by the geometry of the detector, that generates additional azimuthal modulations. In a Fourier expansion in ϕ_h, the function describing the acceptance effects can be represented as

$$\epsilon_{acc}(\phi_h) = A_0 + \sum_{m=1} (A_m \cos(m\phi_h) + B_m \sin(m\phi_h)) \tag{5.4}$$

and the cosines moments (see eq. 5.2) corresponding to geometrical acceptance are found to be non-zero (see below).

Another experimental source of azimuthal modulations are the QED radiative effects (described in section 6.1) that, beyond changing the total cross-section, also

produce cosine modulations, because the radiation of a real photon changes the virtual photon momentum. Since in this case the deviation of the final hadron direction is symmetrical in ϕ_h, only even contributions due to radiative effects enter the cross-section:

$$\epsilon_{rad}(\phi_h) \;=\; C_0 \;+\; \sum_{m=1} C_m \cos(m\phi_h) \tag{5.5}$$

In summary, the hadron azimuthal distributions observed at HERMES result from the sum of three main contributions:

1. *physical* cosine modulations $\langle \mathbf{cos}\, \boldsymbol{n\phi_h} \rangle_{F_{UU}}$ related to the structure functions $F_{UU}^{\cos\phi_h}$ and $F_{UU}^{\cos 2\phi_h}$ (therefore to Cahn and Boer-Mulders effects);
2. *geometrical* cosine modulations $\langle \mathbf{cos}\, \boldsymbol{n\phi_h} \rangle_{acc}$;
3. *radiative* cosine modulations $\langle \mathbf{cos}\, \boldsymbol{n\phi_h} \rangle_{rad}$;

with $n = 1, 2$. In the hypothesis the three contributions factorize the event yields $N(\phi_h)$ distribution can be expressed as:

$$N(\phi_h) = \int L\, \sigma_{F_{UU}}\, \epsilon_{acc}\, \epsilon_{rad}\, dxdydzdP_{h\perp}^2 \tag{5.6}$$

with L the luminosity, and

$$\sigma_{F_{UU}} = \sigma_0^{meas} A_{F_{UU}} \tag{5.7}$$

where σ_0^{meas} contains all the ϕ_h-independent cross-section terms and $A_{F_{UU}} = 1 + 2\langle \mathbf{cos}\, \boldsymbol{\phi_h} \rangle_{F_{UU}} \cos\phi_h + 2\langle \mathbf{cos}\, \mathbf{2\boldsymbol{\phi_h}} \rangle_{F_{UU}} \cos 2\phi_h$.

In order to disentangle the azimuthal modulation related to the structure functions $F_{UU}^{\cos n\phi_h}$, the experimental measurements are compared to a Monte Carlo production including the complete simulation of the instrumental effects [86], but with $A_{F_{UU}} = 1$, so that the azimuthal distribution is generated only by acceptance and radiative contributions:

$$N^{MC}(\phi_h) = \int L^{MC}\, \sigma_0^{MC}\, \epsilon_{acc}^{MC}\, \epsilon_{rad}^{MC}\, dxdydzdP_{h\perp}^2 \tag{5.8}$$

where σ_0^{MC} is the ϕ_h-independent cross-section for MC equivalent to σ_0^{meas}.

By comparing the equations 5.6, 5.7 and 5.8, one can argue that the ratio between the real and the simulated yield distributions could provide, at least in first approximation, the ϕ_h modulations related to $F_{UU}^{\cos\phi_h}$ and $F_{UU}^{\cos 2\phi_h}$:

$$\frac{N}{N^{MC}}(\phi_h) \approx \frac{\int L\, \sigma_0^{meas}\, A_{F_{UU}}\, \epsilon_{acc}\, \epsilon_{rad}\, dxdydzdP_{h\perp}^2}{\int L\, \sigma_0^{MC}\, \epsilon_{acc}^{MC}\, \epsilon_{rad}^{MC}\, dxdydzdP_{h\perp}^2}. \tag{5.9}$$

The integrals in the quotients of Eq. (5.9) do not allow the resolution of the correlation between the physical $A_{F_{UU}}$ and the instrumental ϵ_i contributions, unless the event sample is binned in all the relevant variables simultaneously. Only in this case, in each bin would equation (5.9) reduce to:

$$\frac{N}{N^{MC}}(\phi_h) \approx R_0\, A_{F_{UU}} \tag{5.10}$$

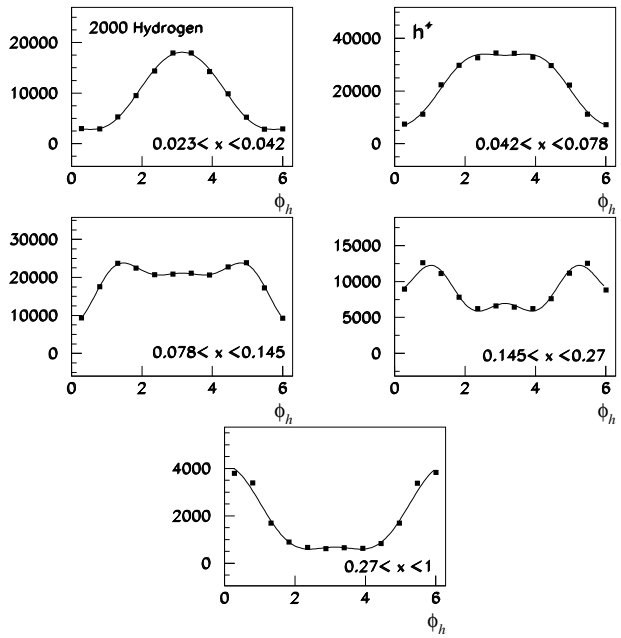

Figure 5.2: ϕ_h distribution and corresponding fit in 5 x-bins for data collected with unpolarized hydrogen target in 2000.

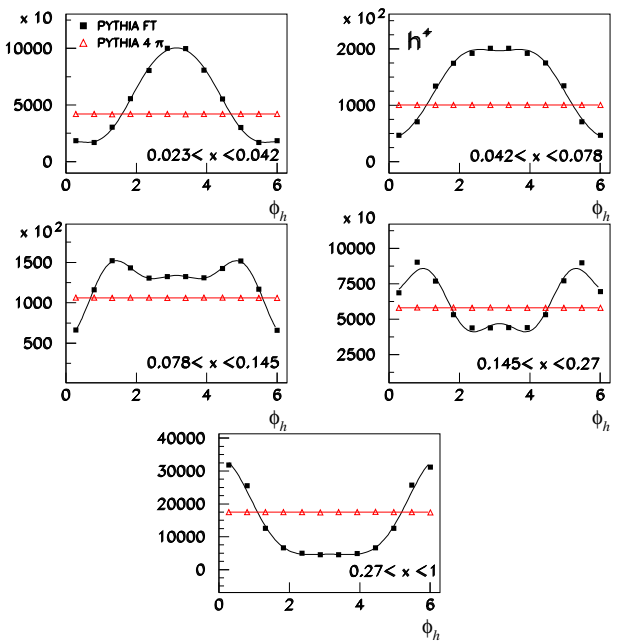

Figure 5.3: ϕ_h distribution in 5 x-bins and corresponding fit for PYTHIA production with hydrogen target and geometry of 2000 year run: the fully-tracked level results (solid squares) show the modulation due to HERMES acceptance and radiative effects, while the 4π-level results (open triangles) are flat, due to a ϕ_h independent cross-section.

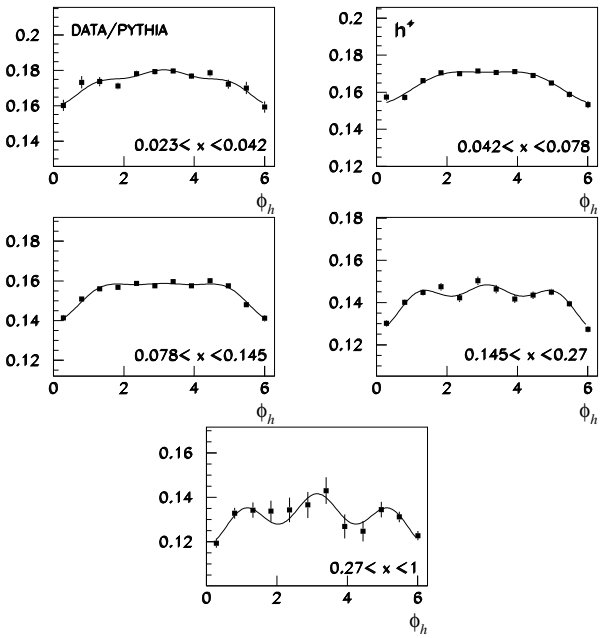

Figure 5.4: Ratio between real data (fig. 5.2) and PYTHIA (fig. 5.3) ϕ_h-distribution and corresponding fit in 5 x-bins. The histograms have been normalized with their areas before making the ratio. The residual modulation in the ratio can be attributed to the structure function cosine moments present in the data but not in the Monte Carlo.

where in $R_0 = (L\,\sigma_0\,\epsilon_{acc}\,\epsilon_{rad})/(L^{MC}\,\sigma_0^{MC}\,\epsilon_{acc}^{MC}\,\epsilon_{rad}^{MC})$ the spurious ϕ_h dependencies cancel out. In the typical case the event sample is binned only in one of the kinematical variables (1-dimensional analysis), the quotients of equation (5.9) are integrated over the full range of all the other fundamental variables and $A_{F_{UU}}$ can not be correctly isolated. Nevertheless, the comparison between 1-dimensional and fully-differential analyses (binned in x, y, z, $P_{h\perp}$ and ϕ_h) are presented in the next sections.

5.1.1 One-dimensional analysis

The cosine modulations from both the data and MC yields distributions are presented in figures 5.2 and 5.3. Data and MC cosine modulations can be easily extracted with the least squares method, which means minimizing the χ^2 defined as:

$$\chi^2 = \sum_i^{N_b} \frac{(N({\phi_h}^i) - f({\phi_h}^i))^2}{(\delta N({\phi_h}^i))^2} \tag{5.11}$$

where N_b is the number of bins in ϕ_h ($= 12$), ${\phi_h}^i$ is the average value of ϕ_h in the i-th bin, $\delta N({\phi_h}^i)$ is the yield uncertainty vector defined by a Poissonian distribution:

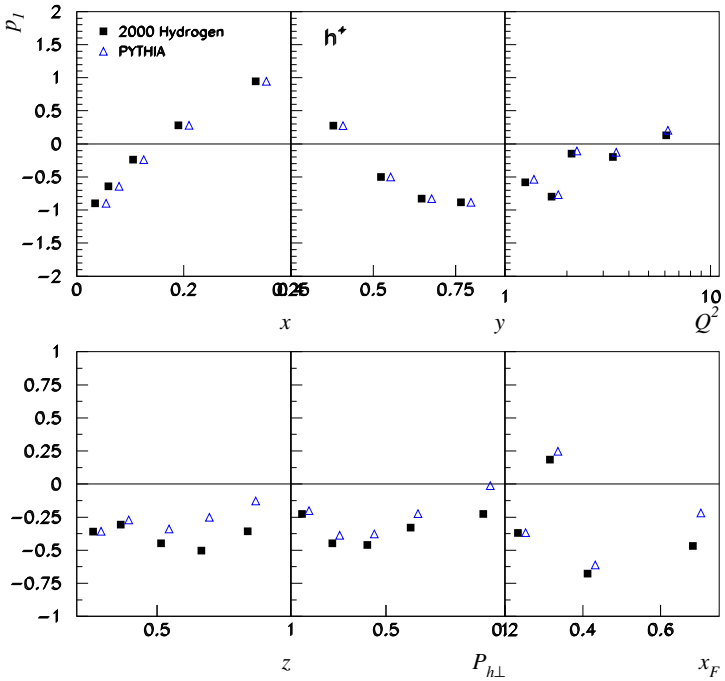

Figure 5.5: p_1 moments for positive hadrons extracted with a 1-dimensional analysis in 2000 data (solid squares) and PYTHIA (open triangles), versus the kinematical variables x, y, Q^2, z, $P_{h\perp}$ and x_F.

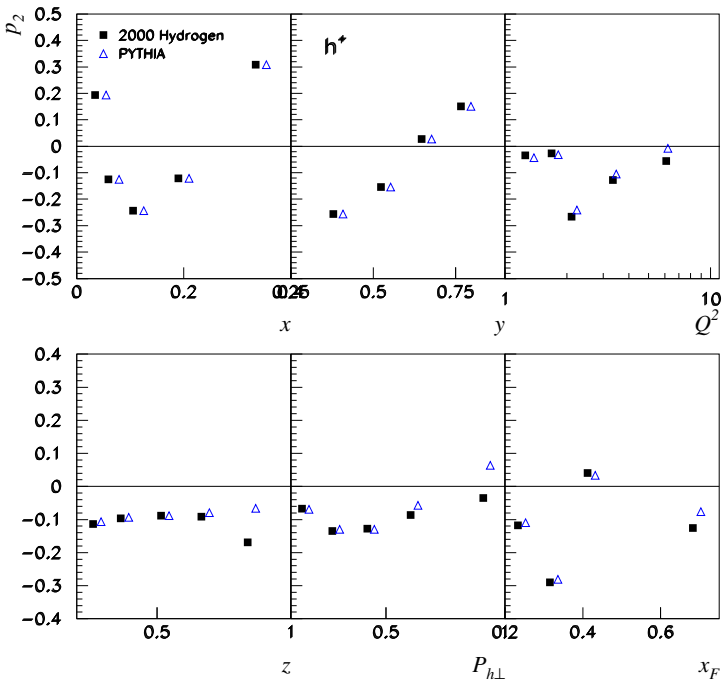

Figure 5.6: p_2 moments for positive hadrons extracted with a 1-dimensional analysis in 2000 data (solid squares) and PYTHIA (open triangles), versus the kinematical variables x, y, z, Q^2, $P_{h\perp}$ and x_F.

$\delta N({\phi_h}^i) = \sqrt{N({\phi_h}^i)}$, and $f({\phi_h}^i)$ is the fit function given by:

$$f({\phi_h}^i) = p_0\,(1 + p_1 \cos {\phi_h}^i + p_2 \cos 2{\phi_h}^i) \tag{5.12}$$

where all the different contributions to $\cos {\phi_h}^i$ ($\cos 2{\phi_h}^i$) enter in the p_1 (p_2) amplitude parameters. The parameter p_0 corresponds to R_0.

The $\cos\phi_h$ and $\cos 2\phi_h$ moments extracted separately for the HERMES and PYTHIA ϕ_h-distributions corresponding to p_1 and p_2 coefficients are presented in figures 5.5 and 5.6. They are mainly due to radiative and geometrical effects, and have similar sizes, anyway there are small differences of the order of few percent, except in the high z and $P_{h\perp}$ regions where the discrepancies become larger. The discrepancies can be attributed to the $\langle \boldsymbol{\cos n\phi_h} \rangle_{F_{UU}}$ moments, which should be present in the data but not in Monte Carlo.

In the one-dimensional analysis, to isolate the latter contributions to the azimuthal modulation, in each bin a fit similar to the one described above is performed on the distribution of the ratio $R(\phi_h) = N(\phi_h)/N^{MC}(\phi_h)$ between DATA and PYTHIA yield distributions (see figure 5.4). In the hypothesis that the contributions of acceptance and radiative effects canceled out in the ratio the parameters in the fit function can be interpreted as the physical moment under study:

$$p1 = 2\langle \boldsymbol{\cos \phi_h} \rangle_{F_{UU}} \quad \text{and} \quad p2 = 2\langle \boldsymbol{\cos 2\phi_h} \rangle_{F_{UU}} \tag{5.13}$$

The uncertainties follow the standard error propagations: in each bin the uncertainty of the ratio $R(i)$ in that bin is

$$\delta R(\phi_h) = R(\phi_h) \cdot \sqrt{\left(\frac{\delta N(\phi_h)}{N(\phi_h)}\right)^2 + \left(\frac{\delta N^{MC}(\phi_h)}{N^{MC}(\phi_h)}\right)^2} = R(\phi_h) \cdot \sqrt{\frac{1}{N(\phi_h)} + \frac{1}{N^{MC}(\phi_h)}} \tag{5.14}$$

The results of this fit are presented in pictures 5.7 and 5.8 for positive hadrons collected with hydrogen target in 2000.

5.1.2 Fake moments with 1-dimensional analysis

The use of Monte Carlo simulation to correct the detector acceptance from the event sample has to be justified. Indeed, differences between real and simulated ϕ_h-independent cross-sections (σ_0) can easily generate false azimuthal modulations [86, 87] when convoluted with detector acceptance. The possible false asymmetries can be estimated with two independent Monte Carlo event samples, generated with $A_{F_{UU}} = 1$, but with slightly different ϕ_h-independent cross-section models. For this test the two event samples were generated using using PYTHIA and LEPTO GMCs. The kinematical distributions of the two Monte Carlo productions are presented in figures 5.9 and 5.10: they are very similar but some discrepancies occur, due to differences in the generator discussed in section 4.1.

The $\cos\phi_h$ and $\cos 2\phi_h$ modulations were extracted fitting the ratio between

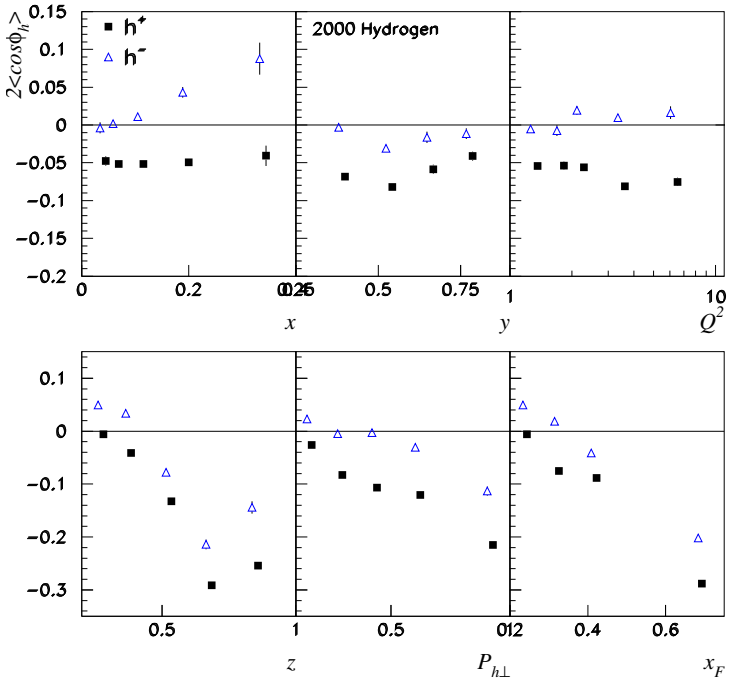

Figure 5.7: $\langle \cos \phi_h \rangle$ moments for positive (solid squares) and negative (open triangles) hadrons extracted in 2000 data with a one-dimensional analysis, versus the kinematical variables x, y, Q^2, z, $P_{h\perp}$ and x_F.

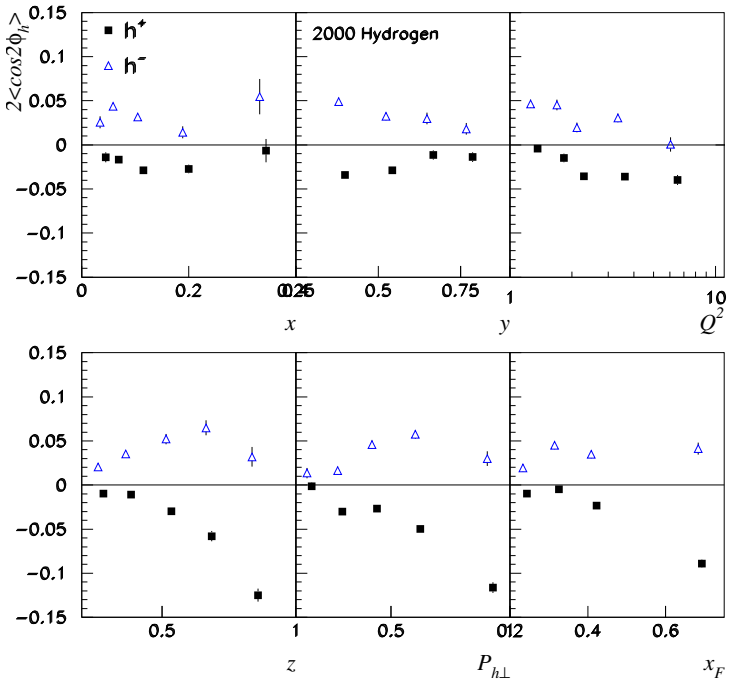

Figure 5.8: $\langle \cos 2\phi_h \rangle$ moments for positive (solid squares) and negative (open triangles) hadrons extracted 2000 data with a one-dimensional analysis, versus the kinematical variables x, y, z, Q^2, $P_{h\perp}$ and x_F.

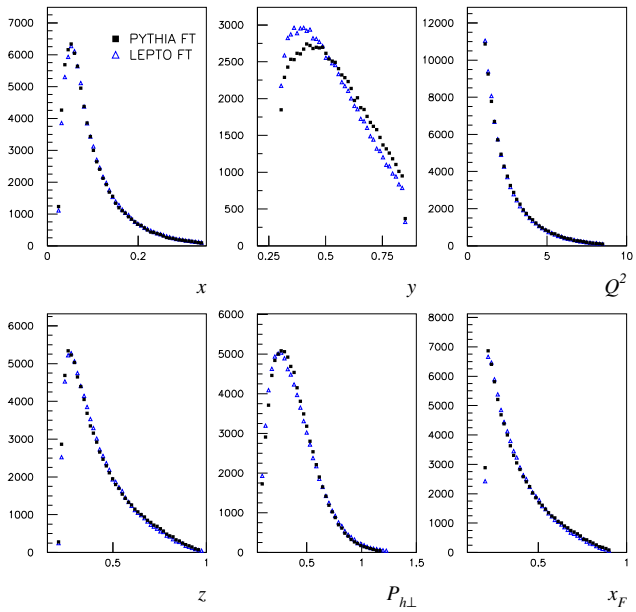

Figure 5.9: Comparison of charged hadron kinematics distributions between Fully-Tracked (FT) PYTHIA (solid squares) and LEPTO simulations (open triangles).

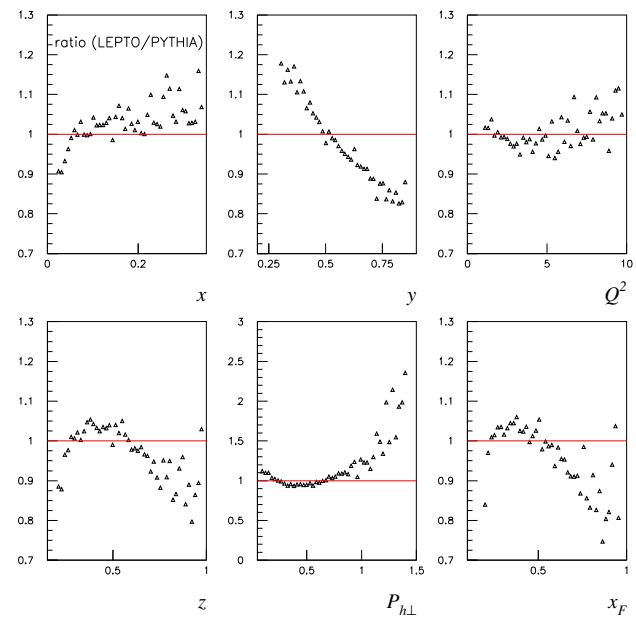

Figure 5.10: Comparison of charged hadron kinematics distributions Fully-Tracked (FT) PYTHIA (solid squares) and LEPTO simulations (open triangles).

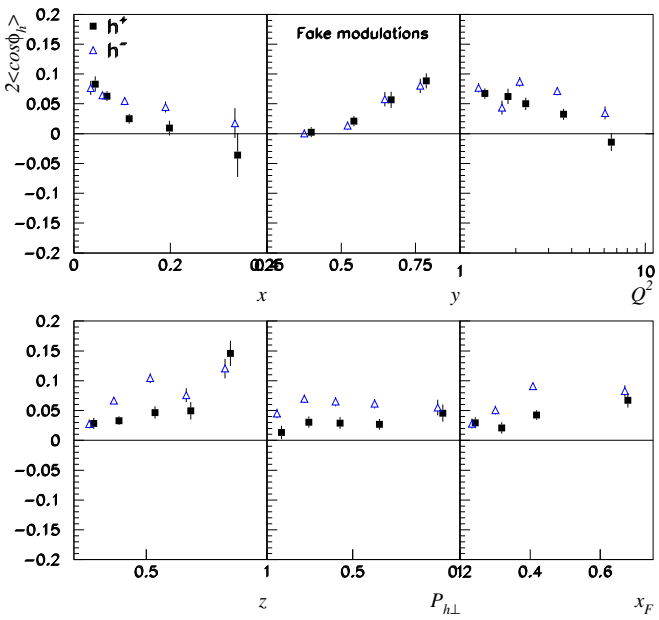

Figure 5.11: $\langle \cos \phi_h \rangle$ fake moments for positive (solid squares) and negative (open triangles) hadrons extracted with a 1-dimensional analysis using two Monte Carlo productions with different ϕ_h independent cross-section kinematical distributions at generator level, both flat in ϕ_h at 4π level.

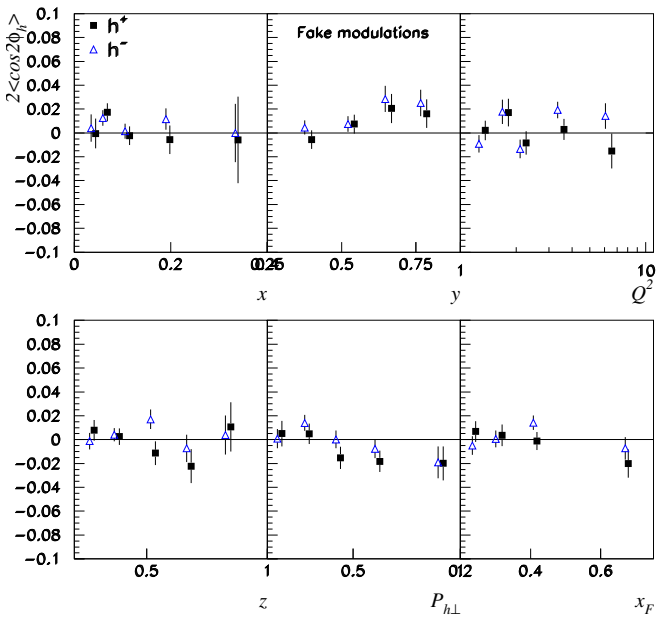

Figure 5.12: $\langle \cos 2\phi_h \rangle$ fake moments for positive (solid squares) and negative (open triangles) hadrons extracted with a 1-dimensional analysis using two Monte Carlo productions with different ϕ_h independent cross-section kinematical distributions, both flat in ϕ_h at 4π level.

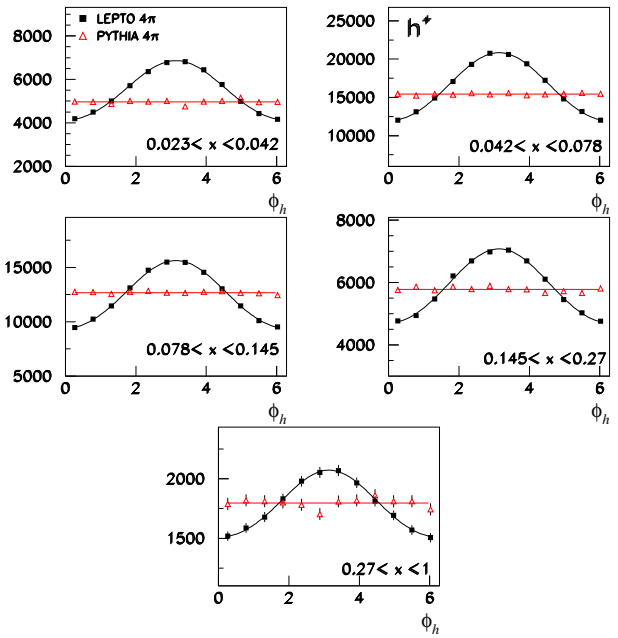

Figure 5.13: ϕ_h distribution in 5 x-bins and relative fits for LEPTO (solid squares) and PYTHIA (open triangles) at 4π-level.

the two MCs productions and the results are shown in figures from 5.11 to 5.12 for positive and negative hadrons. As shown in the figures, the kinematical distribution discrepancies due to slightly differerent ϕ_h-independent cross-section models can generate moments as large as the expected signal, at least as regards the $\cos\phi_h$ modulation. Since the kinematical discrepancies between real data and PYTHIA distributions (figure 4.3) are even bigger that the one found here, this test is a clear indication that the 1-dimensional extraction method, defined in the last section, could be highly biased by fake asymmetries of this kind.

Beyond the false modulation test, another test with different MC productions was performed to test the one-dimensional analysis.

5.1.3 Monte Carlo test of one-dimensional analysis

To estimate the goodness of the cosine moments extraction in a one-dimensional analysis, two different Monte Carlo simulation are considered in the following. The first one is generated using LEPTO GMC (see sec. 4.1) with the Cahn azimuthal dependence implemented in the cross-section [88]. The other production is generated by a standard PYTHIA GMC. For each GMCs, two Monte Carlo samples were generated: the first in a 4π geometry, and the second within acceptance and with radiative effects turned on (*reconstructed-level*). At *true-level* (4π), the LEPTO production shows the azimuthal modulation due only to the Cahn model, presented in figure 5.13 for five x intervals. Fitting these distribution leads to the extraction of the *true moments*. On the contrary PYTHIA does not contain any modulation

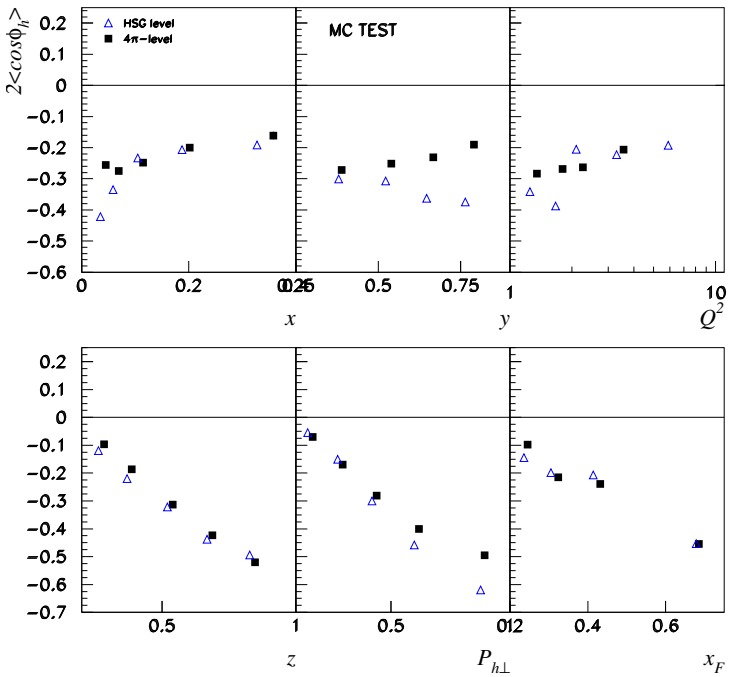

Figure 5.14: $\langle \cos \phi_h \rangle$ moments for positive hadrons extracted with a one-dimensional analysis in the MC test described in the text: the moments extracted at reconstructed level (open triangles) are compared with the *true moments* (solid squares) generated in 4π.

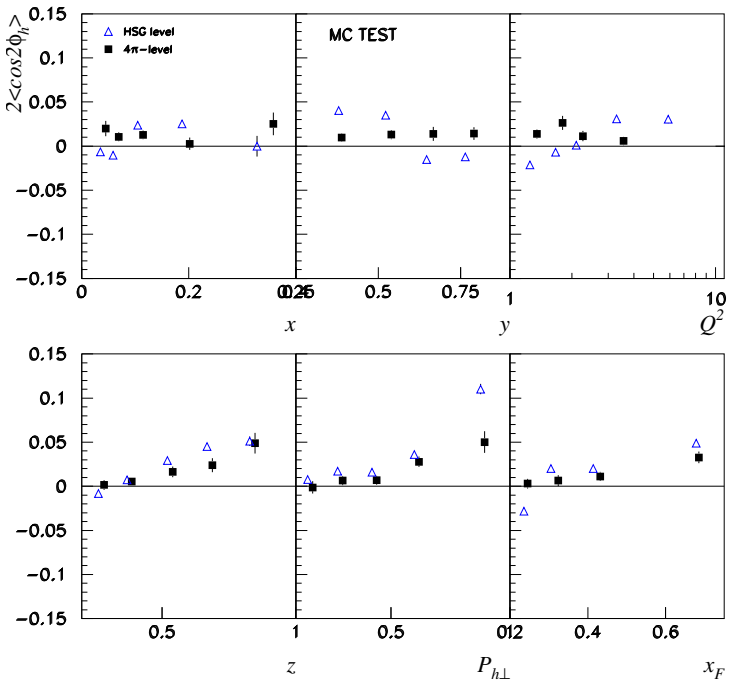

Figure 5.15: $\langle \cos 2\phi_h \rangle$ moments for positive hadrons extracted with a one-dimensional analysis in the MC test described in the text: the moments extracted at reconstructed level (open triangles) are compared with the *true moments* (solid squares) generated in 4π.

in a 4π geometry as shown by the open triangles in figure 5.13.

The other productions are made with HSG to extract the moments correlated to experimental effects. In the HSG samples both productions exhibit an azimuthal modulation, in LEPTO the Cahn model couple to the modulation due to HERMES acceptance and radiative effects, while in PYTHIA only the latter two contributions are present. The event samples are selected with same geometrical and kinematical requirements described in section 4.3, and the collected SIDIS statistics are listed in table 5.1.

MC STATISTICS (Million events)			
4π		HSG	
LEPTO	PYTHIA	LEPTO	PYTHIA
0.50	0.65	1.67	3.95

Table 5.1: Number of SIDIS events collected with LEPTO and PYTHIA GMC for the tests described in section 5.1.3 and 5.1.6.

As in the data, the extraction of the azimuthal modulation of interest is obtained fitting the ratio between LEPTO (used to mimic the data) and PYTHIA samples:

$$\frac{N^{LE}}{N^{MC}}(\phi_h) \approx R_0 \, A_{F_{UU}^{LE}} \tag{5.15}$$

where $A_{F_{UU}^{LE}} = 1 + 2\langle \mathbf{cos}\, \boldsymbol{\phi_h} \rangle_{LE} \cos\phi_h + 2\langle \mathbf{cos}\, \mathbf{2}\boldsymbol{\phi_h} \rangle_{LE} \cos 2\phi_h$. The discrepancies between the *true* and the *reconstructed ratio* results, shown in figures 5.14 and 5.15, indicate the systematic uncertainties related to the one-dimensional extraction: it is clear that one-dimensional analysis provides unsatisfactory results, since the extracted moments deviate significantly from the *truth* (4π). Furthermore is evident in some regions, for instance high x or high Q^2, that even the kinematical variables mean values are influenced by geometrical acceptance: in particular the experimental acceptance seems to eliminate the region of higher Q^2, so that the reconstructed mean Q^2 values result to be lower than the true ones.

From the described tests the monodimensional analysis clearly fails to extract correctly the cosine moments from the data, therefore a multidimensional fully differential analysis is needed [86], binned in each relevant kinematical variable: x, y, z, $P_{h\perp}$ and ϕ_h. In the ideal case, the ratio between data and MC should be calculated for very small intervals of x, y, z and $P_{h\perp}$ in order that acceptance effects are canceled out. In reality the binning cannot be too fine, because it should be compatible with the limited statistics of data. As a consequence, the possible residual acceptance effects should be corrected for using a model independent procedure described in chapter 6.

5.1.4 Multidimensional analysis

In a multi-dimensional analysis, the more is the number of bins, the more correlations can be resolved about kinematical dependence of the measured azimuthal

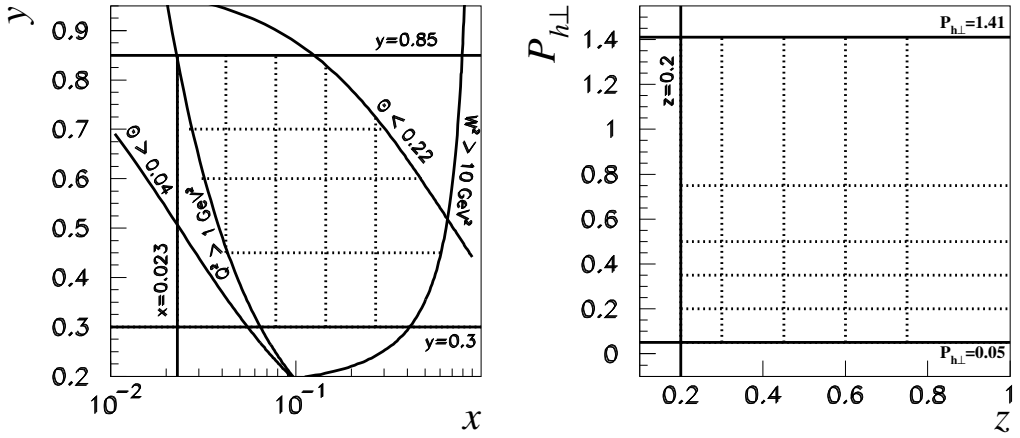

Figure 5.16: Binning for the relevant variables in the leptonic $x - y$ (left) and hadronic $z - P_{h\perp}$ (right) kinematical planes. The solid lines represent the cut applied and the HERMES kinematical region.

distributions [89]. Nevertheless the number of bins should be compatible with the limited statistics provided by the experiment. For the event samples presented in this analysis the binning chosen is presented in table 5.2: there are 4 intervals in y, 5 intervals in x, z and $P_{h\perp}$, for a total of 500 kinematical bins, each of them divided in 12 equidistant ϕ_h bins between 0 and 2π. The binning is shown in the leptonic x-y and hadronic z-$P_{h\perp}$ kinematical planes in figure 5.16.

BINNING 500 kinematical bins × 12 ϕ-bins							
Variable	Bin limits						#
x_{bj}	0.023	0.042	0.078	0.145	0.27	1	5
y_{bj}	0.3	0.45	0.6	0.7	0.85		4
z	0.2	0.3	0.45	0.6	0.75	1	5
P_{h_T}	0.05	0.2	0.35	0.5	0.75	1.41	5

Table 5.2: Multidimensional binning used for the extraction of the cosine modulations.

The ratio of data over PYTHIA ϕ_h-distributions is now performed for each of the kinematical bins in $x, y, z, P_{h\perp}$. As an example figure 5.17 shows the ratio of the ϕ_h-distributions for all the z and $P_{h\perp}$ bins corresponding to the first x-bin and the fifth y-bin.

As in the 1-dimensional analysis, a binned χ^2 fit unsing the fit function of eq. 5.13 can be performed to extract the cosine moments from the ratios, in each of the 500 kinematical bins, yielding 500 $\langle \boldsymbol{\cos \phi_h} \rangle_{F_{UU}}$ and $\langle \boldsymbol{\cos 2\phi_h} \rangle_{F_{UU}}$ moments. The results for positive hadrons are presented in figure 5.18. Although these preliminary results

need to be corrected for systematics (see next section) and detector smearing (see next chapter), a signal different from zero is already visible both in $\langle \mathbf{cos}\, \boldsymbol{\phi_h} \rangle$ and $\langle \mathbf{cos}\, \mathbf{2}\boldsymbol{\phi_h} \rangle$ moments.

The moments can be projected into a single kinematical variable x, by weighting each bin moment with the corresponding cross-section in that bin:

$$\langle \mathbf{cos}\, \boldsymbol{\phi_h} \rangle(x) = \frac{\sum_i \sigma_i^{4\pi}(x) \langle \mathbf{cos}\, \boldsymbol{\phi_h} \rangle_i}{\sum_i \sigma_i^{4\pi}(x)} \tag{5.16}$$

The cross-section $\sigma_i^{4\pi}(x)$ is evaluated from PYTHIA with a 4π geometry in order to obtain a result independent from the HERMES acceptance.

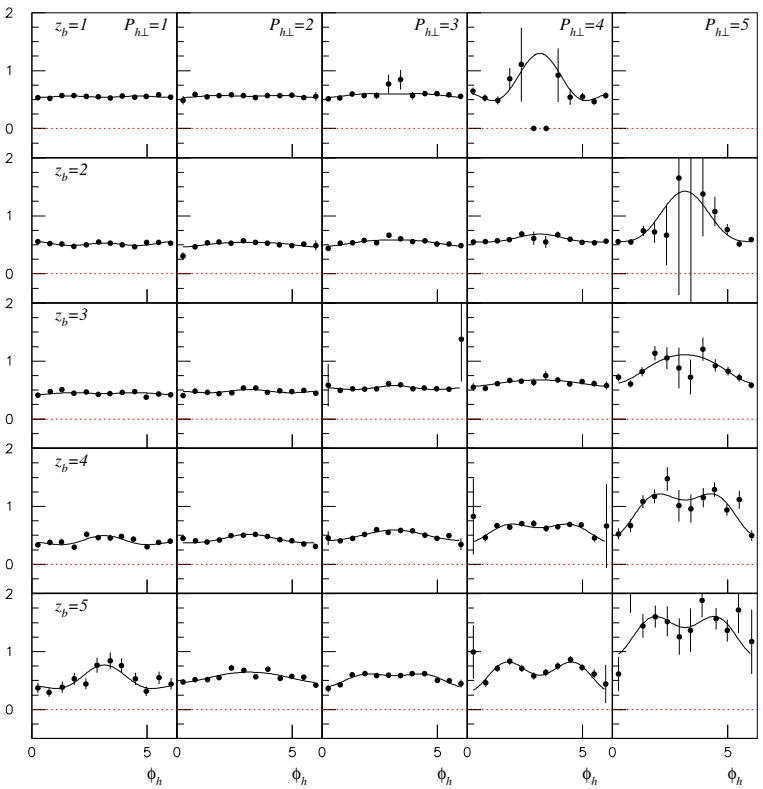

Figure 5.17: Ratio of ϕ_h-distributions between 2000 Hydrogen data and PYTHIA in the different z and $P_{h\perp}$ bins corresponding to the first x-bin and the fifth y-bin. The top right bin is completely empty, and in general the high $P_{h\perp}$ region (right column) is characterized by low statistics bins.

Treatment of low statistics bins

Due to the huge number of bins and limited statistics, in particular kinematical regions some bins contain a very low number of events. Few bins of this kind are shown in right column of figure 5.17. Since the statistics uncertainty of such a bin

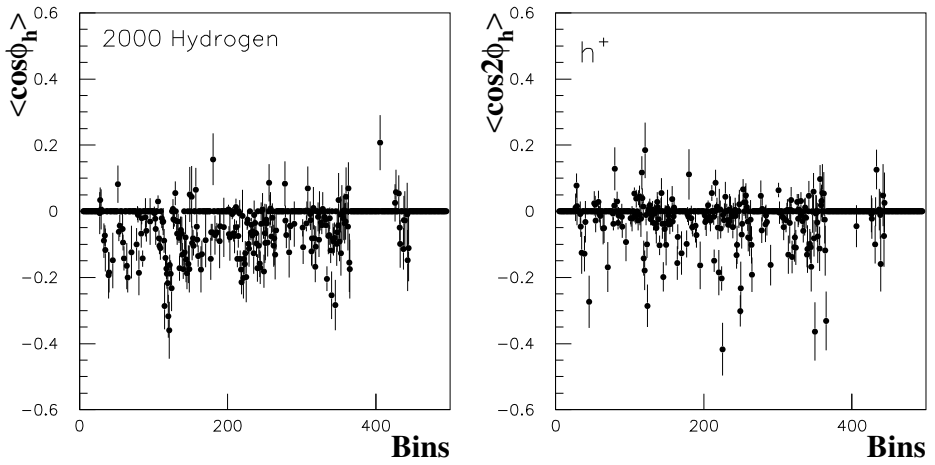

Figure 5.18: $\langle \mathbf{\cos \phi_h} \rangle_{F_{UU}}$ (left) and $\langle \mathbf{\cos 2\phi_h} \rangle_{F_{UU}}$ (right) moments for positive hadrons extracted from data collected with hydrogen target in 2000 in each of the 500 kinematical bins of table 5.2.

is high, its contribution is generally negligible in the projection in one kinematical variable. However, if the low statistics is due to low acceptance in that bin, when weighted by the 4π PYTHIA cross-section, which is independent from acceptance, the bin result can significantly increase the uncertainty of the final results.

For this reason the bins with very low statistics are not accounted in the projection. This can produce some bias in the projected results, therefore Monte Carlo tests were used to validate this procedure.

5.1.5 Fake moments with 5-dimensional analysis

As for the one-dimensional case (see sec. 5.1.2), the $\cos \phi_h$ and $\cos 2\phi_h$ fake modulations were extracted fitting the ratio between standard PYTHIA and LEPTO [1] productions with a multidimensional analysis. The comparison between the 1-dimensional and 5-dimensional fake moments are shown from figure 5.19 to 5.22 for positive and negative hadrons.

The fake moments extracted in the multidimensional analysis are significantly smaller than the mono-dimensional ones, and in general they are compatible with zero. The model-dependence of the 'ratio' method is notably decreased in a fully differential multidimensional analysis.

It is important to notice that the uncertainties in case of multidimensional analysis is significantly increased, even if the statistical significance is identical in two cases, as the event sample is the same. Therefore the error amplification should be attributed only to the analysis procedure. Indeed in a multidimensional fit the correlation between the two parameters, namely $\langle \mathbf{\cos \phi_h} \rangle$ and $\langle \mathbf{\cos 2\phi_h} \rangle$, increase resulting in uncertainties inflation. However, the full statistical information of data

[1] In this test, as for the one-dimensional case, the LEPTO GMC is the standard one, without any modulation in the born azimuthal distribution.

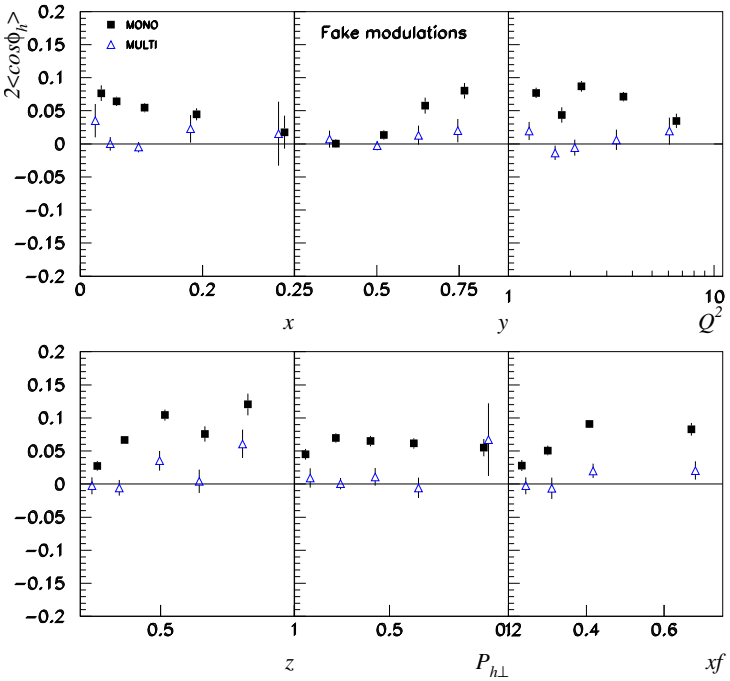

Figure 5.19: $\langle \cos \phi_h \rangle$ fake moments for positive hadrons extracted using two Monte Carlo productions with different kinematical distributions but flat in ϕ_h at 4π level: the solid squares are extracted in a mono-dimensional analysis, while the open triangles are extracted in a multidimensional analysis.

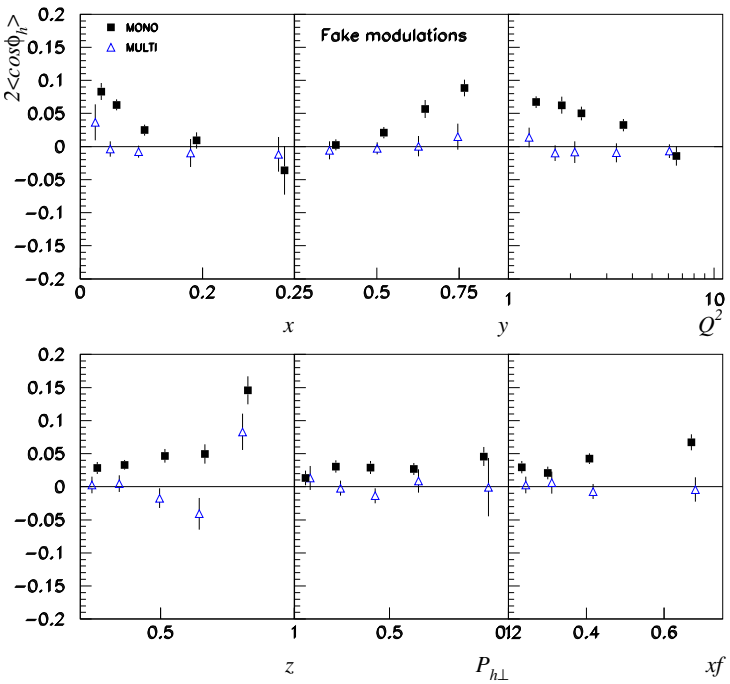

Figure 5.20: $\langle \cos \phi_h \rangle$ fake moments for negative hadrons extracted using two Monte Carlo productions with different kinematical distributions but flat in ϕ_h at 4π level: the solid squares are extracted in a mono-dimensional analysis, while the open triangles are extracted in a multidimensional analysis.

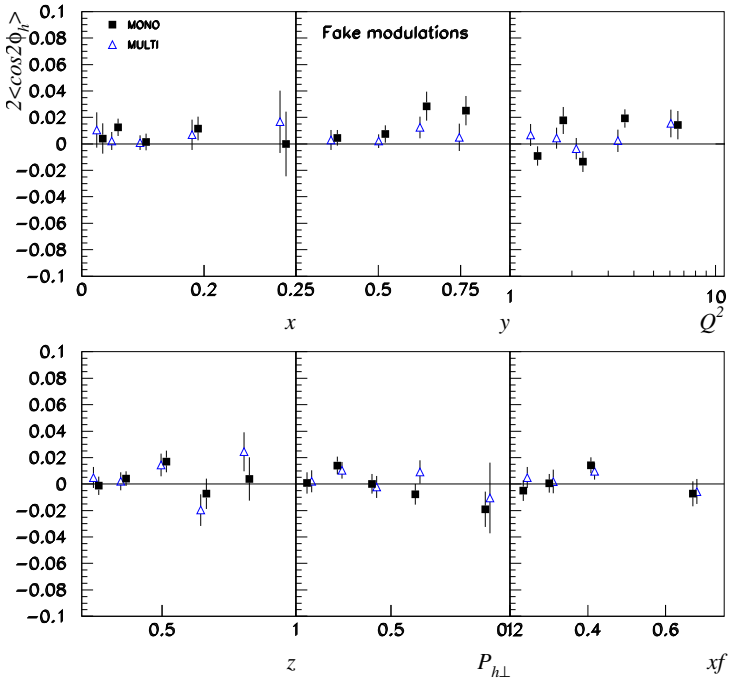

Figure 5.21: $\langle \cos 2\phi_h \rangle$ fake moments for positive hadrons extracted using two Monte Carlo productions with different kinematical distributions: the solid squares are extracted in a mono-dimensional analysis, while the open triangles are extracted in a multidimensional analysis.

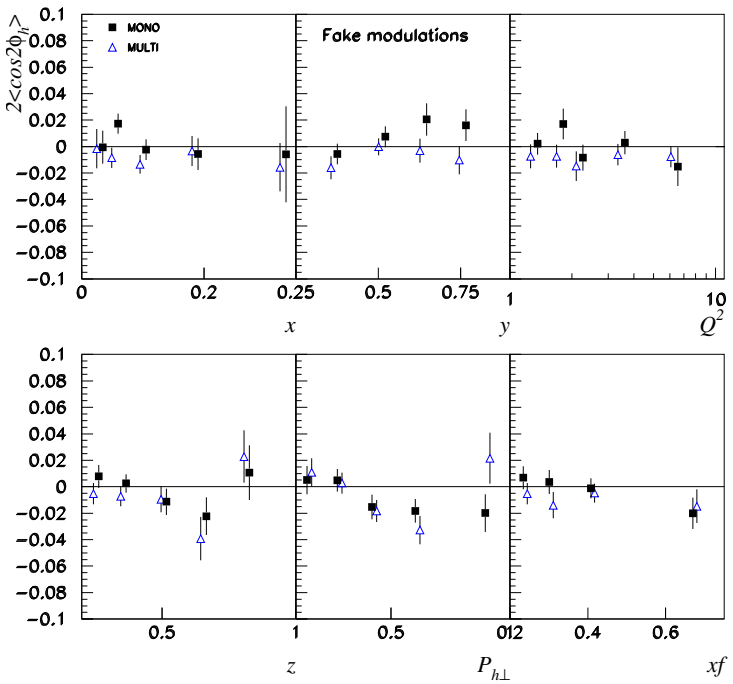

Figure 5.22: $\langle \cos 2\phi_h \rangle$ fake moments for negative hadrons extracted using two Monte Carlo productions with different kinematical distributions: the solid squares are extracted in a mono-dimensional analysis, while the open triangles are extracted in a multidimensional analysis.

sample is stored in the covariance matrix. For the final results, shown in chapter 7, the complete covariance matrix, that would be fundamental for phenomenological fit of the results, is available.

5.1.6 Monte Carlo test of 5-dimensional analysis

The MC productions used for the 5-dimensional test are the same used for the 1-dimensional case: a 4π plus a HSG LEPTO productions with an azimuthal modulation at born level, and a 4π plus a HSG PYTHIA productions flat in ϕ_h at born level.

The comparison between the *true moments* and the *extracted moments* with the analysis procedure described above is presented in figures 5.23 and 5.24 for $\langle \mathbf{cos\,\phi_h} \rangle$ and $\langle \mathbf{cos\,2\phi_h} \rangle$: the major part of the azimuthal contributions due to experimental sources are corrected for with the use of a multidimensional ratio between the two samples, anyway there are still differences between the *extracted* and the *true* moments. The residual discrepancies can be associated to remaining acceptance-radiative effects or to differences in the two MC kinematical descriptions that can produce fake asymmetries. For instance the big discrepancies at high z could be explained because LEPTO does not include the exclusive vector mesons production whose higher contamination is in this region (see sec. 5.2.3), while the discrepancies at large $P_{h\perp}$ can be related to the differences between data and MC distribution observed at high $P_{h\perp}$, as in figures from 4.3 to 4.6.

These discrepancies strongly depend on the Monte Carlo model used in the test, therefore they cannot be considered as indication of systematic uncertainties in the data. Nevertheless this test shows that with a multidimensional analysis the raw moments description of the *truth* is improved by a factor around 2. From this test one can conclude that the treatment of low statistic regions seems not to bias the results significantly.

5.2 Systematic studies

The results shown in last section are subject to different sources of systematic uncertainties, estimated here with a number of tests. In particular sections 5.2.1 and 5.2.2 describe the studies made to understand if the differences between positively and negatively charged hadrons can be due to systematic effects, and to understand the origin of discrepancies between results from different data taking periods.

5.2.1 Top-Bottom discrepancies

In all the Monte Carlo simulations used so far the detector are located in their ideal positions. In reality the detectors are not perfectly aligned, and also a shift of the beam from the z-axis, where it is assumed to lying, is observed. The schematic representation of this two types of misalignments are shown in figure 5.25. Misalignments of this kind should be taken into account in the analysis since can affects track reconstruction and kinematic quantities.

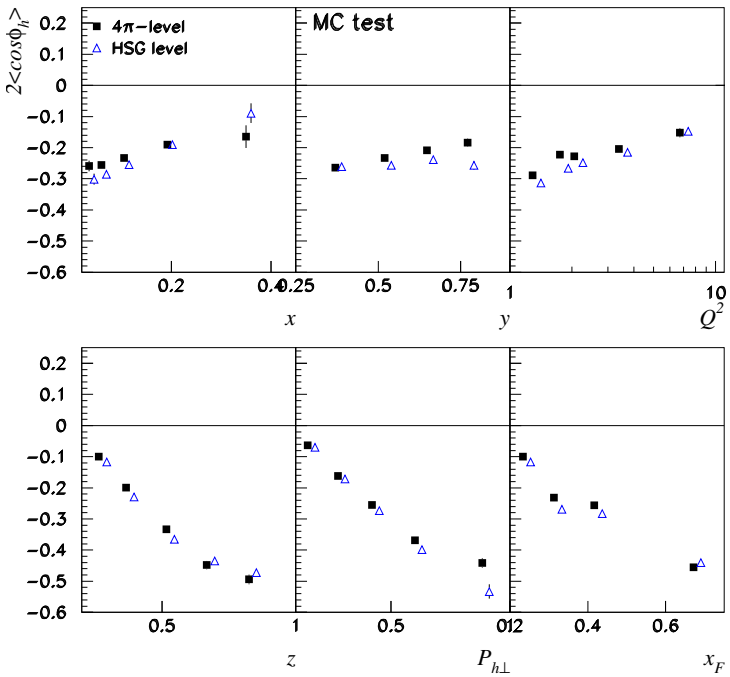

Figure 5.23: $\langle \cos \phi_h \rangle$ moments for positive hadrons extracted with a 5-dimensional analysis in the MC test described in the text: the moments extracted at reconstructed level (open triangles) are compared with the *true moments* (solid squares) generated in 4π.

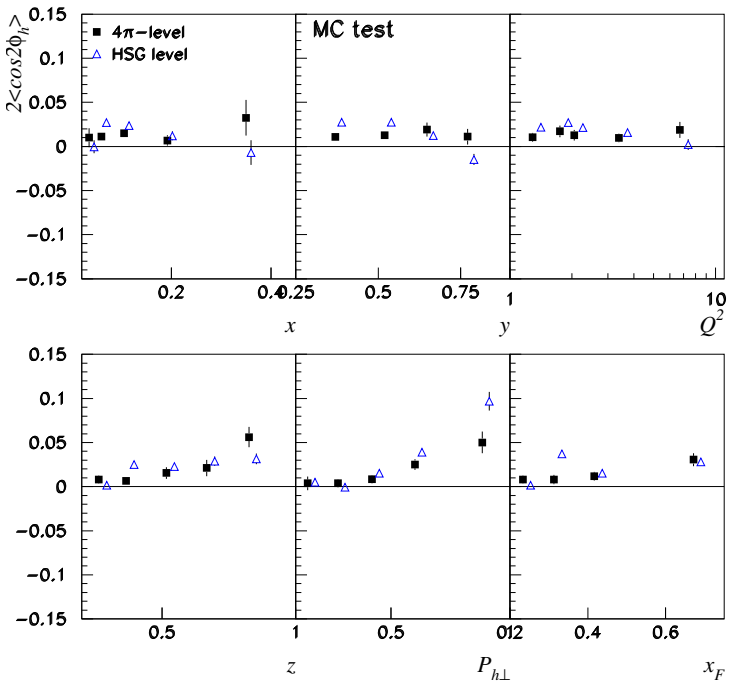

Figure 5.24: $\langle \cos 2\phi_h \rangle$ moments for positive hadrons extracted with a 5-dimensional analysis in the MC test described in the text: the moments extracted at reconstructed level (open triangles) are compared with the *true moments* (solid squares) generated in 4π.

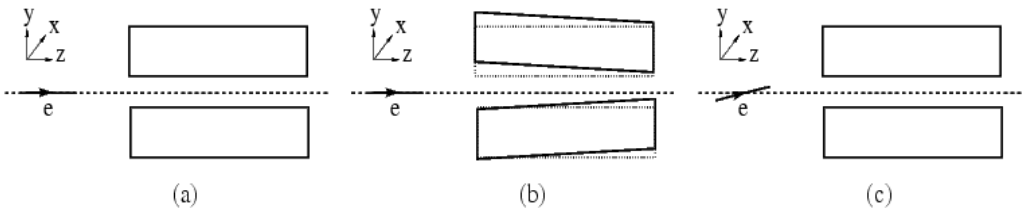

Figure 5.25: Spectrometer and beam misalignment: (a) perfect aligned beam and detector; (b) detector misalignment; (c) beam misalignment.

A misalignment can broke the left-right or top-bottom asymmetries of the spectrometer, resulting in a different acceptance for positively and negatively scattered leptons and produced hadrons due to the bending of the spectrometer magnet. Moreover the Top and the Bottom halves of the spectrometer can be misaligned differently. To evaluate the possible contribution to the analysis of the existing misalignment, the cosine modulations are calculated separately for the scattered lepton detected in the Top half or in the Bottom half. The moments in the Top and in the Bottom halves are shown for positive and negative hadrons in figures 5.26 and 5.27 for 2000 data and in figures 5.28 and 5.29 for 2006 data. A significative discrepancy can be observed for moments extracted in the two detector halves from the 2000 data, while much smaller differences are present in the 2006 data.

	Top	Bottom
x-slope (mrad)	0.44	0.24
y-slope (mrad)	-1.20	0.02
x-offset (cm)	-0.09	-0.11
y-offset (cm)	-0.01	0.11

Table 5.3: Misaligned parameters for the 2000 data taking period [90].

Monte Carlo misaligned productions

To estimate the systematics related to the detector and beam misalignments, MC productions were generated with a modified detector geometry to take into account these effects, and the cosine moments are extracted with the use of this new MC simulations.

The misalignment parameters are available for the 2000 data taking period, and are listed in table 5.3. For the 2006 run, the parameters used are the same of 2000 run, except for an additional shift in the beam position of $+2$ mm in the x axis and -0.3 mm in the y axis. The cosine moments for TOP and BOTTOM halves extracted with the misalignment MC simulations are shown in figures 5.30, 5.31 and in figures 5.32, 5.33 for 2000 and 2006 data respectively: with a misaligned MC the differences between TOP and BOTTOM halves are significantly reduced in the 2000, while remain unchanged in the 2006.

The comparison between the cosine moments extracted with a perfectly aligned and a misaligned MC is shown in figures 5.34, 5.35 for the 2000 run, and in fig-

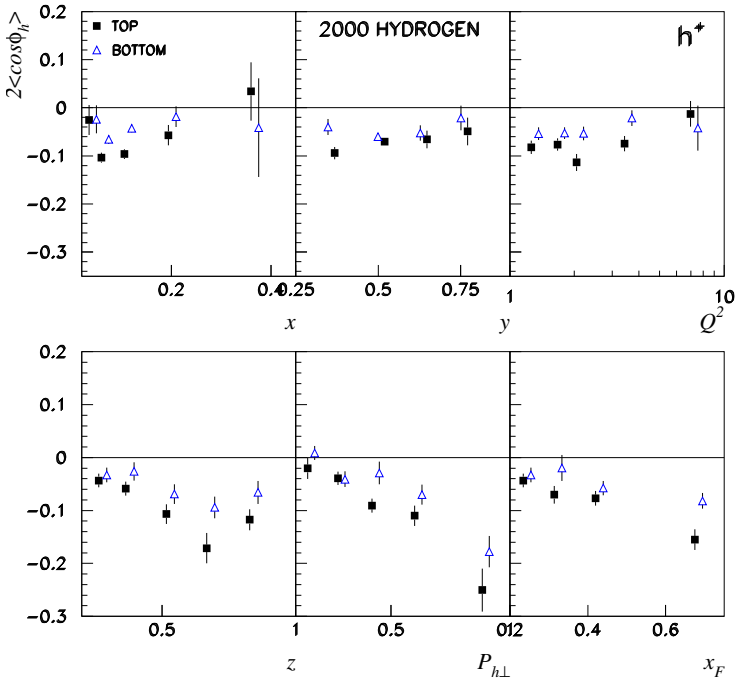

Figure 5.26: $\langle \cos \phi_h \rangle$ moments for positive hadrons extracted from 2000 data on hydrogen target for scattered lepton detected in the top half (solid squares) or in the bottom half (open triangles).

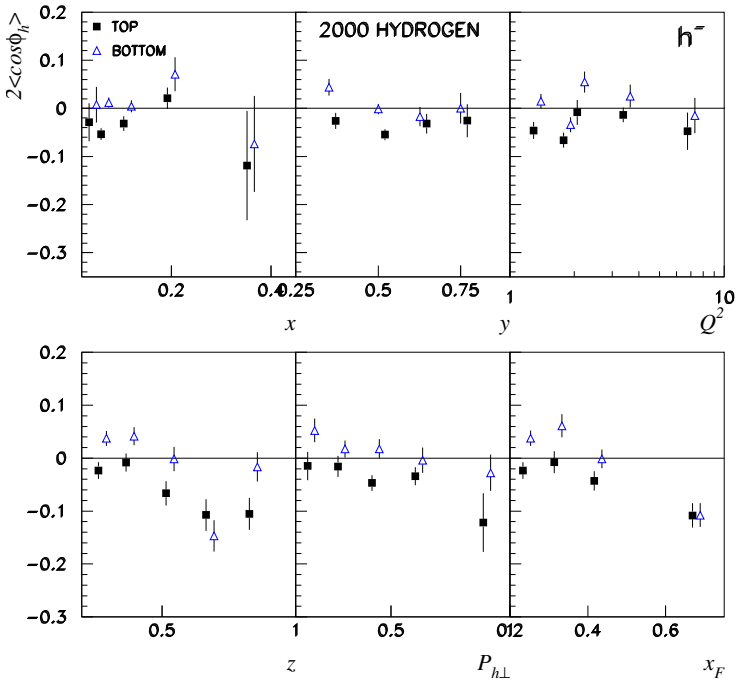

Figure 5.27: $\langle \cos \phi_h \rangle$ moments for negative hadrons extracted from 2000 data on hydrogen target for scattered lepton detected in the top half (solid squares) or in the bottom half (open triangles).

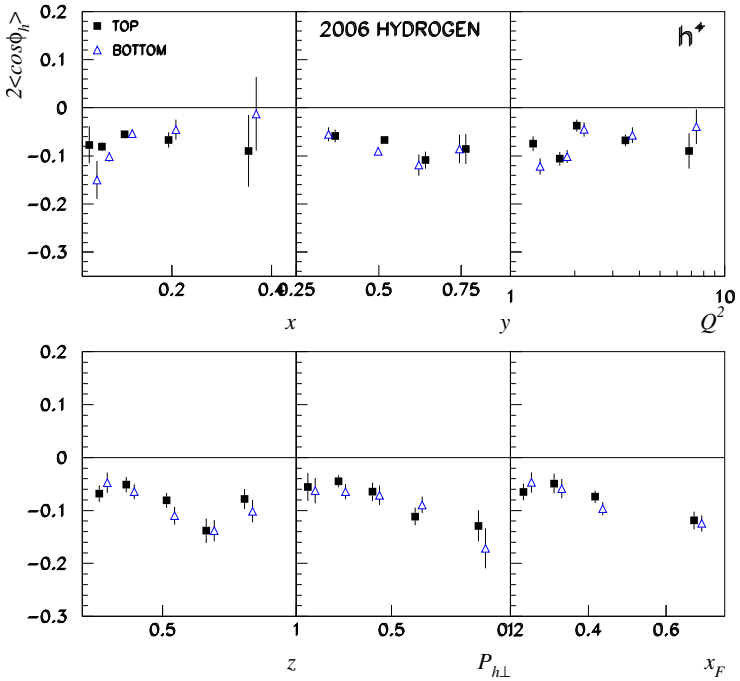

Figure 5.28: $\langle \cos \phi_h \rangle$ moments for positive hadrons extracted from 2006 data on hydrogen target for scattered lepton detected in the top half (solid squares) or in the bottom half (open triangles).

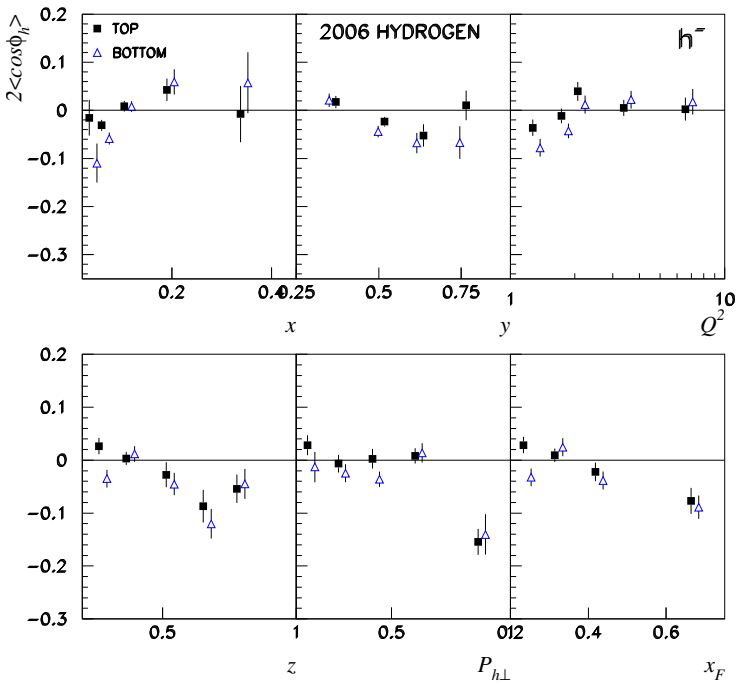

Figure 5.29: $\langle \cos \phi_h \rangle$ moments for negative hadrons extracted from 2006 data on hydrogen target for scattered lepton detected in the top half (solid squares) or in the bottom half (open triangles).

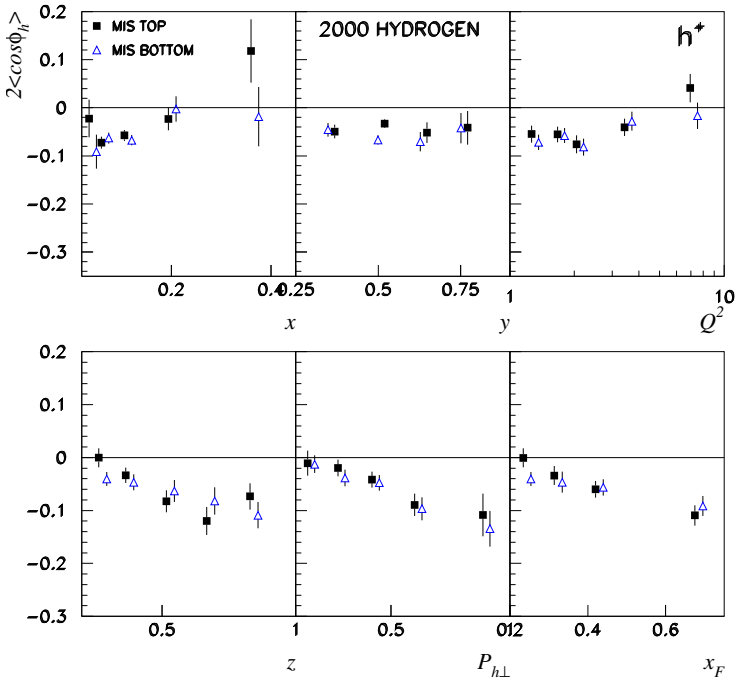

Figure 5.30: $\langle \cos \phi_h \rangle$ moments for positive hadrons extracted from 2000 data on hydrogen target for scattered lepton detected in the top half (solid squares) or in the bottom half (open triangles) with a misaligned MC production, where the misalignment is defined in table 5.3.

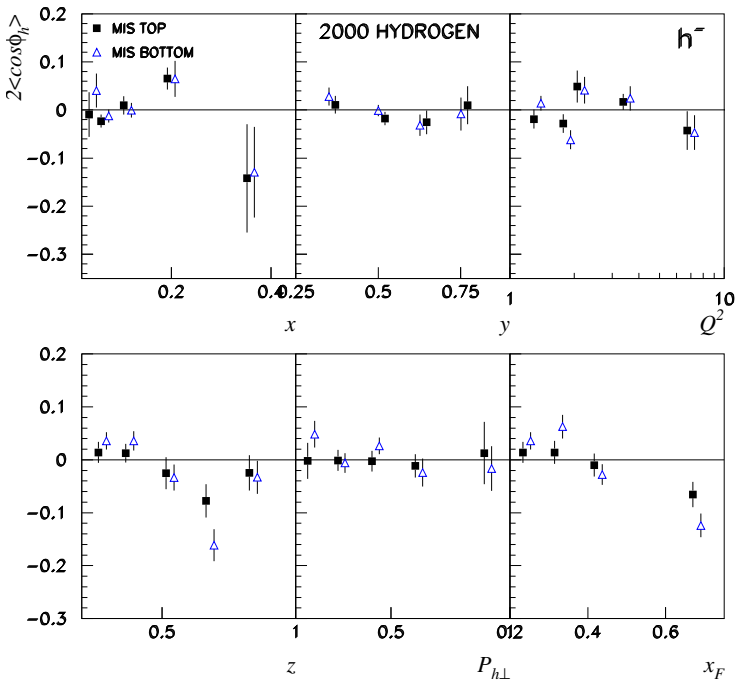

Figure 5.31: $\langle \cos \phi_h \rangle$ moments for negative hadrons extracted from 2000 data on hydrogen target for scattered lepton detected in the top half (solid squares) or in the bottom half (open triangles) with a misaligned MC production, where the misalignment is defined in table 5.3.

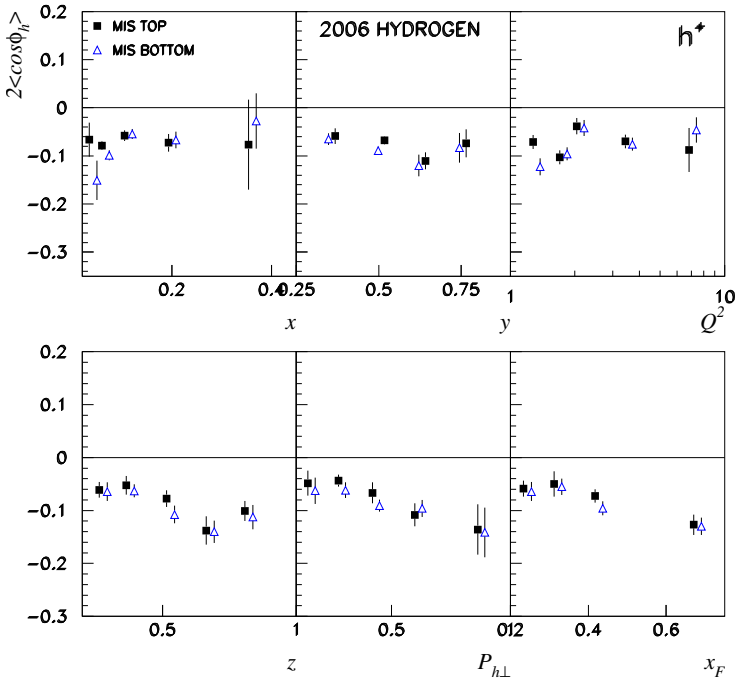

Figure 5.32: $\langle \cos \phi_h \rangle$ moments for positive hadrons extracted from 2006 data on hydrogen target for scattered lepton detected in the top half (solid squares) or in the bottom half (open triangles) with a misaligned MC production.

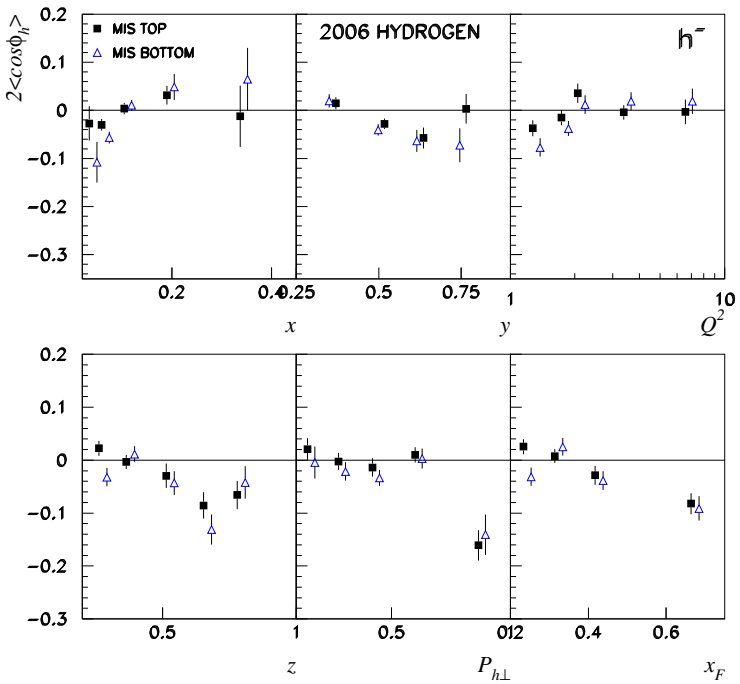

Figure 5.33: $\langle \cos \phi_h \rangle$ moments for negative hadrons extracted from 2006 data on hydrogen target for scattered lepton detected in the top half (solid squares) or in the bottom half (open triangles) with a misaligned MC production.

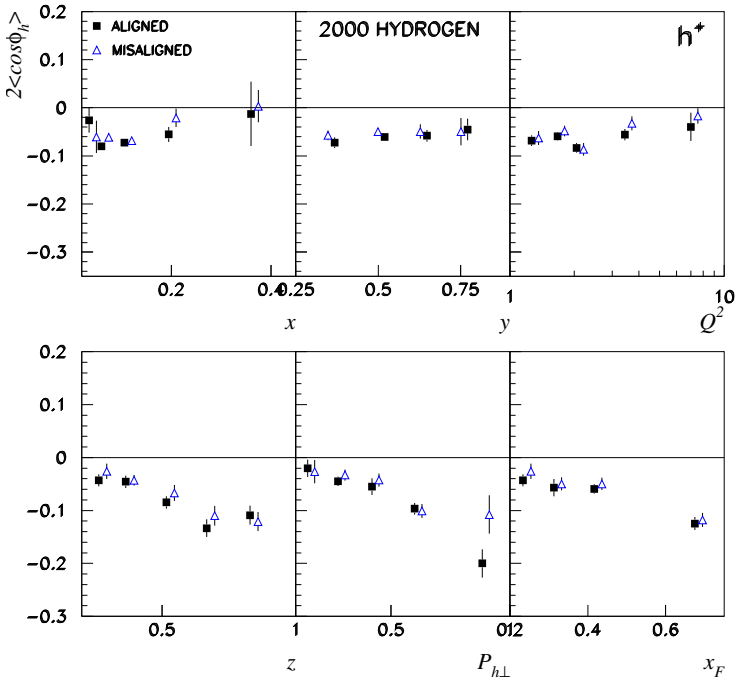

Figure 5.34: Comparison between $\langle \cos \phi_h \rangle$ moments extracted for positive hadrons from 2000 data on hydrogen target with a perfectly aligned MC production (solid squares) and with a misaligned MC production (open triangles), where the misalignment is defined in table 5.3.

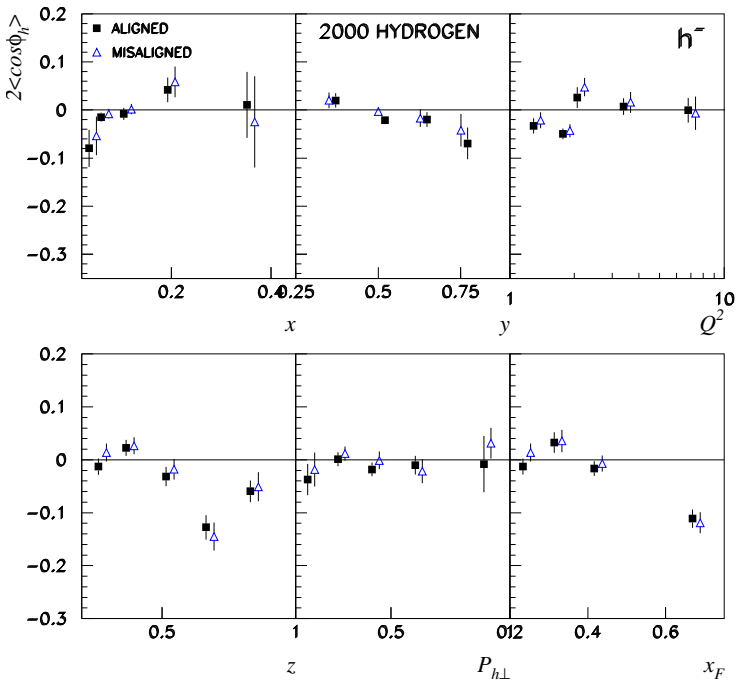

Figure 5.35: Comparison between $\langle \cos \phi_h \rangle$ moments extracted for negative hadrons from 2000 data on hydrogen target with a perfectly aligned MC production (solid squares) and with a misaligned MC production (open triangles), where the misalignment is defined in table 5.3.

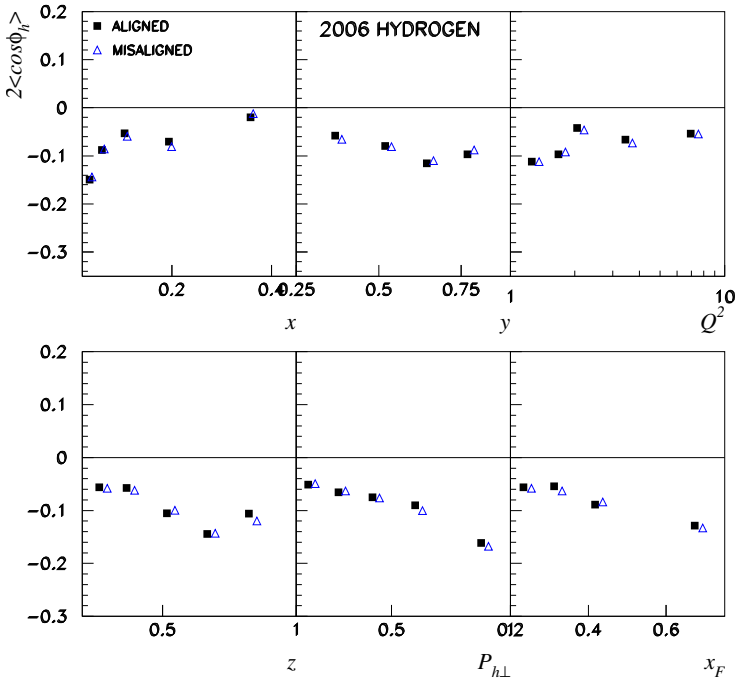

Figure 5.36: Comparison between $\langle \cos \phi_h \rangle$ moments extracted for positive hadrons from 2006 data on hydrogen target with a perfectly aligned MC production (solid squares) and with a misaligned MC production (open triangles).

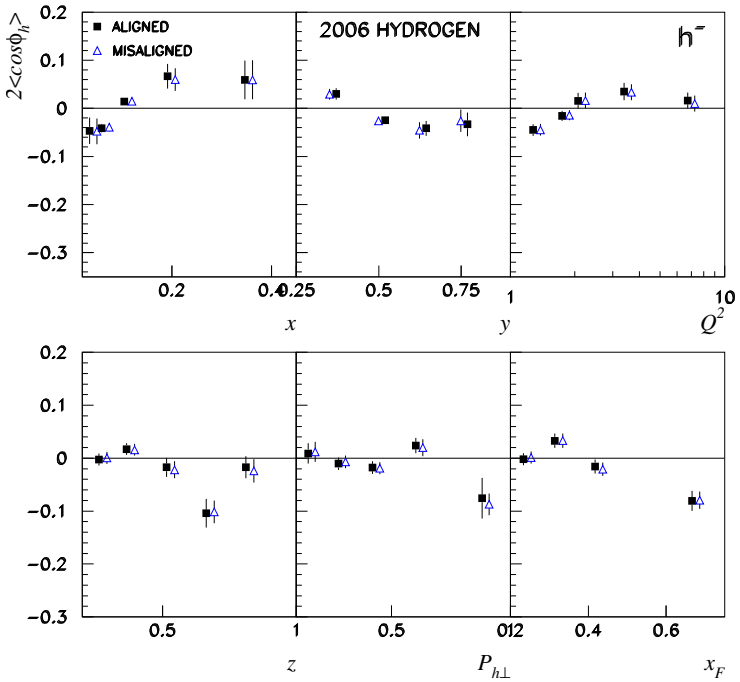

Figure 5.37: Comparison between $\langle \cos \phi_h \rangle$ moments extracted for negative hadrons from 2006 data on hydrogen target with a perfectly aligned MC production (solid squares) and with a misaligned MC production (open triangles).

ures 5.36, 5.37 for the 2006 run. The misalignment effects observed in the TOP-BOTTOM discrepancies are much smaller when the two halves are combined together: even if in 2000 data it is still possible to see a systematic bias related to misalignment, while in 2006 data these effects seem not to affect the results.

The misalignment can not explain the differences between positive and negative hadrons moments, since the effect is too small. Furthermore the results for 2000 run with misaligned MC are systematically shifted upwards for both positive and negative hadrons, therefore the relative differences between the two charges is not affected by this effects.

Plots for the $\langle \cos 2\phi_h \rangle$ moments similar to the ones presented in this section can be found in appendix B.

5.2.2 Target and Recoil magnet effects

Most part of the 2000 deuterium data sample is collected with a longitudinally polarized target, as shown in the following table:

Year	Beam	Target	Target status	Positive hadrons (Million)	Negative hadrons (Million)
2000	e^+	Deuterium	Unpolarized	0.25	0.16
2000	e^+	Deuterium	Polarized	0.67	0.44

The polarization is averaged out in this analysis as samples of data of opposite polarization are summed together. Since the fraction with polarized target is the dominant contribution, it is important to understand if the target magnet (a 0.3 T/m solenoid), turned on for polarized data, can affect the results, for instance by coupling with asymmetries in the detector response, or with detector or beam misalignment in order to change positive and negative hadrons acceptance.

The $\langle \cos \phi_h \rangle$ moments are extracted for the polarized sample only, and compared with the moments extracted from the complete 2000 deuterium sample, see figure 5.38: small differences exist between the moments in the two cases, but there is no evidence of a significative systematic.

A similar situation is present in the hydrogen data for 2006 run: the charged hadrons acceptance can be influenced by the 1 T/m solenoid of the recoil detector installed at the end of 2005. Too few data exist with recoil magnet switched off, therefore to estimate its possible influence on the azimuthal distribution a PYTHIA production has been generated with the magnet switched off, and the moments extracted from 2006 using PYTHIA with and without the recoil magnet on are compared in figure 5.40 and 5.41. From the figures some discrepancies between the two samples can be observed, but they are small and can not explain the differences between positive and negative hadrons, moreover, there are no data with the magnet switched off, thus this test can not be used to estimate a systematics.

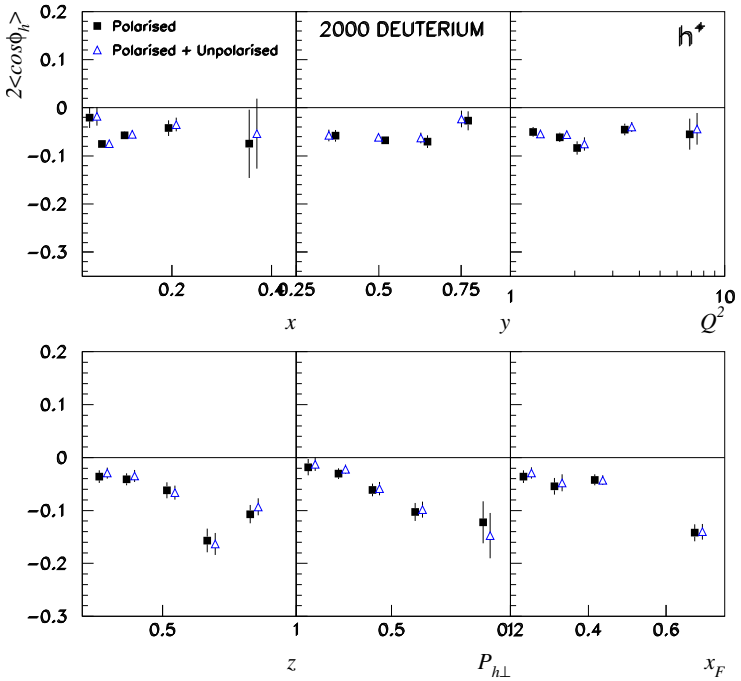

Figure 5.38: $\langle \cos \phi_h \rangle$ moments for positive hadrons extracted in the 2000 data with deuterium target: the solid squares are the moments in the polarized sample, while the open triangles are the moments in the total 2000 deuterium sample.

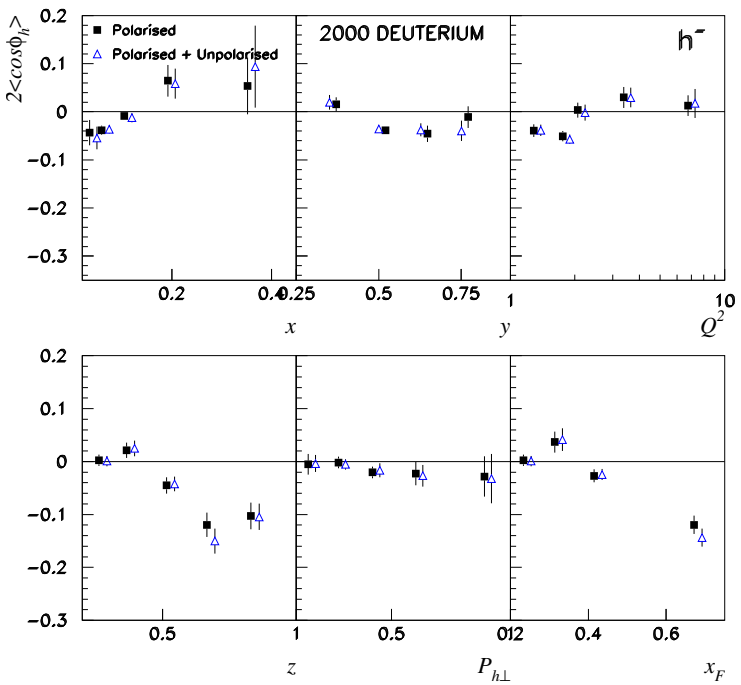

Figure 5.39: $\langle \cos \phi_h \rangle$ moments for negative hadrons extracted in the 2000 data with deuterium target: the solid squares are the moments in the polarized sample, while the open triangles are the moments in the total 2000 deuterium sample.

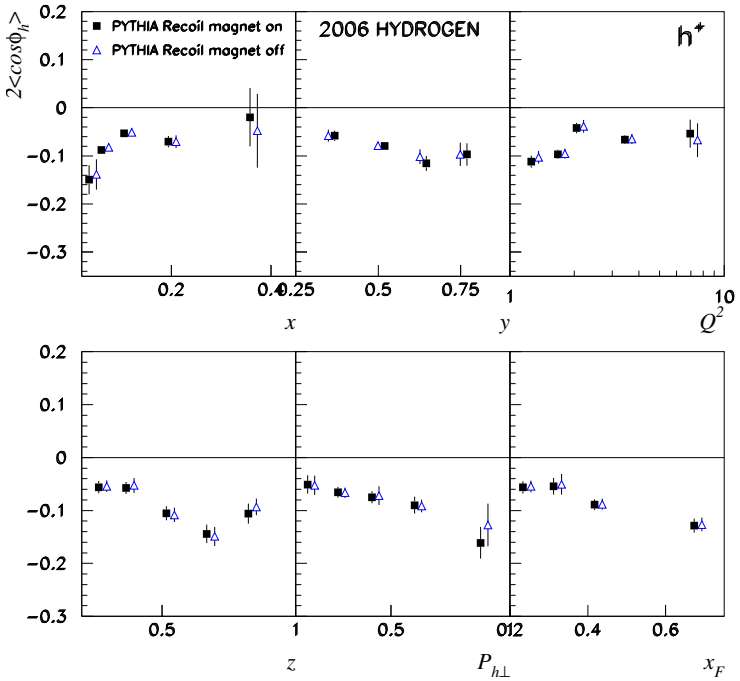

Figure 5.40: $\langle \cos \phi_h \rangle$ moments for positive hadrons extracted in the 2006 data with hydrogen target: the solid squares are the moments where PYTHIA has the recoil magnet switched on, while the open triangles are the moments with PYTHIA recoil magnet is turned off.

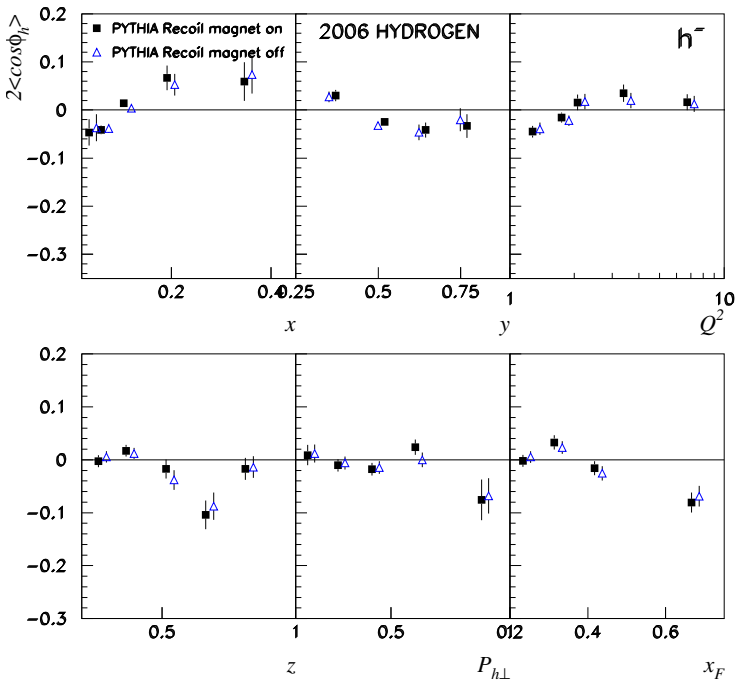

Figure 5.41: $\langle \cos \phi_h \rangle$ moments for negative hadrons extracted in the 2006 data with hydrogen target: the solid squares are the moments where PYTHIA has recoil magnet switched on, while the open triangles are the moments with in PYTHIA the recoil magnet is turned off.

5.2.3 Vector meson contribution

Among the different processes involved in the HERMES kinematics, the production of exclusive vector mesons gives important contributions, especially in particular kinematical regions. These processes constitute a source of background for the SIDIS samples analyzed in the above sections, since they contain particles coming from the decay of exclusive vector mesons, where the biggest contribution is due to the ρ_0 decay.

The azimuthal distribution of the vector mesons and their decay products remains unknown. It is not possible to completely eliminate this background from the event samples because one of the products in most cases falls out of the acceptance, preventing the background identification. The only way to estimate their contributions in the SIDIS sample is to evaluate, with the help of the PYTHIA MC, their fraction of events, also called the *dilution*:

$$d = \frac{N_h^{VM}}{N_h} \tag{5.17}$$

where N_h is the total number of hadrons in the event samples, while N_h^{VM} is the number of vector meson decay products.

The vector meson dilutions estimated for the 2000 run, for both positive and negative hadrons, are shown in figures 5.42. From the pictures it is evident a significative contribution of vector mesons in the high z and low Q^2 region for both the two hadron charges. The dilution is enhanced also at low x and high x_F.

A possibility to decrease the vector meson dilution is to raise the cut on Q^2 as most of the contribution come from low Q^2 region. As can be seen in figures 5.43-5.44, raising the Q^2 cut from 1 to 2 GeV^2, the moments are still compatible with previous ones, although there is a significative loss in statistics resulting in enhanced statistical fluctuations.

5.2.4 Detector edges

Test on azimuthal acceptance

The comparison between Φ_{lab} distributions of positive and negative hadrons in 2000 data and MC are shown in figure 5.45. Φ_{lab} is the azimuthal scattering angle of the hadron with respect to the beam in the laboratory, and the cut $\Phi_{lab} > 0$ ($\Phi_{lab} < 0$) determines the Top (Bottom) part of the spectrometer.

Figure 5.45 shows little discrepancies between data and MC at the edges of the spectrometer, corresponding to $\Phi_{lab} \sim 0$ (2π) or $\Phi_{lab} \sim \pi$. To understand if these differences affect somehow the results, the moments are extracted excluding the events at the edges of the Φ_{lab} distribution both from the data and the MC samples: the results for 2000 hydrogen data are compared to the standard moments in figures 5.46 and 5.47. From the comparison no significative influences can be attributed to DATA/MC discrepancies at the edge of the Φ_{lab} acceptance.

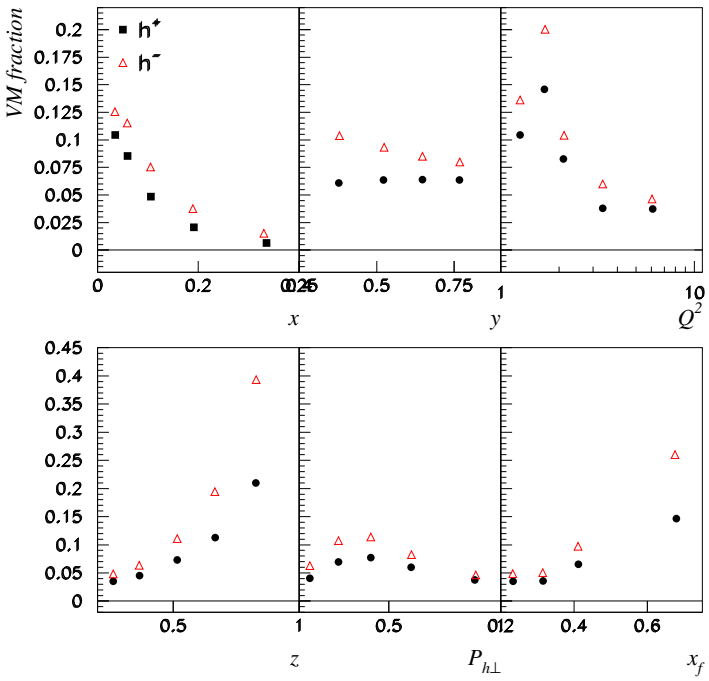

Figure 5.42: Vector meson fraction in a positive (solid squares) and a negative (open triangles) hadron sample.

Test on fiducial volume

A more general systematic test on detector edges response consists in applying a more restrictive fiducial volume, where the cuts on the tracks are hardened by 10% (see table 4.2).

The comparison between results using the standard (table 4.2) and the harder fiducial volume is presented in figures 5.48 and B.14. No discrepancies can be observed changing the requirements on the fiducial volume.

5.2.5 Additional moments

In the unpolarized cross-section of SIDIS hadron productions, in one-photon approximation and up to twist three no sine terms or cosine terms higher than $\langle \mathbf{\cos 2\phi_h} \rangle$ appear:

$$\frac{d\sigma}{dx\,dy\,dz\,dP_{h\perp}^2\,d\phi_h} = \frac{\alpha^2}{xyQ^2}\frac{y^2}{2(1-\epsilon)}(1+\frac{\gamma^2}{2x})\{F_{UU,T} + \epsilon F_{UU,L} + \sqrt{2\epsilon(1+\epsilon)}\cos\phi_h F_{UU}^{\cos\phi_h} + \epsilon\cos 2\phi_h F_{UU}^{\cos 2\phi_h}\}. \tag{5.18}$$

The eventual presence of these terms would indicate residual influence of experimental sources of azimuthal modulation, such as HERMES acceptance and radiative contributions.

To estimate the possible contributions of higher cosine and sine terms, the 2000 hydrogen data were fitted with a generalized fit function with one additional param-

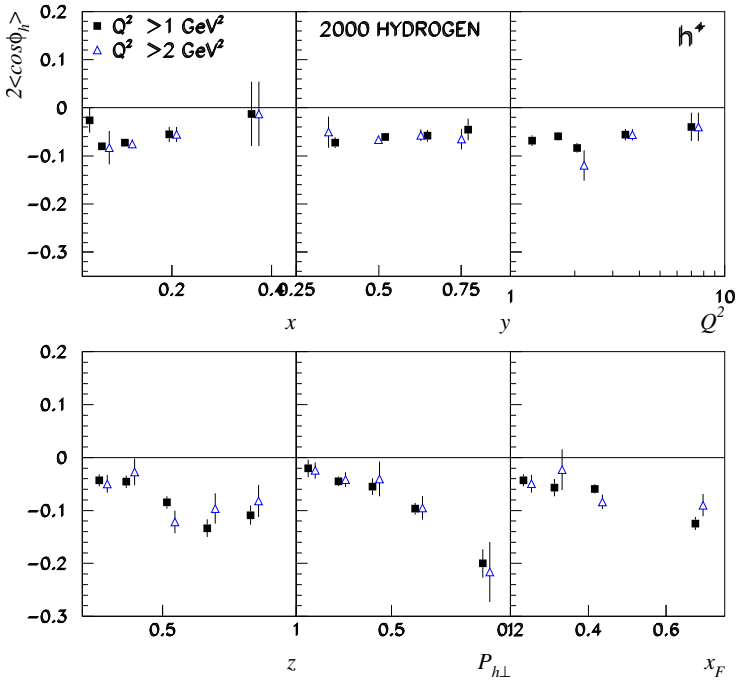

Figure 5.43: $\langle \cos \phi_h \rangle$ moments for positive hadrons extracted in the 2000 data with hydrogen target: the solid squares are the moments with the standard cut $Q^2 > 1\text{GeV}^2$, while the open triangles are the moments with the cut $Q^2 > 2$ GeV^2 hardened to reduce the contribution of the vector mesons.

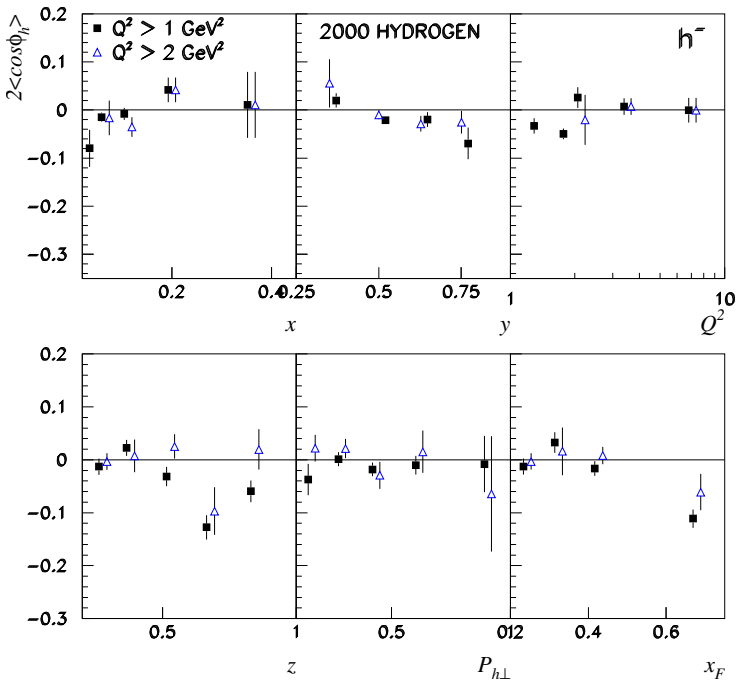

Figure 5.44: $\langle \cos \phi_h \rangle$ moments for negative hadrons extracted in the 2000 data with hydrogen target: the solid squares are the moments with the standard cut $Q^2 > 1\text{GeV}^2$, while the open triangles are the moments with the cut $Q^2 > 2$ GeV^2 hardened to reduce the contribution of the vector mesons.

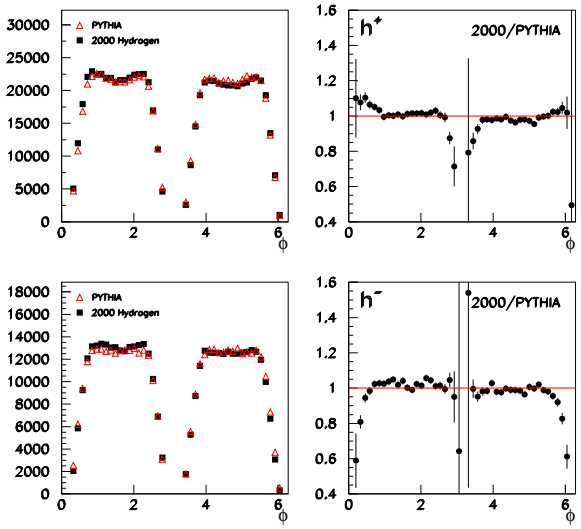

Figure 5.45: Φ_{lab} distributions of positive (upper plots) and negative (lower plots) hadrons in 2000 data (solid squares) and MC (open triangles). The edges of the Φ_{lab} distribution, where discrepancies concentrate, are excluded in the systematic test described in the text.

eter p_3 proportional to $\cos 3\phi_h$

$$f(\phi_h) = R_0 \left(1 + \langle \boldsymbol{\cos \phi_h} \rangle_{F_{UU}} \cos\phi_h + \langle \boldsymbol{\cos 2\phi_h} \rangle_{F_{UU}} \cos 2\phi_h + p_3 \cos 3\phi_h\right) \quad (5.19)$$

or proportional to $\sin \phi_h$

$$f(\phi_h) = R_0 \left(1 + \langle \boldsymbol{\cos \phi_h} \rangle_{F_{UU}} \cos\phi_h + \langle \boldsymbol{\cos 2\phi_h} \rangle_{F_{UU}} \cos 2\phi_h + p_3 \sin \phi_h\right) \quad (5.20)$$

The cosine moments extracted in this way are shown in figures from 5.50 to B.16 and from 5.52 to B.18 for additional cosine and sine terms respectively: the extracted $\langle \boldsymbol{\cos \phi_h} \rangle$ and $\langle \boldsymbol{\cos 2\phi_h} \rangle$ moments remain unchanged.

5.3 Raw ratio results

The moments extracted with the 5-dimensional analysis and projected versus the SIDIS relevant variables are shown in figure 5.54-5.57 for the hydrogen target, and in figure 5.58-5.61 for the deuterium target for positive and negative hadron productions.

The results from all the years show $\langle \boldsymbol{\cos \phi_h} \rangle$ moments which are sizable and negative for positive hadrons, much closer to zero for the negatively charged hadrons. The $\langle \boldsymbol{\cos 2\phi_h} \rangle$ moments are found to be small and negative for positive hadrons, and small and positive for negative hadrons in both the hydrogen and deuterium targets.

Anyway, while in the deuterium samples the results are in good agreement within the statistical error, the hydrogen data show significative differences between 2000

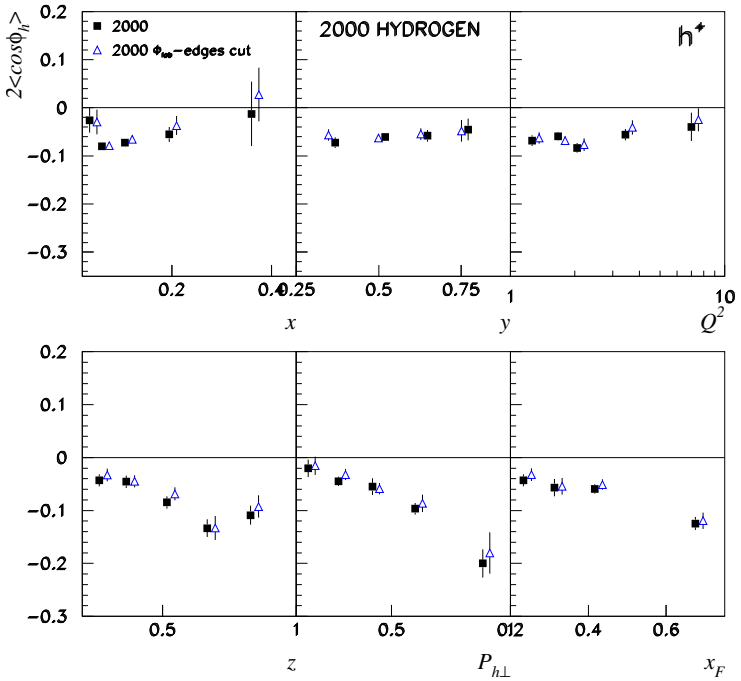

Figure 5.46: $\langle \cos \phi_h \rangle$ moments for positive hadrons extracted in the 2000 data with hydrogen target: the solid squares are the standard moments, while the open triangles are the moments after events at the edges of the Φ_{lab} distribution are eliminated both from the data and the MC (see fig. 5.45).

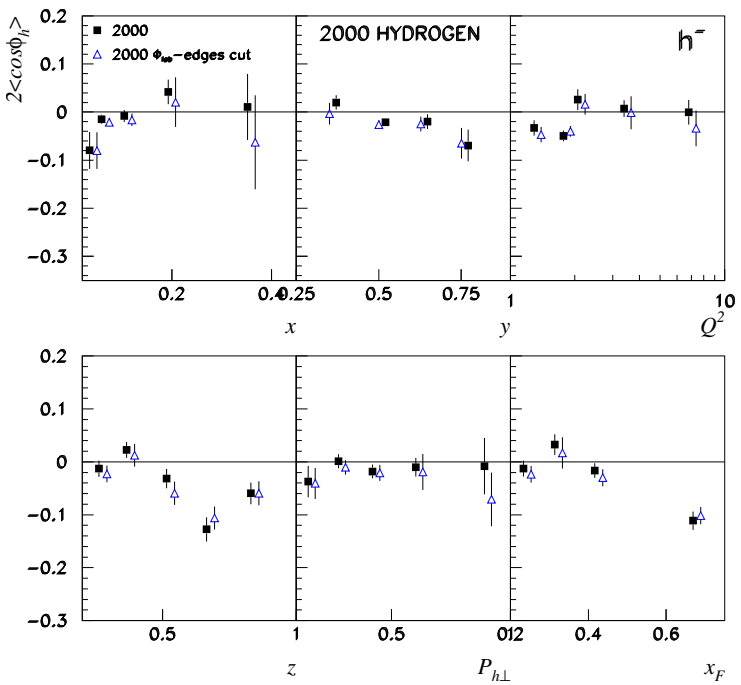

Figure 5.47: $\langle \cos \phi_h \rangle$ moments for negative hadrons extracted in the 2000 data with hydrogen target: the solid squares are the standard moments, while the open triangles are the moments after events at the edges of the Φ_{lab} distribution are eliminated both from the data and the MC (see fig. 5.45).

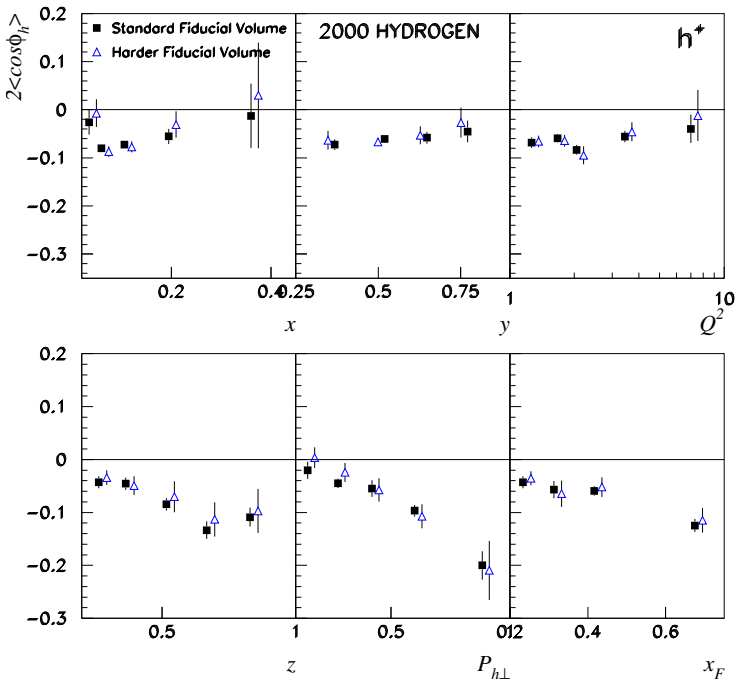

Figure 5.48: $\langle \cos \phi_h \rangle$ moments for positive hadrons extracted in 2000 hydrogen data with the standard (solid squares) and a more restrictive (open triangles) fiducial volume.

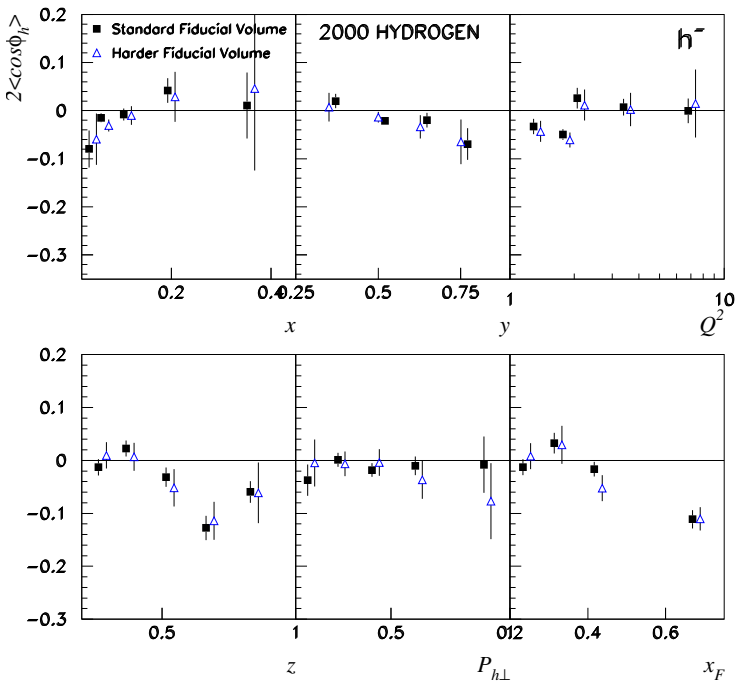

Figure 5.49: $\langle \cos \phi_h \rangle$ moments for negative hadrons extracted in 2000 hydrogen data with the standard (solid squares) and a more restrictive (open triangles) fiducial volume.

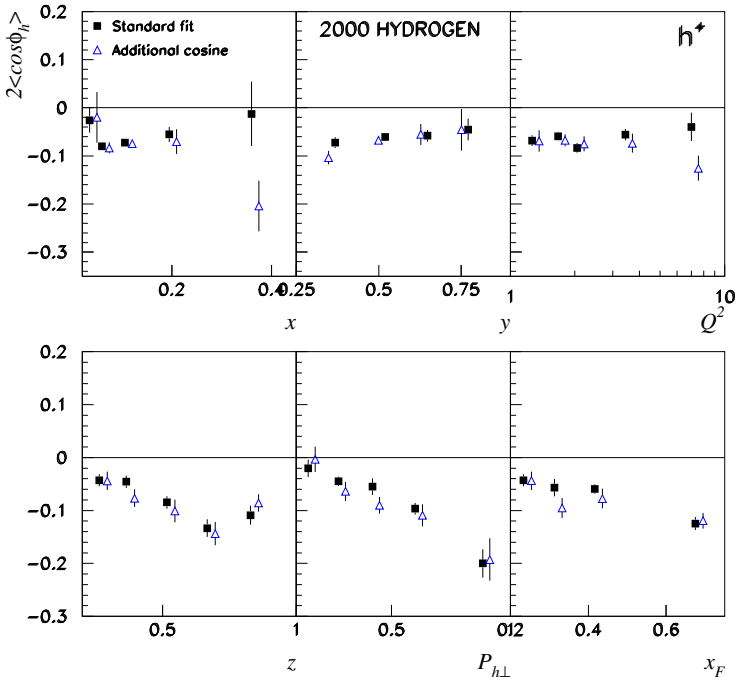

Figure 5.50: $\langle \cos \phi_h \rangle$ moments for positive hadrons extracted in the 2000 data with hydrogen target: the solid squares are the moments extracted with standard fit function, while the open triangles are the moments with the additional cosine moment as in equation 5.19.

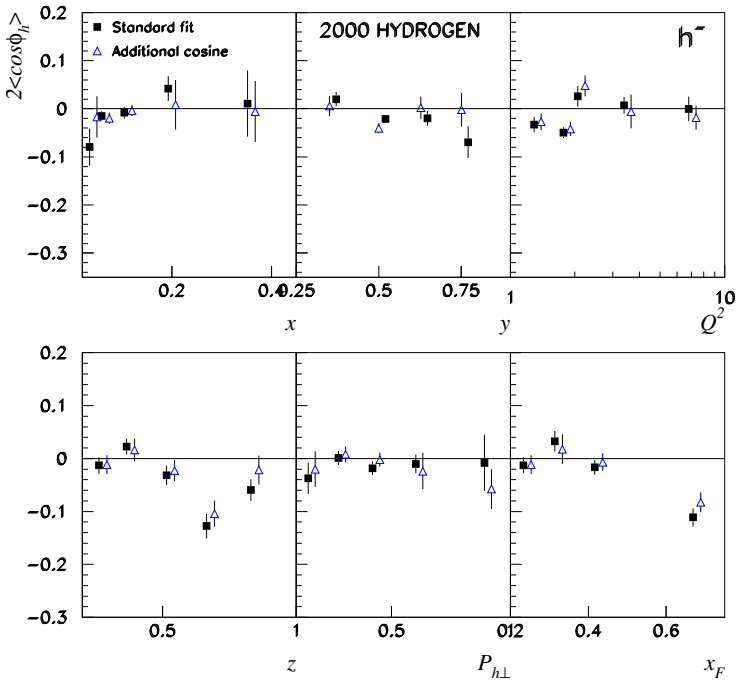

Figure 5.51: $\langle \cos \phi_h \rangle$ moments for negative hadrons extracted in the 2000 data with hydrogen target: the solid squares are the moments extracted with standard fit function, while the open triangles are the moments with the additional cosine moment as in equation 5.19.

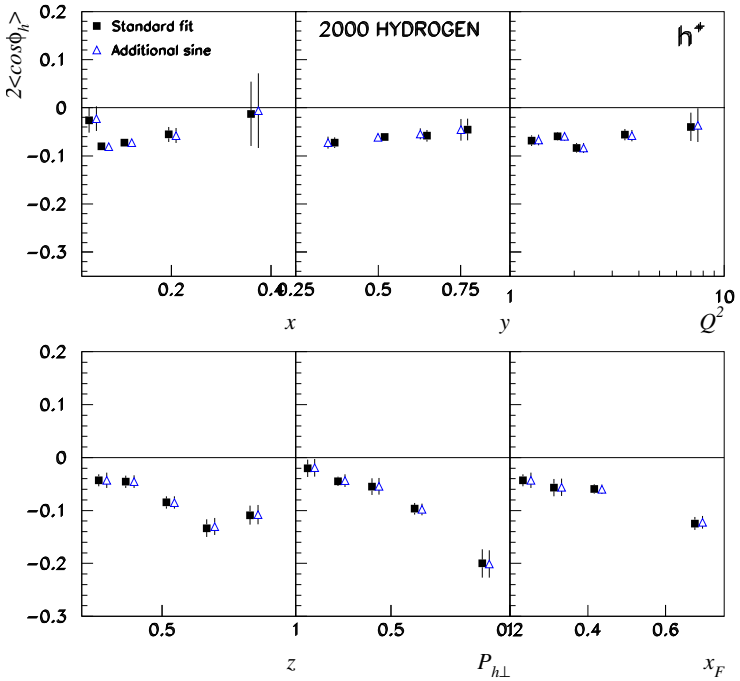

Figure 5.52: $\langle \cos \phi_h \rangle$ moments for positive hadrons extracted in the 2000 data with hydrogen target: the solid squares are the moments extracted with standard fit function, while the open triangles are the moments with the additional sine moment of equation 5.20.

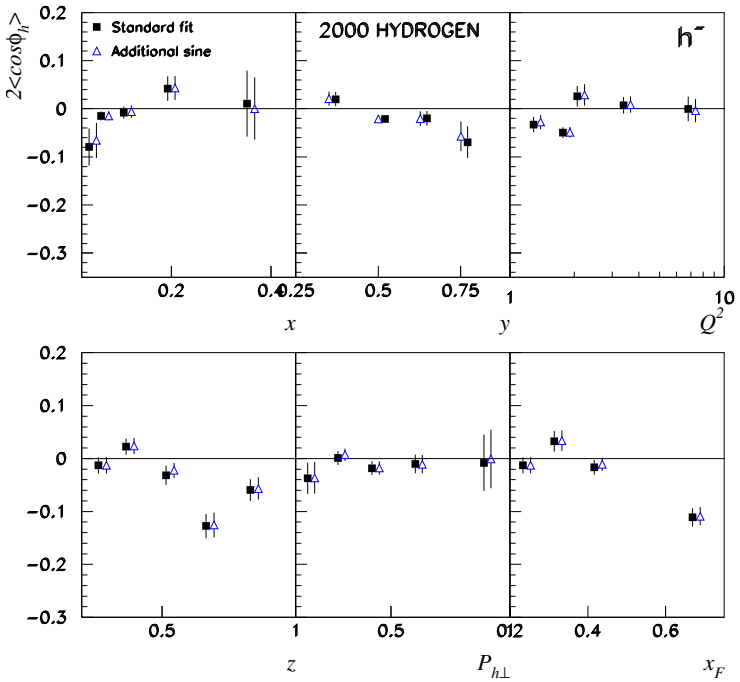

Figure 5.53: $\langle \cos \phi_h \rangle$ moments for negative hadrons extracted in the 2000 data with hydrogen target: the solid squares are the moments extracted with standard fit function, while the open triangles are the moments with the additional sine moment of equation 5.20.

and 2006 sample especially for $\langle \mathbf{cos\,2\phi_h} \rangle$. This discrepancies can be related to main modification in experimental setup, for instance the change of the target cell dimension that passed from 40 cm to 15 cm length. Moreover, at the beginning of 2006, 1 Tm solenoid of the recoil detector surrounding the target area was activate, which could affect the acceptance for charged leptons and hadrons, especially in conjunction with misalignment of the spectrometer.

In any case, as shown by the consistency check of the raw ratio algorithm made at the beginning of section 5.2, the raw results are not expected to be corrected, because the method of the ratio between data and PYTHIA cross-sections is based on the approximate assumptions that the experimental contributions to the azimuthal modulations factorize with the physical ones.

For this reason a procedure able to correct the results for HERMES acceptance, and QED radiative contributions is needed. This procedure, called *unfolding*, correct *raw moments* showed in this section for smearing due to detector and radiative effects, and it is described in chapter 6.2.

As regards the systematic studies, it was shown in last section that, among the possible sources of uncertainties considered, only the misalignment of detector generates a significative systematic effect in the results of 2000 run. However, the discrepancies between other years, much less affected by detector misalignment, already involve differences in detector alignment and setup. For this reason the systematic uncertainty relative to the detector response will be estimated from the difference of the results in the different data taking periods (years), after having applied the unfolding procedure to the raw ratios.

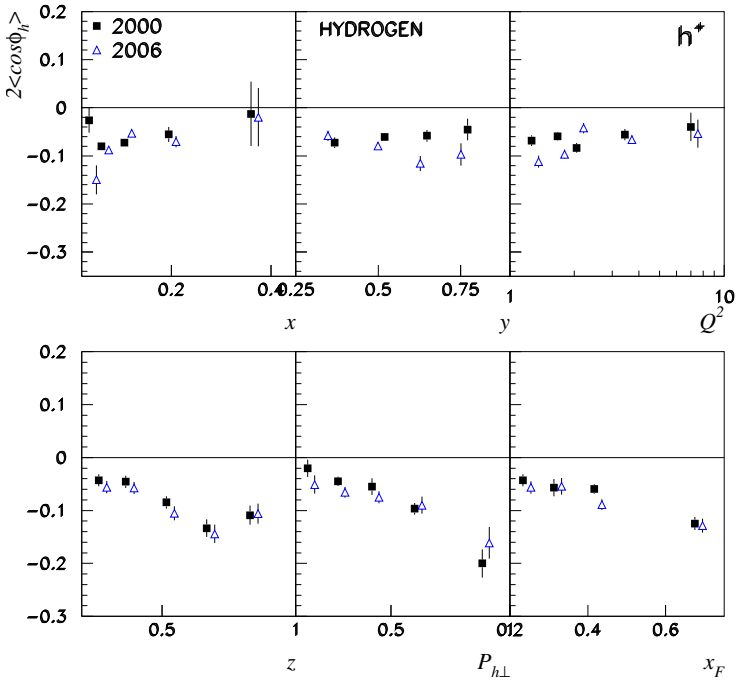

Figure 5.54: $\langle \cos \phi_h \rangle$ moments for positive hadrons from data collected with hydrogen target in 2000 (solid squares) and in 2006 (open triangles) projected versus the kinematical variables x, y, z, $P_{h\perp}$, x_F and Q^2.

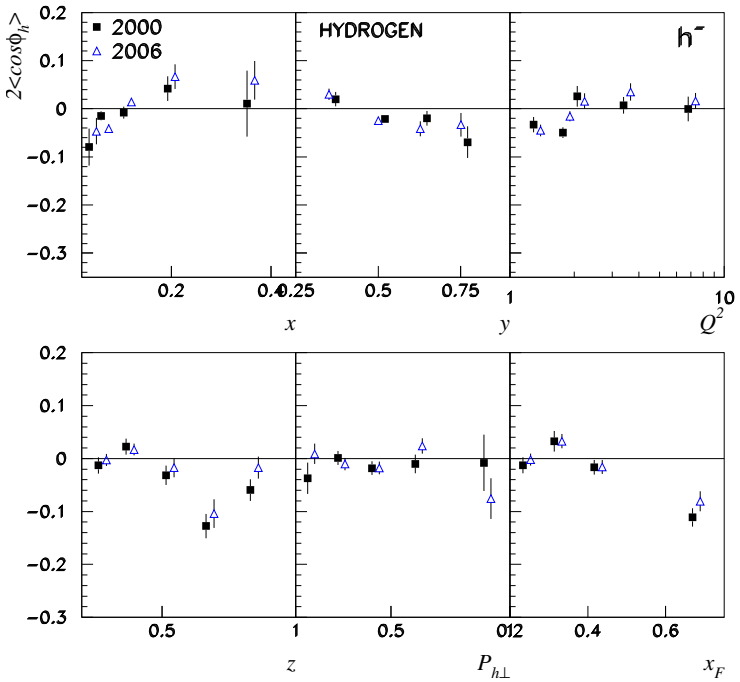

Figure 5.55: $\langle \cos \phi_h \rangle$ moments for negative hadrons from data collected with hydrogen target in 2000 (solid squares) and in 2006 (open triangles) projected versus the kinematical variables x, y, z, $P_{h\perp}$, x_F and Q^2.

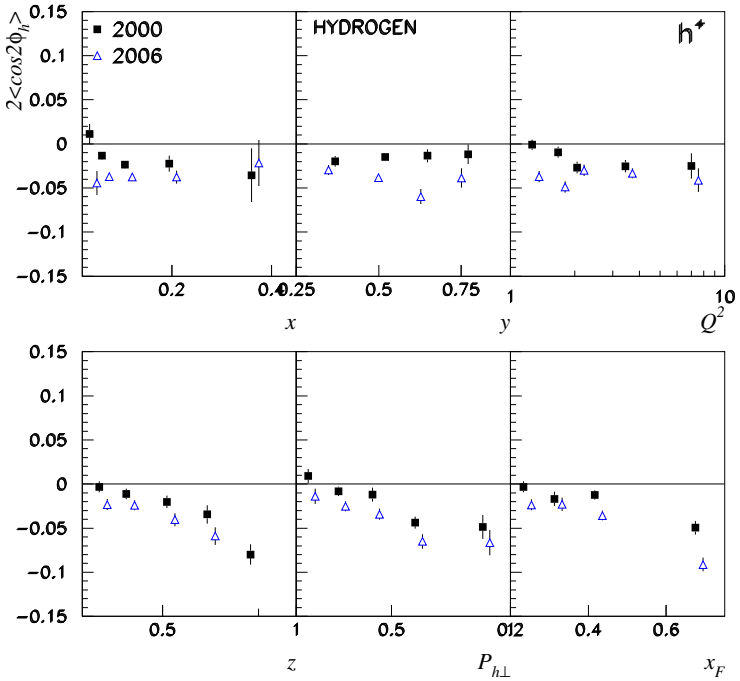

Figure 5.56: $\langle \cos 2\phi_h \rangle$ moments for positive hadrons from data collected with hydrogen target in 2000 (solid squares) and in 2006 (open triangles) projected versus the kinematical variables x, y, z, $P_{h\perp}$, x_F and Q^2.

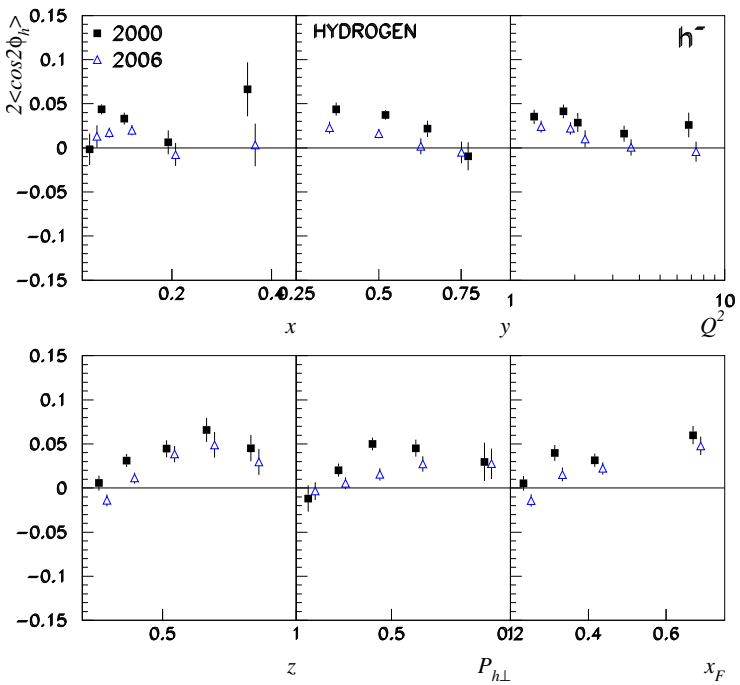

Figure 5.57: $\langle \cos 2\phi_h \rangle$ moments for negative hadrons from data collected with hydrogen target in 2000 (solid squares) and in 2006 (open triangles) projected versus the kinematical variables x, y, z, $P_{h\perp}$, x_F and Q^2.

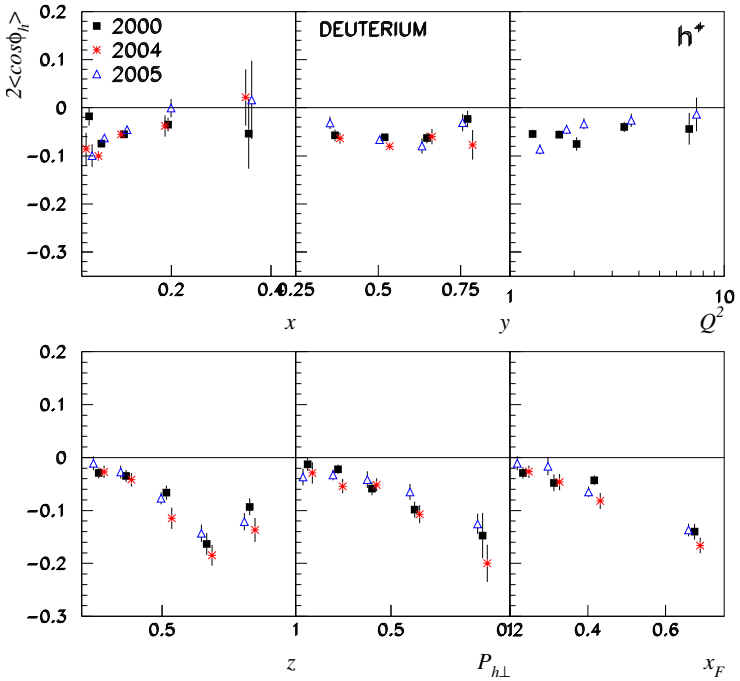

Figure 5.58: $\langle \cos \phi_h \rangle$ moments for positive hadrons from data collected with deuterium target in 2000 (solid squares), in 2004 (stars) and in 2005 (open triangles), projected versus the kinematical variables x, y, z, $P_{h\perp}$, x_F and Q^2.

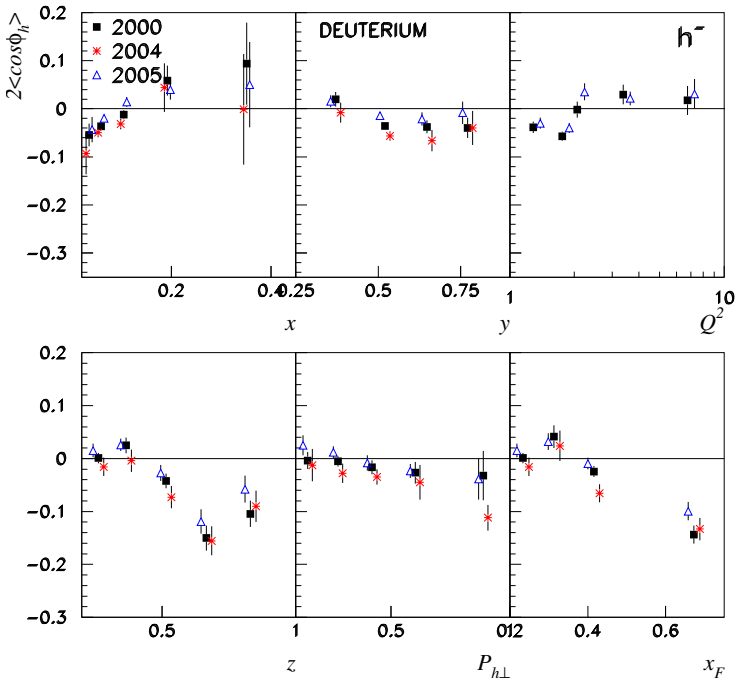

Figure 5.59: $\langle \cos \phi_h \rangle$ moments for negative hadrons from data collected with deuterium target in 2000 (solid squares), in 2004 (stars) and in 2005 (open triangles), projected versus the kinematical variables x, y, z, $P_{h\perp}$, x_F and Q^2.

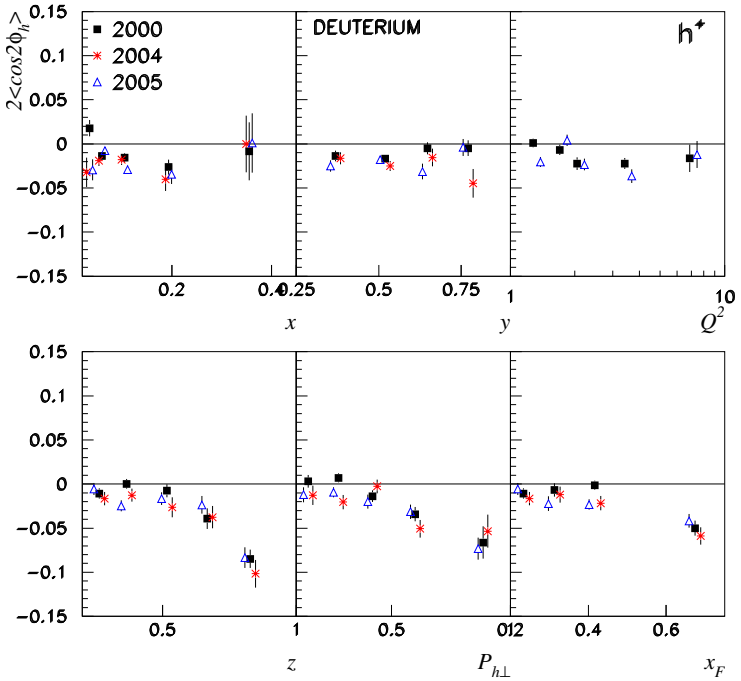

Figure 5.60: $\langle \cos 2\phi_h \rangle$ moments for positive hadrons from data collected with deuterium target in 2000 (solid squares), in 2004 (stars) and in 2005 (open triangles), projected versus the kinematical variables x, y, z, $P_{h\perp}$, x_F and Q^2.

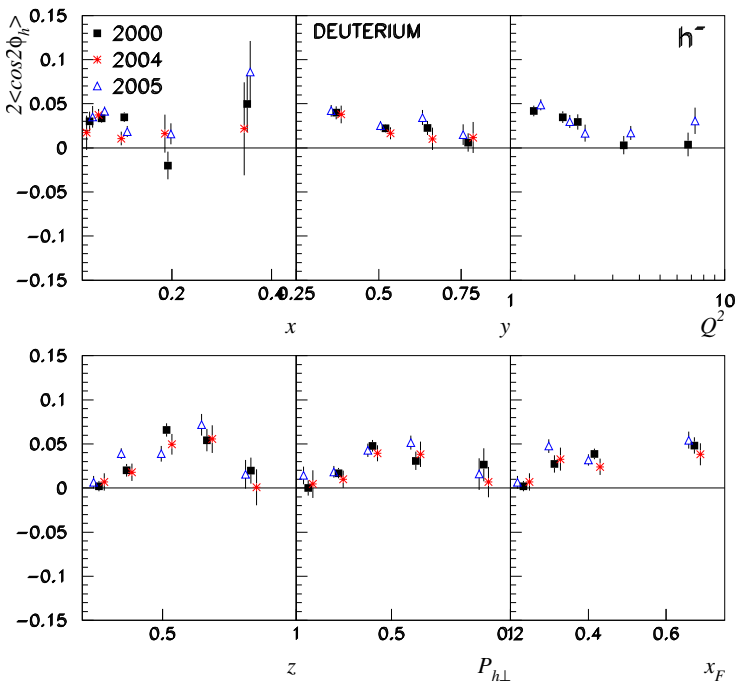

Figure 5.61: $\langle \cos 2\phi_h \rangle$ moments for negative hadrons from data collected with deuterium target in 2000 (solid squares), in 2004 (stars) and in 2005 (open triangles), projected versus the kinematical variables x, y, z, $P_{h\perp}$, x_F and Q^2.

Chapter 6

The Born moments

The extraction method presented in the last chapter corrects only partially for detector acceptance and radiative effects, as anticipated in the Monte Carlo test of section 5.1.6. The raw ratio used in the analysis indeed is inevitably dependent on the PYTHIA unpolarized cross-section model, and its accuracy is strictly related to how well the Monte Carlo describes the experimental data. Moreover QED radiative effects and intrinsic non-perfect resolution of the detector alter somehow the event kinematics, resulting in the migration of the events between different bins. The *raw moments* therefore need to be corrected for all these contributions, possibly in a model independent way, to allow the extraction of the Born moments, free from the experimental distortions due to smearing or acceptance.

In section 6.1 the QED and detector smearing effects are described, then the procedure for a model independent correction procedure is introduce and tested with Monte Carlo productions. Finally the systematic uncertainties are calculated and the corrected results are presented.

6.1 Events migration

6.1.1 QED radiative effects.

Since the measured cross-section involves QED higher order effects, some of which can seriously affect the event kinematics and introduced spurious cosine moments, the final results for the cosine moments should be corrected for their contributions.

The Feynman diagrams of the lepton-nucleon scattering from the tree (Born) level up to the second order QED correction [1] are shown in fig 6.1: the process in (a) represents the Born level, the vertex loop correction (d) and the vacuum polarization (e) affect only the cross-section normalization, while processes described in (b) and (c) are the initial and final state bremsstrahlung, in which the emission of an additional real photon can substantially change the lepton kinematics. To completely define the inclusive DIS kinematics at Born level two variables are needed, here we choose the scattering angle θ and the final lepton energy E' (for

[1] The first order process, or one photon exchange, is usually called the Born-level.

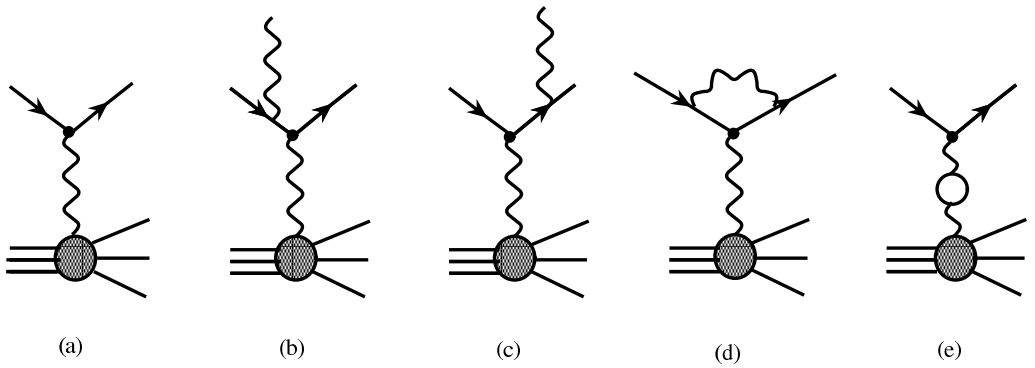

Figure 6.1: The Feynman diagrams of the lepton-nucleon scattering from the tree (Born) level up to the second order QED correction: the process in (a) represents the Born level, (d) and (e) correspond respectively to the vertex loop correction and the vacuum polarization, while processes described in (b) and (c) are the initial and final state bremsstrahlung.

the definitions see chapter 2), all other kinematical variables can be expressed in terms of θ and E'. When an event is detected in the spectrometer, it can either be a non-radiative (Born) or a radiative event, in the second case it should contain a real hard photon with four-momentum $\mathbf{p}_\gamma^\mu = (E_\gamma, \vec{p}_\gamma)$. The existence of the real photon introduces new degrees of freedom, thus three new variables are needed to fix the event kinematics, for instance the real photon energy E_γ and the angles $\theta_{\gamma*\gamma}$, between the real and virtual photon momenta, and $\phi_{\gamma*\gamma}$, between the scattering plane and the plane defined by the two photon momenta. With the use of these quantities and the standard kinematical variables, it is possible to resume the Born variables in the radiative events:

$$\begin{gathered} W^2_{Born} = W^2 \, - \, 2E_\gamma(\nu \, + \, M \, - \, \sqrt{\nu^2 \, + \, Q^2}\cos\theta_\gamma) \\ \nu_{Born} = \nu \, - \, E_\gamma \\ Q^2_{Born} = Q^2 \, + \, 2E_\gamma(\nu \, - \, \sqrt{\nu^2 \, + \, Q^2}\cos\theta_\gamma) \\ x_{Born} = Q^2_{Born}/2M\nu_{Born} \end{gathered}$$

From the latter definition is clear that these kinematical variables do not change if the radiation occurred in the initial or in the final state, since the Born virtual photon momentum $\mathbf{q}_{Born}$ is independent from that condition:

$$\mathbf{q}_{Born} = \left\{ \begin{array}{ll} (\mathbf{k} - \mathbf{p}_\gamma) - \mathbf{k}' : & \text{initial state radiation} \\ \mathbf{k} - (\mathbf{k}' + \mathbf{p}_\gamma) : & \text{final state radiation} \end{array} \right\} = \mathbf{q} - \mathbf{p}_\gamma \qquad (6.1)$$

In the so called *peaking* approximation, used in this work, the real photon is radiated collinear to the lepton momentum, thus the place where the radiation is emitted is irrelevant also for the definition of the scattering plane and the azimuthal angle ϕ_h.

6.1.2 Detector smearing

The interactions of the final state particles with target and detector materials is another source of kinematic smearing. In passing through the matter in fact the particles, especially light leptons, loose part of their energy and deviate from their

original directions. These changes affect the tracking algorithm reconstruction, so the measured angles and momenta differ from the original ones.

6.2 The unfolding formalism

Both the detector and the radiative smearing described above can be simulated by a Monte Carlo, and the effects of the kinematical distortions mentioned together with residual acceptance effects on the raw ratio can be corrected with the use of an unsmearing procedure, called *unfolding* [91, 92]. The unfolding procedure is a standard algorithm that allows the extrapolation in a 4π geometry of experimental results corrected for radiative and detector smearing. In other words the unfolding provides the Born-level results which can directly be compared with those of other experiments as well as with theoretical predictions.

6.2.1 The procedure

Let $X = (X(1), ..., X(n_b))$ be the vector of SIDIS yields in the n_b kinematical bins under study, so that the total number of measured SIDIS events is $X_{tot} = \sum_i X(i)$. Due to the kinematical distortions described in the last section, each event of the sample is characterized by two different kinematics: the measured kinematics ($\mathbf{x}$,ϕ_h)[2], and the unknown Born kinematics ($\mathbf{x}'$,$\phi_h{}'$). As a consequence of the finite bin size the observed bin corresponding to the measured kinematics may differ from the original bin corresponding to the Born kinematics. This may be regarded as migration of the event from the Born bin j to a different measured bin i. The event migration depends only on the detector characteristics and the radiative effects, and can be described with a *Migration matrix* $n(i, j)$ determined by a Monte Carlo simulation of the experimental apparatus and physical processes analyzed.

The dimension of the migration matrix is $n_b \times (n_b + 1)$. The squared sub-matrix describes the event migration between true and measured bins within the geometrical acceptance and kinematical requirements. The additional sub-matrix $n_b \times 1$ contains the events that are smeared in the measured sample from outside the acceptance, due to radiative and detector smearing.

The Born SIDIS yields $n^B(j) = (n^B(1), ..., n^B(n_b))$ in the n_b kinematical bins, can be determined with another, statistically independent Monte Carlo simulation performed at generator level. It is important to notice that:

$$n^B(j) \neq \sum_i^{n_b} n(i, j) \tag{6.2}$$

as the Born vector contains also the events originally generated in the acceptance that migrated outside and thus are not detected.

With the help of the true distribution $n^B(j)$, it is possible to define the probability that an event of true kinematics $(\mathbf{x}', \phi_h{}')$ is observed with measured kinematics

[2]Here $\mathbf{x}$ represents all the kinematical variables (x, y, z, $P_{h\perp}$).

$(\mathbf{x}, \phi_h)$:

$$S(i,j) \equiv \frac{n(i,j)}{n^B(j)} \tag{6.3}$$

where $S(i,j)$ is called the *Smearing matrix*.

If $B(j)$ is the correct, unknown, Born distribution, and $B(0)$ represents the unknown born yield corresponding to the background, the column $j = 0$ can be separated from the smearing matrix, resulting in the $S(i,0) = n(i,0)/B(0)$ vector describing the background contributions and in a square matrix $S'(i,j)$, called the *truncated* smearing matrix.

The truncated smearing matrix only depends on the simulation of detector, which is well known, and, being a relative quantity, is independent on the model of the cross-section. On the contrary, the vector $S(i,0)$ can be a source of systematic uncertainty, as it strongly depend on the Monte Carlo model for the background.

The born $B(j)$ distribution is related to the measured distribution $X(i)$ by:

$$\begin{aligned} X(i) &= \sum_{j=1}^{n_b} S'(i,j)B(j) + S(i,0)B(0) = \\ &= \sum_{j=1}^{n_b} S'(i,j)B(j) + n(i,0) \end{aligned} \tag{6.4}$$

Assuming that $S'(i,j)$ is not singular, it can be inverted giving access to the Born yield distribution:

$$B(j) = \sum_{i=1}^{n_b} S'^{-1}(j,i)\big[X(i) - n(i,0)\big] \tag{6.5}$$

Since the original measured yields are independent Poisson variables, their covariance V is diagonal, with $V(k,k) = \delta^2 X(k) = X(k)$, and the covariance matrix for the Born distribution is

$$U_B(i,j) = S'^{-1}\, V\, (S'^{-1})^T = \sum_{k}^{n_b} S'^{-1}(i,k)\, X(k)\, S'^{-1}(j,k). \tag{6.6}$$

In this analysis the data to be corrected are the ratio $R_X(i)$ between data and PYTHIA ϕ_h-distributions. Therefore relation 6.5 should be rewritten as:

$$B(j) = \sum_{i=1}^{n_b} S'^{-1}(j,i)\big[R_X(i) \cdot n_{PY}(i) - n(i,0)\big] \tag{6.7}$$

where $n_{PY}(i)$ is the fully-tracked PYTHIA yield distribution. The relative covariance matrix remains unchanged, because PYTHIA contribution cancels out in the product $R_X(i) \cdot n_{PY}(i)$.

With the unfolding procedure, the unknown systematic uncertainties due to kinematic smearing is eliminated. The price is that the statistical errors are inflated since the data points become statistically correlated. The unfolding algorithm provides the correlation matrix that should be used to calculate the statistical uncertainties on quantities obtained from the Born yields:

$$\delta^2 B(i) = U_B(i,i) = \sum_k^{n_b} \left(S'^{-1}(i,k)\right)^2 \delta^2 X(k) \tag{6.8}$$

treating the uncertainties as uncorrelated would result in overestimating the uncertainty.

Fitting the unfolded results

After the unfolding procedure a least squares fit has to be applied to the corrected ϕ_h distributions to extract the cosine moments, since the covariance matrix $U_B(i,j)$ of the corrected yields $B(j)$ is no more diagonal, the χ^2 should be generalized:

$$\chi^2 = (B - f(\phi_h))^T U_B^{-1} (B - f(\phi_h)) \tag{6.9}$$

with the usual fit function:

$$f(\phi_h) = R_0 \left(1 + \langle \mathbf{\cos \phi_h} \rangle_{F_{UU}} \cos\phi_h + \langle \mathbf{\cos 2\phi_h} \rangle_{F_{UU}} \cos 2\phi_h\right) \tag{6.10}$$

Since the $f(\phi_h)$ dependence on the parameters is linear, a *linear regression* can be used in order to extract the moments to take into account simultaneously all the correlations between the 500 kinematical bins. In a matricial form, the function $f(\phi_h)$ can be written as $\mathbf{A}p$ where $\mathbf{A}$ is a 500×500 block-diagonal matrix, each block $\mathbf{A^i}$ consisting in a 3×12 matrix given by:

$$\mathbf{A^i} = \begin{pmatrix} 1 & \cos\phi_{h1} & \cos 2\phi_{h1} \\ 1 & \cos\phi_{h2} & \cos 2\phi_{h2} \\ \vdots & \vdots & \vdots \\ 1 & \cos\phi_{h15} & \cos 2\phi_{h12} \end{pmatrix}$$

while p is the vector of the 1500 parameters (3 parameters for each of the 500 bins):

$$p = \begin{pmatrix} p_0^1 \\ p_1^1 \\ p_2^1 \\ \vdots \\ p_0^{500} \\ p_1^{500} \\ p_2^{500} \end{pmatrix} = \begin{pmatrix} R_0^1 \\ \langle \mathbf{\cos \phi_h} \rangle_{F_{UU}}^1 \\ \langle \mathbf{\cos 2\phi_h} \rangle_{F_{UU}}^1 \\ \vdots \\ R_0^{500} \\ \langle \mathbf{\cos \phi_h} \rangle_{F_{UU}}^{500} \\ \langle \mathbf{\cos 2\phi_h} \rangle_{F_{UU}}^{500} \end{pmatrix}$$

where the superscript indicates the kinematical bin.

With this notation equation 6.9 assume the form:

$$\chi^2(\phi_h) = (B - \mathbf{A}p)^T U_B^{-1} (B - \mathbf{A}p) \tag{6.11}$$

To find the minimum χ^2, its derivatives with respect to the parameter should be set to zero:

$$\nabla\chi^2 = -2(\mathbf{A}^T U_B^{-1} B - \mathbf{A}^T U_B^{-1} \mathbf{A} p) = 0 \tag{6.12}$$

In the hypothesis that the matrix $\mathbf{A}^T U_B^{-1} \mathbf{A}$ is not singular, the solution for the parameter vector p is given by a system of linear functions of the corrected yields B:

$$p = \left[(\mathbf{A}^T U_B^{-1} \mathbf{A})^{-1} \mathbf{A}^T U_B^{-1}\right] B \equiv \mathbf{C}\, B \tag{6.13}$$

where the matrix product in square parentheses is rewritten in terms of a global matrix $\mathbf{C}$. The covariance matrix of the extracted moments is easily calculated:

$$\mathrm{Cov}_p = \mathbf{C}\, U_B\, \mathbf{C}^T = (\mathbf{A}^T U_B^{-1} \mathbf{A})^{-1} \tag{6.14}$$

Smearing Matrices

To correct the raw ratios, for each data taking period and hadron charge a matrix was builded based on fully-tracked PYTHIA productions, with a dimension of (6000×6001) (the total number of bins is 6000 as defined in table 5.2). As an example, for the 2000 hydrogen data and positive hadrons the migration of the events between the y, z and $P_{h\perp}$ bins in the second x-bin is presented in the left-hand side of figure 6.2. The typical migration between the 12 ϕ_h-bins in one kinematical bin, depicted in the right-hand side of figure 6.2, shows that the smearing between different ϕ_h bins within the same kinematical bin is small. This can be related to the ϕ_h bin width, which are larger than the HERMES angular resolution. For simplicity in this analysis the smearing on ϕ_h is neglected.

Due to limited Monte Carlo statistics and the very big number of elements, in general a Smearing matrix is singular and cannot be inverted. To avoid this an iterative procedure was builded that gradually eliminates from the matrix the bins that make it singular. This can eventually bias the final results, therefore a Monte Carlo test was performed to check the unfolding procedure before being used on the data.

6.2.2 Monte Carlo test of the unfolding method

The MC productions used for the test are the same described in the previous section: a 4π and a HSG LEPTO productions with an azimuthal modulation, and a 4π and a HSG PYTHIA productions flat in ϕ_h. Figures 6.3 and 6.4 show the comparison between true and unfolded $\langle \boldsymbol{\cos \phi_h} \rangle$ and $\langle \boldsymbol{\cos 2\phi_h} \rangle$ moments. The unfolded values completely recover the Born ones in case of $\langle \boldsymbol{\cos \phi_h} \rangle$ moments. This is an important result because it is an indication that the unfolding procedure provides a model independent correction, since, as mentioned in sections 4.1, 5.1.3 and 5.1.6, the LEPTO and PYTHIA simulations are generated using different cross-section models. In particular PYTHIA does not account for any ϕ_h modulation, i.e. does not reproduce data.

The unfolded $\langle \boldsymbol{\cos 2\phi_h} \rangle$ moments are in good agreement with the Born ones, even if some discrepancies can still be observed, especially in the high y region.

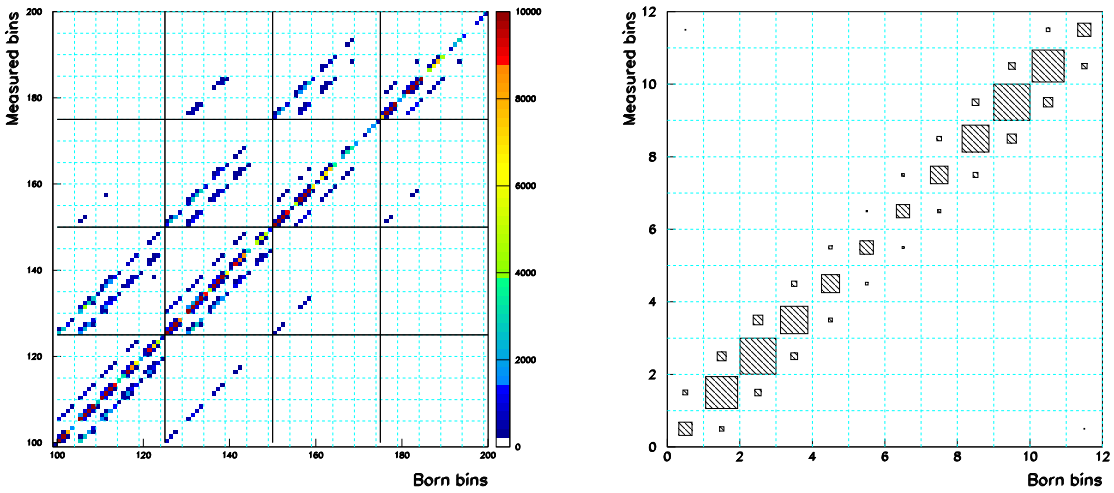

Figure 6.2: Left: the event migration between the kinematical bins of y, z and $P_{h\perp}$ variables (indicated respectively by squares of decreasing size) in one of the x bin. Right: the event migration between the 12 ϕ_h bins in the same kinematical bin.

The relative differences between unfolded and 4π mean values is used as systematic uncertainty due to possible model dependence in the unfolding procedure.

6.3 Unfolded results

The unfolded results extracted with the 5-dimensional analysis for the different data taking periods are presented in figures from 6.5 to 6.8 for hydrogen data, and in figures from 6.9 to 6.12 for deuterium data.

After the unfolding procedure, the $\langle \mathbf{cos}\, \boldsymbol{\phi_h} \rangle$ moments are sizable and negative for positive hadrons, almost compatible with zero for the negatively charged hadrons. The $\langle \mathbf{cos}\, \mathbf{2}\boldsymbol{\phi_h} \rangle$ moments for positive hadrons are found to be slightly negative as in the raw ratios, although the signal seems to be reduced here. The $\langle \mathbf{cos}\, \mathbf{2}\boldsymbol{\phi_h} \rangle$ moments for negative hadrons remain slightly positive.

In most of the cases the discrepancies between the years seem to be reduced by the unfolding. However there exist still differences, i. e. in $\langle \mathbf{cos}\, \mathbf{2}\boldsymbol{\phi_h} \rangle$. The signals become almost compatible along the different data taking periods, suggesting the hypothesis of results stable in time. The remaining discrepancies between the different data taking samples can be attributed to variations in detector setup during the years, like, for instance, different beam position or detector misalignment, as discussed in last chapter. The year dependence left over in the data after the correcting procedure will be therefore treated as systematic uncertainty.

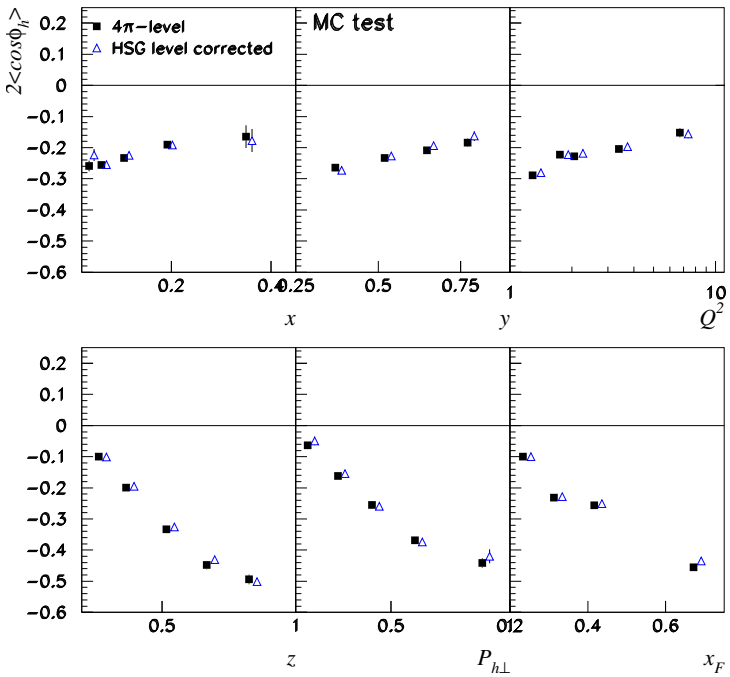

Figure 6.3: $\langle \cos \phi_h \rangle$ moments for positive hadrons extracted with a 5-dimensional analysis in the MC test described in the text: the moments extracted at HSG-level (black open triangles) are compared with the *true moments* (red closed square) generated in 4π.

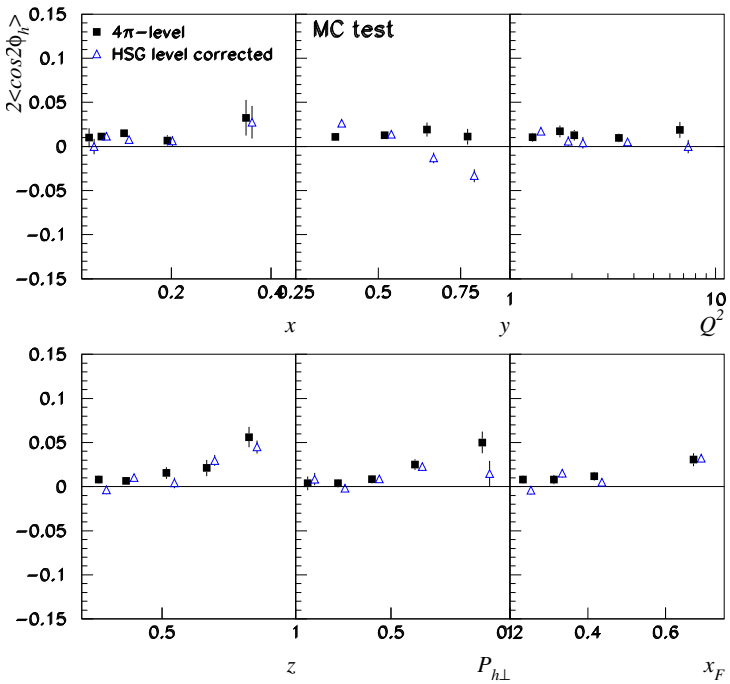

Figure 6.4: $\langle \cos 2\phi_h \rangle$ moments for positive hadrons extracted with a 5-dimensional analysis in the MC test described in the text: the moments extracted at HSG-level (black open triangles) are compared with the *true moments* (red closed square) generated in 4π.

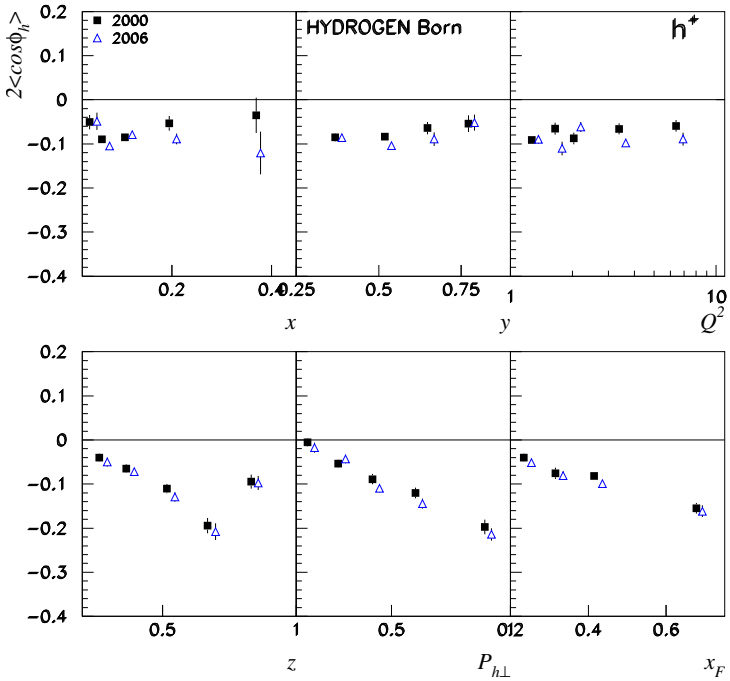

Figure 6.5: Unfolded $\langle \cos \phi_h \rangle_{F_{UU}}$ moments for positive hadrons from data collected with hydrogen target in 2000 (solid squares) and in 2006 (open triangles) projected versus the kinematical variables x, y, z, $P_{h\perp}$, x_F and Q^2.

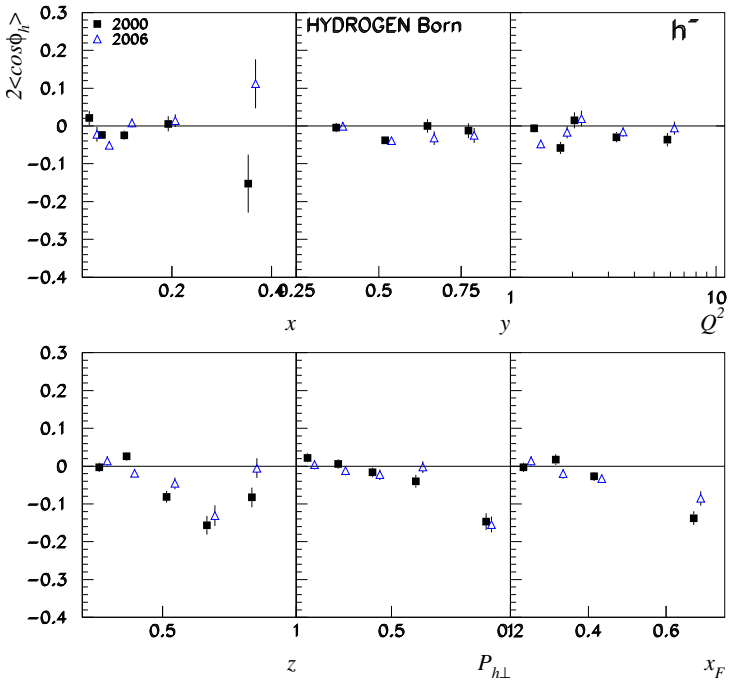

Figure 6.6: Unfolded $\langle \cos \phi_h \rangle_{F_{UU}}$ moments for negative hadrons from data collected with hydrogen target in 2000 (solid squares) and in 2006 (open triangles) projected versus the kinematical variables x, y, z, $P_{h\perp}$, x_F and Q^2.

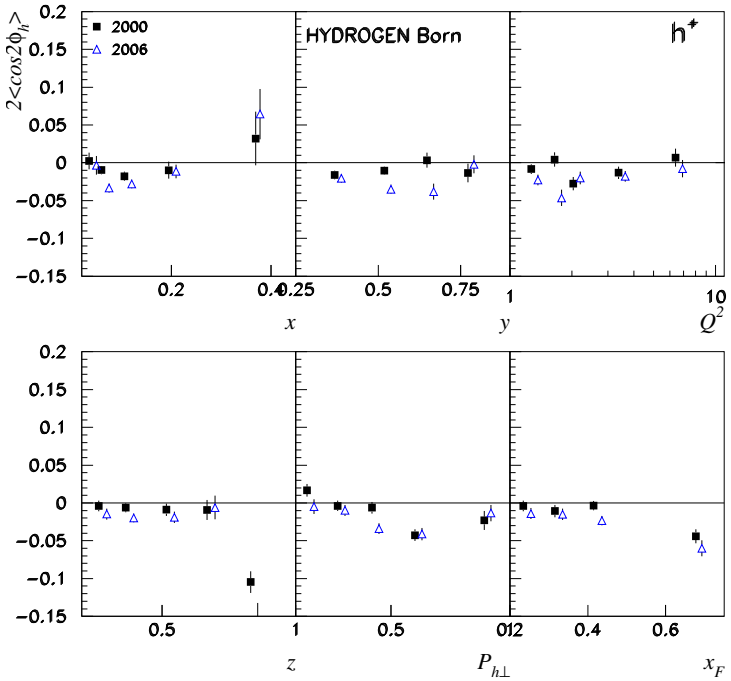

Figure 6.7: Unfolded $\langle \mathbf{cos\,2}\phi_{\boldsymbol{h}} \rangle_{F_{UU}}$ moments for positive hadrons from data collected with hydrogen target in 2000 (solid squares) and in 2006 (open triangles) projected versus the kinematical variables x, y, z, $P_{h\perp}$, x_F and Q^2.

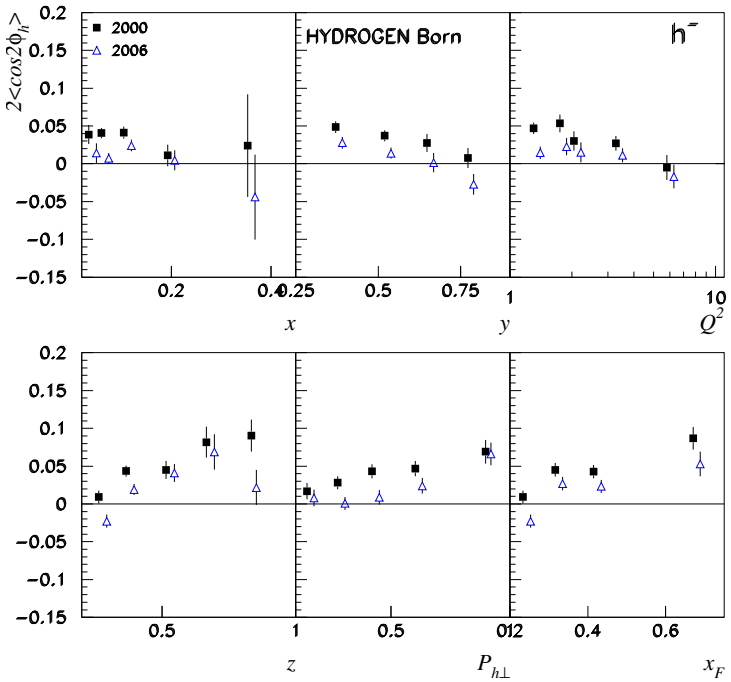

Figure 6.8: Unfolded $\langle \mathbf{cos\,2}\phi_{\boldsymbol{h}} \rangle_{F_{UU}}$ moments for negative hadrons from data collected with hydrogen target in 2000 (solid squares) and in 2006 (open triangles) projected versus the kinematical variables x, y, z, $P_{h\perp}$, x_F and Q^2.

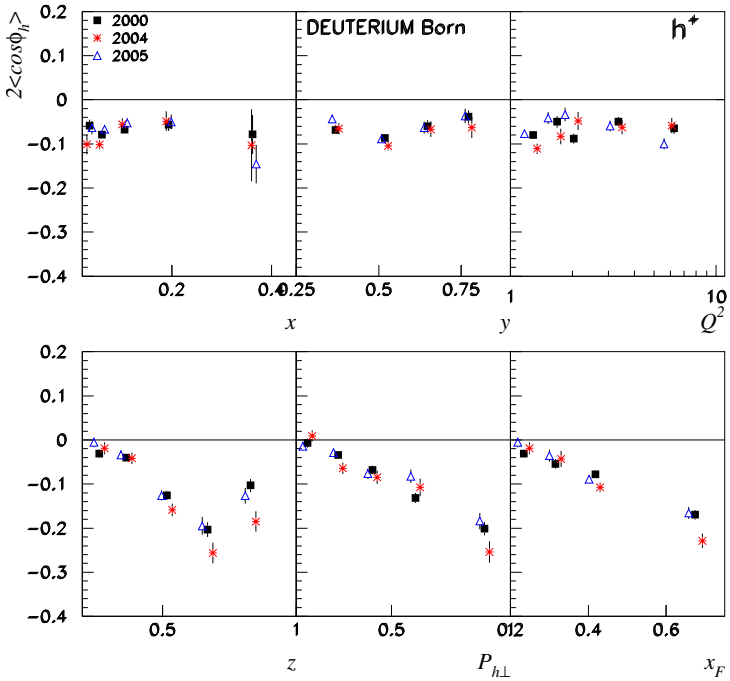

Figure 6.9: Unfolded $\langle \cos \phi_h \rangle_{F_{UU}}$ moments for positive hadrons from data collected with deuterium target in 2000 (solid squares), in 2004 (red stars) and in 2005 (open triangles), projected versus the kinematical variables x, y, z, $P_{h\perp}$, x_F and Q^2.

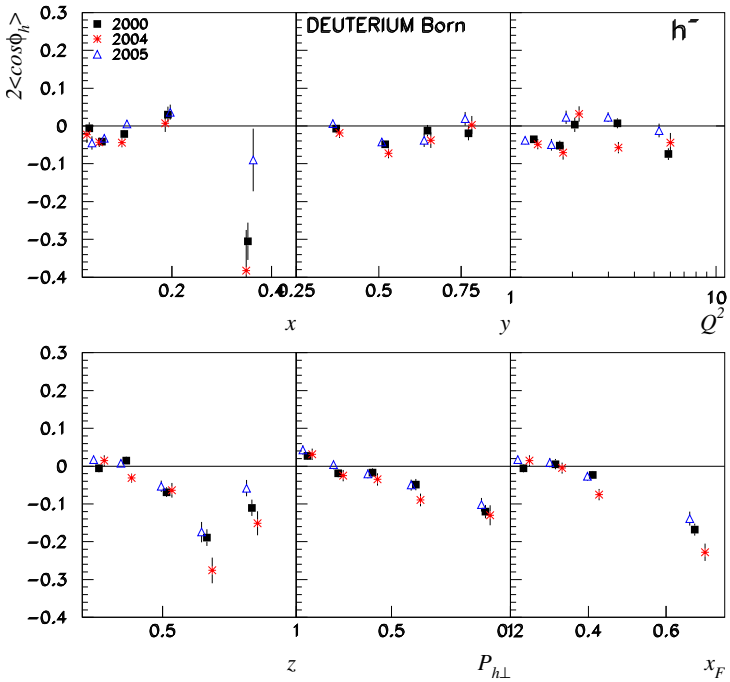

Figure 6.10: Unfolded $\langle \cos \phi_h \rangle_{F_{UU}}$ moments for negative hadrons from data collected with deuterium target in 2000 (solid squares), in 2004 (red stars) and in 2005 (open triangles), projected versus the kinematical variables x, y, z, $P_{h\perp}$, x_F and Q^2.

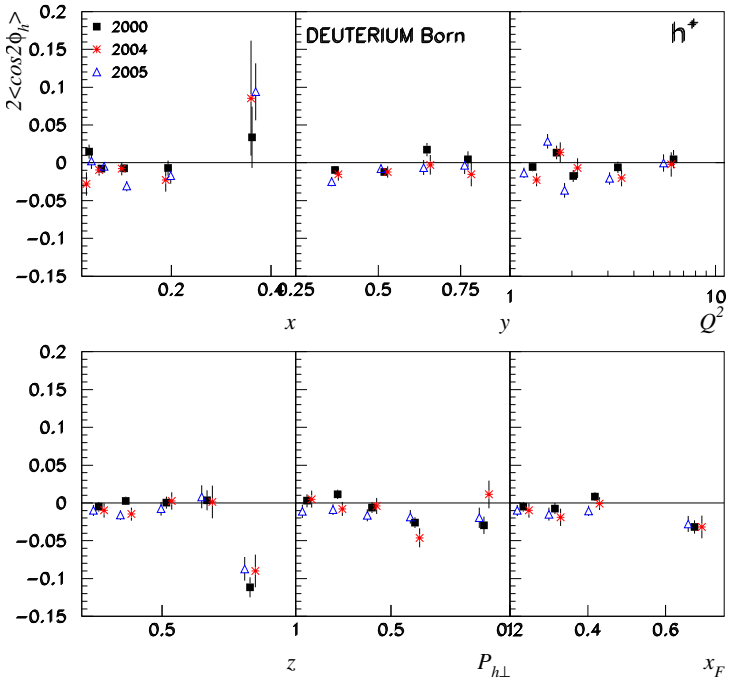

Figure 6.11: Unfolded $\langle \mathbf{cos}\, \boldsymbol{\phi_h} \rangle_{F_{UU}}$ moments for positive hadrons from data collected with deuterium target in 2000 (solid squares), in 2004 (red stars) and in 2005 (open triangles), projected versus the kinematical variables x, y, z, $P_{h\perp}$, x_F and Q^2.

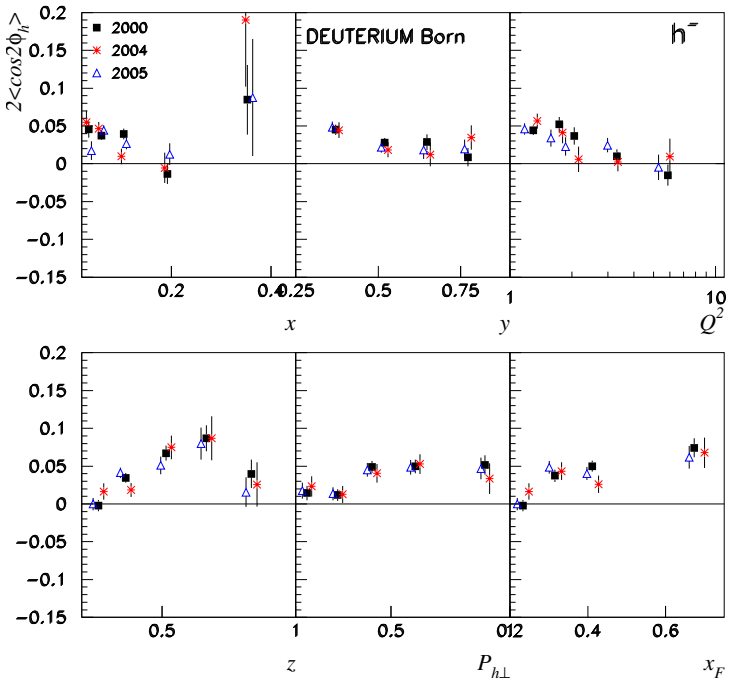

Figure 6.12: Unfolded $\langle \mathbf{cos}\, \boldsymbol{\phi_h} \rangle_{F_{UU}}$ moments for negative hadrons from data collected with deuterium target in 2000 (solid squares), in 2004 (stars) and in 2005 (open triangles), projected versus the kinematical variables x, y, z, $P_{h\perp}$, x_F and Q^2.

Chapter 7

Final results and interpretations

The analysis described in this thesis concentrates on the study of the unpolarized cross-section for semi-inclusive DIS processes given by:

$$\frac{d\sigma}{dx\,dy\,dz\,dP_{h\perp}^2\,d\phi_h} = \frac{\alpha^2}{xyQ^2}\frac{y^2}{2(1-\epsilon)}(1+\frac{\gamma^2}{2x})\{F_{UU,T}+\epsilon F_{UU,L}+ \sqrt{2\epsilon(1+\epsilon)}\cos\phi_h F_{UU}^{\cos\phi_h}+\epsilon\cos 2\phi_h F_{UU}^{\cos 2\phi_h}\} \tag{7.1}$$

in particular its aim was the extraction of the unpolarized structure functions $F_{UU}^{\cos\phi_h}$ and $F_{UU}^{\cos 2\phi_h}$ related to the cosine modulations in hadron production. In a *twist* expansion of the cross-section these structure functions can be related to a number of contributions (see sec. 2.3.1), among which the best known theoretically are the Boer-Mulders and the Cahn effects (see sections 2.4 and 2.5).

The $\cos 2\phi_h$ modulation appears in the cross-section as leading term and up to twist three is entirely due to the Boer-Mulders effect, related to the existence of quark spin-orbit correlations. The Boer-Mulders effect is also involved in the first next-to-leading contribution, which has a $\cos\phi_h$ modulation, but in this case it is coupled to other contributions, in particular to the Cahn effect, which is a pure kinematical effect due to intrinsic motion.

The 5-dimensional analysis used for the extraction of the mentioned structure functions was described in chapter 5, then several systematic checks were performed and finally the results were corrected for QED radiative contributions and detector smearing (chapter 6).

In this chapter the final azimuthal moments extracted from hydrogen and deuterium targets are presented separately for positive and negative hadrons. The $\langle\boldsymbol{\cos\phi_h}\rangle$ and $\langle\boldsymbol{\cos 2\phi_h}\rangle$ moments are discussed as regards their flavour dependence due to different target gas type and hadron charges, and finally they are compared to theoretical predictions and models.

x-bin	$\langle x \rangle$	$\langle y \rangle$	$\langle Q^2 \rangle$	$\langle z \rangle$	$\langle P_{h\perp} \rangle$	$\langle x_F \rangle$
1	0.0353	0.6510	1.1770	0.5059	0.4929	0.4699
2	0.0579	0.5662	1.6919	0.5118	0.4757	0.4692
3	0.1033	0.5578	3.0068	0.5080	0.4711	0.4631
4	0.1890	0.5532	5.4747	0.5063	0.4643	0.4588
5	0.3525	0.5452	10.2100	0.5056	0.4526	0.4494
y-bin	$\langle x \rangle$	$\langle y \rangle$	$\langle Q^2 \rangle$	$\langle z \rangle$	$\langle P_{h\perp} \rangle$	$\langle x_F \rangle$
1	0.1780	0.3671	3.3650	0.5425	0.4446	0.4782
2	0.1459	0.5038	3.8596	0.5045	0.4558	0.4568
3	0.1487	0.6431	4.9265	0.5062	0.4892	0.4664
4	0.1434	0.7395	5.5424	0.4833	0.4880	0.4484
Q^2-bin	$\langle x \rangle$	$\langle y \rangle$	$\langle Q^2 \rangle$	$\langle z \rangle$	$\langle P_{h\perp} \rangle$	$\langle x_F \rangle$
1	0.0449	0.5700	1.2290	0.5213	0.4725	0.4804
2	0.0603	0.5769	1.7651	0.4777	0.4627	0.4371
3	0.0812	0.5657	2.1224	0.5139	0.4926	0.4670
4	0.1299	0.5626	3.5390	0.5184	0.4735	0.4726
5	0.2918	0.5929	8.8162	0.5127	0.4767	0.4628

Table 7.1: Mean values of kinematical variable in x, y and Q^2 bins.

7.1 Final results

The final results are extracted with a weighted average of the different data taking years separately for hydrogen and deuterium targets and for positive and negative hadrons. Half the difference between values in each bin is taken as systematic uncertainties due to data compatibility. The results for the hydrogen and deuterium targets extracted fitting the measured yields in a grid of 500 independent kinematical bins are available in appendix A. Of the initially 500 bins, about half have enough statistics to provide reasonable results. These values, together with the corresponding covariance matrix [1], can be used for phenomenological fits to extract informations on transverse momentum dependent correlation functions (sec. 2.3.1).

The projection in the relevant kinematical variables for the hydrogen and deuterium targets are shown in figures from 7.1 to 7.8. The dashed areas represent the global systematic uncertainties including discrepancies between data taking periods and the systematic error for the unfolding procedure extracted in the Monte Carlo test presented in section 6.2.2. The average kinematic values found in the final data samples are summarized for each kinematical bin in table 7.1 and 7.2.

The $\langle \boldsymbol{\cos \phi_h} \rangle$ moments are found to be sizable and negative for positive hadrons. The results show signals almost constant in x, y and Q^2 variables. The signal becomes larger at larger $P_{h\perp}$, confirming the Cahn expectations of a signal proportional to transverse momentum addressed in section 2.5. The increasing with x_F of the

[1] The covariance matrix is available from the author under request.

z-bin	$\langle x \rangle$	$\langle y \rangle$	$\langle Q^2 \rangle$	$\langle z \rangle$	$\langle P_{h\perp} \rangle$	$\langle x_F \rangle$
1	0.1426	0.5881	4.3110	0.2626	0.3960	0.2215
2	0.1571	0.5882	4.6946	0.3660	0.4667	0.3186
3	0.1534	0.5674	4.4464	0.5010	0.4726	0.4560
4	0.1609	0.5675	4.6439	0.6628	0.5127	0.6160
5	0.1502	0.5385	4.1701	0.7811	0.5076	0.7316
$P_{h\perp}$-bin	$\langle x \rangle$	$\langle y \rangle$	$\langle Q^2 \rangle$	$\langle z \rangle$	$\langle P_{h\perp} \rangle$	$\langle x_F \rangle$
1	0.1477	0.5050	3.9094	0.4011	0.1532	0.3760
2	0.1565	0.5749	4.5601	0.5130	0.2816	0.4849
3	0.1584	0.5876	4.7324	0.5295	0.4210	0.4921
4	0.1571	0.5895	4.7168	0.5317	0.5966	0.4783
5	0.1428	0.5814	4.2319	0.5402	0.8492	0.4571
x_F-bin	$\langle x \rangle$	$\langle y \rangle$	$\langle Q^2 \rangle$	$\langle z \rangle$	$\langle P_{h\perp} \rangle$	$\langle x_F \rangle$
1	0.1470	0.6030	4.4891	0.2686	0.3941	0.2295
2	0.1727	0.5634	4.9789	0.3679	0.5831	0.3049
3	0.1502	0.5841	4.4270	0.4726	0.4249	0.4331
4	0.1568	0.5662	4.4994	0.7376	0.5203	0.6905

Table 7.2: Mean values of kinematical variable in z, $P_{h\perp}$ and x_F bins.

results denotes a larger signal in the current region, where hadrons produced are originated directly by the struck quark, and is in qualitative agreement with the EMC results shown in figure 2.19. The signal increases with the hadron energy fraction z, thanks to the reduced dilution by transverse momentum randomly added by fragmentation. The only exception is in the very high z range, where a sizable contribution from vector mesons (sec. 5.2.3) is expected. The results for the negatively charged hadrons exhibit features similar to the positively charged hadrons, but the signal size is significantly lower.

The $\langle \mathbf{\cos 2\phi_h} \rangle$ moments are found to be slightly negative for positive hadrons. The high z region behaves differently, resulting in a larger signal, and, as before, this might be attributed to large vector meson contribution. The $\langle \mathbf{\cos 2\phi_h} \rangle$ moments for negative hadrons are slightly positive, resulting in a significative difference between signals of differently charged hadrons. This is not completely unexpected because several theoretical models predict different Boer-Mulders contributions for differently charged hadrons (as discussed below). This could be responsible for the shift between positive and negative hadrons results in the $\langle \mathbf{\cos \phi_h} \rangle$ moments. The measured $\langle \mathbf{\cos 2\phi_h} \rangle$ moments is in qualitatively agreement with the ZEUS results of figure 2.12. Indeed the ZEUS moments, extracted without separating positive and negative hadrons, might get a dominating contribution from the signal of the negative hadrons, which here is found to be larger than the signal of the positive particles.

Figures 7.9- 7.12 show the comparison between hydrogen and deuterium targets: no significant discrepancies can be attributed to different target gas type. This can

be explained by the u-dominance regime both in hydrogen and deuterium reactions. Indeed, even if in deuterium the number of up and down quark is the same, the up quark is still dominating the cross-section due to the e_q^2 factor in the hadronic tensor (section 2.3.1), since the up charge is twice the down one ($2/3e$ compared to $1/3e$).

7.2 Theoretical predictions and interpretations

The final azimuthal moments (figures from 7.1 to 7.8) extracted at HERMES can be compared to existing theoretical predictions of sections 2.4 and 2.5.

In order to interpret the results in terms of distribution and fragmentation functions, the expectations for $\langle \boldsymbol{\cos \phi_h} \rangle$ and $\langle \boldsymbol{\cos 2\phi_h} \rangle$ in HERMES kinematical region are calculated using the formalism described in section 2.3 [7], where distribution and fragmentation functions up to twist three are considered.

According to [9], the full kinematic of intrinsic κ_T is accounted for in the photon-quark elementary process and also in the quark distribution and fragmentation function. This introduces higher order kinematic corrections in the calculations, exactly computed in [9]. In particular, the full kinematic of intrinsic κ_T results in new kinematic variables x' and z', related to the standard x and z by

$$\begin{aligned} x' &= x + \mathcal{O}(\kappa_T^2/Q^2) \\ z' &= z + \mathcal{O}(\kappa_T^2/Q^2) \end{aligned} \tag{7.2}$$

Applying these corrections to the unpolarized cross-section of equation 2.40 and neglecting the quark-gluon-quark interactions, the cosine modulations can be associated with two contributions, the Cahn (sec. 2.5) and the Boer-Mulders (sec. 2.4) mechanisms.

The Cahn effect is a pure kinematical mechanism originated by the existence of quark intrinsic motion, and provides a twist-three contribution to $\cos\phi_h$ modulation and a twist-four contribution to $\cos 2\phi_h$ modulation. On the contrary, the Boer-Mulders mechanism, appears as leading twist term in the $\cos 2\phi_h$ moments, and as twist-three term in the $\cos\phi_h$ moments. In the following calculations, when not explicitly stated, the predictions are based on Gaussian ansatz (sec. 2.5) with average quark transverse momenta extracted by a fit to the world data [9]

$$\begin{aligned} \langle \kappa_T^2 \rangle &\sim 0.25\,\mathrm{GeV}^2/\mathrm{c}^2 \\ \langle p_T^2 \rangle &\sim 0.20\,\mathrm{GeV}^2/\mathrm{c}^2. \end{aligned} \tag{7.3}$$

These values have been extracted with a global fit from the existing data collected in different kinematical regions, involving data with combined production of all charged hadrons, thus is valid under the assumption of constant, flavour independent values in the whole kinematical region. For further details see section 2.5.1.

7.2.1 Cahn contributions

Considering only the pure kinematical terms, i.e. the Cahn effect (sec. 2.5), and taking into account all kinematical orders in (κ_T/Q) [9], the contributions to the

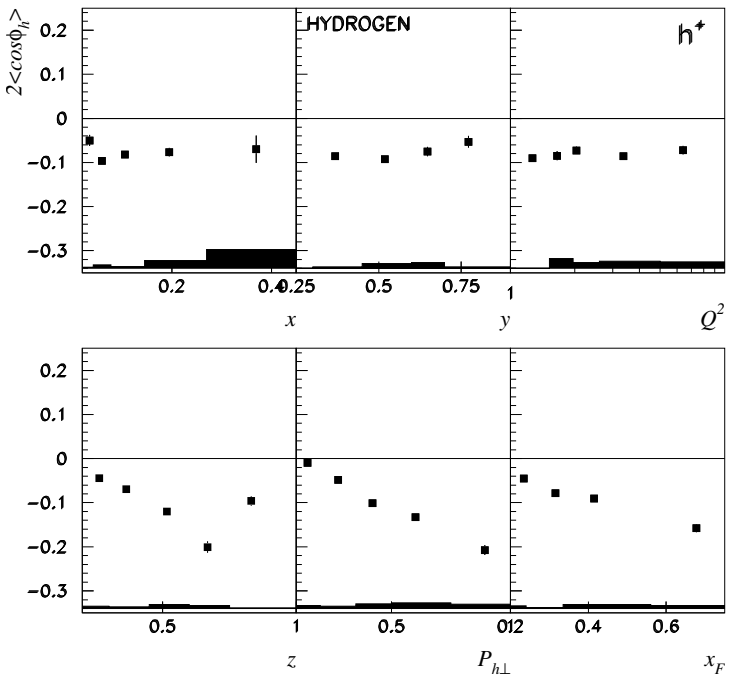

Figure 7.1: Final born $\langle \mathbf{cos}\, \boldsymbol{\phi_h} \rangle_{F_{UU}}$ born moments for positive hadrons from data collected with hydrogen target projected versus the kinematical variables x, y, z, $P_{h\perp}$, x_F and Q^2.

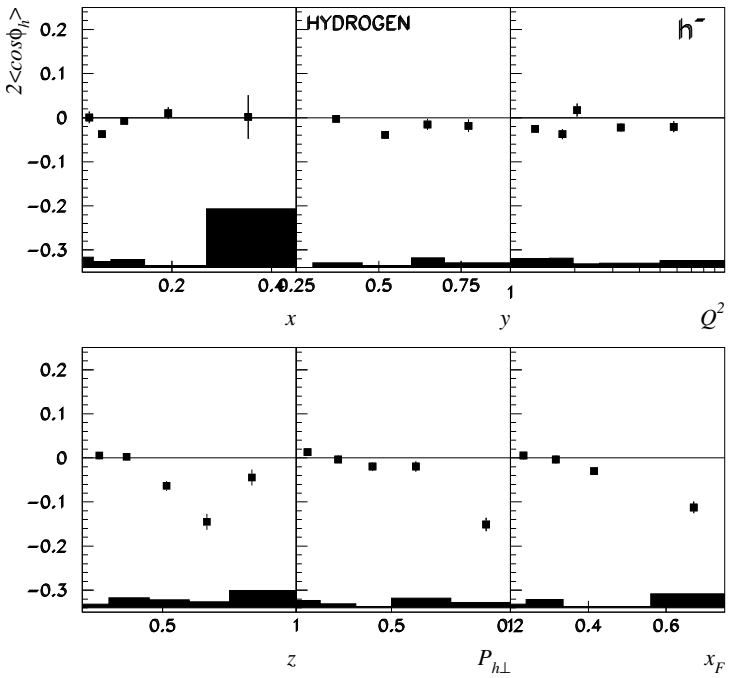

Figure 7.2: Final $\langle \mathbf{cos}\, \boldsymbol{\phi_h} \rangle_{F_{UU}}$ born moments for negative hadrons from data collected with hydrogen target projected versus the kinematical variables x, y, z, $P_{h\perp}$, x_F and Q^2.

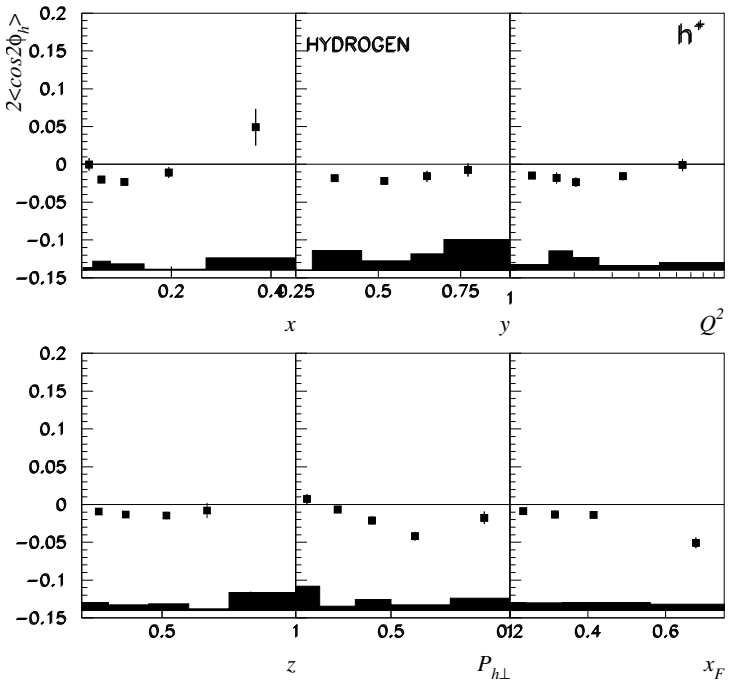

Figure 7.3: Final $\langle \mathbf{cos\,2}\phi_{\boldsymbol{h}} \rangle_{F_{UU}}$ born moments for positive hadrons from data collected with hydrogen target projected versus the kinematical variables x, y, z, $P_{h\perp}$, x_F and Q^2.

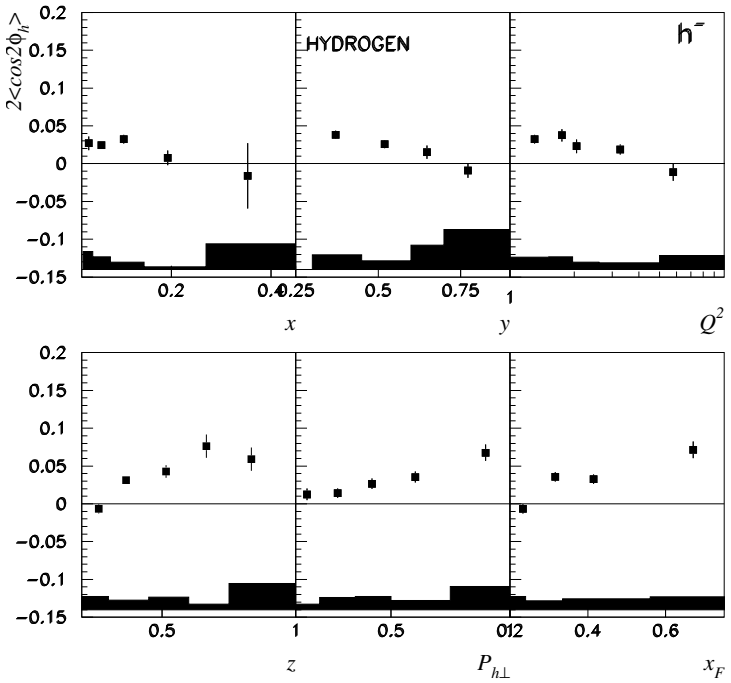

Figure 7.4: Final $\langle \mathbf{cos\,2}\phi_{\boldsymbol{h}} \rangle_{F_{UU}}$ born moments for negative hadrons from data collected with hydrogen target projected versus the kinematical variables x, y, z, $P_{h\perp}$, x_F and Q^2.

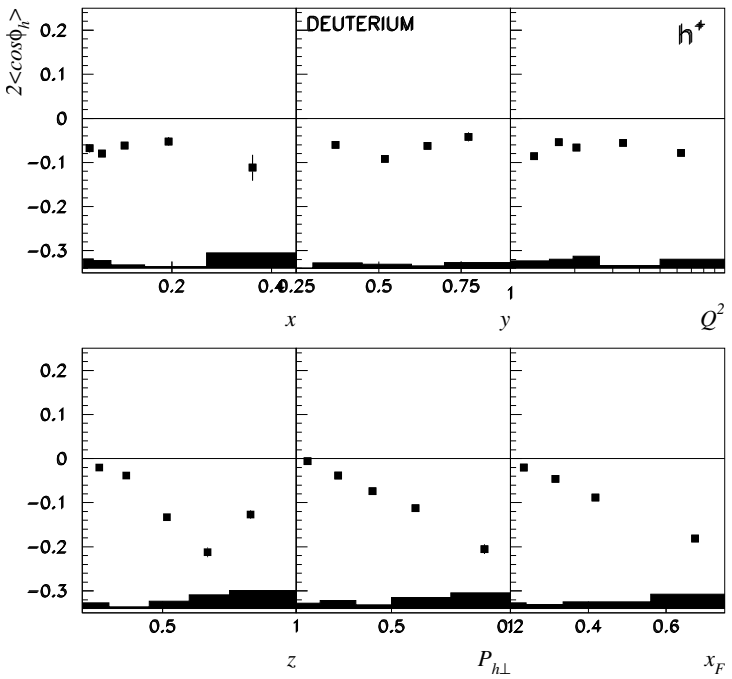

Figure 7.5: Final $\langle \mathbf{cos}\, \boldsymbol{\phi_h} \rangle_{F_{UU}}$ born moments for positive hadrons from data collected with deuterium target projected versus the kinematical variables x, y, z, $P_{h\perp}$, x_F and Q^2.

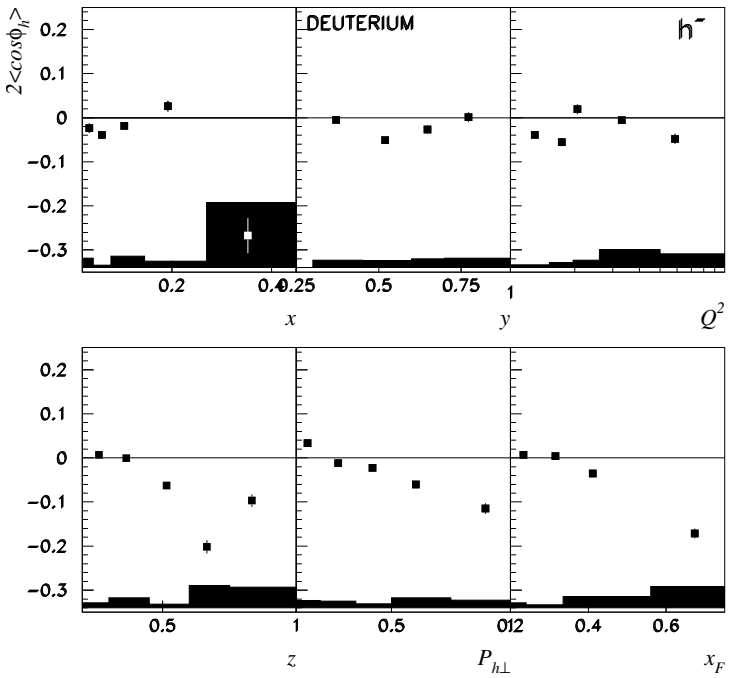

Figure 7.6: Final $\langle \mathbf{cos}\, \boldsymbol{\phi_h} \rangle_{F_{UU}}$ born moments for negative hadrons from data collected with deuterium target projected versus the kinematical variables x, y, z, $P_{h\perp}$, x_F and Q^2.

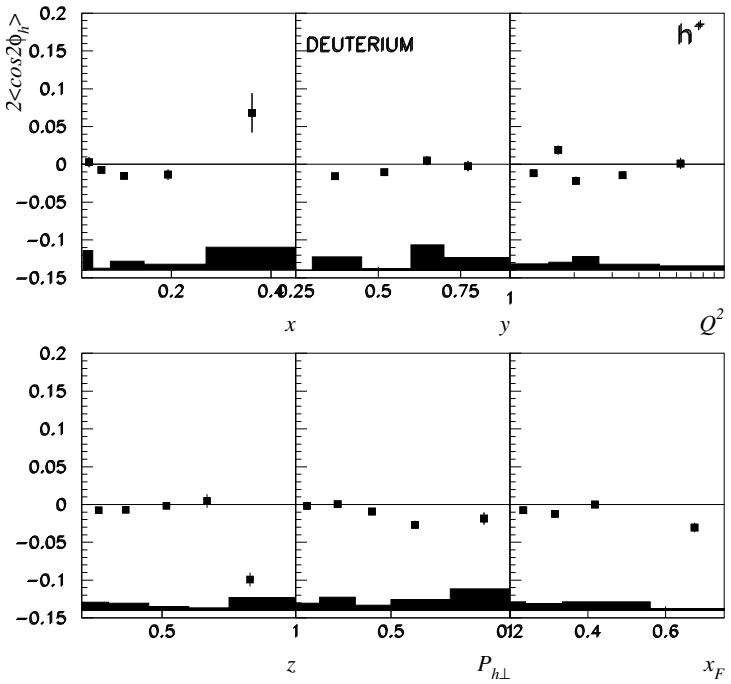

Figure 7.7: Final $\langle \mathbf{cos\,2}\phi_{\boldsymbol{h}} \rangle_{F_{UU}}$ born moments for positive hadrons from data collected with deuterium target projected versus the kinematical variables x, y, z, $P_{h\perp}$, x_F and Q^2.

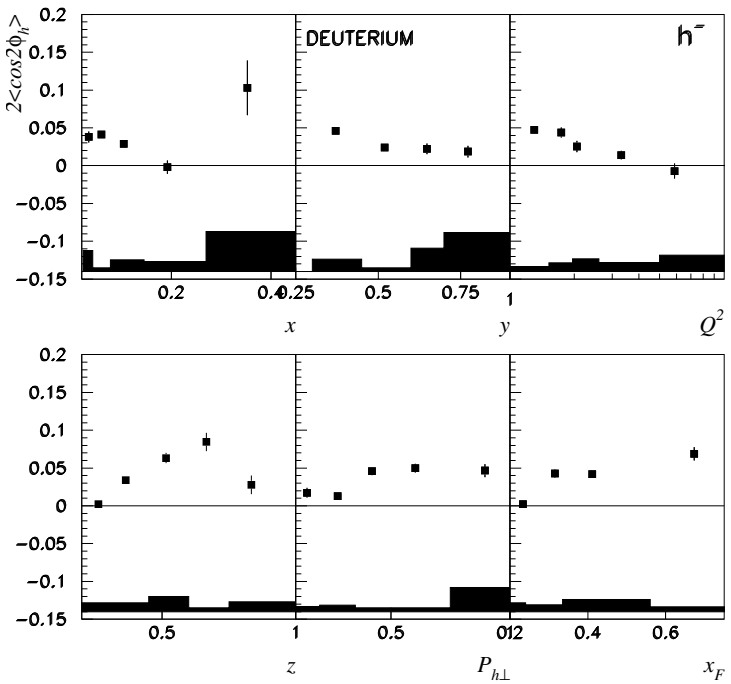

Figure 7.8: Final $\langle \mathbf{cos\,2}\phi_{\boldsymbol{h}} \rangle_{F_{UU}}$ born moments for negative hadrons from data collected with deuterium target projected versus the kinematical variables x, y, z, $P_{h\perp}$, x_F and Q^2.

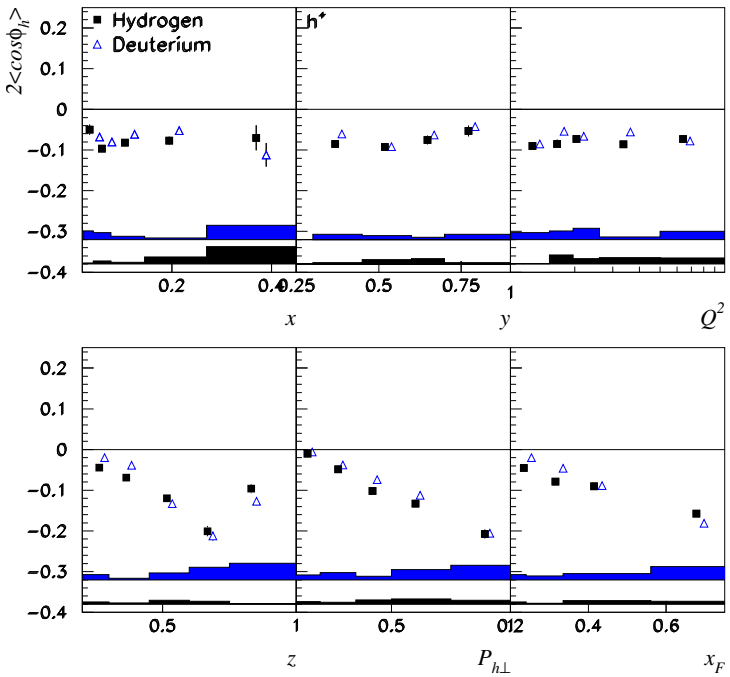

Figure 7.9: Final $\langle \cos \phi_h \rangle_{F_{UU}}$ born moments for positive hadrons from data collected with hydrogen (black closed square) and deuterium (blue opened triangles) targets projected versus the kinematical variables x, y, z, $P_{h\perp}$, x_F and Q^2.

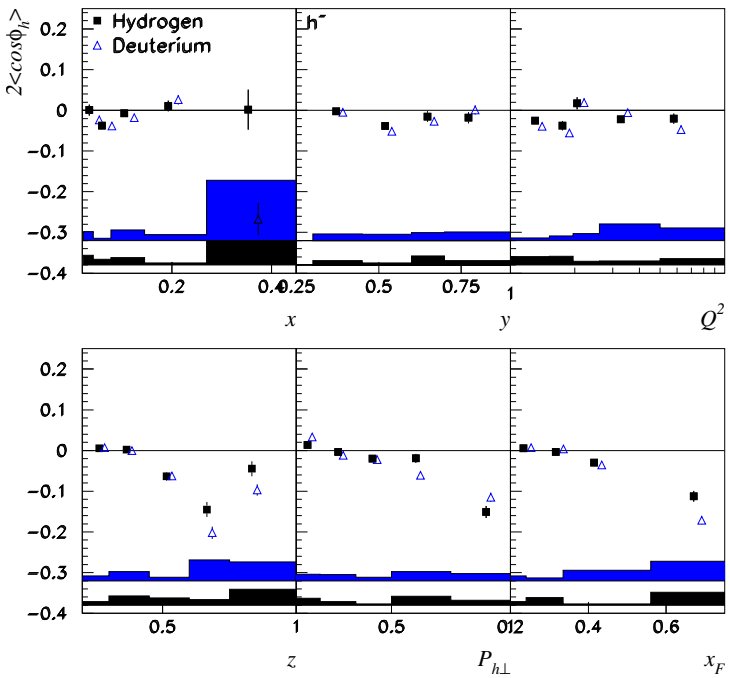

Figure 7.10: Final $\langle \cos \phi_h \rangle_{F_{UU}}$ born moments for negative hadrons from data collected with hydrogen (black closed square) and deuterium (blue opened triangles) targets projected versus the kinematical variables x, y, z, $P_{h\perp}$, x_F and Q^2.

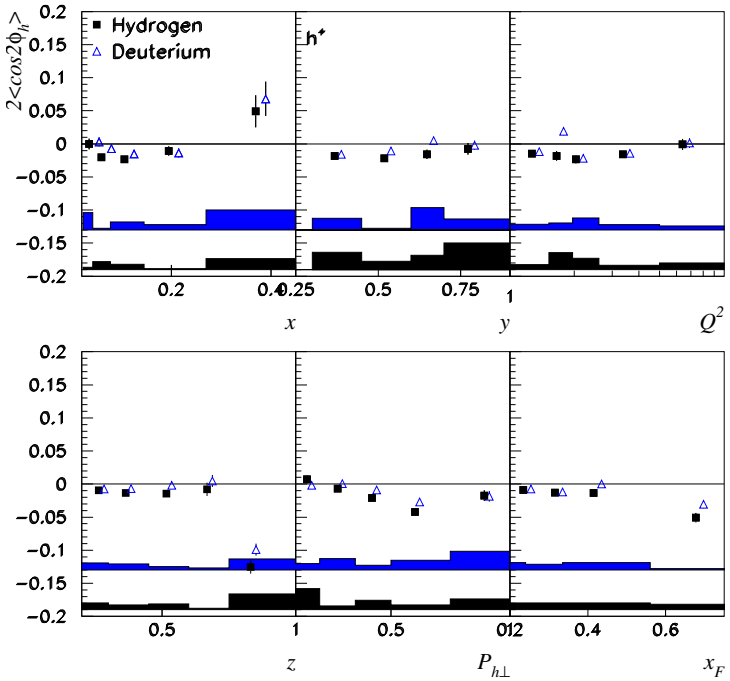

Figure 7.11: Final $\langle \mathbf{cos\,2\phi_h} \rangle_{F_{UU}}$ born moments for positive hadrons from data collected with hydrogen (black closed square) and deuterium (blue opened triangles) projected versus the kinematical variables x, y, z, $P_{h\perp}$, x_F and Q^2.

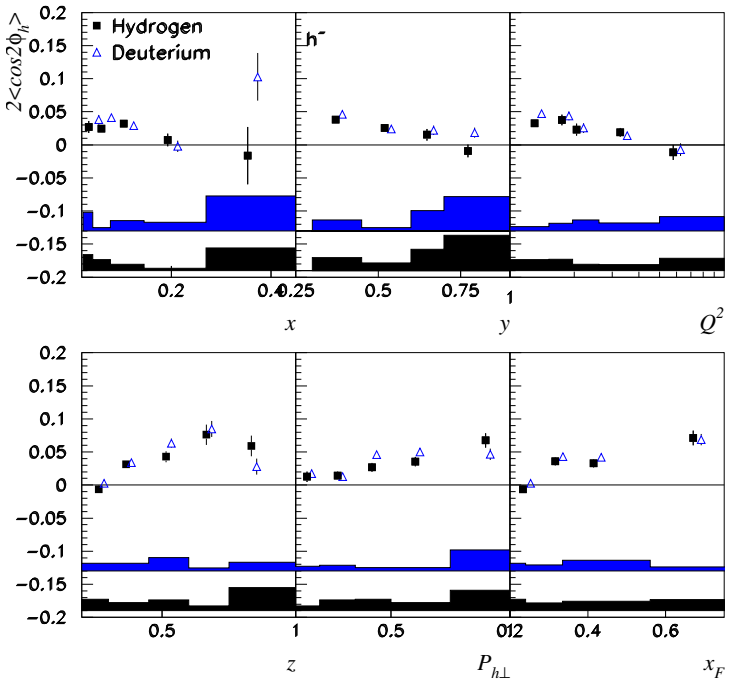

Figure 7.12: Final $\langle \mathbf{cos\,2\phi_h} \rangle_{F_{UU}}$ born moments for negative hadrons from data collected with hydrogen (black closed square) and deuterium (blue opened triangles) projected versus the kinematical variables x, y, z, $P_{h\perp}$, x_F and Q^2.

cross-section are

$$\begin{aligned} F_{UU,Cahn}^{\langle \cos \boldsymbol{\phi_h} \rangle} &\approx \frac{2M}{Q} C \Big[- \frac{\hat{h} \cdot \vec{\kappa}_T}{M} f_1(x', \kappa_T^2) D_1(z', p_T^2) \Big] \\ F_{UU,Cahn}^{\langle \cos \boldsymbol{2\phi_h} \rangle} &\approx \frac{M^2}{Q^2} C \Big[\frac{\kappa_T^2}{M^2} f_1(x', \kappa_T^2) D_1(z', p_T^2) \Big] \end{aligned} \tag{7.4}$$

where both $f_1(x', \kappa_T^2)$ and $D_1(z', p_T^2)$ are well known experimentally.

The predictions for $\langle \cos \boldsymbol{\phi_h} \rangle$ and $\langle \cos \boldsymbol{2\phi_h} \rangle$ moments at HERMES regime with an hydrogen target, extracted with the above assumptions, are presented in figures 7.13 and 7.14 compared to HERMES results. The model predicts sizable negative signals for the $\langle \cos \boldsymbol{\phi_h} \rangle$ modulations, and small positive signals for $\langle \cos \boldsymbol{2\phi_h} \rangle$ moments. The shadowed areas in figures correspond to a variation of 20% of the averaged transverse momenta $\langle \kappa_T^2 \rangle$ and $\langle p_T^2 \rangle$.

The comparison with the measurements shows that the size of the predicted Cahn contribution is much larger than the measured $\langle \cos \boldsymbol{\phi_h} \rangle$, meaning that the Cahn effect, alone, can not describe data. It is worth to notice that the predicted $\langle \cos \boldsymbol{\phi_h} \rangle$ Cahn moments would be even more sizable if the κ_T kinematics is not fully taken into account, but only leading κ_T/Q terms are considered. Moreover, contrary to HERMES data, the expectations for Cahn effect show no significative differences between positively (shadowed areas) and negatively (white areas) charged hadrons neither in the $\langle \cos \boldsymbol{\phi_h} \rangle$ nor in the $\langle \cos \boldsymbol{2\phi_h} \rangle$ moments.

As regards the $\cos 2\phi_h$ modulation, the Cahn effect does not reproduced data, but provides non-negligible contribution, indicating that higher order terms could give sizable signals, at least in the HERMES kinematical regime, where the Q^2 is only relatively high: $\langle Q^2 \rangle \sim 2-3$ GeV^2.

The parameters in equations 7.3 are extracted from few existing experimental data sets (see section 2.5.1) in kinematical regions very different from the HERMES one. In order to improve the predictions, a new set of parameters (the *HERMES set*) for the averaged transverse momenta is used. The HERMES set is extracted directly from HERMES data, and introduces a z dependence in fragmentation generated by transverse momentum:

$$\begin{aligned} \langle \kappa_T^2 \rangle &\sim 0.18\,\mathrm{GeV}^2/\mathrm{c}^2 \\ \langle p_T^2 \rangle &\sim 0.42 \cdot (1-z)^{0.54} \cdot z^{0.37}\,\mathrm{GeV}^2/\mathrm{c}^2 \end{aligned} \tag{7.5}$$

The cosine modulations calculated using these parameters are shown in figures 7.15 and 7.16: the predictions for the $\langle \cos \boldsymbol{\phi_h} \rangle$ moments become closer to the measured moments, but still the Cahn effect alone does not reproduce the data.

7.2.2 Boer-Mulders contributions

From the previous discussion, it is clear that the pure kinematical terms, related to the Cahn effect, are not able to describe the measured moments, therefore also

dynamical contributions should be considered. If the Boer-Mulders mechanism is taken into account, the contributions

$$\begin{aligned} F_{UU,BM}^{\cos 2\phi_h,BM} &\approx -C\Big[\frac{2(\hat{h}\cdot\vec{p}_T)(\hat{h}\cdot\vec{\kappa}_T) \;-\; \vec{p}_T\cdot\vec{\kappa}_T}{MM_h}\, h_1^{\perp}(x',\kappa_T^2)H_1^{\perp}(z',p_T^2)\Big] \\ F_{UU,BM}^{\cos\phi_h} &\approx \frac{2M}{Q}C\Big[-\frac{\hat{h}\cdot\vec{p}_T}{M_h}h_1^{\perp}(x',\kappa_T^2)H_1^{\perp}(z',p_T^2)\Big] \end{aligned} \tag{7.6}$$

have to be considered in the cross-section, where $h_1^{\perp}(x',\kappa_T^2)$ is the Boer-Mulders distribution function, and $H_1^{\perp}(z',p_T^2)$ is the Collins fragmentation function (sec. 2.4). The function $H_1^{\perp}$ has been recently extracted [43] by fitting $e^+e^- \to h^+h^-X$ data measured by the Belle Collaboration at KEK [44], while the Boer-Mulders function is completely unknown, thus a model is needed to implement this function in the calculations. The Boer-Mulders distribution function is expected to be proportional to the Sivers function [17] $f_{1T}^{\perp}$ (see sec. 2.4), rescaled by the ratio of transverse to standard magnetic moments, extracted from lattice calculations [33]:

$$h_1^{\perp,q} \approx (\kappa_T^q \diagup \kappa^q) f_{1T}^{\perp,q}. \tag{7.7}$$

where q stands for the quark flavour. Therefore the Boer-Mulders mechanism is implemented in the calculation using the parameterization for the Sivers distribution and the Collins fragmentation functions provided by [93, 43], and the HERMES set for the quark transverse momenta.

The resulting cosine moments are shown in figures 7.17 and 7.18, where the shadowed areas correspond to the variation of 20% of averaged intrinsic transverse momenta, added up to the uncertainties in Sivers and Collins function parameterizations, as provided by [43, 93].

The measured $\cos 2\phi_h$ modulation is in qualitative agreement with the predicted Boer-Mulders effect, validating the connection of the Boer-Mulders distribution function with the Sivers function. In particular, data support Boer-Mulders effect with opposite sign for positively and negatively charged hadrons. Here the larger contribution to the model uncertainties is given by the Sivers and the Collins functions parameterizations, while the variation of the transverse momenta affects the prediction only slightly.

The Boer-Mulders contribution to $\langle \boldsymbol{\cos\phi_h} \rangle$ moments generates a distinction between differently charged hadrons, which is compatible with the differences present in the data. Anyway the global size of the predicted $\langle \boldsymbol{\cos\phi_h} \rangle$ moments generated by the sum of Cahn and Boer-Mulders contributions, is still not compatible to the measurements. This is not completely unexpected, because in the above calculation the twist-three quark-gluon-quark contributions are neglected, as well as all higher order terms.

If higher order terms are not negligible at HERMES kinematics, they could provide sizable effects, as suggested by the calculated non-negligible Cahn twist-four contribution to the $\langle \boldsymbol{\cos 2\phi_h} \rangle$ moment. Indeed in the high Q^2 region, where the higher twist terms should become smaller, the measured results seem to approach the model predictions, confirming that the discrepancies between measurements and

calculations at lower Q^2 can be attributed to higher order corrections missing in the model. Although the Boer-Mulders effect is a leading twist contribution, at high Q^2 the signal and the difference between hadron charges seem to reduce. This can be explained considering that x and Q^2 are highly correlated at HERMES, and high Q^2 corresponds to x higher than the valence, a kinematical region where parton distribution function rapidly vanish.

7.2.3 Predictions from diquark models

Figures 7.19 and 7.20 propose again the predictions for the $\langle \mathbf{cos\,2\phi_h} \rangle$ moments at HERMES kinematical regime (see sec. 2.4), calculated within two different diquark spectator models [42, 40]. Both the models lead to signal of few percent, but with different relative sign between positive and negative hadrons. The comparison with measured $\langle \mathbf{cos\,2\phi_h} \rangle$ moments seems to be in qualitative agreement with the predictions of the model in [42].

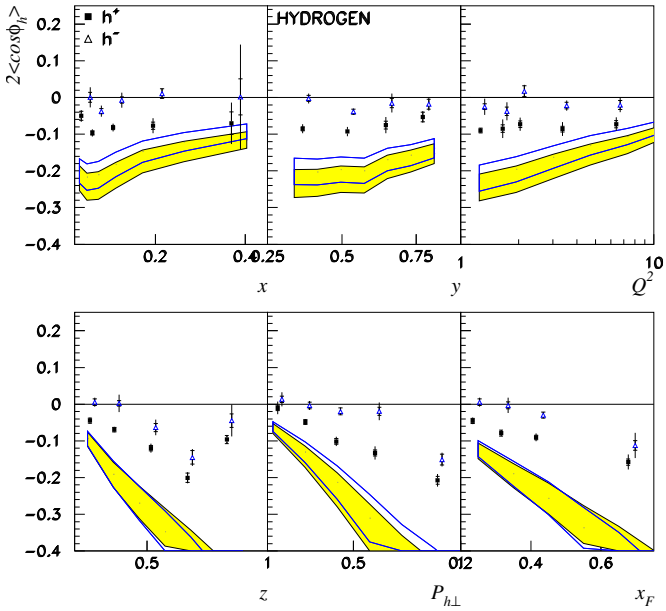

Figure 7.13: Comparison between measured $\langle \cos \phi_h \rangle$ moments and the predictions based on the Cahn effect, for positive (solid squares and shadowed areas) and negative (open triangles and white areas) hadrons. The areas defined by the predictions correspond to a variation of 20% f the averaged transverse momenta $\langle \kappa_T^2 \rangle$ and $\langle p_T^2 \rangle$. The uncertainties of data results comprehend statistical and systematic errors added in quadrature.

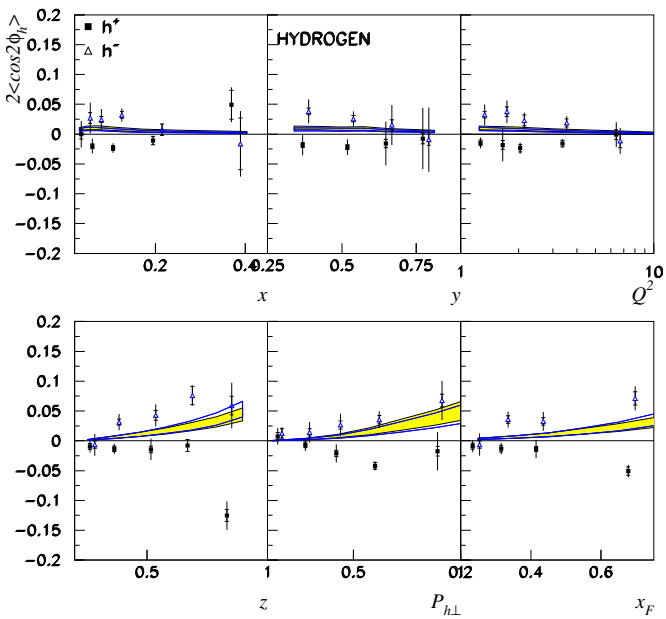

Figure 7.14: Comparison between measured $\langle \cos 2\phi_h \rangle$ moments and the predictions based on the Cahn effect, for positive (solid squares and shadowed areas) and negative (open triangles and white areas) hadrons. The areas defined by the predictions correspond to a variation of 20% of the averaged transverse momenta $\langle \kappa_T^2 \rangle$ and $\langle p_T^2 \rangle$. The uncertainties of data results comprehend statistical and systematic errors added in quadrature.

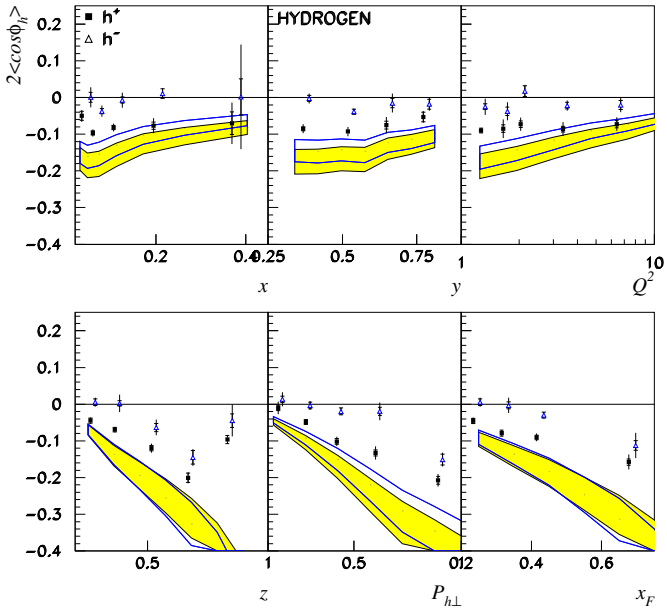

Figure 7.15: Comparison between measured $\langle \cos \phi_h \rangle$ moments and the predictions based on the Cahn effect, for positive (solid squares and shadowed areas) and negative (open triangles and white areas) hadrons. The HERMES set is used here for the parameters $\langle \kappa_T^2 \rangle$ and $\langle p_T^2 \rangle$. A variation of 20% in the latter parameters define the areas of uncertainties. The uncertainties of data results comprehend statistical and systematic errors added in quadrature.

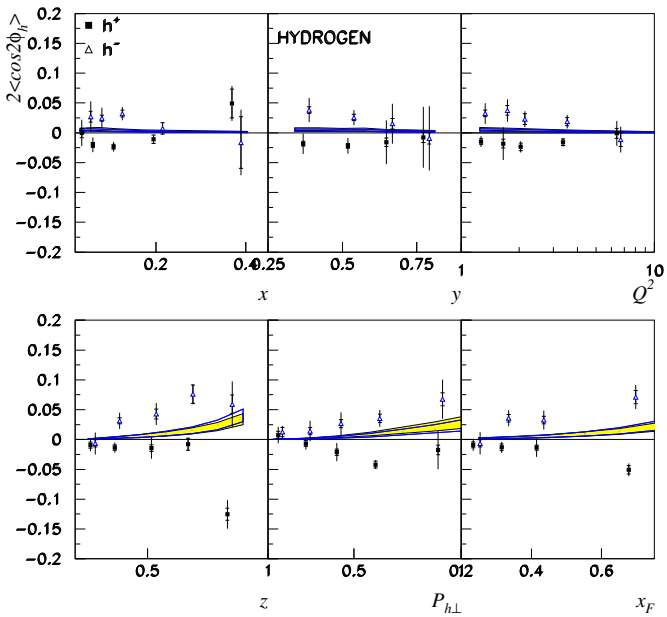

Figure 7.16: Comparison between measured $\langle \cos 2\phi_h \rangle$ moments and the predictions based on the Cahn effect, for positive (solid squares and shadowed areas) and negative (open triangles and white areas) hadrons. The HERMES set is used here for the parameters $\langle \kappa_T^2 \rangle$ and $\langle p_T^2 \rangle$. A variation of 20% in the latter parameters define the areas of uncertainties. The uncertainties of data results comprehend statistical and systematic errors added in quadrature.

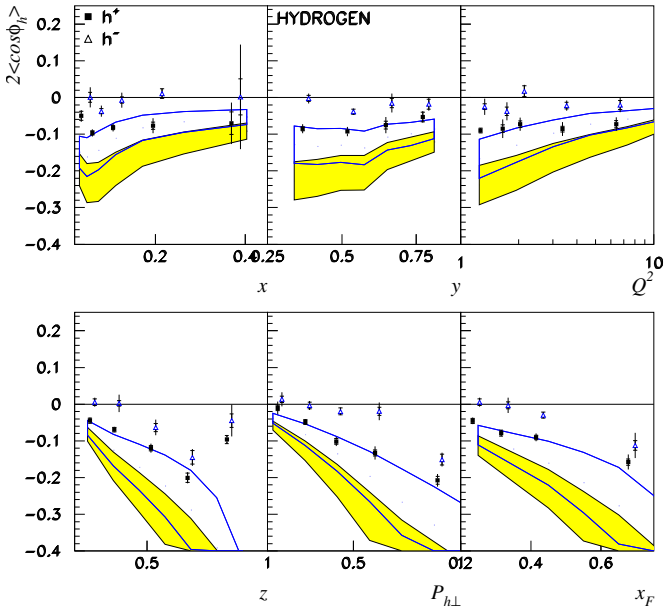

Figure 7.17: Comparison between measured $\langle \cos \phi_h \rangle$ moments and the predictions based on the Cahn plus Boer-Mulders effects. The HERMES set is used here for the parameters $\langle \kappa_T^2 \rangle$ and $\langle p_T^2 \rangle$. The areas defined by the predictions correspond to a variation of 20% of the averaged transverse momenta $\langle \kappa_T^2 \rangle$ and $\langle p_T^2 \rangle$, together with the uncertainties in extraction of distribution and fragmentation function [93, 43]. For the symbol definitions see figure 7.15.

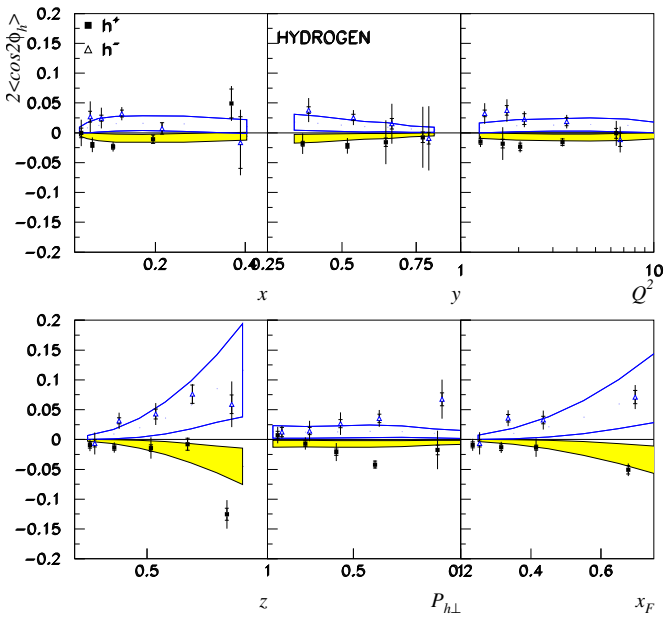

Figure 7.18: Comparison between measured $\langle \cos 2\phi_h \rangle$ moments and the predictions based on the Cahn plus Boer-Mulders effects. The HERMES set is used here for the parameters $\langle \kappa_T^2 \rangle$ and $\langle p_T^2 \rangle$. The areas defined by the predictions correspond to a variation of 20% of the averaged transverse momenta $\langle \kappa_T^2 \rangle$ and $\langle p_T^2 \rangle$, together with the uncertainties in extraction of distribution and fragmentation function [93, 43]. For the symbol definitions see figure 7.15 and 7.17.

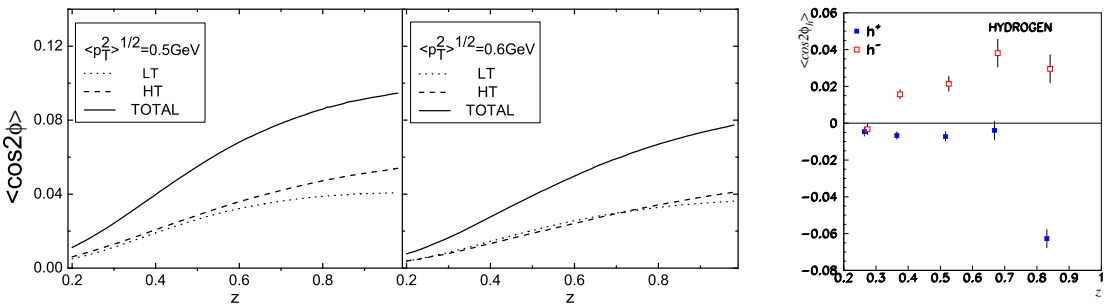

Figure 7.19: $\langle \cos 2\phi_h \rangle$ azimuthal moments. Right: moments predicted in [40] for positive pion production at the HERMES experiments; the negative hadrons should exhibit similar behaviors. The dotted and the dashed curves indicate respectively the leading and Next-To-Leading twist calculation. The solid line is the sum of the above two contributions. Left: measured moments for positive (solid squares) and negative (open squares) hadrons. The scale size is the same in the two figures.

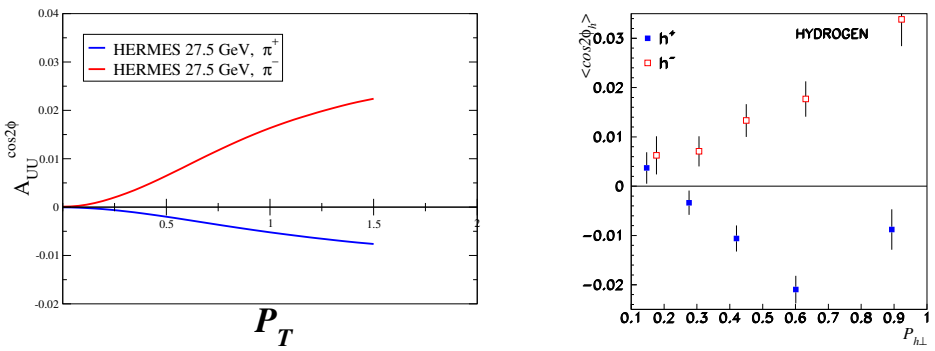

Figure 7.20: $\langle \cos 2\phi_h \rangle$ moments for positive and negative hadrons. Right: moments predicted in [42] within the HERMES kinematical region. Left: measured moments for positive (solid squares) and negative (open squares) hadrons. The scale size is the same in the two figures.

Chapter 8

Summary and conclusions

The description of quark intrinsic transverse motion and spin dynamics represents an important missing piece for a complete understanding of the internal nucleon structure. Despite the intense theoretical effort performed in order to achieve a comprehension on this subject as detailed as possible, only few experimental investigations of this field are presently available.

The theoretical framework of collinear Semi Inclusive Deep Inelastic Scattering has been described. Then a non-zero intrinsic transverse motion of quarks was introduced in the theoretical model, resulting in cosine azimuthal modulations in the hadron production directions. Depending on the experimental kinematical region, several contributions can originate the cosine moments, and they have been described in some extent. In particular two mechanisms have been considered: Cahn and Boer-Mulders effects. A pure kinematical effect, the Cahn effect, is generated if a non-zero intrinsic transverse motion of quarks is taken into account [5], and provides a twist-three contribution to $\cos\phi_h$ modulation and a twist-four contribution to $\cos 2\phi_h$ modulation. The coupling of quark transverse momentum and spin (spin-orbit correlations), gives rise to leading non-trivial mechanisms which are T-odd, like the Boer-Mulders effect, that is expected to appear as leading twist term in the $\cos 2\phi_h$ moments, and as twist-three term in the $\cos\phi_h$ moments. An overview has been provided of the theoretical model predictions and the scarce existing experimental measurements.

The azimuthal modulations of hadron production has been measured in Semi Inclusive Deep Inelastic Scattering processes at HERMES, and the results, compatible between different data taking periods, have been presented. Several systematic checks were performed in order to estimate possible biases, and finally the results are corrected for acceptance and QED higher order contributions. The corrected cosine moments are provided in 500 independent kinematical bins providing for the first time a full differential description of the cross-section azimuthal dependent terms. Their projections in the relevant kinematical variables have been presented for comparison with expections. The results extracted for hydrogen and deuterium data do not show significative discrepancies, and this can be explained taking into account the u-dominance hypothesis in deep inelastic scattering.

The extraction of the $\langle \mathbf{cos}\,\boldsymbol{\phi_h} \rangle$ and $\langle \mathbf{cos}\,\mathbf{2}\boldsymbol{\phi_h} \rangle$ azimuthal moments at HERMES shown in this work distinguishes, for the first time, between positive and negative hadrons, resulting in a flavour dependent measurement. Thanks to this flavour sensitivity of the final results, the discrimination power between the theoretical models in the HERMES kinematical regime is enhanced. Thus the measurements have been compared with the existing theoretical model and have been interpreted in terms of *Cahn* and *Boer-Mulders* effects.

A non-zero $\langle \mathbf{cos}\,\mathbf{2}\boldsymbol{\phi_h} \rangle$ signal is found, confirming the existence of a leading T-odd effect[1]. The prediction for the Boer-Mulders mechanism is found to be qualitatively compatible with data, supporting the relationship between Boer-Mulders and Sivers functions. The Boer-Mulders effect could be responsible for the sizable differences observed between differently charged hadrons in $\langle \mathbf{cos}\,\boldsymbol{\phi_h} \rangle$ cross-section modulations, which has never been measured so far.

A significative $\langle \mathbf{cos}\,\boldsymbol{\phi_h} \rangle$ signal is extracted from data with a kinematical dependence in qualitative agreement with expectations. However, the theoretical expectation for the Cahn effect, which is expected to be the largest contribution in the $\langle \mathbf{cos}\,\boldsymbol{\phi_h} \rangle$ moments, is not able to reproduce measurements. This can be explained if the higher order contributions to $\cos\phi_h$ modulation, missing in the calculations, are non-negligible at HERMES energies.

[1]The first leading T-odd effect observed is the Sivers mechanism [17], measured at HERMES [18]

Appendix A

Results in 5-dimensional binning

Hydrogen results							
$\langle x \rangle$	$\langle y \rangle$	$\langle Q^2 \rangle$	$\langle z \rangle$	$\langle P_{h\perp} \rangle$	$\langle x_F \rangle$	$2\langle \mathbf{cos}\, \boldsymbol{\phi_h} \rangle$	$2\langle \mathbf{cos}\, \mathbf{2}\boldsymbol{\phi_h} \rangle$
0.0385	0.5479	1.0908	0.2525	0.1444	0.2386	0.0633 ± 0.0828	0.1050 ± 0.0461
0.0385	0.5485	1.0934	0.2584	0.2741	0.2365	-0.0038 ± 0.0350	0.0030 ± 0.0225
0.0386	0.5495	1.0957	0.2671	0.4167	0.2314	0.0549 ± 0.0175	0.0992 ± 0.0171
0.0383	0.5522	1.0936	0.2800	0.5808	0.2234	0.1017 ± 0.0303	-0.2052 ± 0.0530
0.0386	0.5466	1.0917	0.3559	0.1580	0.3400	-0.0845 ± 0.1007	-0.1474 ± 0.0566
0.0386	0.5479	1.0940	0.3637	0.2774	0.3423	-0.2225 ± 0.0629	-0.0123 ± 0.0361
0.0385	0.5489	1.0943	0.3635	0.4207	0.3317	-0.1881 ± 0.0282	-0.0902 ± 0.0207
0.0385	0.5477	1.0917	0.3652	0.6053	0.3137	-0.0887 ± 0.0165	-0.0480 ± 0.0165
0.0383	0.5508	1.0923	0.3726	0.8801	0.2805	-0.0490 ± 0.0446	-0.1581 ± 0.0363
0.0385	0.5468	1.0882	0.5169	0.2787	0.4936	-0.1645 ± 0.0997	0.1229 ± 0.0567
0.0385	0.5485	1.0934	0.5148	0.4209	0.4843	0.1128 ± 0.0981	0.1750 ± 0.1026
0.0387	0.5450	1.0901	0.5159	0.6041	0.4714	-0.2875 ± 0.0457	-0.1214 ± 0.0354
0.0387	0.5486	1.0975	0.5167	0.9126	0.4381	-0.2037 ± 0.0508	-0.0422 ± 0.0494
0.0385	0.5453	1.0860	0.6647	0.2813	0.6382	-0.5646 ± 0.1406	-0.0605 ± 0.0833
0.0387	0.5446	1.0889	0.6651	0.4202	0.6330	-0.2139 ± 0.1625	0.1195 ± 0.0969
0.0387	0.5475	1.0951	0.6682	0.6048	0.6255	-0.0162 ± 0.1763	0.1831 ± 0.1021
0.0385	0.5475	1.0900	0.6643	0.9092	0.5954	-0.2423 ± 0.0946	-0.2996 ± 0.0987
0.0387	0.5470	1.0948	0.8412	0.4240	0.8059	-0.3104 ± 0.2162	-0.2476 ± 0.1221
0.0385	0.5468	1.0883	0.8344	0.5924	0.7915	-0.2688 ± 0.2541	-0.2329 ± 0.1461
0.0384	0.5507	1.0940	0.8303	0.9086	0.7662	-0.2852 ± 0.6023	-0.4894 ± 0.3789
0.0355	0.6513	1.1943	0.2499	0.1507	0.2380	0.1606 ± 0.1233	0.0633 ± 0.0549
0.0353	0.6519	1.1911	0.2559	0.2740	0.2375	0.1015 ± 0.0279	0.0283 ± 0.0173
0.0352	0.6516	1.1874	0.2645	0.4176	0.2344	-0.0805 ± 0.0115	0.0172 ± 0.0117
0.0351	0.6531	1.1871	0.2753	0.5857	0.2266	-0.0453 ± 0.0156	-0.0379 ± 0.0155

Hydrogen results							
$\langle x \rangle$	$\langle y \rangle$	$\langle Q^2 \rangle$	$\langle z \rangle$	$\langle P_{h\perp} \rangle$	$\langle x_F \rangle$	$2\langle \cos \phi_h \rangle$	$2\langle \cos 2\phi_h \rangle$
0.0348	0.6601	1.1870	0.2904	0.8003	0.2118	0.9789 ± 0.0728	-0.4697 ± 0.0638
0.0354	0.6489	1.1865	0.3565	0.1667	0.3428	-0.0270 ± 0.2090	0.0201 ± 0.0896
0.0354	0.6514	1.1925	0.3658	0.2782	0.3478	-0.1272 ± 0.0674	-0.0756 ± 0.0345
0.0353	0.6518	1.1899	0.3643	0.4226	0.3375	-0.0765 ± 0.0240	0.0202 ± 0.0171
0.0353	0.6512	1.1898	0.3630	0.6082	0.3196	-0.1269 ± 0.0114	0.0039 ± 0.0117
0.0352	0.6530	1.1892	0.3678	0.8965	0.2875	-0.1527 ± 0.0221	0.0462 ± 0.0195
0.0359	0.6389	1.1854	0.4863	0.1853	0.4697	1.1670 ± 1.2964	0.3949 ± 0.4999
0.0354	0.6500	1.1889	0.5163	0.4207	0.4906	-0.2237 ± 0.1032	-0.0175 ± 0.1053
0.0352	0.6516	1.1853	0.5137	0.6077	0.4763	-0.2224 ± 0.0386	-0.0538 ± 0.0286
0.0351	0.6498	1.1807	0.5176	0.9232	0.4506	-0.3217 ± 0.0336	0.0179 ± 0.0338
0.0354	0.6496	1.1901	0.6671	0.4238	0.6400	-0.0657 ± 0.2179	0.1572 ± 0.1026
0.0353	0.6489	1.1861	0.6623	0.6012	0.6266	-0.0193 ± 0.1577	0.0280 ± 0.0882
0.0352	0.6506	1.1847	0.6644	0.9120	0.6065	-0.1460 ± 0.0924	-0.1146 ± 0.0903
0.0353	0.6496	1.1847	0.8420	0.4212	0.8124	0.9433 ± 0.4186	0.3928 ± 0.1800
0.0352	0.6538	1.1910	0.8290	0.6006	0.7929	-0.9571 ± 0.3297	-0.6496 ± 0.1617
0.0354	0.6508	1.1925	0.8358	0.8926	0.7829	-0.3337 ± 0.4256	-0.1376 ± 0.2968
0.0322	0.7763	1.2946	0.2541	0.2755	0.2386	-0.1756 ± 0.0186	-0.0063 ± 0.0120
0.0325	0.7758	1.3040	0.2614	0.4187	0.2360	-0.0201 ± 0.0073	-0.0557 ± 0.0074
0.0325	0.7786	1.3098	0.2713	0.5943	0.2292	-0.0042 ± 0.0085	0.0111 ± 0.0150
0.0315	0.7829	1.2767	0.2858	0.8288	0.2150	-0.2563 ± 0.0286	0.1919 ± 0.0257
0.0326	0.7663	1.2927	0.3473	0.1739	0.3357	0.7648 ± 0.5540	0.3166 ± 0.2021
0.0323	0.7747	1.2927	0.3637	0.2775	0.3487	-0.1262 ± 0.0879	0.0232 ± 0.0380
0.0323	0.7745	1.2920	0.3656	0.4215	0.3433	-0.1411 ± 0.0176	-0.0330 ± 0.0122
0.0325	0.7749	1.3037	0.3639	0.6071	0.3277	-0.0180 ± 0.0075	-0.0228 ± 0.0076
0.0323	0.7760	1.2978	0.3676	0.9034	0.2995	-0.1694 ± 0.0115	0.0202 ± 0.0111
0.0324	0.7708	1.2918	0.5100	0.2886	0.4933	0.5090 ± 0.3001	0.1892 ± 0.1160
0.0322	0.7744	1.2907	0.5148	0.4214	0.4933	0.3348 ± 0.1449	0.2144 ± 0.0630
0.0326	0.7734	1.3023	0.5150	0.6066	0.4837	-0.1226 ± 0.0312	-0.0435 ± 0.0220
0.0321	0.7755	1.2883	0.5119	0.9182	0.4562	-0.0994 ± 0.0230	0.0142 ± 0.0237
0.0330	0.7656	1.3050	0.6558	0.3131	0.6363	-0.6015 ± 1.2590	-0.3286 ± 0.4306
0.0324	0.7726	1.2962	0.6634	0.4217	0.6408	0.3450 ± 0.3693	0.1952 ± 0.1506
0.0322	0.7743	1.2892	0.6647	0.6057	0.6346	-0.5848 ± 0.1690	-0.2533 ± 0.0829
0.0325	0.7726	1.2969	0.6636	0.9113	0.6150	-0.0772 ± 0.0758	-0.0305 ± 0.0670
0.0322	0.7728	1.2860	0.8252	0.4286	0.8003	-0.5229 ± 0.8950	0.2402 ± 0.3472
0.0323	0.7758	1.2969	0.8321	0.6016	0.8016	-0.6157 ± 0.6189	0.0089 ± 0.4207
0.0327	0.7734	1.3072	0.8231	0.8904	0.7787	-0.4128 ± 0.2787	-0.3518 ± 0.2074
0.0632	0.3794	1.2405	0.2577	0.1378	0.2375	-0.0129 ± 0.0082	-0.0154 ± 0.0077
0.0629	0.3822	1.2442	0.2661	0.2722	0.2343	-0.0422 ± 0.0135	-0.0712 ± 0.0118
0.0626	0.3868	1.2527	0.2772	0.4124	0.2267	-0.0928 ± 0.0262	0.0279 ± 0.0187
0.0609	0.4012	1.2640	0.2883	0.5519	0.2155	-0.4357 ± 0.1732	0.0091 ± 0.1424
0.0636	0.3751	1.2341	0.3614	0.1462	0.3383	0.0478 ± 0.0087	0.0652 ± 0.0084
0.0634	0.3771	1.2371	0.3633	0.2773	0.3316	-0.1039 ± 0.0099	-0.0167 ± 0.0085

Hydrogen results							
$\langle x \rangle$	$\langle y \rangle$	$\langle Q^2 \rangle$	$\langle z \rangle$	$\langle P_{h\perp} \rangle$	$\langle x_F \rangle$	$2\langle \cos \boldsymbol{\phi_h} \rangle$	$2\langle \cos \mathbf{2}\boldsymbol{\phi_h} \rangle$
0.0634	0.3780	1.2394	0.3653	0.4212	0.3179	-0.1218 ± 0.0113	-0.0454 ± 0.0098
0.0631	0.3799	1.2402	0.3689	0.5991	0.2938	-0.1366 ± 0.0196	0.0562 ± 0.0129
0.0624	0.3877	1.2504	0.3914	0.8540	0.2671	-0.6521 ± 0.1929	0.2050 ± 0.0817
0.0638	0.3725	1.2299	0.5129	0.1571	0.4842	0.0017 ± 0.0118	-0.0602 ± 0.0122
0.0632	0.3777	1.2354	0.5167	0.2779	0.4825	-0.0469 ± 0.0106	0.0609 ± 0.0097
0.0634	0.3781	1.2393	0.5176	0.4223	0.4722	-0.0742 ± 0.0178	0.0403 ± 0.0154
0.0633	0.3782	1.2390	0.5174	0.6032	0.4516	-0.1383 ± 0.0187	-0.0545 ± 0.0165
0.0627	0.3801	1.2327	0.5174	0.9016	0.4025	-0.4158 ± 0.0739	0.0823 ± 0.0423
0.0646	0.3640	1.2159	0.6649	0.1688	0.6291	-0.1866 ± 0.0220	0.0594 ± 0.0217
0.0636	0.3760	1.2372	0.6673	0.2794	0.6283	-0.1631 ± 0.0124	0.0798 ± 0.0120
0.0636	0.3757	1.2367	0.6691	0.4227	0.6214	-0.2696 ± 0.0201	0.0320 ± 0.0178
0.0636	0.3756	1.2364	0.6689	0.6043	0.6052	-0.2784 ± 0.0311	-0.0693 ± 0.0543
0.0636	0.3742	1.2312	0.6669	0.8975	0.5648	-0.3615 ± 0.0675	-0.2227 ± 0.0501
0.0659	0.3505	1.1939	0.8204	0.1803	0.7762	-0.5608 ± 0.0577	0.2375 ± 0.0546
0.0635	0.3736	1.2273	0.8396	0.2769	0.7942	-0.1373 ± 0.0155	-0.0222 ± 0.0152
0.0640	0.3728	1.2334	0.8346	0.4199	0.7824	-0.1614 ± 0.0192	-0.1414 ± 0.0182
0.0639	0.3743	1.2361	0.8286	0.6003	0.7640	-0.2638 ± 0.0313	-0.2618 ± 0.0480
0.0644	0.3766	1.2537	0.8275	0.8744	0.7353	-0.1561 ± 0.1034	-0.1331 ± 0.0890
0.0570	0.5168	1.5225	0.2522	0.1424	0.2372	-0.0142 ± 0.0143	-0.0172 ± 0.0106
0.0570	0.5196	1.5327	0.2599	0.2740	0.2364	-0.0091 ± 0.0132	0.0372 ± 0.0094
0.0569	0.5202	1.5310	0.2693	0.4159	0.2312	-0.0237 ± 0.0088	-0.0415 ± 0.0083
0.0571	0.5255	1.5531	0.2812	0.5755	0.2216	0.1439 ± 0.0171	0.0357 ± 0.0252
0.0541	0.5559	1.5562	0.2955	0.7741	0.2065	-0.5402 ± 1.0619	-0.2070 ± 0.9618
0.0573	0.5145	1.5236	0.3596	0.1559	0.3425	-0.0129 ± 0.0150	-0.0028 ± 0.0119
0.0570	0.5160	1.5200	0.3637	0.2776	0.3406	-0.1009 ± 0.0147	-0.0659 ± 0.0102
0.0572	0.5168	1.5286	0.3649	0.4225	0.3304	-0.0607 ± 0.0116	0.0075 ± 0.0090
0.0570	0.5169	1.5244	0.3657	0.6052	0.3102	-0.1099 ± 0.0080	-0.0018 ± 0.0075
0.0568	0.5207	1.5295	0.3761	0.8763	0.2781	-0.1958 ± 0.0298	0.0235 ± 0.0191
0.0570	0.5073	1.4965	0.5055	0.1726	0.4841	-0.0681 ± 0.0243	-0.0773 ± 0.0210
0.0572	0.5160	1.5257	0.5166	0.2784	0.4915	-0.1598 ± 0.0167	-0.0273 ± 0.0129
0.0571	0.5150	1.5201	0.5151	0.4227	0.4820	-0.0487 ± 0.0288	0.0501 ± 0.0324
0.0569	0.5165	1.5197	0.5172	0.6067	0.4691	-0.1873 ± 0.0186	-0.0146 ± 0.0152
0.0570	0.5162	1.5225	0.5163	0.9121	0.4312	-0.2552 ± 0.0275	-0.0222 ± 0.0230
0.0580	0.4857	1.4567	0.6411	0.1858	0.6145	0.3588 ± 0.0685	1.1563 ± 0.0551
0.0574	0.5130	1.5231	0.6660	0.2790	0.6374	-0.1853 ± 0.0216	0.0204 ± 0.0176
0.0575	0.5159	1.5337	0.6663	0.4233	0.6316	-0.2160 ± 0.0330	0.0399 ± 0.0240
0.0573	0.5160	1.5299	0.6650	0.6044	0.6189	-0.4205 ± 0.0401	-0.1274 ± 0.0286
0.0568	0.5163	1.5160	0.6647	0.9019	0.5910	-0.3214 ± 0.0495	-0.0996 ± 0.0468
0.0571	0.5062	1.4949	0.8340	0.2947	0.8000	-0.1201 ± 0.0270	-0.0394 ± 0.0235
0.0561	0.5130	1.4896	0.8354	0.4204	0.7974	-0.2303 ± 0.0333	-0.1031 ± 0.0269
0.0573	0.5138	1.5218	0.8340	0.5998	0.7871	0.0691 ± 0.0649	-0.0943 ± 0.0425
0.0564	0.5125	1.4943	0.8254	0.8798	0.7577	0.0730 ± 0.1588	-0.2511 ± 0.1074

Hydrogen results							
$\langle x \rangle$	$\langle y \rangle$	$\langle Q^2 \rangle$	$\langle z \rangle$	$\langle P_{h\perp} \rangle$	$\langle x_F \rangle$	$2\langle \cos \phi_h \rangle$	$2\langle \cos 2\phi_h \rangle$
0.0571	0.6462	1.9093	0.2498	0.1509	0.2375	-0.1882 ± 0.0477	-0.1156 ± 0.0278
0.0570	0.6468	1.9070	0.2563	0.2752	0.2373	-0.1845 ± 0.0205	-0.0562 ± 0.0139
0.0570	0.6488	1.9131	0.2643	0.4170	0.2334	-0.0751 ± 0.0102	-0.0209 ± 0.0099
0.0569	0.6493	1.9117	0.2759	0.5852	0.2259	-0.0935 ± 0.0139	-0.0405 ± 0.0132
0.0567	0.6451	1.8919	0.3555	0.1661	0.3416	-0.5521 ± 0.0618	-0.3166 ± 0.0368
0.0571	0.6469	1.9102	0.3634	0.2770	0.3449	0.1007 ± 0.0353	0.0525 ± 0.0209
0.0572	0.6475	1.9140	0.3645	0.4205	0.3372	-0.1662 ± 0.0207	-0.0768 ± 0.0149
0.0570	0.6462	1.9053	0.3646	0.6057	0.3202	-0.1262 ± 0.0099	-0.0191 ± 0.0097
0.0566	0.6485	1.8982	0.3690	0.8891	0.2877	-0.1429 ± 0.0221	0.0436 ± 0.0180
0.0557	0.6375	1.8381	0.4849	0.1855	0.4680	0.0762 ± 0.1959	0.1229 ± 0.1128
0.0569	0.6476	1.9042	0.5157	0.2786	0.4957	-0.1640 ± 0.0556	-0.0881 ± 0.0329
0.0570	0.6473	1.9086	0.5154	0.4227	0.4890	-0.1771 ± 0.0552	-0.1469 ± 0.0568
0.0571	0.6466	1.9104	0.5147	0.6074	0.4762	-0.3550 ± 0.0311	-0.2439 ± 0.0240
0.0577	0.6486	1.9339	0.5146	0.9002	0.4484	-0.1842 ± 0.0303	-0.0001 ± 0.0292
0.0571	0.6434	1.9006	0.6600	0.2923	0.6368	-0.5466 ± 0.0941	-0.1476 ± 0.0562
0.0569	0.7671	2.2580	0.6635	0.8899	0.6149	0.1568 ± 0.1899	0.1665 ± 0.1359
0.0570	0.7630	2.2507	0.8278	0.4251	0.8021	0.1411 ± 0.6482	0.2386 ± 0.2793
0.0564	0.7635	2.2267	0.8149	0.8711	0.7700	-0.3464 ± 0.6628	-0.0744 ± 0.4565
0.1054	0.3647	1.9883	0.2598	0.1374	0.2380	0.0206 ± 0.0127	-0.0464 ± 0.0128
0.1050	0.3675	1.9959	0.2684	0.2715	0.2340	-0.0195 ± 0.0203	-0.0204 ± 0.0189
0.1048	0.3736	2.0250	0.2791	0.4096	0.2253	-0.1935 ± 0.0713	0.1479 ± 0.0441
0.1032	0.3940	2.1036	0.2897	0.5444	0.2141	-0.8320 ± 0.6648	0.2791 ± 0.2865
0.1058	0.3607	1.9740	0.3615	0.1444	0.3366	-0.0153 ± 0.0118	-0.0304 ± 0.0122
0.1057	0.3623	1.9810	0.3635	0.2771	0.3292	0.0377 ± 0.0112	-0.0239 ± 0.0101
0.1051	0.3664	1.9922	0.3697	0.5967	0.2890	-0.1241 ± 0.0473	0.0162 ± 0.0261
0.1045	0.3733	2.0184	0.3967	0.8457	0.2652	-0.7987 ± 0.5891	0.2980 ± 0.2216
0.1057	0.3591	1.9630	0.5142	0.1544	0.4834	-0.0068 ± 0.0166	0.0314 ± 0.0173
0.1059	0.3634	1.9900	0.5172	0.2784	0.4801	-0.0288 ± 0.0123	-0.0244 ± 0.0115
0.1054	0.3645	1.9866	0.5173	0.6027	0.4462	-0.1692 ± 0.0318	-0.0428 ± 0.0286
0.1056	0.3643	1.9894	0.5183	0.8850	0.3967	0.4298 ± 0.1725	-0.2330 ± 0.0904
0.1066	0.3498	1.9281	0.6659	0.1666	0.6273	-0.0042 ± 0.0275	0.0692 ± 0.0300
0.1062	0.3589	1.9711	0.6700	0.2773	0.6276	-0.1642 ± 0.0167	0.0438 ± 0.0157
0.1062	0.3591	1.9716	0.6702	0.4217	0.6184	-0.1781 ± 0.0210	0.0500 ± 0.0186
0.1063	0.3594	1.9766	0.6697	0.6035	0.6005	-0.1207 ± 0.0314	-0.0401 ± 0.0283
0.1065	0.3610	1.9875	0.6699	0.8818	0.5623	-0.2575 ± 0.1509	0.1120 ± 0.1036
0.1054	0.3386	1.8448	0.8245	0.1781	0.7770	-0.2091 ± 0.0632	-0.1111 ± 0.0705
0.1064	0.3572	1.9661	0.8353	0.2767	0.7863	-0.0945 ± 0.0220	0.0011 ± 0.0213
0.1061	0.3578	1.9629	0.8328	0.4212	0.7764	-0.0762 ± 0.0241	-0.1558 ± 0.0222
0.1064	0.3609	1.9855	0.8262	0.5999	0.7566	-0.1069 ± 0.0318	-0.3519 ± 0.0287
0.1056	0.3626	1.9794	0.8189	0.8725	0.7193	-0.3283 ± 0.1283	-0.5635 ± 0.1253
0.1052	0.5171	2.8123	0.2523	0.1437	0.2366	-0.0411 ± 0.0151	-0.0094 ± 0.0147
0.1055	0.5190	2.8315	0.2598	0.2730	0.2352	-0.0867 ± 0.0192	-0.1041 ± 0.0167

Hydrogen results							
$\langle x \rangle$	$\langle y \rangle$	$\langle Q^2 \rangle$	$\langle z \rangle$	$\langle P_{h\perp} \rangle$	$\langle x_F \rangle$	$2\langle \cos \boldsymbol{\phi_h} \rangle$	$2\langle \cos \mathbf{2}\boldsymbol{\phi_h} \rangle$
0.1052	0.5202	2.8313	0.2705	0.4162	0.2305	-0.0395 ± 0.0221	0.0171 ± 0.0202
0.1049	0.5261	2.8549	0.2828	0.5735	0.2208	0.0061 ± 0.0461	-0.1715 ± 0.0342
0.1057	0.5133	2.8060	0.3599	0.1552	0.3419	-0.0341 ± 0.0168	0.0318 ± 0.0169
0.1058	0.5169	2.8279	0.3641	0.2781	0.3399	-0.0876 ± 0.0150	-0.0002 ± 0.0136
0.1053	0.5166	2.8141	0.3655	0.6024	0.3075	-0.0934 ± 0.0189	0.0145 ± 0.0167
0.1049	0.5205	2.8238	0.3775	0.8673	0.2766	-0.0735 ± 0.0746	0.0242 ± 0.0448
0.1056	0.5064	2.7667	0.5071	0.1719	0.4847	-0.0676 ± 0.0330	-0.2246 ± 0.0341
0.1054	0.5165	2.8148	0.5171	0.2778	0.4909	-0.0691 ± 0.0176	0.0663 ± 0.0169
0.1061	0.5162	2.8321	0.5168	0.6071	0.4662	-0.2604 ± 0.0313	-0.1096 ± 0.0282
0.1055	0.5163	2.8171	0.5160	0.8983	0.4286	-0.2566 ± 0.0683	-0.0347 ± 0.0551
0.1032	0.4874	2.6020	0.6375	0.1869	0.6100	0.6748 ± 0.1285	-0.0134 ± 0.1175
0.1059	0.5114	2.8019	0.6650	0.2781	0.6350	-0.2251 ± 0.0228	0.0047 ± 0.0225
0.1052	0.5115	2.7820	0.6672	0.4223	0.6306	-0.0138 ± 0.0296	0.0273 ± 0.0273
0.1051	0.5153	2.8002	0.6658	0.6025	0.6176	-0.3058 ± 0.0422	-0.1678 ± 0.0387
0.1059	0.5155	2.8234	0.6661	0.8888	0.5901	-0.0997 ± 0.1072	-0.0815 ± 0.1025
0.1047	0.5056	2.7385	0.8273	0.2912	0.7922	-0.2981 ± 0.0328	-0.1481 ± 0.0338
0.1051	0.5128	2.7886	0.8332	0.4225	0.7934	0.0005 ± 0.0348	-0.1623 ± 0.0345
0.1053	0.5130	2.7936	0.8274	0.6043	0.7780	-0.1098 ± 0.0543	-0.1223 ± 0.0494
0.1055	0.5130	2.7983	0.8261	0.8719	0.7560	-0.2545 ± 0.1958	-0.2790 ± 0.1798
0.1060	0.6462	3.5431	0.2504	0.1499	0.2376	0.0228 ± 0.0349	0.0749 ± 0.0286
0.1049	0.6472	3.5127	0.2571	0.2737	0.2373	-0.1552 ± 0.0404	-0.0808 ± 0.0284
0.1050	0.6495	3.5265	0.2769	0.5837	0.2247	0.0344 ± 0.0285	-0.0517 ± 0.0266
0.1030	0.6464	3.4440	0.2923	0.7877	0.2090	-0.0349 ± 0.3769	0.1947 ± 0.2217
0.1058	0.6448	3.5271	0.3557	0.1656	0.3411	-0.0705 ± 0.0407	-0.0661 ± 0.0342
0.1058	0.6470	3.5401	0.3624	0.2773	0.3431	-0.0277 ± 0.0325	0.0143 ± 0.0246
0.1046	0.6466	3.4992	0.3652	0.6065	0.3186	-0.1637 ± 0.0242	-0.0022 ± 0.0225
0.1052	0.6482	3.5281	0.3700	0.8780	0.2864	-0.2083 ± 0.0546	0.0627 ± 0.0397
0.1051	0.6366	3.4613	0.4872	0.1871	0.4694	-0.6923 ± 0.1647	0.3566 ± 0.1447
0.1059	0.6469	3.5417	0.5134	0.2806	0.4923	-0.2027 ± 0.0417	-0.0497 ± 0.0342
0.1048	0.6471	3.5062	0.5156	0.9001	0.4460	-0.1098 ± 0.0712	-0.0192 ± 0.0653
0.1042	0.6435	3.4689	0.6601	0.2928	0.6359	-0.3203 ± 0.0555	-0.0423 ± 0.0496
0.1059	0.6463	3.5411	0.6646	0.4207	0.6357	-0.2305 ± 0.0718	0.0153 ± 0.0557
0.1053	0.6452	3.5151	0.6617	0.6065	0.6229	-0.2240 ± 0.1115	-0.1624 ± 0.0791
0.1069	0.6476	3.5798	0.6655	0.9036	0.6037	-0.2015 ± 0.1730	-0.1227 ± 0.1517
0.1056	0.6430	3.5111	0.8372	0.4208	0.8053	0.1781 ± 0.0999	0.0553 ± 0.0783
0.1053	0.6457	3.5169	0.8278	0.6080	0.7883	-0.0973 ± 0.1911	-0.1376 ± 0.1298
0.1052	0.6512	3.5419	0.8248	0.8832	0.7688	-0.4216 ± 0.3869	-0.5460 ± 0.2861
0.1051	0.7694	4.1820	0.2486	0.1565	0.2376	0.1858 ± 0.1091	0.0783 ± 0.0635
0.1051	0.7715	4.1926	0.2546	0.2748	0.2379	-0.0352 ± 0.0519	0.0370 ± 0.0354
0.1046	0.7707	4.1699	0.2624	0.4174	0.2350	-0.0667 ± 0.0260	-0.0100 ± 0.0238
0.1051	0.7723	4.1965	0.2731	0.5873	0.2285	-0.0201 ± 0.0228	-0.0780 ± 0.0220
0.1032	0.7746	4.1350	0.2882	0.8093	0.2147	0.3342 ± 0.1148	-0.7807 ± 0.0919

Hydrogen results							
$\langle x \rangle$	$\langle y \rangle$	$\langle Q^2 \rangle$	$\langle z \rangle$	$\langle P_{h\perp} \rangle$	$\langle x_F \rangle$	$2\langle \mathbf{\cos \phi_h} \rangle$	$2\langle \mathbf{\cos 2\phi_h} \rangle$
0.1048	0.7639	4.1397	0.3461	0.1754	0.3336	-0.1499 ± 0.1982	0.0587 ± 0.1155
0.1054	0.7695	4.1961	0.3629	0.2777	0.3466	-0.0954 ± 0.0733	-0.0746 ± 0.0457
0.1054	0.7692	4.1933	0.3642	0.4208	0.3401	-0.1871 ± 0.0545	-0.0716 ± 0.0377
0.1050	0.7695	4.1809	0.3651	0.6063	0.3260	-0.0117 ± 0.0257	0.0317 ± 0.0235
0.1058	0.7710	4.2187	0.3665	0.8864	0.2948	0.0340 ± 0.0390	-0.0103 ± 0.0337
0.1051	0.7653	4.1594	0.5112	0.2867	0.4932	-0.2058 ± 0.1167	-0.0312 ± 0.0711
0.1054	0.7687	4.1924	0.5147	0.4220	0.4914	-0.0569 ± 0.1057	-0.1329 ± 0.0662
0.1049	0.7698	4.1787	0.5122	0.6072	0.4783	-0.2534 ± 0.0682	-0.0824 ± 0.0524
0.1044	0.7673	4.1432	0.5169	0.9079	0.4576	-0.2293 ± 0.0749	-0.2214 ± 0.0751
0.1053	0.7679	4.1835	0.6622	0.4200	0.6379	0.1901 ± 0.2071	0.2406 ± 0.1214
0.1048	0.7709	4.1795	0.6646	0.6020	0.6324	-0.1570 ± 0.1678	-0.2271 ± 0.1126
0.1055	0.7692	4.1950	0.6648	0.9111	0.6123	-0.0770 ± 0.3785	-0.1179 ± 0.2773
0.1060	0.7581	4.1572	0.8225	0.4317	0.7953	0.8110 ± 0.4178	0.2801 ± 0.2550
0.1049	0.7674	4.1628	0.8336	0.6050	0.8004	0.5103 ± 0.4426	0.1125 ± 0.2489
0.1034	0.7704	4.1187	0.8169	0.8881	0.7693	-0.0907 ± 0.8559	0.2422 ± 0.6304
0.1938	0.3654	3.6618	0.2614	0.1359	0.2378	-0.0097 ± 0.0212	-0.0656 ± 0.0196
0.1938	0.3682	3.6909	0.2703	0.2702	0.2331	-0.0938 ± 0.0461	0.0138 ± 0.0274
0.1918	0.3761	3.7310	0.2817	0.4075	0.2238	-0.1258 ± 0.2284	-0.1009 ± 0.1183
0.1865	0.4021	3.8776	0.2912	0.5360	0.2126	-0.8488 ± 1.7982	0.3414 ± 0.7583
0.1961	0.3595	3.6461	0.3624	0.1442	0.3354	0.0200 ± 0.0185	0.0411 ± 0.0190
0.1955	0.3616	3.6563	0.3647	0.2774	0.3271	0.0197 ± 0.0202	0.0083 ± 0.0147
0.1948	0.3625	3.6521	0.3651	0.4211	0.3087	-0.2205 ± 0.0511	0.0329 ± 0.0287
0.1936	0.3660	3.6651	0.3717	0.5921	0.2844	-0.0686 ± 0.1623	-0.0335 ± 0.0748
0.1902	0.3769	3.7087	0.4002	0.8366	0.2610	-0.5697 ± 0.9111	0.2915 ± 0.3504
0.1948	0.3580	3.6076	0.5146	0.1551	0.4811	-0.0569 ± 0.0272	0.1279 ± 0.0279
0.1951	0.3618	3.6510	0.5177	0.2796	0.4773	0.0091 ± 0.0232	-0.0394 ± 0.0185
0.1950	0.3633	3.6638	0.5201	0.6047	0.4418	-0.4446 ± 0.0968	0.0901 ± 0.0505
0.1937	0.3651	3.6588	0.5211	0.8794	0.3896	-0.3970 ± 0.6049	0.1804 ± 0.2619
0.1961	0.3496	3.5451	0.6682	0.1659	0.6265	0.1083 ± 0.0436	-0.0106 ± 0.0551
0.1966	0.3566	3.6261	0.6711	0.2773	0.6249	-0.0487 ± 0.0291	0.1494 ± 0.0248
0.1962	0.3578	3.6316	0.6715	0.4228	0.6148	-0.0651 ± 0.0372	-0.0260 ± 0.0262
0.1964	0.3586	3.6431	0.6696	0.6047	0.5937	-0.3485 ± 0.0673	0.0130 ± 0.0382
0.1952	0.3601	3.6356	0.6669	0.8787	0.5490	0.0938 ± 0.4886	-0.4043 ± 0.2341
0.1966	0.3392	3.4491	0.8163	0.1782	0.7656	-0.3769 ± 0.0955	-0.0323 ± 0.1068
0.1967	0.3565	3.6264	0.8292	0.2780	0.7763	0.1421 ± 0.0306	-0.1470 ± 0.0307
0.1968	0.3609	3.6729	0.8291	0.4194	0.7686	-0.0949 ± 0.0359	-0.2314 ± 0.0293
0.1958	0.3584	3.6296	0.8231	0.6021	0.7467	-0.1373 ± 0.0623	-0.0660 ± 0.0407
0.1941	0.3587	3.6014	0.8168	0.8752	0.7063	0.3239 ± 0.2537	-0.4495 ± 0.1527
0.1926	0.5158	5.1374	0.2549	0.1433	0.2378	-0.0221 ± 0.0170	0.0165 ± 0.0176
0.1926	0.5176	5.1556	0.2620	0.2733	0.2351	-0.0723 ± 0.0186	-0.0351 ± 0.0176
0.1935	0.5206	5.2090	0.2729	0.4153	0.2294	-0.1203 ± 0.0349	-0.0818 ± 0.0322
0.1921	0.5286	5.2524	0.2844	0.5643	0.2186	-0.0085 ± 0.1310	0.0196 ± 0.0828

Hydrogen results							
$\langle x \rangle$	$\langle y \rangle$	$\langle Q^2 \rangle$	$\langle z \rangle$	$\langle P_{h\perp} \rangle$	$\langle x_F \rangle$	$2\langle \mathbf{cos}\, \boldsymbol{\phi_h} \rangle$	$2\langle \mathbf{cos}\, \mathbf{2}\boldsymbol{\phi_h} \rangle$
0.1923	0.5111	5.0842	0.3608	0.1551	0.3413	-0.0313 ± 0.0211	0.0634 ± 0.0218
0.1943	0.5156	5.1812	0.3634	0.2779	0.3369	-0.0520 ± 0.0149	-0.0439 ± 0.0146

Deuterium results							
$\langle x \rangle$	$\langle y \rangle$	$\langle Q^2 \rangle$	$\langle z \rangle$	$\langle P_{h\perp} \rangle$	$\langle x_F \rangle$	$2\langle \mathbf{cos}\, \boldsymbol{\phi_h} \rangle$	$2\langle \mathbf{cos}\, \mathbf{2}\boldsymbol{\phi_h} \rangle$
0.0385	0.5486	1.0928	0.2518	0.1450	0.2379	-0.3264 ± 0.0496	-0.2318 ± 0.0286
0.0385	0.5491	1.0943	0.2582	0.2746	0.2363	-0.0578 ± 0.0204	-0.0409 ± 0.0135
0.0386	0.5493	1.0953	0.2671	0.4173	0.2314	-0.0475 ± 0.0111	0.0995 ± 0.0108
0.0383	0.5526	1.0937	0.2797	0.5836	0.2227	-0.1748 ± 0.0204	0.0700 ± 0.0332
0.0378	0.5616	1.0982	0.2955	0.7865	0.2065	-0.6715 ± 0.6834	0.5600 ± 0.3985
0.0386	0.5470	1.0926	0.3580	0.1588	0.3421	-0.3400 ± 0.0605	-0.1955 ± 0.0338
0.0386	0.5477	1.0937	0.3639	0.2770	0.3425	0.0081 ± 0.0397	-0.0464 ± 0.0230
0.0386	0.5484	1.0938	0.3636	0.4212	0.3318	0.0117 ± 0.0217	0.0435 ± 0.0136
0.0385	0.5488	1.0933	0.3659	0.6049	0.3147	-0.1026 ± 0.0103	-0.0312 ± 0.0104
0.0384	0.5507	1.0944	0.3734	0.8824	0.2810	-0.1910 ± 0.0292	-0.0117 ± 0.0222
0.0385	0.5469	1.0883	0.5163	0.2778	0.4931	-0.5495 ± 0.0519	-0.0183 ± 0.0316
0.0386	0.5469	1.0931	0.5149	0.4202	0.4844	0.0202 ± 0.0656	0.0099 ± 0.0701
0.0387	0.5458	1.0911	0.5149	0.6033	0.4705	-0.2893 ± 0.0280	-0.1298 ± 0.0218
0.0387	0.5480	1.0960	0.5176	0.9161	0.4385	-0.1676 ± 0.0297	-0.2348 ± 0.0292
0.0385	0.5466	1.0891	0.6672	0.2832	0.6406	-0.4681 ± 0.1008	-0.1789 ± 0.0572
0.0386	0.5454	1.0900	0.6664	0.4230	0.6342	-0.7927 ± 0.0993	-0.2361 ± 0.0587
0.0386	0.5467	1.0927	0.6670	0.6036	0.6243	-0.4053 ± 0.1044	-0.0192 ± 0.0635
0.0385	0.5472	1.0897	0.6627	0.9000	0.5945	-0.3355 ± 0.0563	-0.2451 ± 0.0554
0.0387	0.5468	1.0938	0.8338	0.5958	0.7906	-0.6921 ± 0.1421	-0.8485 ± 0.0830

Deuterium results							
$\langle x \rangle$	$\langle y \rangle$	$\langle Q^2 \rangle$	$\langle z \rangle$	$\langle P_{h\perp} \rangle$	$\langle x_F \rangle$	$2\langle \cos \phi_h \rangle$	$2\langle \cos 2\phi_h \rangle$
0.0387	0.5443	1.0888	0.8218	0.8862	0.7586	-0.3479 ± 0.2073	-0.3763 ± 0.1534
0.0354	0.6514	1.1918	0.2499	0.1503	0.2380	0.0044 ± 0.0756	-0.0084 ± 0.0340
0.0353	0.6521	1.1898	0.2561	0.2741	0.2377	-0.1003 ± 0.0167	-0.0348 ± 0.0108
0.0353	0.6519	1.1888	0.2642	0.4177	0.2341	-0.0349 ± 0.0079	-0.0300 ± 0.0072
0.0351	0.6538	1.1881	0.2756	0.5869	0.2268	-0.0505 ± 0.0099	0.0033 ± 0.0098
0.0353	0.6518	1.1906	0.3645	0.2783	0.3465	-0.2576 ± 0.0381	-0.1559 ± 0.0201
0.0353	0.6515	1.1904	0.3645	0.4224	0.3378	-0.1111 ± 0.0173	0.0320 ± 0.0108
0.0353	0.6514	1.1880	0.3639	0.6056	0.3208	-0.1011 ± 0.0070	-0.0245 ± 0.0072
0.0352	0.6526	1.1877	0.3694	0.8947	0.2895	-0.2701 ± 0.0144	0.0913 ± 0.0125
0.0353	0.6485	1.1828	0.5137	0.2785	0.4942	-0.0281 ± 0.0939	0.0271 ± 0.0426
0.0353	0.6513	1.1889	0.5171	0.4211	0.4915	0.3008 ± 0.0833	0.1066 ± 0.0616
0.0352	0.6520	1.1880	0.5142	0.6068	0.4769	-0.2519 ± 0.0254	-0.0586 ± 0.0175
0.0351	0.6508	1.1806	0.5157	0.9193	0.4491	-0.3259 ± 0.0203	0.0498 ± 0.0206
0.0353	0.6496	1.1857	0.6650	0.4241	0.6380	0.3161 ± 0.1469	0.2010 ± 0.0676
0.0353	0.6495	1.1862	0.6629	0.6047	0.6271	-0.4834 ± 0.1096	-0.0348 ± 0.0590
0.0353	0.6515	1.1889	0.6630	0.9105	0.6052	-0.2697 ± 0.0544	-0.0306 ± 0.0518
0.0355	0.6438	1.1805	0.8099	0.3196	0.7835	0.9384 ± 0.9037	0.4914 ± 0.3246
0.0352	0.6522	1.1881	0.8283	0.5979	0.7921	-0.4427 ± 0.1971	-0.2888 ± 0.0993
0.0353	0.6490	1.1864	0.8322	0.8890	0.7794	-0.5383 ± 0.2104	-0.3952 ± 0.1466
0.0325	0.7735	1.2986	0.2476	0.1563	0.2374	-0.6894 ± 0.1068	-0.1944 ± 0.0434
0.0322	0.7764	1.2942	0.2537	0.2755	0.2382	-0.1684 ± 0.0137	-0.0816 ± 0.0077
0.0325	0.7758	1.3027	0.2613	0.4187	0.2358	-0.0088 ± 0.0046	0.0307 ± 0.0046
0.0324	0.7784	1.3041	0.2712	0.5938	0.2292	0.0054 ± 0.0052	-0.0175 ± 0.0100
0.0318	0.7833	1.2869	0.2864	0.8307	0.2154	0.5953 ± 0.0166	-0.1565 ± 0.0162
0.0326	0.7668	1.2925	0.3470	0.1742	0.3354	0.3444 ± 0.3173	0.2134 ± 0.1191
0.0323	0.7748	1.2962	0.3633	0.2776	0.3483	0.1976 ± 0.0576	0.0557 ± 0.0247
0.0323	0.7750	1.2943	0.3648	0.4221	0.3425	-0.0071 ± 0.0116	0.0033 ± 0.0080
0.0325	0.7744	1.3002	0.3643	0.6068	0.3281	-0.0428 ± 0.0047	-0.0382 ± 0.0048
0.0324	0.7762	1.2999	0.3671	0.9033	0.2990	-0.1224 ± 0.0072	0.0010 ± 0.0070
0.0324	0.7709	1.2918	0.5098	0.2878	0.4931	-0.8385 ± 0.1676	-0.4459 ± 0.0661
0.0322	0.7746	1.2897	0.5153	0.4228	0.4938	-0.0023 ± 0.0817	0.0363 ± 0.0363
0.0324	0.7736	1.2981	0.5155	0.6067	0.4843	-0.0826 ± 0.0186	-0.0354 ± 0.0135
0.0321	0.7750	1.2876	0.5118	0.9180	0.4561	-0.1956 ± 0.0142	0.0262 ± 0.0147
0.0322	0.7728	1.2871	0.6645	0.4201	0.6419	-0.3856 ± 0.2755	0.0554 ± 0.1114
0.0322	0.7715	1.2851	0.6625	0.9154	0.6136	-0.1525 ± 0.0469	-0.0445 ± 0.0420
0.0323	0.7701	1.2864	0.8262	0.4272	0.8013	0.5987 ± 0.5719	0.3526 ± 0.2103
0.0323	0.7727	1.2906	0.8247	0.8865	0.7806	0.0241 ± 0.1928	0.0724 ± 0.1251
0.0632	0.3796	1.2403	0.2575	0.1379	0.2373	-0.0322 ± 0.0059	-0.0081 ± 0.0055
0.0628	0.3825	1.2431	0.2657	0.2721	0.2339	-0.0238 ± 0.0088	-0.0150 ± 0.0077
0.0625	0.3872	1.2520	0.2769	0.4121	0.2265	0.1003 ± 0.0160	-0.0471 ± 0.0116
0.0608	0.4019	1.2633	0.2880	0.5517	0.2154	-0.5635 ± 0.1225	0.3501 ± 0.1151
0.0635	0.3761	1.2351	0.3625	0.1464	0.3394	-0.0169 ± 0.0056	0.0077 ± 0.0054

Deuterium results							
$\langle x \rangle$	$\langle y \rangle$	$\langle Q^2 \rangle$	$\langle z \rangle$	$\langle P_{h\perp} \rangle$	$\langle x_F \rangle$	$2\langle \cos \boldsymbol{\phi_h} \rangle$	$2\langle \cos \mathbf{2}\boldsymbol{\phi_h} \rangle$
0.0633	0.3777	1.2367	0.3641	0.2770	0.3324	-0.0157 ± 0.0067	-0.0022 ± 0.0057
0.0633	0.3783	1.2382	0.3658	0.4213	0.3185	-0.0308 ± 0.0073	-0.0461 ± 0.0063
0.0631	0.3807	1.2415	0.3685	0.5987	0.2936	-0.0617 ± 0.0131	-0.0143 ± 0.0087
0.0624	0.3882	1.2518	0.3916	0.8550	0.2673	-0.3122 ± 0.1399	0.1387 ± 0.0590
0.0637	0.3731	1.2288	0.5136	0.1571	0.4849	0.0032 ± 0.0074	-0.0114 ± 0.0078
0.0631	0.3782	1.2352	0.5167	0.2778	0.4825	-0.1120 ± 0.0067	0.0343 ± 0.0060
0.0633	0.3778	1.2379	0.5170	0.4224	0.4716	-0.1502 ± 0.0122	0.0742 ± 0.0096
0.0633	0.3787	1.2388	0.5170	0.6038	0.4512	-0.1969 ± 0.0119	-0.0544 ± 0.0101
0.0627	0.3807	1.2351	0.5181	0.9011	0.4035	-0.1998 ± 0.0421	-0.1175 ± 0.0252
0.0647	0.3643	1.2185	0.6651	0.1691	0.6293	-0.1170 ± 0.0132	-0.0679 ± 0.0139
0.0635	0.3755	1.2324	0.6682	0.2794	0.6292	-0.2865 ± 0.0078	0.1169 ± 0.0075
0.0637	0.3752	1.2354	0.6691	0.4227	0.6213	-0.3204 ± 0.0118	0.0636 ± 0.0109
0.0636	0.3750	1.2333	0.6689	0.6052	0.6050	-0.3369 ± 0.0168	-0.1369 ± 0.0155
0.0633	0.3756	1.2300	0.6676	0.8987	0.5658	-0.1388 ± 0.0436	-0.2191 ± 0.0319
0.0657	0.3510	1.1923	0.8198	0.1803	0.7756	-0.3924 ± 0.0327	0.0078 ± 0.0336
0.0634	0.3741	1.2276	0.8380	0.2772	0.7927	-0.2350 ± 0.0104	-0.0363 ± 0.0094
0.0637	0.3738	1.2325	0.8330	0.4205	0.7810	-0.1914 ± 0.0119	-0.0866 ± 0.0113
0.0637	0.3742	1.2326	0.8274	0.6002	0.7629	-0.2051 ± 0.0197	-0.0720 ± 0.0342
0.0639	0.3782	1.2507	0.8243	0.8777	0.7320	-0.2596 ± 0.0622	-0.2120 ± 0.0558
0.0570	0.5168	1.5236	0.2524	0.1432	0.2374	-0.0207 ± 0.0090	-0.0202 ± 0.0068
0.0569	0.5193	1.5286	0.2597	0.2740	0.2362	-0.0532 ± 0.0081	0.0108 ± 0.0058
0.0568	0.5207	1.5302	0.2690	0.4161	0.2309	0.0145 ± 0.0065	0.0022 ± 0.0054
0.0568	0.5254	1.5445	0.2814	0.5768	0.2215	-0.0193 ± 0.0120	0.0623 ± 0.0177
0.0542	0.5565	1.5607	0.2955	0.7732	0.2068	-0.5783 ± 0.3549	1.7469 ± 0.4825
0.0571	0.5138	1.5164	0.3595	0.1556	0.3423	0.0140 ± 0.0095	-0.0419 ± 0.0075
0.0569	0.5164	1.5203	0.3639	0.2778	0.3407	-0.0989 ± 0.0097	-0.0389 ± 0.0067
0.0570	0.5165	1.5236	0.3648	0.4221	0.3303	-0.0769 ± 0.0077	0.0066 ± 0.0055
0.0571	0.5175	1.5276	0.3658	0.6053	0.3104	-0.1453 ± 0.0052	0.0232 ± 0.0048
0.0568	0.5205	1.5296	0.3764	0.8764	0.2785	-0.2271 ± 0.0184	0.1082 ± 0.0120
0.0569	0.5079	1.4949	0.5066	0.1723	0.4852	0.0018 ± 0.0157	0.0884 ± 0.0134
0.0570	0.5160	1.5199	0.5158	0.2784	0.4907	-0.1311 ± 0.0109	0.0162 ± 0.0083
0.0570	0.5149	1.5186	0.5155	0.4228	0.4824	-0.3540 ± 0.0180	-0.0293 ± 0.0227
0.0569	0.5160	1.5179	0.5168	0.6071	0.4686	-0.0763 ± 0.0133	0.0041 ± 0.0096
0.0570	0.5153	1.5182	0.5161	0.9065	0.4316	-0.2269 ± 0.0168	0.0068 ± 0.0144
0.0578	0.4862	1.4526	0.6394	0.1853	0.6129	0.1214 ± 0.0463	-0.0750 ± 0.0421
0.0572	0.5135	1.5178	0.6656	0.2795	0.6371	-0.3374 ± 0.0142	-0.0385 ± 0.0109
0.0572	0.5152	1.5245	0.6673	0.4226	0.6326	-0.2975 ± 0.0213	0.0893 ± 0.0151
0.0570	0.5148	1.5183	0.6657	0.6049	0.6194	-0.3996 ± 0.0307	-0.1206 ± 0.0190
0.0569	0.5163	1.5192	0.6657	0.9004	0.5922	-0.2403 ± 0.0341	-0.0880 ± 0.0281
0.0568	0.5078	1.4923	0.8321	0.2936	0.7984	-0.1952 ± 0.0200	-0.0016 ± 0.0157
0.0562	0.5127	1.4904	0.8357	0.4200	0.7977	-0.1174 ± 0.0241	-0.1086 ± 0.0169
0.0571	0.5132	1.5146	0.8306	0.5993	0.7837	-0.1281 ± 0.0418	-0.2072 ± 0.0250

Deuterium results							
$\langle x \rangle$	$\langle y \rangle$	$\langle Q^2 \rangle$	$\langle z \rangle$	$\langle P_{h\perp} \rangle$	$\langle x_F \rangle$	$2\langle \mathbf{\cos \phi_h} \rangle$	$2\langle \mathbf{\cos 2\phi_h} \rangle$
0.0567	0.5133	1.5055	0.8221	0.8839	0.7541	-0.1495 ± 0.0823	-0.2774 ± 0.0575
0.0569	0.6463	1.9030	0.2497	0.1505	0.2374	-0.1662 ± 0.0347	-0.0646 ± 0.0178
0.0569	0.6474	1.9057	0.2562	0.2749	0.2372	0.1102 ± 0.0167	0.0515 ± 0.0096
0.0570	0.6482	1.9110	0.2645	0.4172	0.2336	-0.0088 ± 0.0074	0.0151 ± 0.0063
0.0569	0.6495	1.9114	0.2757	0.5845	0.2258	-0.0601 ± 0.0099	-0.0722 ± 0.0083
0.0565	0.6536	1.9095	0.2916	0.7985	0.2111	0.1277 ± 0.0640	0.1789 ± 0.0460
0.0569	0.6455	1.8984	0.3555	0.1656	0.3416	-0.0164 ± 0.0430	0.0186 ± 0.0230
0.0570	0.6472	1.9090	0.3634	0.2779	0.3449	0.0998 ± 0.0245	0.0756 ± 0.0130
0.0570	0.6473	1.9081	0.3641	0.4211	0.3367	-0.1114 ± 0.0148	0.0184 ± 0.0094
0.0568	0.6468	1.8997	0.3642	0.6064	0.3198	-0.0814 ± 0.0070	-0.0023 ± 0.0061
0.0568	0.6483	1.9046	0.3704	0.8905	0.2891	-0.1262 ± 0.0154	-0.0284 ± 0.0113
0.0566	0.6466	1.8933	0.5151	0.2787	0.4951	-0.3219 ± 0.0397	-0.1810 ± 0.0204
0.0571	0.6469	1.9092	0.5155	0.4229	0.4891	-0.1879 ± 0.0357	0.0035 ± 0.0394
0.0570	0.6466	1.9054	0.5154	0.6070	0.4770	-0.3887 ± 0.0224	-0.1285 ± 0.0151
0.0574	0.6480	1.9238	0.5144	0.9029	0.4478	-0.3113 ± 0.0214	0.0312 ± 0.0185
0.0565	0.6436	1.8824	0.6606	0.2925	0.6374	-0.2301 ± 0.0677	-0.0322 ± 0.0347
0.0567	0.7672	2.2479	0.6624	0.6065	0.6313	-0.1692 ± 0.0852	0.0294 ± 0.0480
0.0569	0.7689	2.2622	0.6608	0.9042	0.6112	-0.1430 ± 0.0674	0.0782 ± 0.0552
0.0575	0.7658	2.2768	0.8277	0.6000	0.7962	0.8493 ± 0.2721	0.3911 ± 0.2103
0.0564	0.7652	2.2307	0.8161	0.8764	0.7710	0.0598 ± 0.3409	-0.1558 ± 0.1974
0.1051	0.3648	1.9836	0.2593	0.1370	0.2375	0.0274 ± 0.0050	-0.0138 ± 0.0049
0.1050	0.3678	1.9978	0.2678	0.2717	0.2335	-0.0284 ± 0.0093	0.0331 ± 0.0083
0.1045	0.3736	2.0185	0.2789	0.4095	0.2251	-0.0357 ± 0.0326	-0.0263 ± 0.0189
0.1054	0.3615	1.9712	0.3622	0.1446	0.3374	0.0287 ± 0.0051	0.0267 ± 0.0052
0.1053	0.3625	1.9741	0.3642	0.2769	0.3298	0.0257 ± 0.0050	0.0085 ± 0.0045
0.1050	0.3672	1.9934	0.3704	0.5968	0.2900	0.2276 ± 0.0244	-0.1378 ± 0.0129
0.1047	0.3747	2.0288	0.3957	0.8465	0.2643	-0.3770 ± 0.2274	0.2260 ± 0.0880
0.1054	0.3586	1.9545	0.5139	0.1546	0.4830	-0.0510 ± 0.0067	-0.0528 ± 0.0073
0.1054	0.3634	1.9819	0.5170	0.2780	0.4800	-0.0852 ± 0.0056	0.0330 ± 0.0052
0.1054	0.3641	1.9843	0.5179	0.6039	0.4466	-0.2086 ± 0.0145	0.0642 ± 0.0125
0.1053	0.3644	1.9848	0.5194	0.8875	0.3975	0.4821 ± 0.0821	-0.3977 ± 0.0394
0.1060	0.3486	1.9110	0.6667	0.1665	0.6280	-0.1155 ± 0.0116	0.2549 ± 0.0120
0.1060	0.3590	1.9685	0.6707	0.2778	0.6283	-0.1221 ± 0.0068	-0.0539 ± 0.0065
0.1059	0.3584	1.9635	0.6703	0.4221	0.6183	-0.1851 ± 0.0089	-0.0165 ± 0.0076
0.1061	0.3596	1.9727	0.6699	0.6038	0.6007	-0.3405 ± 0.0136	0.0266 ± 0.0201
0.1056	0.3610	1.9708	0.6679	0.8835	0.5599	-0.0866 ± 0.0522	0.0291 ± 0.0358
0.1054	0.3394	1.8496	0.8227	0.1776	0.7754	0.3442 ± 0.0282	-0.3287 ± 0.0302
0.1059	0.3583	1.9633	0.8329	0.2768	0.7841	-0.2164 ± 0.0095	0.0143 ± 0.0093
0.1058	0.3588	1.9625	0.8296	0.4214	0.7734	-0.0830 ± 0.0111	0.0475 ± 0.0097
0.1056	0.3607	1.9696	0.8238	0.6005	0.7542	-0.1210 ± 0.0140	-0.3442 ± 0.0220
0.1058	0.3622	1.9825	0.8174	0.8743	0.7174	-0.1847 ± 0.0490	-0.6936 ± 0.0438
0.1051	0.5164	2.8072	0.2524	0.1436	0.2367	-0.0277 ± 0.0064	0.0129 ± 0.0062

Deuterium results							
$\langle x \rangle$	$\langle y \rangle$	$\langle Q^2 \rangle$	$\langle z \rangle$	$\langle P_{h\perp} \rangle$	$\langle x_F \rangle$	$2\langle \cos \boldsymbol{\phi_h} \rangle$	$2\langle \cos \mathbf{2}\boldsymbol{\phi_h} \rangle$
0.1050	0.5194	2.8220	0.2599	0.2731	0.2354	-0.0268 ± 0.0083	-0.0040 ± 0.0072
0.1050	0.5206	2.8266	0.2703	0.4160	0.2304	-0.0355 ± 0.0093	-0.0649 ± 0.0084
0.1048	0.5262	2.8512	0.2827	0.5728	0.2208	0.1188 ± 0.0218	-0.0511 ± 0.0277
0.1053	0.5140	2.8006	0.3604	0.1558	0.3425	-0.0412 ± 0.0070	-0.0251 ± 0.0072
0.1055	0.5167	2.8183	0.3645	0.2777	0.3403	-0.0161 ± 0.0064	0.0170 ± 0.0057
0.1050	0.5169	2.8084	0.3651	0.6032	0.3071	-0.1110 ± 0.0081	-0.0117 ± 0.0071
0.1042	0.5211	2.8091	0.3779	0.8663	0.2774	-0.2116 ± 0.0394	-0.0092 ± 0.0215
0.1060	0.5062	2.7738	0.5085	0.1723	0.4860	-0.0084 ± 0.0139	-0.0448 ± 0.0137
0.1054	0.5161	2.8142	0.5158	0.2771	0.4897	-0.1265 ± 0.0073	0.0209 ± 0.0124
0.1055	0.5163	2.8167	0.5170	0.6065	0.4665	-0.2866 ± 0.0127	-0.1225 ± 0.0117
0.1051	0.5161	2.8058	0.5167	0.8970	0.4296	-0.2393 ± 0.0262	-0.0189 ± 0.0206
0.1025	0.4850	2.5705	0.6418	0.1870	0.6140	0.6829 ± 0.0540	0.2991 ± 0.0490
0.1057	0.5114	2.7968	0.6656	0.2793	0.6356	-0.2534 ± 0.0092	-0.0531 ± 0.0093
0.1053	0.5135	2.7969	0.6668	0.4233	0.6303	-0.1860 ± 0.0121	-0.0957 ± 0.0183
0.1052	0.5151	2.8025	0.6661	0.6048	0.6176	-0.1961 ± 0.0172	0.0557 ± 0.0155
0.1056	0.5163	2.8212	0.6671	0.8900	0.5912	-0.2015 ± 0.0419	0.0120 ± 0.0388
0.1046	0.5052	2.7337	0.8273	0.2914	0.7921	-0.1186 ± 0.0163	0.1178 ± 0.0163
0.1052	0.5118	2.7847	0.8308	0.4231	0.7910	-0.0842 ± 0.0149	-0.0335 ± 0.0145
0.1049	0.5117	2.7767	0.8283	0.6005	0.7790	-0.1432 ± 0.0193	-0.2685 ± 0.0186
0.1043	0.5134	2.7707	0.8229	0.8781	0.7523	-0.1963 ± 0.0742	-0.1704 ± 0.0663
0.1054	0.6463	3.5223	0.2504	0.1499	0.2375	-0.1696 ± 0.0140	-0.1989 ± 0.0117
0.1046	0.6473	3.5030	0.2573	0.2740	0.2374	-0.1053 ± 0.0141	-0.0581 ± 0.0106
0.1048	0.6495	3.5201	0.2773	0.5855	0.2249	0.0246 ± 0.0134	0.0582 ± 0.0120
0.1044	0.6518	3.5206	0.2925	0.7917	0.2091	1.3412 ± 0.1171	-0.1984 ± 0.0780
0.1059	0.6452	3.5348	0.3561	0.1655	0.3415	0.0835 ± 0.0195	0.0709 ± 0.0156
0.1054	0.6471	3.5275	0.3627	0.2776	0.3433	-0.1539 ± 0.0133	-0.0913 ± 0.0105
0.1044	0.6467	3.4916	0.3647	0.6059	0.3181	-0.0609 ± 0.0095	0.0016 ± 0.0088
0.1052	0.6472	3.5210	0.3703	0.8781	0.2867	-0.2227 ± 0.0218	0.0856 ± 0.0167
0.1054	0.6464	3.5244	0.5140	0.2786	0.4930	0.0748 ± 0.0175	0.0848 ± 0.0141
0.1046	0.6465	3.4986	0.5139	0.8970	0.4445	-0.1134 ± 0.0286	-0.1198 ± 0.0265
0.1045	0.6424	3.4724	0.6601	0.2943	0.6359	-0.1606 ± 0.0251	-0.1020 ± 0.0213
0.1047	0.6463	3.4988	0.6654	0.4235	0.6364	-0.1876 ± 0.0304	-0.1200 ± 0.0245
0.1046	0.6459	3.4946	0.6653	0.6059	0.6266	-0.3791 ± 0.0402	-0.1871 ± 0.0310
0.1067	0.6474	3.5743	0.6661	0.9016	0.6045	-0.1151 ± 0.0775	-0.0388 ± 0.0688
0.1061	0.6452	3.5391	0.8351	0.4204	0.8034	-0.1589 ± 0.0370	-0.3212 ± 0.0332
0.1053	0.6455	3.5146	0.8273	0.6080	0.7877	-0.0745 ± 0.0611	0.1351 ± 0.0456
0.1047	0.6459	3.4985	0.8248	0.8955	0.7674	0.0860 ± 0.2434	0.1284 ± 0.1651
0.1051	0.7681	4.1747	0.2480	0.1556	0.2370	-0.3010 ± 0.0437	-0.0519 ± 0.0266
0.1048	0.7710	4.1797	0.2548	0.2754	0.2381	-0.0710 ± 0.0223	-0.1346 ± 0.0150
0.1046	0.7700	4.1646	0.2623	0.4175	0.2350	0.0912 ± 0.0120	0.1424 ± 0.0106
0.1048	0.7720	4.1839	0.2729	0.5890	0.2281	-0.0639 ± 0.0106	-0.1188 ± 0.0181
0.1051	0.7628	4.1458	0.3481	0.1749	0.3356	-0.5787 ± 0.0639	-0.1428 ± 0.0375

Deuterium results							
$\langle x \rangle$	$\langle y \rangle$	$\langle Q^2 \rangle$	$\langle z \rangle$	$\langle P_{h\perp} \rangle$	$\langle x_F \rangle$	$2\langle \cos \phi_h \rangle$	$2\langle \cos 2\phi_h \rangle$
0.1047	0.7694	4.1680	0.3624	0.2772	0.3461	-0.0896 ± 0.0313	-0.0579 ± 0.0194
0.1050	0.7702	4.1817	0.3634	0.4215	0.3393	0.0003 ± 0.0225	0.0613 ± 0.0160
0.1050	0.7691	4.1781	0.3652	0.6063	0.3261	-0.1564 ± 0.0106	0.0454 ± 0.0099
0.1049	0.7707	4.1806	0.3670	0.8861	0.2954	0.0022 ± 0.0164	-0.1130 ± 0.0145
0.1048	0.7654	4.1493	0.5091	0.2866	0.4912	0.1773 ± 0.0570	0.0081 ± 0.0338
0.1050	0.7681	4.1700	0.5140	0.4224	0.4907	0.0061 ± 0.0515	-0.0328 ± 0.0560
0.1053	0.7690	4.1898	0.5133	0.6091	0.4792	-0.4198 ± 0.0357	-0.2413 ± 0.0261
0.1044	0.7675	4.1460	0.5143	0.8967	0.4560	0.1503 ± 0.0331	0.0051 ± 0.0321
0.1049	0.7682	4.1673	0.6616	0.4204	0.6373	0.2705 ± 0.1005	-0.1750 ± 0.0564
0.1048	0.7686	4.1669	0.6636	0.6052	0.6311	-0.7130 ± 0.0785	-0.1813 ± 0.0890
0.1038	0.7665	4.1171	0.6644	0.9090	0.6119	-0.3486 ± 0.1011	-0.1900 ± 0.0911
0.1056	0.7633	4.1704	0.8252	0.4336	0.7981	0.5221 ± 0.1671	0.4945 ± 0.0970
0.1030	0.7719	4.1104	0.8190	0.8787	0.7721	-0.0160 ± 0.3763	-0.0354 ± 0.2600
0.1930	0.3656	3.6493	0.2609	0.1361	0.2374	0.0137 ± 0.0096	-0.0023 ± 0.0092
0.1929	0.3678	3.6690	0.2698	0.2707	0.2325	0.1859 ± 0.0222	-0.0533 ± 0.0132
0.1849	0.4000	3.8260	0.2912	0.5364	0.2122	-0.8922 ± 1.0433	0.3548 ± 0.6837
0.1948	0.3603	3.6293	0.3625	0.1442	0.3355	0.0144 ± 0.0086	-0.0117 ± 0.0088
0.1944	0.3622	3.6420	0.3646	0.2773	0.3271	0.0543 ± 0.0096	-0.0312 ± 0.0069
0.1937	0.3628	3.6348	0.3656	0.4212	0.3093	0.0165 ± 0.0271	-0.0672 ± 0.0247
0.1927	0.3671	3.6586	0.3719	0.5929	0.2848	0.4627 ± 0.0820	-0.2399 ± 0.0643
0.1938	0.3578	3.5855	0.5147	0.1553	0.4813	0.0199 ± 0.0116	0.0938 ± 0.0211
0.1946	0.3620	3.6446	0.5178	0.2793	0.4774	-0.0915 ± 0.0101	0.0237 ± 0.0158
0.1939	0.3621	3.6308	0.5199	0.6035	0.4417	-0.2784 ± 0.0424	0.0105 ± 0.0371
0.1954	0.3485	3.5219	0.6673	0.1656	0.6256	-0.1216 ± 0.0183	0.3064 ± 0.0368
0.1959	0.3571	3.6179	0.6710	0.2777	0.6248	0.0069 ± 0.0112	-0.1579 ± 0.0182
0.1952	0.3589	3.6235	0.6698	0.4231	0.6134	-0.4779 ± 0.0168	0.1334 ± 0.0213
0.1950	0.3590	3.6206	0.6699	0.6042	0.5942	-0.2769 ± 0.0316	-0.0639 ± 0.0304
0.1947	0.3609	3.6335	0.6669	0.8771	0.5497	-0.2239 ± 0.1801	-0.1567 ± 0.1281
0.1952	0.3583	3.6178	0.8265	0.2781	0.7741	-0.0951 ± 0.0153	0.0741 ± 0.0266
0.1950	0.3616	3.6476	0.8255	0.4202	0.7653	-0.0571 ± 0.0192	-0.1590 ± 0.0256
0.1950	0.3592	3.6231	0.8191	0.6032	0.7429	-0.1324 ± 0.0274	-0.0734 ± 0.0331
0.1919	0.5159	5.1200	0.2546	0.1432	0.2376	0.0472 ± 0.0078	0.0330 ± 0.0140
0.1918	0.5182	5.1413	0.2619	0.2727	0.2351	0.0425 ± 0.0085	-0.0014 ± 0.0143
0.1917	0.5210	5.1647	0.2726	0.4154	0.2291	0.1100 ± 0.0167	-0.0064 ± 0.0269
0.1923	0.5133	5.1038	0.3607	0.1551	0.3412	-0.0499 ± 0.0108	-0.0320 ± 0.0183
0.1931	0.5155	5.1471	0.3642	0.2779	0.3377	-0.0826 ± 0.0069	-0.0541 ± 0.0115
0.1966	0.5120	5.2051	0.8243	0.6062	0.7702	-0.2051 ± 0.0373	-0.1682 ± 0.0376
0.1935	0.6473	6.4786	0.3650	0.6032	0.3141	-0.0806 ± 0.0279	-0.0536 ± 0.0269
0.1903	0.6488	6.3876	0.3712	0.8722	0.2808	-0.3162 ± 0.0994	0.1742 ± 0.0649
0.1926	0.6342	6.3190	0.4863	0.1852	0.4669	0.1500 ± 0.1128	-0.0047 ± 0.1149
0.1944	0.6470	6.5040	0.5152	0.2793	0.4924	-0.0560 ± 0.0306	-0.0569 ± 0.0293
0.1942	0.6461	6.4890	0.5160	0.6081	0.4717	-0.1915 ± 0.0475	-0.1511 ± 0.0474

Deuterium results							
$\langle x \rangle$	$\langle y \rangle$	$\langle Q^2 \rangle$	$\langle z \rangle$	$\langle P_{h\perp} \rangle$	$\langle x_F \rangle$	$2\langle \cos \boldsymbol{\phi_h} \rangle$	$2\langle \cos \mathbf{2}\boldsymbol{\phi_h} \rangle$
0.1973	0.6469	6.6004	0.5189	0.8992	0.4424	-0.2600 ± 0.0878	-0.1021 ± 0.0827
0.1980	0.6427	6.5802	0.6616	0.2937	0.6352	0.1311 ± 0.0679	0.1923 ± 0.0623
0.1919	0.6454	6.4063	0.6667	0.4219	0.6352	-0.5655 ± 0.0429	-0.1768 ± 0.0450
0.1932	0.6467	6.4610	0.6627	0.6057	0.6205	-0.1010 ± 0.0730	-0.0238 ± 0.0709
0.1950	0.6500	6.5552	0.6630	0.9108	0.5946	-0.0459 ± 0.3035	-0.0324 ± 0.2307
0.1936	0.6453	6.4625	0.8248	0.4224	0.7905	0.3696 ± 0.0710	0.0332 ± 0.0637
0.1861	0.6480	6.2367	0.8138	0.9086	0.7504	-0.1039 ± 0.3347	-0.2485 ± 0.3363
0.1913	0.7674	7.5942	0.2486	0.1552	0.2367	0.3669 ± 0.1233	0.4170 ± 0.0879
0.1930	0.7698	7.6839	0.2563	0.2745	0.2380	0.2763 ± 0.1028	0.1179 ± 0.0703
0.1933	0.7694	7.6915	0.2642	0.4163	0.2343	-0.0376 ± 0.0658	-0.0391 ± 0.0593
0.1962	0.7619	7.7298	0.3456	0.1738	0.3320	0.6305 ± 0.2026	0.3448 ± 0.1626
0.1930	0.7675	7.6609	0.3631	0.2777	0.3453	-0.1908 ± 0.0814	0.0047 ± 0.0663
0.1923	0.7688	7.6445	0.3651	0.4220	0.3386	-0.2405 ± 0.0939	-0.0397 ± 0.0731
0.1928	0.7688	7.6652	0.3647	0.6052	0.3217	-0.3172 ± 0.0513	-0.0564 ± 0.0512
0.1896	0.7695	7.5478	0.3683	0.8859	0.2899	-0.0608 ± 0.1104	0.1639 ± 0.0887
0.1918	0.7671	7.6079	0.5125	0.2875	0.4930	0.0573 ± 0.1414	0.4013 ± 0.0988
0.1934	0.7690	7.6936	0.5154	0.4222	0.4900	0.1482 ± 0.1455	-0.4781 ± 0.1152
0.1925	0.7696	7.6635	0.5118	0.6097	0.4744	-0.6203 ± 0.1184	-0.3672 ± 0.0941
0.1919	0.7693	7.6356	0.5154	0.8938	0.4519	-0.6425 ± 0.1746	-0.0361 ± 0.1852
0.1960	0.7518	7.6224	0.6514	0.3080	0.6285	1.0555 ± 0.8024	0.5322 ± 0.4558
0.1958	0.7656	7.7532	0.6665	0.4235	0.6397	0.6260 ± 0.3100	0.0043 ± 0.1894
0.1934	0.7650	7.6536	0.6649	0.6023	0.6294	0.2315 ± 0.2720	0.3503 ± 0.2118
0.1913	0.7609	7.5294	0.6598	0.9002	0.6025	0.3770 ± 0.5639	-0.0171 ± 0.4721
0.1966	0.7689	7.8176	0.8177	0.4295	0.7887	0.3450 ± 0.5041	-0.4279 ± 0.3234
0.1945	0.7601	7.6444	0.8340	0.9019	0.7802	0.1322 ± 0.9115	-0.4976 ± 0.8734
0.3486	0.3674	6.6247	0.2648	0.1356	0.2375	-0.2341 ± 0.0939	0.1495 ± 0.0594
0.3441	0.3715	6.6119	0.2746	0.2678	0.2318	0.0843 ± 0.3897	0.0283 ± 0.1463
0.3363	0.3823	6.6496	0.2859	0.4021	0.2204	1.0396 ± 1.1563	-0.3363 ± 0.4425
0.3522	0.3615	6.5853	0.3621	0.1441	0.3312	0.3353 ± 0.0525	-0.3276 ± 0.0478
0.3521	0.3638	6.6265	0.3639	0.2766	0.3202	-0.2282 ± 0.1188	0.0321 ± 0.0547
0.3454	0.3682	6.5778	0.3793	0.5856	0.2785	-0.8171 ± 0.5960	0.2303 ± 0.2089
0.3520	0.3625	6.6008	0.5203	0.2768	0.4738	-0.1557 ± 0.1153	0.2261 ± 0.0628
0.3512	0.3615	6.5666	0.6690	0.2785	0.6170	-0.2852 ± 0.1781	0.1406 ± 0.0880
0.3519	0.3618	6.5856	0.6690	0.4218	0.6044	-0.6403 ± 0.1126	0.3287 ± 0.0613
0.3480	0.3668	6.6022	0.6677	0.8702	0.5322	-1.8179 ± 1.3309	0.6310 ± 0.5207
0.3428	0.3474	6.1593	0.8066	0.1782	0.7516	-1.9551 ± 1.1406	1.9361 ± 0.5787
0.3467	0.3654	6.5528	0.8218	0.2773	0.7638	-0.5019 ± 0.1835	-0.1383 ± 0.1159
0.3443	0.3658	6.5135	0.8194	0.4224	0.7515	-0.8404 ± 0.1860	0.3653 ± 0.1022
0.3364	0.3684	6.4101	0.8069	0.8619	0.6836	-1.0513 ± 1.5879	0.3931 ± 0.6280
0.3629	0.5120	9.6112	0.2572	0.1429	0.2368	0.0543 ± 0.0294	-0.0806 ± 0.0307
0.3600	0.5198	9.6772	0.2661	0.2722	0.2341	0.1338 ± 0.0401	-0.0745 ± 0.0343
0.3486	0.5222	9.4140	0.2775	0.4120	0.2264	0.3292 ± 0.0934	-0.0345 ± 0.0664

Deuterium results							
$\langle x \rangle$	$\langle y \rangle$	$\langle Q^2 \rangle$	$\langle z \rangle$	$\langle P_{h\perp} \rangle$	$\langle x_F \rangle$	$2\langle \mathbf{\cos \phi_h} \rangle$	$2\langle \mathbf{\cos 2\phi_h} \rangle$
0.3710	0.5111	9.8084	0.3615	0.1556	0.3384	-0.0239 ± 0.0374	0.1019 ± 0.0412
0.3681	0.5145	9.7950	0.3654	0.2774	0.3338	0.0093 ± 0.0304	0.1311 ± 0.0270
0.3622	0.5179	9.7029	0.3678	0.5955	0.2915	0.2474 ± 0.1308	-0.0116 ± 0.0767
0.3483	0.5263	9.4820	0.3947	0.8582	0.2681	-1.2091 ± 1.5236	0.3267 ± 0.5815
0.3667	0.5022	9.5242	0.5059	0.1689	0.4778	-0.0494 ± 0.0832	-0.2267 ± 0.0841
0.3714	0.5161	9.9133	0.5167	0.2783	0.4831	-0.0780 ± 0.0433	0.0403 ± 0.0372
0.3643	0.5139	9.6823	0.5203	0.6074	0.4530	0.1273 ± 0.0889	-0.2641 ± 0.0653
0.3584	0.5186	9.6150	0.5198	0.8753	0.4083	-0.0772 ± 0.5179	0.2096 ± 0.2832
0.3811	0.4821	9.5039	0.6505	0.1873	0.6149	0.6232 ± 0.2496	-0.5326 ± 0.2617
0.3749	0.5111	9.9104	0.6699	0.2801	0.6318	0.0532 ± 0.0488	-0.2266 ± 0.0483
0.3794	0.5127	10.0611	0.6705	0.4220	0.6231	-0.4130 ± 0.0567	-0.0795 ± 0.0493
0.3765	0.5144	10.0171	0.6699	0.6061	0.6055	-0.3719 ± 0.0797	0.1595 ± 0.0591
0.3695	0.5061	9.6704	0.8226	0.2907	0.7787	-0.3621 ± 0.0563	-0.1726 ± 0.0619
0.3690	0.5116	9.7650	0.8258	0.4223	0.7754	-0.0965 ± 0.0771	-0.0028 ± 0.0703
0.3690	0.5115	9.7600	0.8208	0.6026	0.7569	0.2710 ± 0.0704	-0.5740 ± 0.0695
0.3657	0.5142	9.7258	0.8151	0.8757	0.7219	0.3316 ± 0.2962	-0.4732 ± 0.3291
0.3716	0.6472	12.4373	0.2536	0.1480	0.2370	0.4882 ± 0.1145	0.6736 ± 0.1032
0.3653	0.6482	12.2454	0.2614	0.2745	0.2352	-0.2718 ± 0.0937	-0.0708 ± 0.1005
0.3698	0.6448	12.3341	0.3611	0.1682	0.3421	-0.4774 ± 0.1432	-1.2601 ± 0.1404
0.3650	0.6459	12.1928	0.3646	0.2786	0.3393	0.2735 ± 0.0839	0.0586 ± 0.0839
0.3619	0.6455	12.0801	0.3681	0.5993	0.3064	-0.1614 ± 0.1083	0.4873 ± 0.1173
0.3706	0.6462	12.3880	0.5158	0.2790	0.4889	-0.4166 ± 0.0782	0.3866 ± 0.0837
0.3592	0.6399	11.8872	0.5139	0.8962	0.4195	-1.0476 ± 0.5393	0.1087 ± 0.5746
0.3852	0.6453	12.8547	0.6610	0.2865	0.6302	0.7122 ± 0.3141	-0.3692 ± 0.2593
0.3839	0.6454	12.8166	0.6641	0.4218	0.6262	0.2006 ± 0.2626	0.0904 ± 0.2387
0.3701	0.6439	12.3261	0.6647	0.6042	0.6136	0.8005 ± 0.3541	0.5153 ± 0.2562
0.3774	0.6486	12.6579	0.8179	0.4249	0.7776	0.2840 ± 0.2090	-0.1086 ± 0.2482
0.3764	0.6451	12.5582	0.8227	0.6075	0.7711	0.4837 ± 0.3638	-0.4330 ± 0.3461

Appendix B

Additional figures

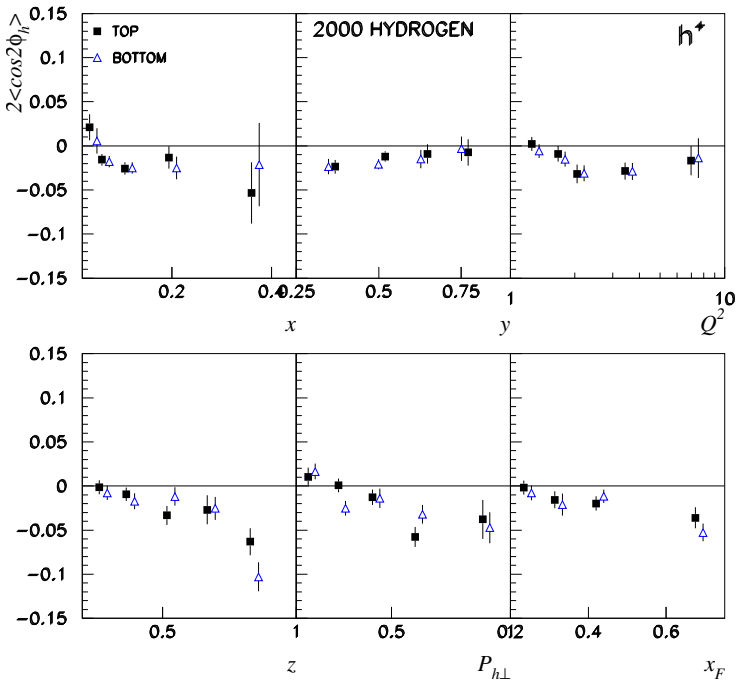

Figure B.1: $\langle \mathbf{cos\ 2}\phi_{\boldsymbol{h}} \rangle$ moments for positive hadrons extracted from 2000 data on hydrogen target for scattered lepton detected in the top half (black closed squares) or in the bottom half (blue open triangles).

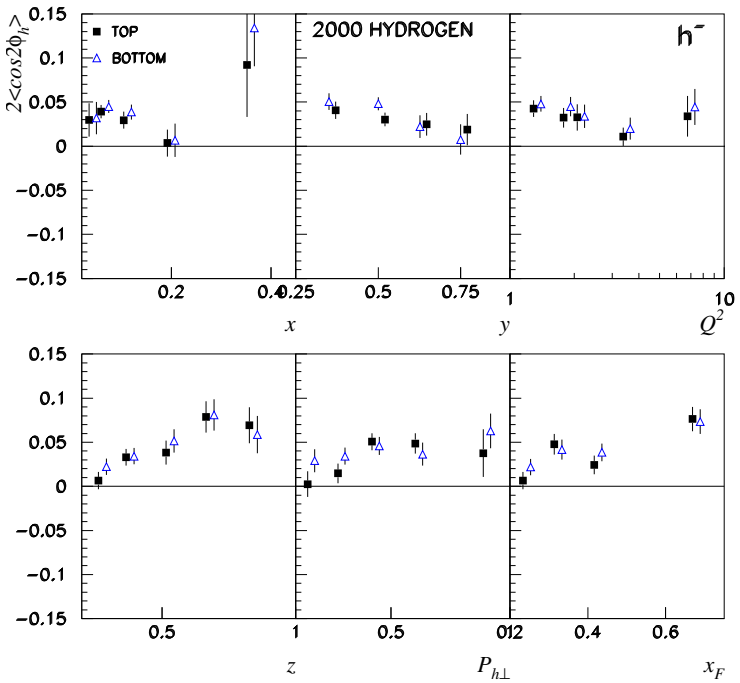

Figure B.2: $\langle \cos 2\phi_h \rangle$ moments for negative hadrons extracted from 2000 data on hydrogen target for scattered lepton detected in the top half (black closed squares) or in the bottom half (blue open triangles).

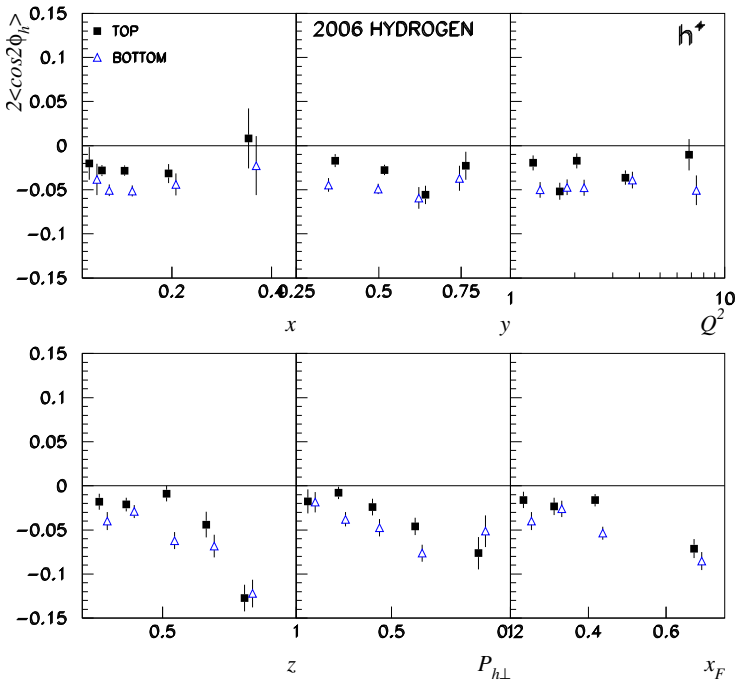

Figure B.3: $\langle \cos 2\phi_h \rangle$ moments for positive hadrons extracted from 2006 data on hydrogen target for scattered lepton detected in the top half (black closed squares) or in the bottom half (blue open triangles).

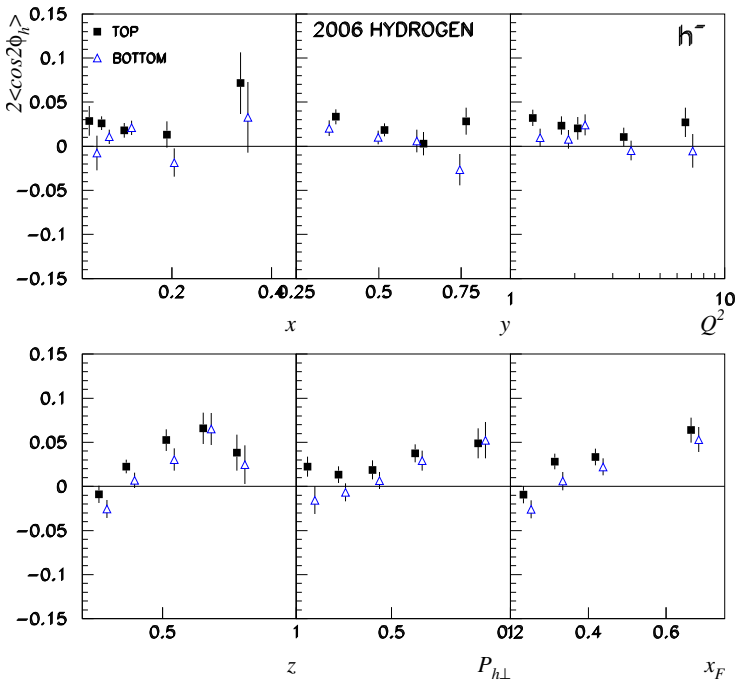

Figure B.4: $\langle \cos 2\phi_h \rangle$ moments for negative hadrons extracted from 2006 data on hydrogen target for scattered lepton detected in the top half (black closed squares) or in the bottom half (blue open triangles).

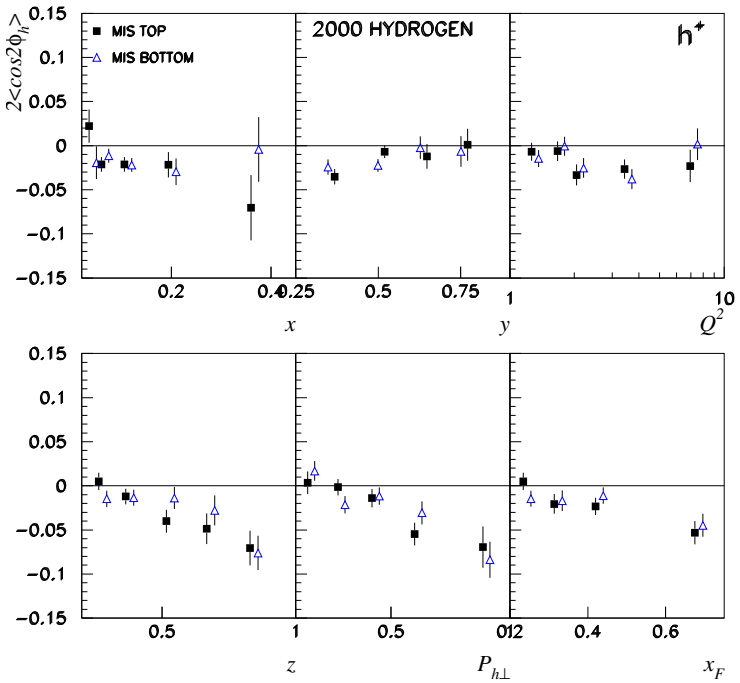

Figure B.5: $\langle \cos 2\phi_h \rangle$ moments for positive hadrons extracted from 2000 data on hydrogen target for scattered lepton detected in the top half (black closed squares) or in the bottom half (blue open triangles) with a misaligned MC production, where the misalignment is defined in table 5.3.

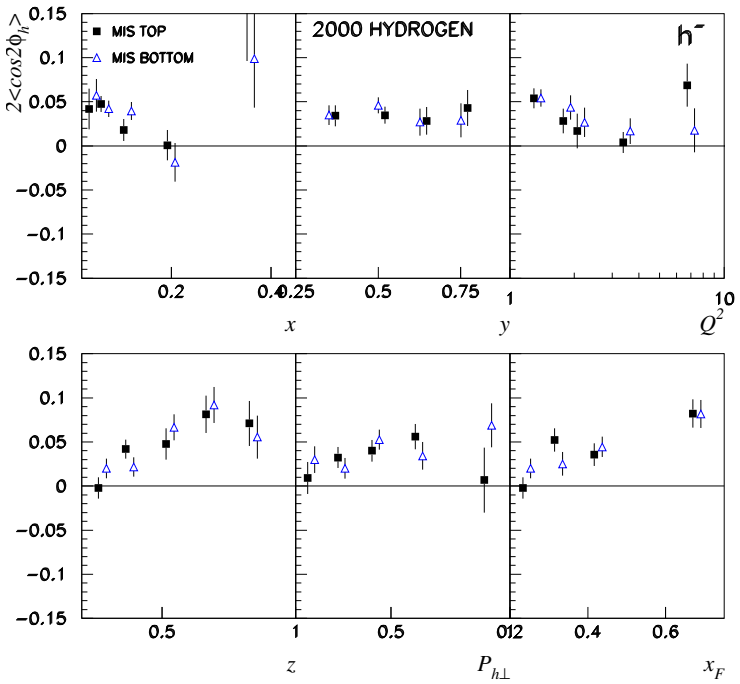

Figure B.6: $\langle \cos 2\phi_h \rangle$ moments for negative hadrons extracted from 2000 data on hydrogen target for scattered lepton detected in the top half (black closed squares) or in the bottom half (blue open triangles) with a misaligned MC production, where the misalignment is defined in table 5.3.

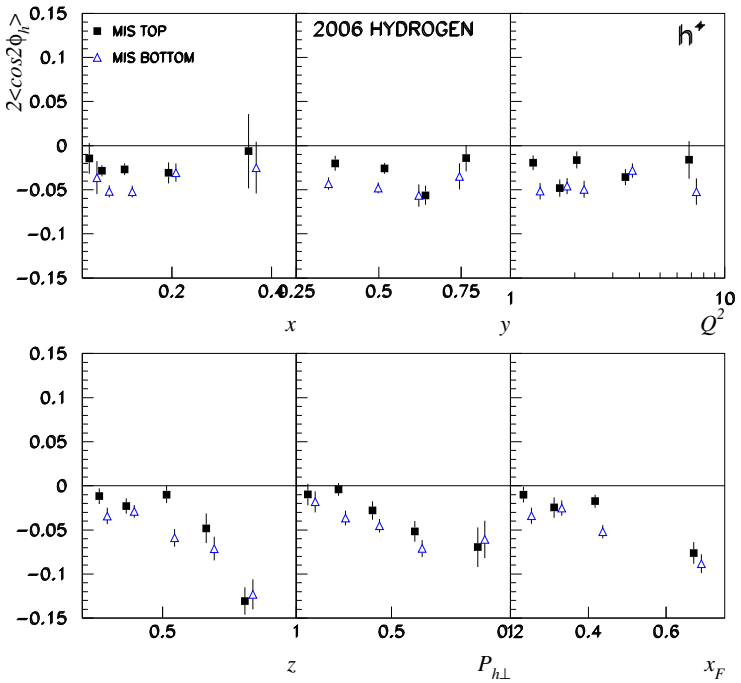

Figure B.7: $\langle \cos 2\phi_h \rangle$ moments for positive hadrons extracted from 2006 data on hydrogen target for scattered lepton detected in the top half (black closed squares) or in the bottom half (blue open triangles) with a misaligned MC production.

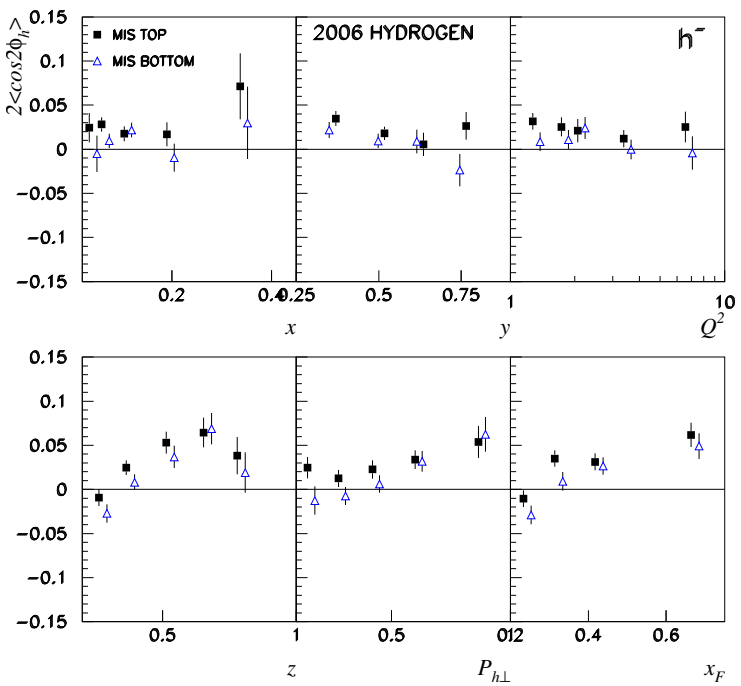

Figure B.8: $\langle \cos 2\phi_h \rangle$ moments for negative hadrons extracted from 2006 data on hydrogen target for scattered lepton detected in the top half (black closed squares) or in the bottom half (blue open triangles) with a misaligned MC production.

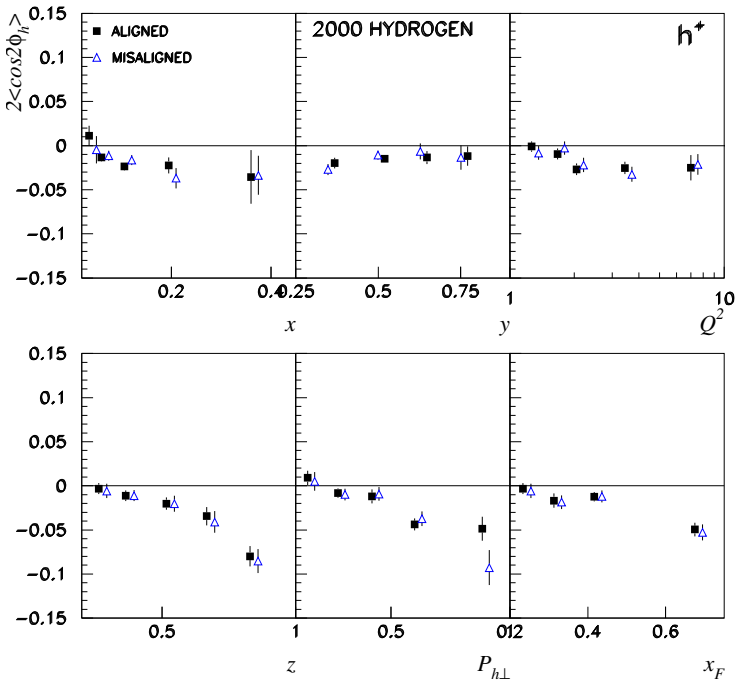

Figure B.9: Comparison between $\langle \cos 2\phi_h \rangle$ moments extracted for positive hadrons from 2000 data on hydrogen target with a perfectly aligned MC production (black closed squares) and with a misaligned MC production (blue open triangles), where the misalignment is defined in table 5.3.

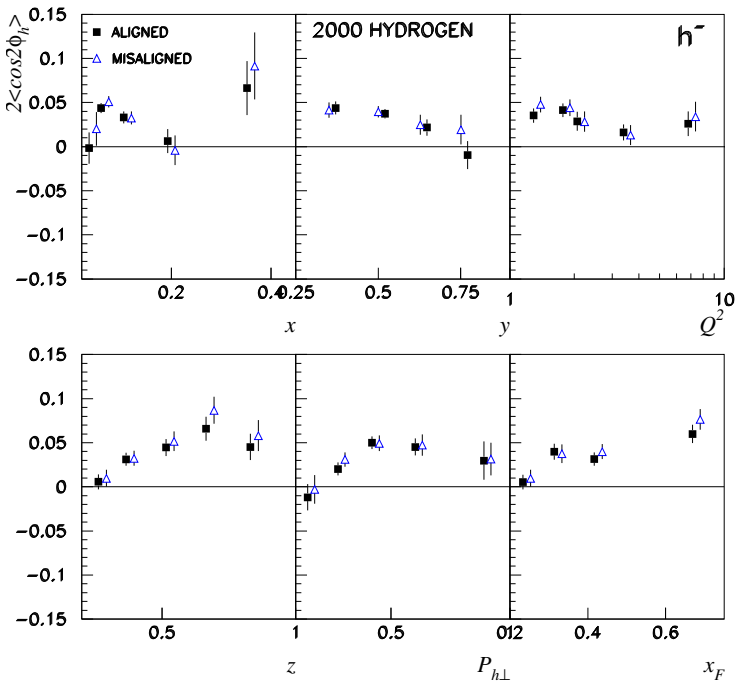

Figure B.10: Comparison between $\langle \cos 2\phi_h \rangle$ moments extracted for negative hadrons from 2000 data on hydrogen target with a perfectly aligned MC production (black closed squares) and with a misaligned MC production (blue open triangles), where the misalignment is defined in table 5.3.

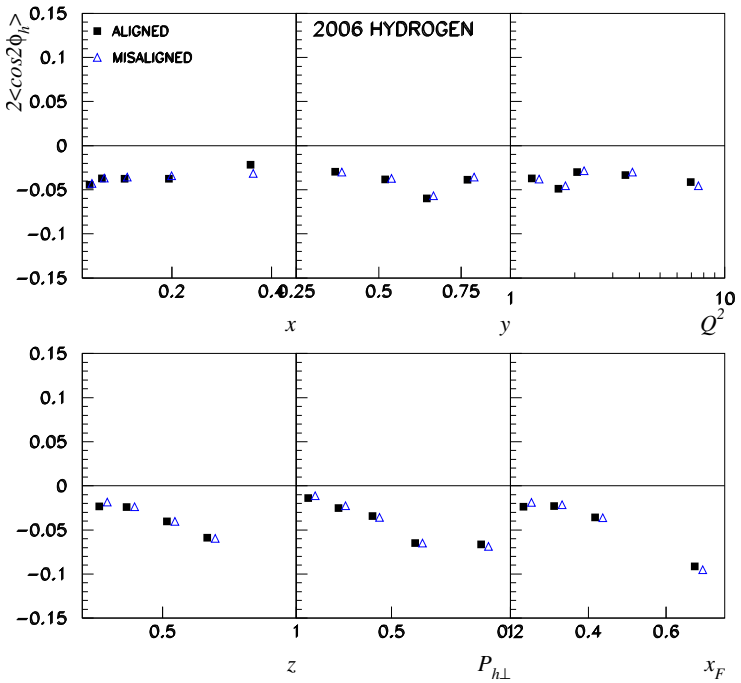

Figure B.11: Comparison between $\langle \cos 2\phi_h \rangle$ moments extracted for positive hadrons from 2006 data on hydrogen target with a perfectly aligned MC production (black closed squares) and with a misaligned MC production (blue open triangles).

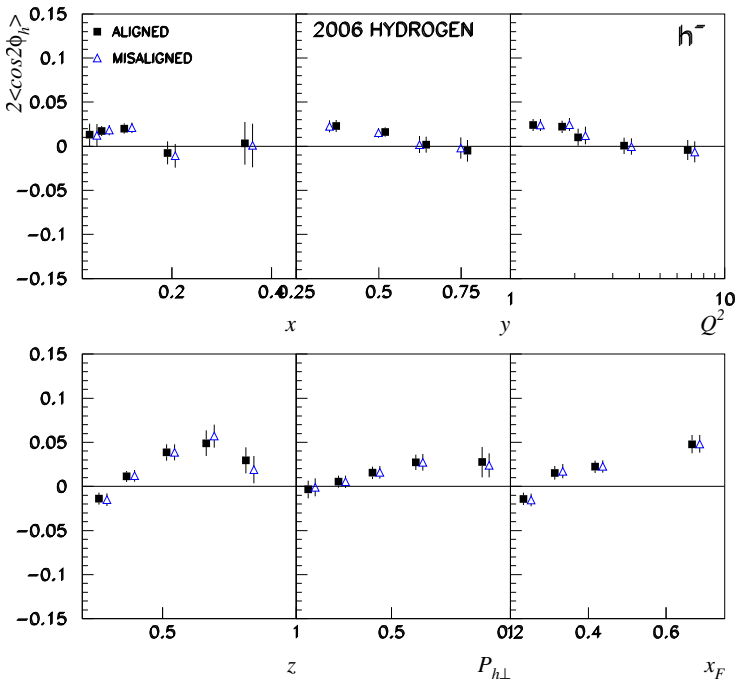

Figure B.12: Comparison between $\langle \cos 2\phi_h \rangle$ moments extracted for negative hadrons from 2006 data on hydrogen target with a perfectly aligned MC production (black closed squares) and with a misaligned MC production (blue open triangles).

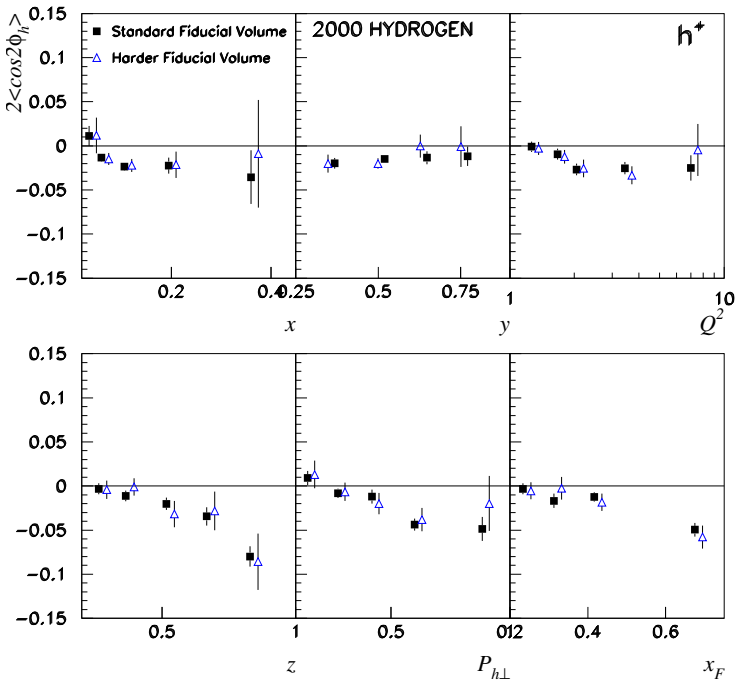

Figure B.13: $\langle \cos 2\phi_h \rangle$ moments for positive hadrons extracted in 2000 hydrogen data with the standard (solid squares) and a more restrictive (open triangles) fiducial volume.

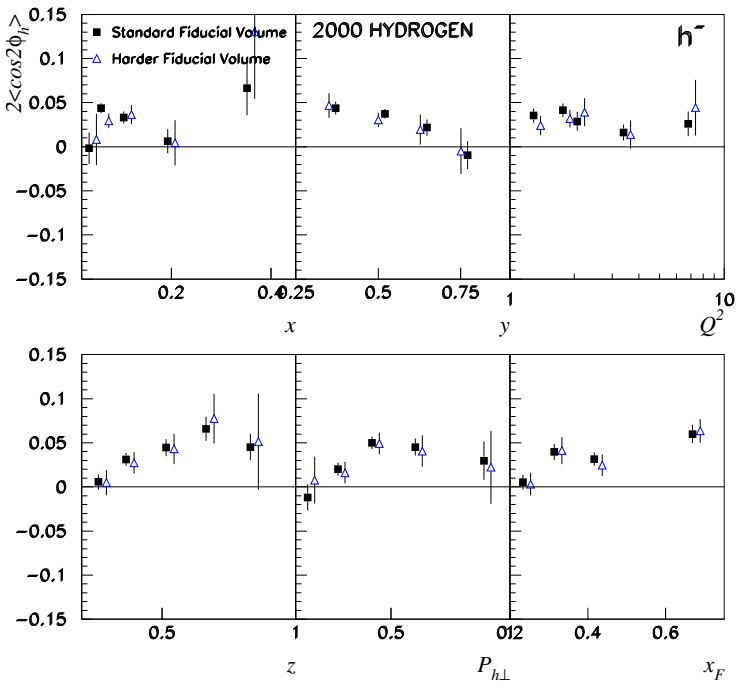

Figure B.14: $\langle \cos 2\phi_h \rangle$ moments for negative hadrons extracted in 2000 hydrogen data with the standard (solid squares) and a more restrictive (open triangles) fiducial volume.

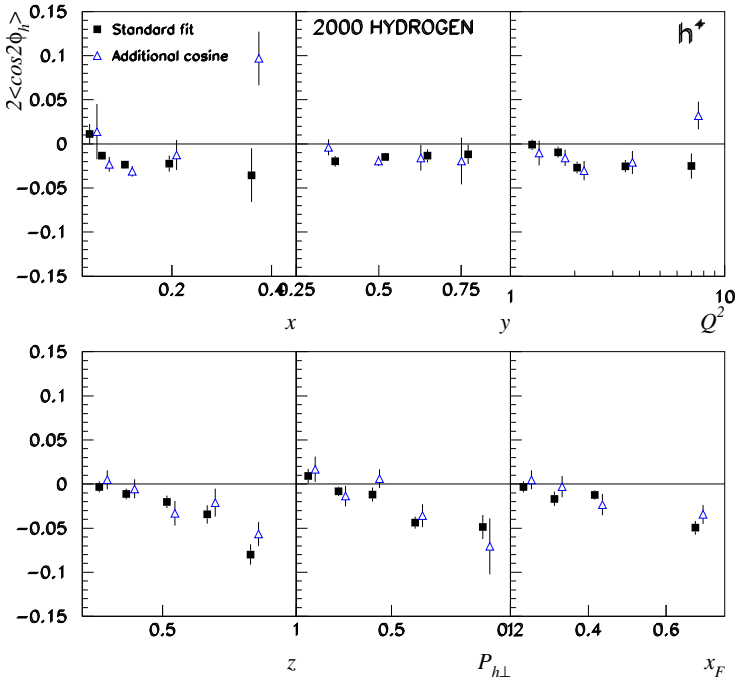

Figure B.15: $\langle \cos 2\phi_h \rangle$ moments for positive hadrons extracted in the 2000 data with hydrogen target: the solid squares are the moments extracted with standard fit function, while the open triangles are the moments with the additional cosine moment as in equation 5.19.

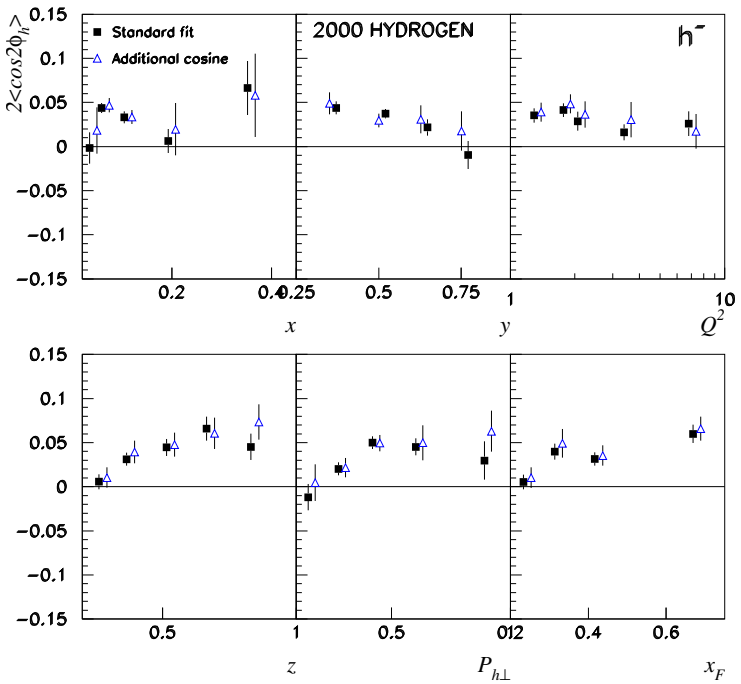

Figure B.16: $\langle \cos 2\phi_h \rangle$ moments for negative hadrons extracted in the 2000 data with hydrogen target: the solid squares are the moments extracted with standard fit function, while the open triangles are the moments with the additional cosine moment as in equation 5.19.

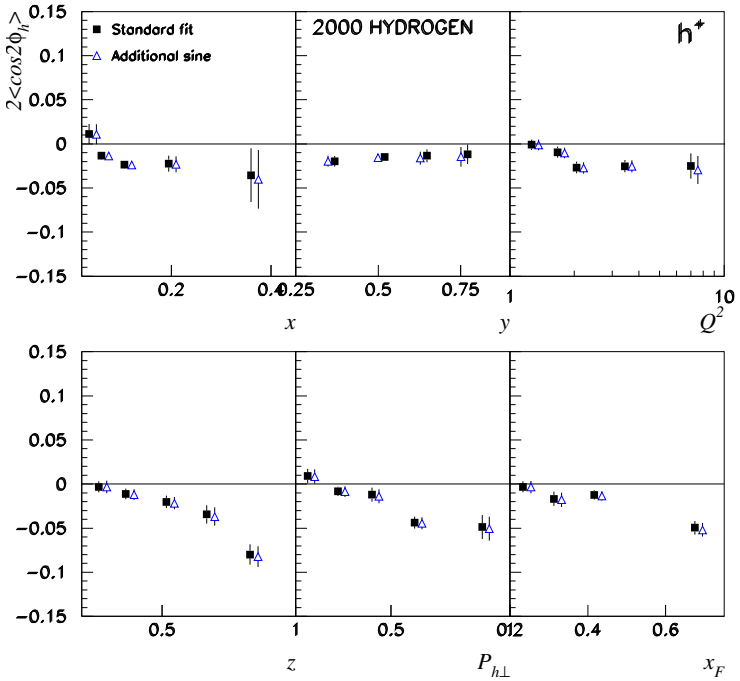

Figure B.17: $\langle \cos 2\phi_h \rangle$ moments for positive hadrons extracted in the 2000 data with hydrogen target: the solid squares are the moments extracted with standard fit function, while the open triangles are the moments with the additional sine moment of equation 5.20.

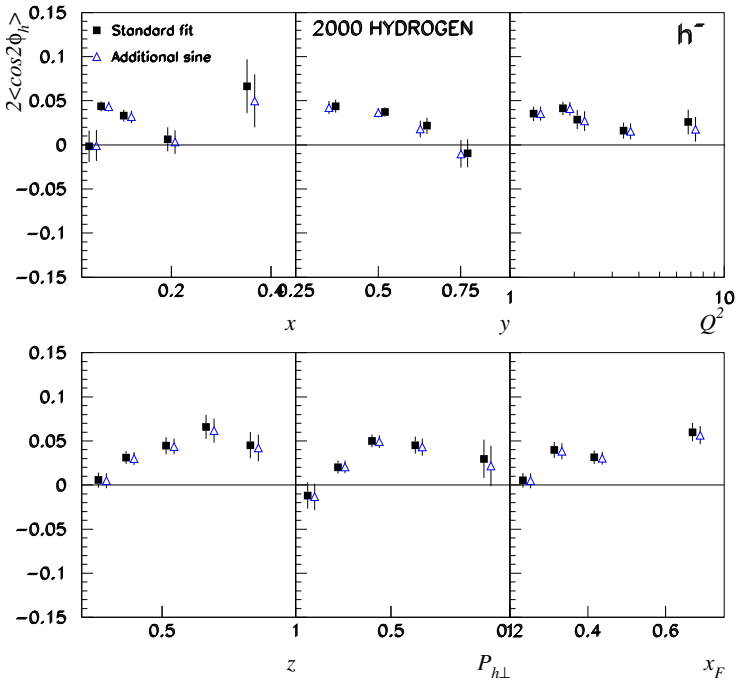

Figure B.18: $\langle \cos 2\phi_h \rangle$ moments for negative hadrons extracted in the 2000 data with hydrogen target: the solid squares are the moments extracted with standard fit function, while the open triangles are the moments with the additional sine moment of equation 5.20.

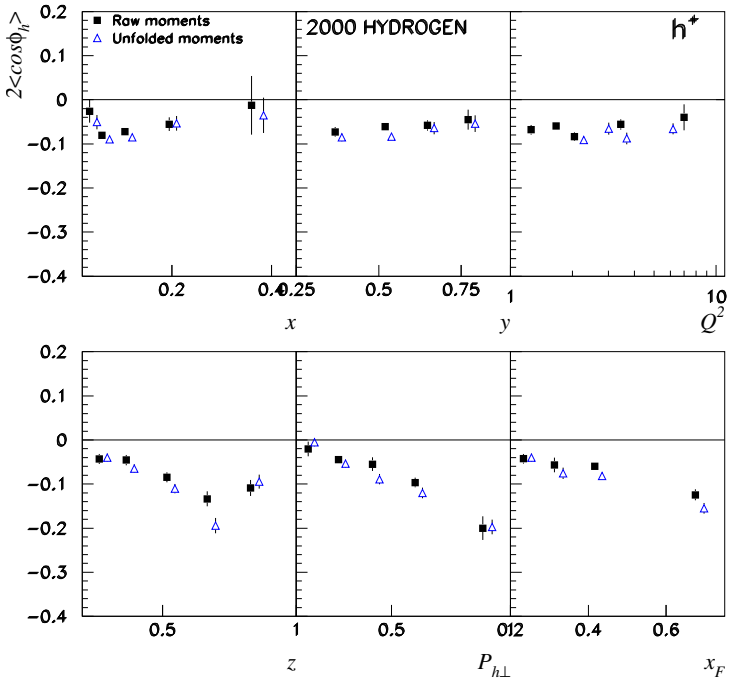

Figure B.19: Comparison between the raw $\langle \cos \phi_h \rangle$ moments (black closed square) and the unfolded moments (blue open triangles) for positive hadrons from data collected with deuterium target in 2000.

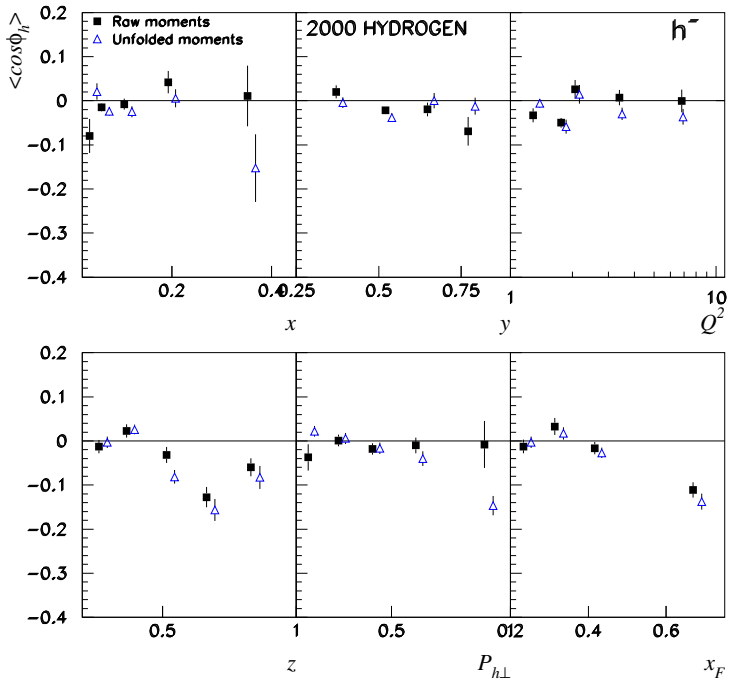

Figure B.20: Comparison between the raw $\langle \cos \phi_h \rangle$ moments (black closed square) and the unfolded moments (blue open triangles) for negative hadrons from data collected with deuterium target in 2000.

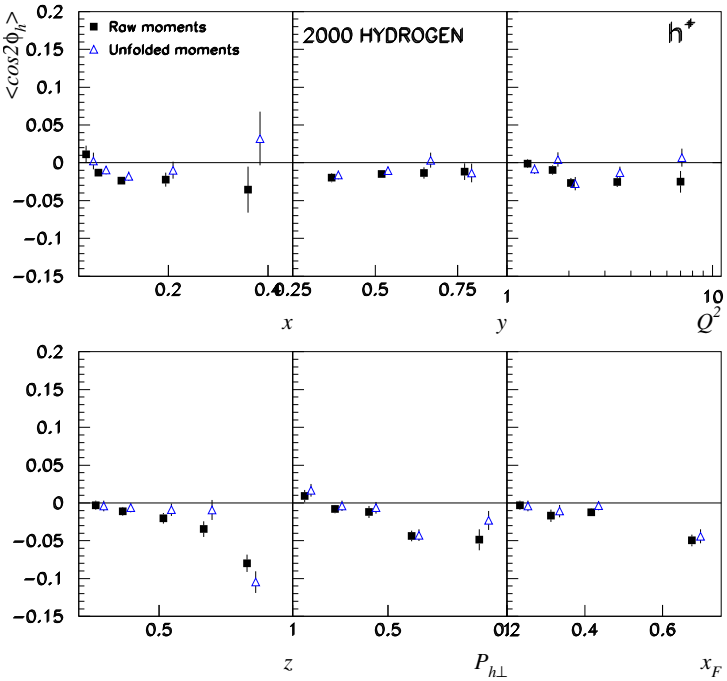

Figure B.21: Comparison between the raw $\langle \cos 2\phi_h \rangle$ moments (black closed square) and the unfolded moments (blue open triangles) for positive hadrons from data collected with deuterium target in 2000.

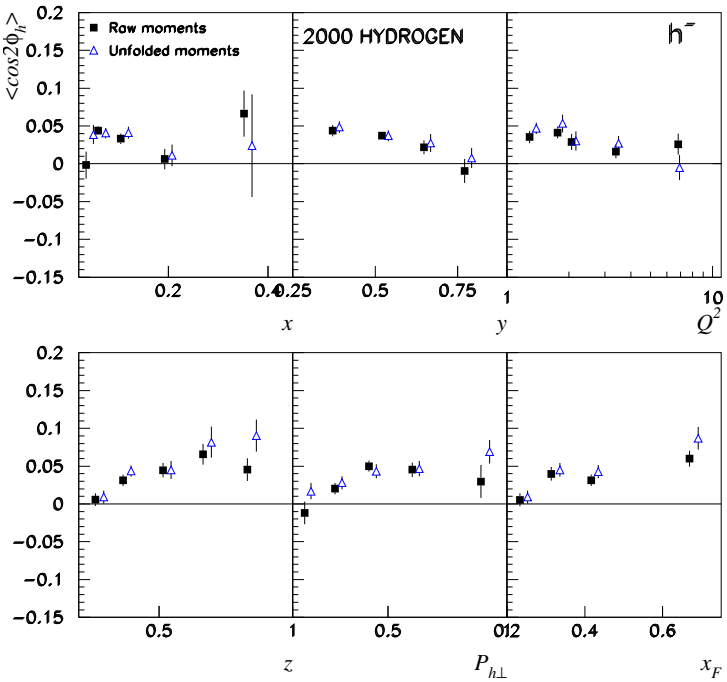

Figure B.22: Comparison between the raw $\langle \cos 2\phi_h \rangle$ moments (black closed square) and the unfolded moments (blue open triangles) for negative hadrons from data collected with deuterium target in 2000.

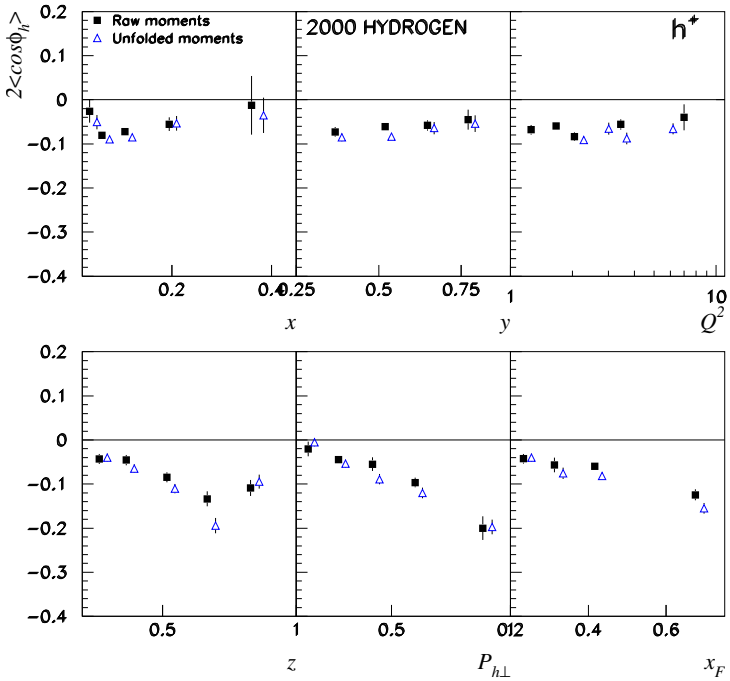

Figure B.23: Comparison between the raw $\langle \cos \phi_h \rangle$ moments (black closed square) and the unfolded moments (blue open triangles) for positive hadrons from data collected with deuterium target in 2004.

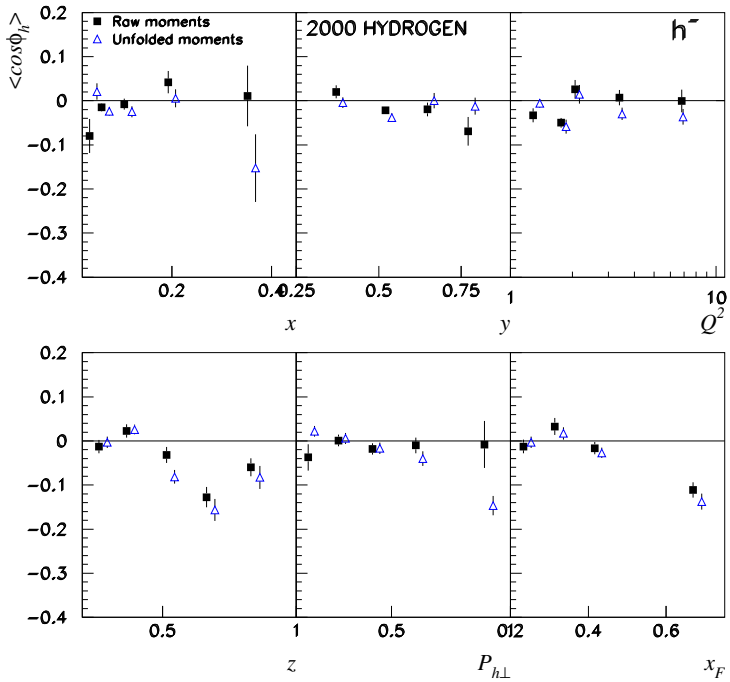

Figure B.24: Comparison between the raw $\langle \cos \phi_h \rangle$ moments (black closed square) and the unfolded moments (blue open triangles) for negative hadrons from data collected with deuterium target in 2004.

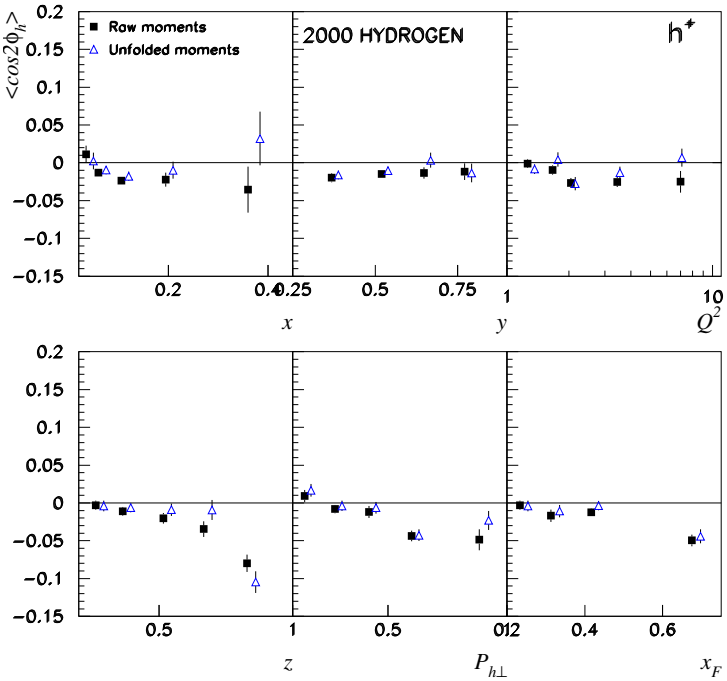

Figure B.25: Comparison between the raw $\langle \cos 2\phi_h \rangle$ moments (black closed square) and the unfolded moments (blue open triangles) for positive hadrons from data collected with deuterium target in 2004.

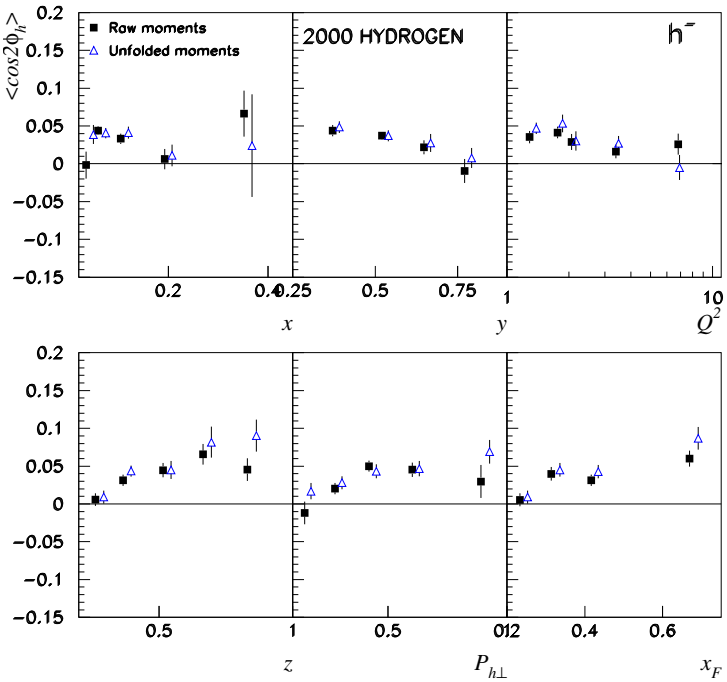

Figure B.26: Comparison between the raw $\langle \cos 2\phi_h \rangle$ moments (black closed square) and the unfolded moments (blue open triangles) for negative hadrons from data collected with deuterium target in 2004.

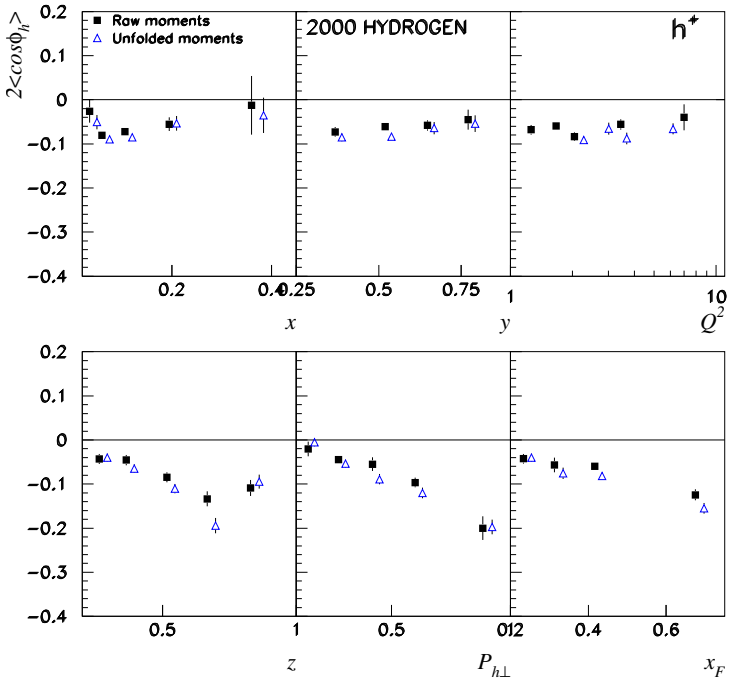

Figure B.27: Comparison between the raw $\langle \cos \phi_h \rangle$ moments (black closed square) and the unfolded moments (blue open triangles) for positive hadrons from data collected with deuterium target in 2005.

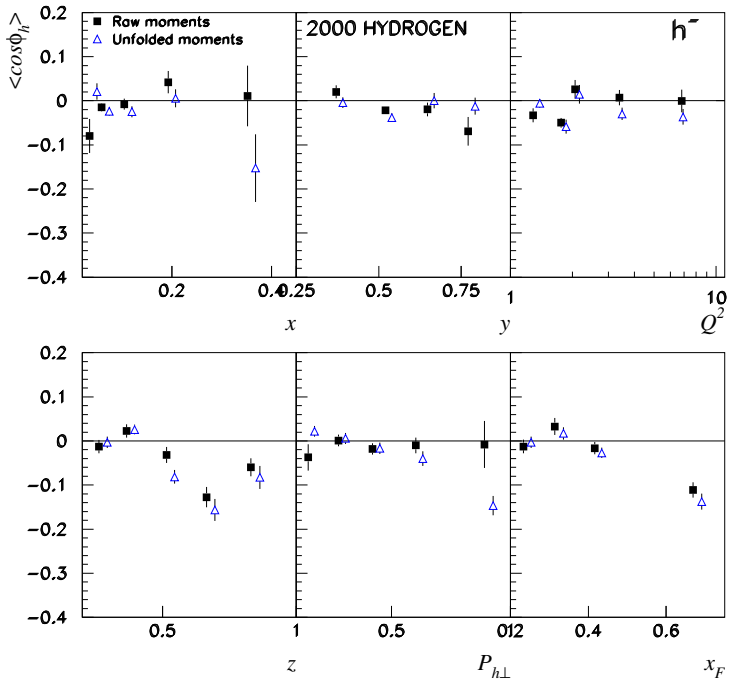

Figure B.28: Comparison between the raw $\langle \cos \phi_h \rangle$ moments (black closed square) and the unfolded moments (blue open triangles) for negative hadrons from data collected with deuterium target in 2005.

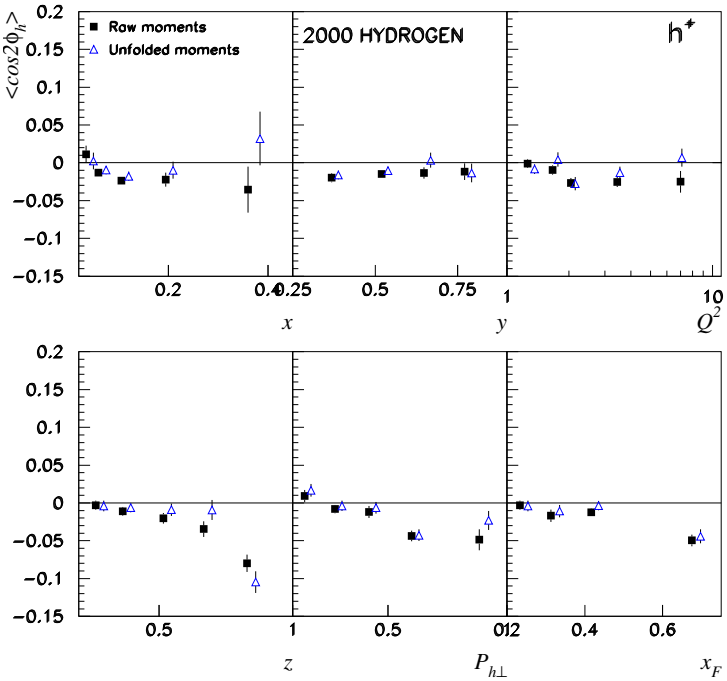

Figure B.29: Comparison between the raw $\langle \cos 2\phi_h \rangle$ moments (black closed square) and the unfolded moments (blue open triangles) for positive hadrons from data collected with deuterium target in 2005.

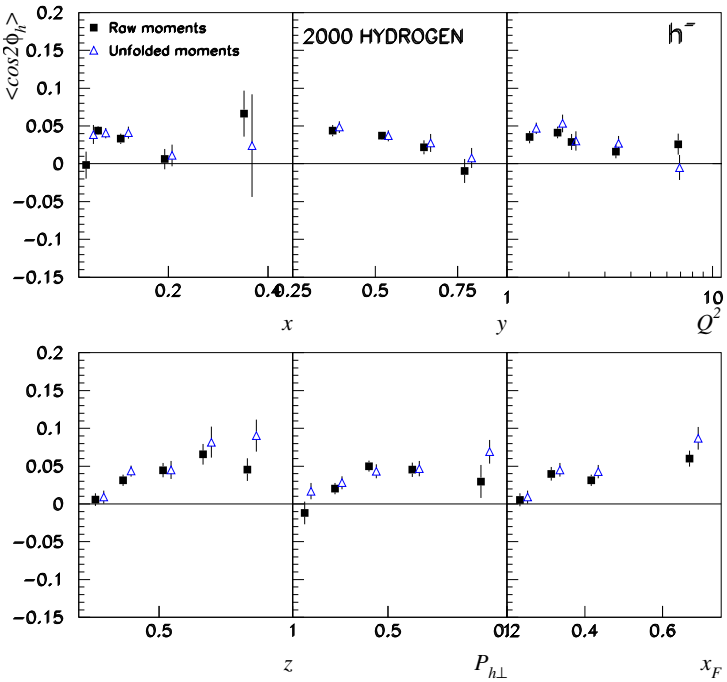

Figure B.30: Comparison between the raw $\langle \cos 2\phi_h \rangle$ moments (black closed square) and the unfolded moments (blue open triangles) for negative hadrons from data collected with deuterium target in 2005.

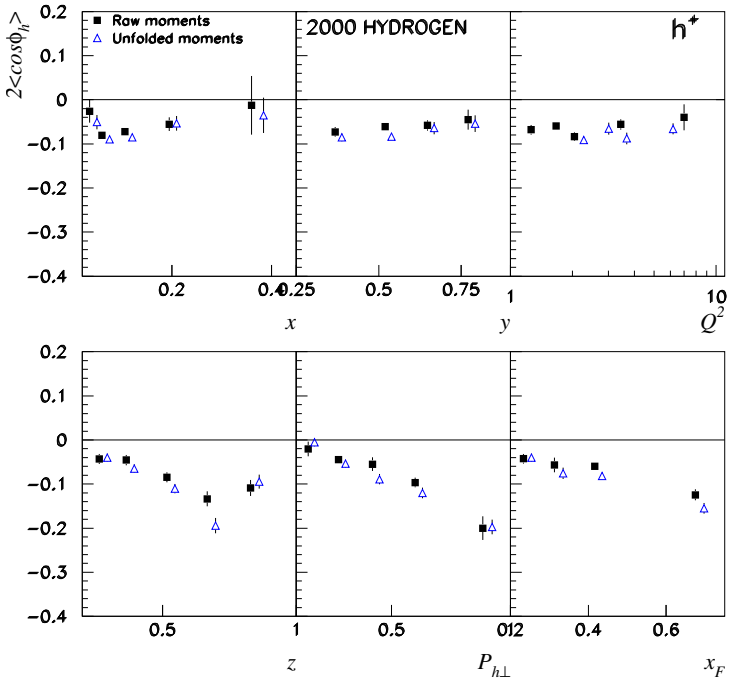

Figure B.31: Comparison between the raw $\langle \cos \phi_h \rangle$ moments (black closed square) and the unfolded moments (blue open triangles) for positive hadrons from data collected with hydrogen target in 2006.

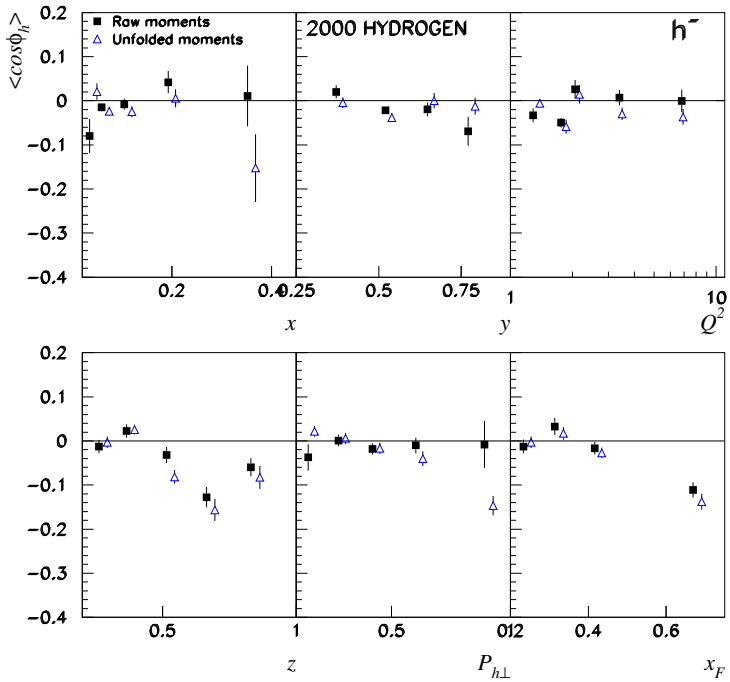

Figure B.32: Comparison between the raw $\langle \cos \phi_h \rangle$ moments (black closed square) and the unfolded moments (blue open triangles) for negative hadrons from data collected with hydrogen target in 2006.

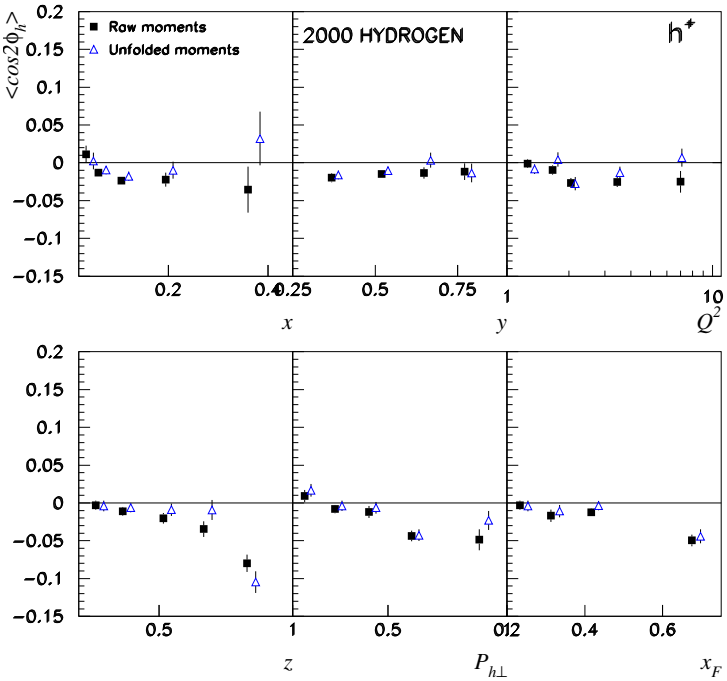

Figure B.33: Comparison between the raw $\langle \cos 2\phi_h \rangle$ moments (black closed square) and the unfolded moments (blue open triangles) for positive hadrons from data collected with hydrogen target in 2006.

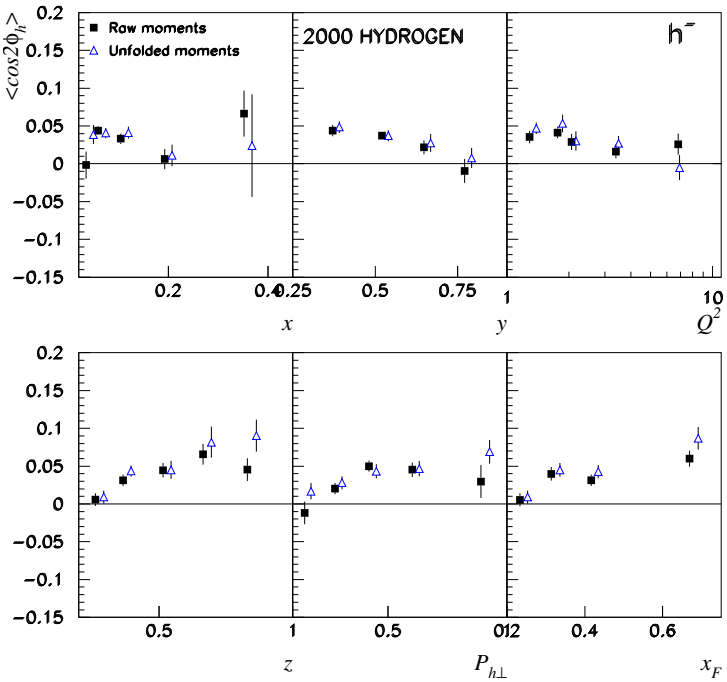

Figure B.34: Comparison between the raw $\langle \cos 2\phi_h \rangle$ moments (black closed square) and the unfolded moments (blue open triangles) for negative hadrons from data collected with hydrogen target in 2006.

Bibliography

[1] E. D. Bloom et al., Phys. Rev. Lett. 23:930, 1969
E. D. Bloom et al., Phys. Rev. Lett. 23:935, 1969

[2] P. L. Anthony et al., E142 Collaboration, Phys. Rev. D54:6620, 1996
K.Abe et al., E154 Collaboration, Phys. Rev. Lett. 79:26, 1997
J. Ashman et al., EMC Collaboration, Nucl. Phys. B328:1, 1989
A. Airapetian et al., HERMES Collaboration, Phys.Lett. B442:484, 1998
K. Ackerstaff et al., HERMES Collaboration, Phys.Lett. B404:383, 1997

[3] K.Abe et al., E143 Collaboration, Phys. Rev. D58:112003, 1998
B. Adeva et al., SMC Collaboration, Phys. Rev. D58:112002, 1998
B. Adeva et al., SMC Collaboration, Phys. Rev. D60:072004, 1999
P. L. Anthony et al., E155 Collaboration, Phys. Lett. B493:19, 1990
P. L. Anthony et al., E155 Collaboration, Phys. Lett. B463:339, 1999

[4] A. Airapetian et al., HERMES Collaboration, Phys.Rev.D75:012007,2007

[5] R. N. Cahn, Phys. Lett. B78: 269, 1978
R. N. Cahn, Phys. Rev. D40 : 3107, 1989

[6] D. Boer, P. J. Mulders, Phys. Rev. D57:5780, 1998

[7] A. Bacchetta, JHEP. 0702: 093, 2007

[8] V. Barone et al., Phys. Rept. 359:1, 2002

[9] M. Anselmino et al., Phys. Rev. D71:074006, 2005
M.Anselmino et al., Eur. Phys. J. A31:373, 2007

[10] H. Georgi, H. D. Politzer, Phys. Rev. Lett. 40:1, 1978

[11] J. C. Collins and A. Metz, Phys. Rev. Lett. 93:252001, 2004
X. Ji et al., Phys. Rev. D71:034005, 2005
X. Ji et al., Phys. Lett. B597:299, 2004
J. C. Collins and D. E. Soper, Nucl. Phys. B193:381,1981

[12] R. L. Jaffe hep-ph/9602236, 1996

[13] K. Goeke et al., Phys. Lett. B618:90, 2005

[14] S. Chekanov et al., (ZEUS Collaboration), Eur. Phys. J. C21:443, 2001
C. Adloff et al., (H1 Collaboration), Eur. Phys. J. C21:33, 2001
C. Adloff et al., (H1 Collaboration), Eur. Phys. J. C30:1, 2003
M. R. Adams et al., (E665 Collaboration), Phys. Rev. D54:3006, 1996
M. Arneodo et al., (New Muon Collaboration), Nucl. Phys. B483:3, 1997
A. C. Benvenuti et al., (BCDMS Collaboration), Phys.Lett. B223:485, 1989
L. W. Whitlow et al., Phys. Lett. B282:475, 1992

[15] J. Ralston et al., Nucl. Phys. B152:109, 1979
R. L. Jaffe and X. D. Ji, Phys. Rev. Lett 67:552, 1991
J. L. Cortes et al., Z. Phys. C55:409, 1992
X. D. Ji, Phys. Lett B284:137, 1992
G. Bunce et al., Ann. Rev. Nuc;. Part. Sci. 50:525, 2000

[16] S. D. Drell and T. Yan, Phys. Rev. Lett. 25:316, 1970
R. L. Jaffe and X. D. Ji, Nucl. Phys. B375:527. 1992

[17] D. Sivers, Phys. Rev. D41:83, 1990;
D. Sivers, Phys. Rev. D43:261, 1991.

[18] A. Airapetian et al., HERMES Collaboration, Phys. Rev. Lett. 84:4047, 2000
A. Airapetian et al., HERMES Collaboration, Phys. Rev. Lett. 94:012002, 2005

[19] V. Alexakhin et al., COMPASS Collaboration, Phys. Rev. Lett. 94:202002, 2005

[20] R. L. Jaffe hep-ph/9710465, 1997

[21] J. C. Collins, Nucl. Phys. B396:161, 1993

[22] H. Avakian, Phys.Rev. D77:014023, 2008

[23] X. Zheng et al. (JLab Hall A Collaboration), Phys. Rev. C70:065207, 2004

[24] M. Amarian et al. (JLab E94-010 Collaboration),
Phys. Rev. Lett. 92:022301, 2004

[25] P. L. Anthony et al., (E155 Collaboration), Phys. Lett. B553:18, 2003

[26] M. Gockeler et al., Phys. Rev. D63:074506, 2001

[27] M. Gockeler et al., Phys. Rev. D72:054507, 2005

[28] J. Balla et al., Nucl. Phys. B510:327, 1998

[29] S. J. Brodsky, D. S. Hwang and I. Schmidt, Phys. Lett. B530:99, 2002

[30] M. Burkardt Nucl. Phys. A735:185, 2004
M. Burkardt, Phys. Rev. D69:074032, 2004
M. Burkardt, Phys. Rev. D69:057501, 2004
M. Burkardt, Phys. Rev. D72:094020, 2005
M. Burkardt, Phys. Lett. B658:130, 2007

[31] A. V. Belitsky et al., Nucl. Phys. B656:165, 2003

[32] J. C. Collins, Phys. Lett. B536:43, 2002

[33] M. Gockeler, Phys. Rev. Lett. 98:222001, 2007

[34] F. Yuan, Phys. Lett. B575:45, 2003

[35] P. V. Pobylitsa, hep-ph/0301236, 2003

[36] R. Jakob et al., Nucl. Phys. A626:937, 1997

[37] Z. Lu and B. Q. Ma, Phys. Lett. B615:200, 2005

[38] G. R. Goldstein and L. P. Gamberg, hep-ph/0209085, 2002

[39] A. Bacchetta et al., Phys. Lett. B578:109, 2004

[40] V. Barone et al., Phys. Lett. B632:277, 2006

[41] Z. Lu et al., Phys. Lett. B639:494, 2006

[42] L. P. Gamberg et al., Phys. Rev. D67:071504, 2003
L. P. Gamberg and G. R. Goldstein, arXiv:0708.0324, 2007

[43] M. Anselmino et al., Phys. Rev. D75:054032, 2007

[44] Belle Collaboration, R.Seidl et al., Phys. Rev. Lett. 96:232002, 2006

[45] EMC Collaboration, J. J. Aubert et al., Phys. Lett. B130:118, 1983
EMC Collaboration, M. Arneodo et al., Z. Phys. C34:277,1987

[46] ZEUS Collaboration, M. Derrick et al., Z. Phys. C25:361, 1991
ZEUS Collaboration, J. Breitweg et al., Phys. Lett.B481:199, 2000

[47] L. Y Zhu et al, FNAL E866/NuSea Collaboration,
Phys, Rev. Lett. 99:082301, 2007

[48] D. Boer, Phys. Rev. D60:014012, 1999

[49] S. Falciano et al., NA10 Collaboration, Z. Phys. C31:513, 1986
M. Guanziroli et al., NA10 Collaboration, Z. Phys. C37:545, 1988

[50] J. S. Conway et al., E615 Collaboration, Phys. Rev. D39:92, 1989
J.G. Heinrich et al., E615 Collaboration, Phys. Rev. D44:1909,1991

[51] A. Bacchetta et al., DESY. 07-105 (hep-ph/0707.3372)

[52] U. D'Alesio, F. Murgia, Phys. Rev. D70:074009, 2004

[53] J. C. Collins et al., Phys. Rev. D73:014021, 2006

[54] A. Bacchetta, Private comunication

[55] E665 Collaboration, M. R. Adam et al., Phys. Rev. D48:5057, 1993

[56] K. Ackerstaff et al., HERMES collaboration, Nucl. Instr. Meth. A417:230, 1998

[57] K. Rith, Prog. Part. Nucl. Phys. 49:145, 2002

[58] A. A. Sokolov and I. M. Ternov, Sov. Phys. Dokladi 8:1203, 1964

[59] D. P. Barber et al., Nucl. Instr. Meth. A338:21, 2000

[60] M. Beckmann et al., Nucl. Instr. Meth. A461:21, 2000

[61] A. Nass et al., Nucl. Instr. Meth. A505:633, 2003

[62] C. Baumgarten et al., Nucl. Instr. Meth. A508:268, 2003

[63] C. Baumgarten et al., Nucl. Instr. Meth. A482:606, 2002

[64] C. Baumgarten et al., Nucl. Instr. Meth. A496:277, 2003

[65] T. Benisch et al., Nucl. Instr. Meth. A471:314, 2001

[66] J. T. Brack et al., Nucl. Instr. Meth. A469:47, 2001

[67] A. Andreev et al., Nucl. Instr. Meth. A465:482, 2001

[68] S.Bernreuther et al., Nucl. Instr. Meth. A367:96, 1995
S.Bernreuther et al., Nucl. Instr. Meth. A416:45, 1998

[69] W. Wander PhD Thesis, HERMES-97-031, 1996

[70] N. Akopov et al., Nucl. Instr. Meth. A479:522, 2002
H. E. Jackson, Nucl. Instr. Meth. A553:205, 2005

[71] X. Artru et al., Phys. Rev. D12:1289, 1975

[72] H. Avakian et al., Nucl. Instr. Meth. A417:69,1998

[73] J. Wendland, PhD Thesis, DESY-THESIS-2003-032, 2003

[74] R. Kaiser, Internal report, HERMES-97-025, 1997

[75] J. Wendland, Internal report, HERMES-01-067, 2001

[76] L. De Nardo, PhD Thesis, HERMES-02-038, 2002

[77] A. Ernst, PhD Thesis, University of Freiburg, 1985

[78] I. Akushevich et al., hep-ph/9906408, 1998

[79] T. Sjostrand, Comput. Phys. Commun. 84:74, 1994

[80] A. Hillenbrand, Phd thesis, DESY-THESIS-2005-035, 2005

[81] P. Liebing, Phd thesis, DESY-THESIS-2004-036

[82] T. Sjostrand, Phys. Rev. D71:043509, 2005

[83] G. Ingelman, Comput. Phys. Commun. 101:108, 1997

[84] CERN Computing and Network division, CERN Program Library Long Writeup W5013, 1993

[85] F. M. Menden, Phd thesis, DESY-THESIS-2001-060, 2001

[86] A. A. Jgoun, Internal report, HERMES-03-001, 2003

[87] A. P. Dvoredsky, Phd thesis, DESY-THESIS-99-042, 1999

[88] A. A. Jgoun, S. I. Manayenkov, Internal report, HERMES-04-027, 2004

[89] A. A. Jgoun, S. I. Manayenkov, Internal report, HERMES-05-027, 2004

[90] Z. Ye, E. C. Aschenauer, Internal report, HERMES-05-038, 2005

[91] G. Cowan, Statistical Data Analysis, Clarendon Press, Oxford, 1998

[92] A. C. Miller, HERMES Internal report, 2002

[93] A. Prokudin, Private comunication

Acknowledgment

First of all I would like to thank my supervisor, Prof. Paola Ferretti Dalpiaz, who gave me the opportunity to take part in an international community like HERMES, and to work in new exciting aspects of nucleon physics.
Thanks to Marco Contalbrigo, for his guidance and support, but especially for his infinite patience in this long adventure. This thesis would have not be possible without your help, grazie!
I am grateful to Alessandro Bacchetta for myriad of discussions on the theoretical aspects involved in this thesis, and a lot of thanks for having published the inestimable *new testament*! Thanks to Alexei Prokudin, who helped me in improving the understanding of theoretical interpretations and provided the most recent results of the Torino group.

Special thanks to Naomi, Elke, Andy, Gunar, Uli, Bino, Lara, Markus, Luciano, Rebecca, Anton and all the '*Transversity & Co*' enthusiasts, for the invaluable discussions and suggestions essential to develop a so interesting as well as complicated analysis.

Naturalmente non poteva mancare il gruppo italiani!!! Grazie a Pasquale, Erika, Lara, Ignazio, Luigi, Paolo, tutti i Marco, Alessandro e Lucia per avermi iniziato alle meraviglie di Amburgo, per le fantastiche cene all'italiana, e per avermi dato l'opportunitá di partecipare, e vincere, il piú ambito premio che sia mai esistito nella storia dell'umanitá: il premio TAMO.

Molto di questa tesi non sarebbe stato possibile senza l'aiuto di Luca, conoscitore e mentore per utilizzo pc: un omaggio per te: !! Grazie!
Thank you Michelle for encouraging me in stressful periods, for interesting discussions and *language* support!

Cosa sarebbero state le giornate full-immersion senza la ricarica periodica dei nostri 'coffee' e pettegolezzi? Grazie a Nicoletta e Melissa! E cosa senza i commenti agli articoli e alle immagini di *Repubblica on-line*, le pause rubate al bar o l'organizzazione di fughe all'estero per sfuggire alla full-immersion suddetta? Grazie Luciano!

Infine grazie alla mia meravigliosa famiglia: a mia madre, mio padre e mio fratello per il loro amore e per esserci sempre, e a Davide, per il suo appoggio incondizionato e per fare parte della mia vita, vi voglio bene!